

Universit   Pierre et Marie Curie  
Laboratoire Kastler Brossel

TH  SE DE DOCTORAT DE L'UNIVERSIT   PARIS VI  
sp  cialit   : Physique Quantique

pr  sent   par  
Vu TRAN

pour obtenir le titre de  
Docteur de l'Universit   Paris VI

Sujet de la th  se :

TOWARDS HIGH PRECISION SPECTROSCOPY OF HYDROGEN MOLECULAR IONS  $H_2^+$   
AND  $HD^+$  : *Theory and Experiment*

SOUTENUE LE 17 DECEMBRE 2001 DEVANT LE JURY COMPOS   DE :

M. A. B	RAPPORTEUR
M. C. D	RAPPORTEUR
M. E. F	PR��SIDENT
M. G. H	EXAMINATEUR
M. I. K	DIRECTEUR DE TH��SE



*To my parents ...*

## Acknowledgements

And I would like to acknowledge ...

## **Abstract**

This is where you write your abstract ...

## Résumé

C'est ici que l'on va écrire le résumé

# Contents

<b>1</b>	<b>Precision Spectroscopy of Molecular Hydrogen Ions : A Survey</b>	<b>11</b>
1.1	Motivation . . . . .	11
1.2	Context . . . . .	13
1.2.1	Proton's mass determination . . . . .	14
1.2.2	Electron's mass determination . . . . .	14
1.3	Direct optical determination of $m_p/m_e$ . . . . .	15
1.3.1	Atoms or molecules ? . . . . .	15
1.3.2	Choice of transitions . . . . .	16
1.4	Principle of experiment . . . . .	18
1.4.1	Ion trapping . . . . .	19
1.4.2	Molecular Ion sympathetic cooling . . . . .	22
1.4.3	Ion detection : REMPD . . . . .	23
1.4.4	Ion source preparation . . . . .	23
1.5	Precision spectroscopy of molecular hydrogen ions : Status . . . . .	25
1.5.1	Brief history . . . . .	25
1.5.2	Theoretical developpments . . . . .	28
1.5.2.1	Highly accurate nonrelativistic energy calculations . . . . .	28
1.5.3	Energy corrections . . . . .	29
1.5.3.1	Hyperfine structure . . . . .	33
1.5.3.2	Two-photon transition probability . . . . .	34
1.5.4	Status of $H_2^+$ experiment . . . . .	35
1.6	Comparision between $H_2^+$ and $HD^+$ . . . . .	40
<b>2</b>	<b>State-Selected Ion Production by REMPI Method</b>	<b>41</b>
2.1	Ion source using REMPI technique : Theory . . . . .	41
2.1.1	Introduction . . . . .	41
2.1.2	Vibrational and rotational distribuiton of $H_2^+$ ions . . . . .	42
2.1.2.1	Vibrational distribution . . . . .	44
2.1.2.2	Rotational distribution . . . . .	45
2.2	Experimental set-up . . . . .	51
2.2.1	Laser source at 303 nm . . . . .	52
2.2.1.1	Pulsed Dye Laser . . . . .	53
2.2.1.2	YAG laser . . . . .	54
2.2.1.3	Optimization of frequency doubler of the Sirah dye laser . . . . .	56
2.2.2	Automatic scanning of laser wavelength . . . . .	56
2.2.3	Beam shaping . . . . .	57

2.2.4	The ion source . . . . .	60
2.2.4.1	Conception . . . . .	60
2.2.4.2	Ion optical bench test the system with Simion . . . . .	65
2.2.4.3	Experimental results . . . . .	67
<b>3</b>	<b>Quasi-degenerate two-photon HD<sup>+</sup> spectroscopy in the Lamb-Dicke regime</b>	<b>69</b>
3.1	Introduction . . . . .	69
3.1.1	Two-photon spectroscopy . . . . .	69
3.1.2	Lamb-Dicke regime . . . . .	70
3.1.3	HD <sup>+</sup> spectroscopy : limits of single-photon transition method . . . . .	71
3.2	Complementary informations to the article . . . . .	88
3.2.1	Hyperfine structure of two-photon transition . . . . .	88
3.2.2	Physical interpretation of Bloch equations . . . . .	89
3.2.3	Molecular Dynamics simulation of trapped HD <sup>+</sup> ions : . . . . .	89
3.2.4	Dressed atom approach . . . . .	90
3.2.4.1	Two-photon rate . . . . .	92
3.2.4.2	ac Stark shift . . . . .	94
3.2.5	Comparison of two approaches . . . . .	95
3.2.5.1	Analytical formula for $\rho_{44}$ . . . . .	95
3.2.5.2	Laser phase noise influence . . . . .	96
3.2.5.3	Misalignment of two counterpropagating lasers . . . . .	97
<b>4</b>	<b>...</b>	<b>99</b>
<b>A</b>	<b>Notes on H<sub>2</sub><sup>+</sup></b>	<b>101</b>
A.1	Exact three-body problem . . . . .	101
A.2	Born-Oppenheimer approximation . . . . .	102
A.3	Two-photon transitions . . . . .	104
<b>B</b>	<b>Mathematica program for the calculation of rotational distribution of H<sub>2</sub><sup>+</sup> ions</b>	<b>105</b>
B.1	Table of matrix elements . . . . .	105
B.2	Photoionization rate . . . . .	106
B.3	Rotational distribution of H <sub>2</sub> <sup>+</sup> ions . . . . .	108
<b>C</b>	<b>LabVIEW program for the external trigger of YAG laser</b>	<b>111</b>
<b>D</b>	<b>Notes on Diatomic Molecules</b>	<b>115</b>
D.1	Born-Oppenheimer approximation for diatomic molecules . . . . .	115
D.2	Symmetries in the diatomic molecules . . . . .	117
D.3	Rotational and vibrational energies . . . . .	119
D.4	Hund's cases . . . . .	121
D.4.1	Hund's case (a) : $ \Delta E  \gg  A  \gg B$ . . . . .	121
D.4.2	Hund's case (b) : $ \Delta E  \gg B \gg  A $ . . . . .	122
D.4.3	Hund's case (c) : $ A  \gg  \Delta E  \gg B$ . . . . .	123
D.4.4	Hund's case (d) : $B \gg  \Delta E  \gg  A $ . . . . .	123
D.4.5	Hund's case (e) : $ A  \gg B \gg  \Delta E $ . . . . .	123

<b>E</b>	<b>Multiphoton transition in Lamb-Dicke regime</b>	<b>125</b>
E.1	Introduction . . . . .	125
E.2	Single-photon transition or Lamb-Dicke regime . . . . .	126
E.3	Two-photon transition . . . . .	127
E.3.1	$\Lambda$ -configuration . . . . .	127
E.3.2	Ladder configuration . . . . .	128
E.4	Dressed atom approach . . . . .	128
E.5	Evolution operator approach . . . . .	131



# Chapter 1

## Precision Spectroscopy of Molecular Hydrogen Ions : A Survey

High precision spectroscopy plays an important role in the development of both fundamental and applied physics. For fundamental physics, one can cite the detection of small discrepancy in energy between two energy levels  $^2S_{1/2}$  and  $^2P_{1/2}$  of hydrogen atom (commonly known as Lamb shift) as the origin of the birth of Quantum Electrodynamics and for applied physics, the high precision measurement of frequency of Cs as a base for atomic clocks.

The most interesting systems for high precision spectroscopy are always simple systems because the energy structure is simple and the highly accurate theoretical calculations are possible. Therefore, from the early days of precision spectroscopy, hydrogen-like systems like H,  $\text{He}^+$  has been the most favorable systems. We can also mention hydrogen molecules  $\text{H}_2$  and molecular hydrogen ions  $\text{H}_2^+$ ,  $\text{HD}^+$ ,  $\bar{p}\text{He}^+$  antiprotonic helium or two-electron atomic system like He ...

There're a lot of challenges for high precision spectroscopy such as Doppler broadening, laser phase noise, collision shift, light shift, Zeeman shift ... But today, with the spectacular achievement of the cooling and trapping techniques and frequency comb technology, these measurements are strongly improved. Recently, there're many wonderful progresses and achievements in this fields for example, the high precision proton radius determination [1, 2], tests of time-variation of fundamental constants [3], the highly stable and accurate atomic clocks [4, 5] ...

In this chapter, i will present the motivation of the quest for higher precision spectroscopy in molecular hydrogen ions  $\text{H}_2^+$  and  $\text{HD}^+$ , describe the theoretical developments and present the principle of the experiment and the present results.

### 1.1 Motivation

Since the invention of ion trapping techniques using Penning trap, the mass or mass ratio measurements are the "private affair" of mass spectrometers relying on RF or microwave frequency measurements. With the development of laser frequency comb technique, one can now easily measure the transition frequency in the optical domain with an unprecedented accuracy. This triggers the interest among the laser spectroscopists to use this technique as an alternative method to determine mass ratios and especially the proton-to-

electron mass ratio using hydrogen molecular ions  $\text{H}_2^+$  and  $\text{HD}^+$ . There are three groups actively tackling the hydrogen molecular ions for the measurement of proton-to-electron mass ratio : one  $\text{H}_2^+$  group at LKB Paris led by L. Hilico, two  $\text{HD}^+$  groups at Düsseldorf and Amsterdam led by S. Schiller and J. C. J. Koelemeij respectively. The main motivations are :

- One of the objectives of this research is to **improve the proton-to-electron mass ratio  $m_p/m_e$  using laser-based spectroscopy**. Up to now, this ratio is determined by measuring separately the electron mass and proton mass using mass spectroscopy techniques. The electron mass  $m_e$  is determined through Larmor-to-cyclotron frequency ratio measurements [6] and the proton mass is determined through the comparison of cyclotron frequencies using those measurements, the proton-to-electron mass ratio is determined to be :

$$\frac{m_p}{m_e} = 1836.15267245(75)[4.1 \cdot 10^{-10}] .$$

A direct optical determination of  $m_p/m_e$  at the  $10^{-10}$  accuracy level or better with a completely different method is very important from the metrological point of view.

- **The fine structure constant  $\alpha$**  - one of the most important fundamental constants in physics - is linked to  $m_p/m_e$  is through the relation [7]:

$$\alpha^2 = \frac{R_\infty}{c} [6.6 \times 10^{-12}] \frac{m_X}{m_p} [2.0 \times 10^{-10}] \frac{m_p}{m_e} [4.1 \times 10^{-10}] \frac{h}{m_X} [6.6 \times 10^{-10}], \quad (1.1)$$

where  $X$  is Rb [8] or Cs [7] and the values in the square brackets are the relative uncertainties.

Note that the measurement of  $h/m_X$  should soon reach the accuracy level of  $4.0 \times 10^{-10}$ , therefore, making the proton-to-electron mass ratio the main source of uncertainty.

- The third motivation of the  $m_p/m_e$  measurement is **the test of QED**. Quantum Electrodynamics (QED) is the most precisely tested theory until now. It stands firm against many extremely precise measurements. Taking advantage of the permanent progress of high precision techniques (laser frequency comb, cooling techniques, . . .), experimentalists perform more and more stringent QED tests using simple atomic or molecular species. Spectroscopy at the  $10^{-11}$  or  $10^{-12}$  accuracy level in  $\text{H}_2^+$  or  $\text{HD}^+$  would open avenues for molecular bound state QED.
- The fourth and long term motivation is **the quest for time-variation of fundamental constants**. Indeed, the foundation of general relativity is based on the Einstein equivalence principle. The tests of time-independence of fundamental constants aim at verifying the validity of Einstein equivalence principle. Among all the fundamental constants, the proton-to-electron mass ratio seems to be one of the most favorable candidates due to a high sensitivity [9, 10, 11, 12]. As an

exemple, using the transition between the  $H_2^+$  rovibrational states  $\{A = (\nu = 0, L = 0) \rightarrow B = (\nu = 0, L = 1)\}$  and  $\{C = (\nu = 0, L = 0) \rightarrow D = (\nu = 2, L = 0)\}$  the transition frequency ratio  $\Delta E_{AB}/\Delta E_{CD}$  depends only on  $m_p/m_e$  and we have :

$$\frac{d}{dt} \ln\left(\frac{\Delta E_{AB}}{\Delta E_{CD}}\right) = 0.545 \frac{d}{dt} \ln\left(\frac{m_p}{m_e}\right) .$$

Measuring the transition frequencies at the  $10^{-14}$  accuracy level on a 10 years time scale would make it possible to test the  $m_p/m_e$  time dependence at the  $2 \times 10^{-15} \text{ year}^{-1}$  level. We should note also that there are many possible good candidates for the tests of time independence of  $m_p/m_e$ . For exemple, by comparing a rovibrational transition in  $SL_6$  with the fundamental hyperfine transition in Cs, A. Shelkonikov *et al.* [13] reported a limit of the temporal variation of  $m_p/m_e$  as :

$$\frac{1}{(m_p/m_e)} \frac{d}{dt} (m_p/m_e) = (-3.8 \pm 5.6) \times 10^{-14} \text{ year}^{-1}$$

Using both  $C \rightarrow D$   $H_2^+$  two-photon transition and  $\{I = (\nu = 0, L = 2) \rightarrow J = (\nu = 3, L = 3)\}$  one-photon transition in  $HD^+$ , the time dependence of  $m_p/m_d$  can also be tested since :

$$\frac{d}{dt} \ln\left(\frac{\Delta E_{IJ}}{\Delta E_{CD}}\right) = -0.0008 \frac{d}{dt} \ln\left(\frac{m_p}{m_e}\right) + 0.151 \frac{d}{dt} \ln\left(\frac{m_p}{m_d}\right)$$

## 1.2 Context

In this section, i will discuss the principles of the experiments of determination of  $m_p/m_e$  using mass spectroscopy techniques and give the most recent results. This will help understanding the traditional ways of mass and mass ratio determination and the radical difference between them and our optical direct method of measurement.

The device used in most of mass measurements is the Penning trap. This ion trap technique requires both a static electric field and a static magnetic field in order to confine the particles. The static electric field is created by three electrodes : two endcap and a ring as shown in the left part of Fig. 1.1. In the ideal Penning trap, the electrodes are hyperboloids of revolution. The strong homogeneous axial magnetic field  $\vec{B}$  is used to confined axially the charged particles. The trajectory of a charged particle in the Penning trap is characterized by three frequencies : the modified cyclotron frequency  $\omega'_c$ , the axial frequency  $\omega_z$  and the magnetron frequency  $\omega_m$ . These frequencies are experimentally observable using different methods. For example, the axial frequency  $\omega_z$  can be determined by applying an alternative voltage between one of two endcaps and the ring and using a phase-sensitive technique to detect the driven oscillation of the charged particle [14]. The free cyclotron frequency  $\omega_c = qB/m$  which is important for the mass determination is obtained from these three observable frequencies via the invariance theorem, which is valid in spite of a possible misalignment of magnetic field  $\vec{B}$  or some imperfections of electrodes [14], and that states that :

$$\omega_c^2 = \omega_c'^2 + \omega_z^2 + \omega_m^2 .$$

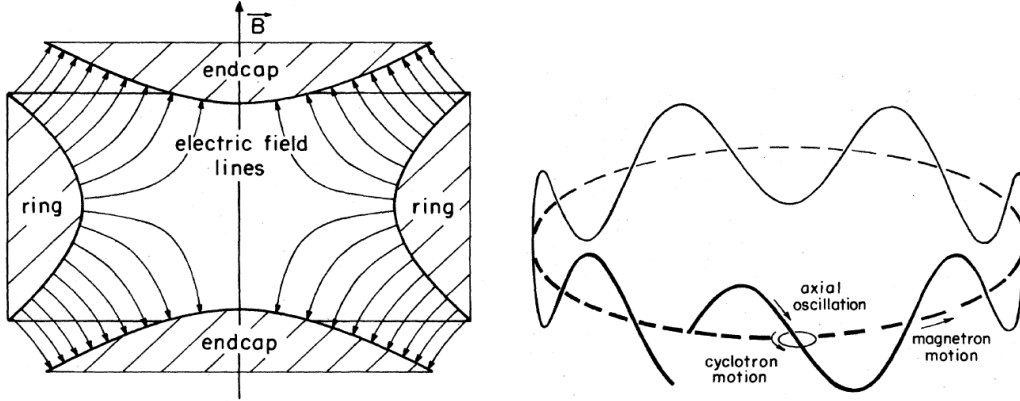


Figure 1.1: Penning trap and the orbit of charged particle in the trap [14]

### 1.2.1 Proton's mass determination

In order to obtain the proton's mass, the idea is to compare the cyclotron frequency of a proton  $\omega_c^1 = q_1 B/m_p$  with the cyclotron frequency of a reference ion of well-determined mass  $\omega_c^2 = q_2 B/m_{ion}$  through the relation :

$$m_p = \frac{q_2 \omega_c^1}{q_1 \omega_c^2} m_{ion} .$$

Using this principle, in 1999, R.S. Van Dyck, Jr et al. [15] used an improved Penning trap mass spectrometer to compare the cyclotron frequency of a single proton and that of a single  $^{12}\text{C}^{+4}$  ion and determined the value of proton mass  $m_p$  in atomic units :

$$m_p = 1.007\,276\,466\,89\,(14)\,u \quad [1.4\,10^{-10}] .$$

and in 2008, Solders et al. [16] used the SMILETRAP and  $D^+$  as the reference ion to determine the proton mass and they obtained a similar result :

$$m_p = 1.007\,276\,466\,95\,(18)\,u \quad [1.8\,10^{-10}] .$$

### 1.2.2 Electron's mass determination

The principle of electron's mass measurement is to compare the electronic Larmor frequency  $\omega_L = g \frac{e}{2m_e} B$  and the cyclotron frequency of an ion  $\omega_c = \frac{q}{m_{ion}} B$  in the same magnetic field. One can then determine the electron mass  $m_e$  through the following relation [6] :

$$m_e = \frac{g e \omega_c}{2 q \omega_L} m_{ion}$$

In the experiment at Mainz [6], a single  $^{12}\text{C}^{+5}$  ion is trapped by a cryogenic Penning trap. The ratio  $\omega_c/\omega_L$  is determined experimentally using the spin-flip rate method [17]

and using a highly accurate theoretical value of the  $^{12}\text{C}^{+5}$   $g$ -factor leading to  $m_e/m_{^{12}\text{C}^{+5}}$ . Taking into account the mass of 5 missing electron and computed binding energies, the electro's mass in atomic mass unit is obtained to be:

$$m_e = 0.0005485799092(4) u$$

**Comments :**

1. The "direct" determination of  $m_p/m_e$  have been also done by several groups using a similar method by computing directly the cyclotron frequencies of electrons and protons [18] alternately confined to the same uniform magnetic field in a Penning trap.

2. In 1983, D. J. Wineland *et al.* [19] measured indirectly the proton-to-electron mass ratio by measuring the electron  $g_j$  factor of  $^9\text{Be}^+$  confined in a Penning trap. The interesting point of this result is that the cyclotron resonance frequencies are measured by the laser-fluorescence techniques not by observing the induced currents in the ring electrode as in the previous experiments.

3. From an internal communication, we learned that the group of Klaus Blaum at Heidelberg, Germany improved the electron mass in atomic unit by a factor of 15 using a novel technique which allows a phase-sensitive cyclotron frequency measurement at very low temperatures [20]. With this new determination of the electron mass, the relative accuracy on  $m_p/m_e$  will soon be now only limited by the value of proton mass in atomic mass unit.

### 1.3 Direct optical determination of $m_p/m_e$

In this section, i explain why molecular hydrogen ions are the most favorable candidates for a direct optical measurement of  $m_p/m_e$  and i also discuss the most interesting transitions in these systems.

#### 1.3.1 Atoms or molecules ?

The basic idea of a direct optical determination of  $m_p/m_e$  is to combine an absolute frequency measurement and a highly accurate theoretical calculation of energy levels to deduce the proton-to-electron mass ratio. Therefore, the candidates must satisfy the following conditions:

- The particle must be simple to allow the highly accurate energy calculations and QED corrections.
- The transition frequency range must be accessible with actual laser i.e., in between  $9 \mu\text{m}$  and  $0.2 \mu\text{m}$ . The  $10^{-10}$  relative accuracy level is achievable with transition widths of 1 – 10 kHz. In the visible domain, this corresponds to Doppler free spectroscopy.
- The sensitivity  $S$  of  $m_p/m_e$  on the transition frequency is an important criterion. It is defined by  $\Delta\nu/\nu = S\Delta\mu/\mu$ .

The simplest and most explored systems are the hydrogenlike atoms. High precision measurement of  $1S$ - $2S$  transition frequency in atomic hydrogen can reach the level of accuracy of 10 Hz which corresponds to a relative accuracy of  $4.2 \times 10^{-15}$  [21, 22].

The energy of the  $(n, l)$  level of hydrogenlike atom is given by :

$$E_{nl} = -m_r c^2 \frac{(Z\alpha)^2}{2n^2} ,$$

where the reduced mass is  $m_r = m_e m_N / (m_e + m_N) = m_e A \mu / (1 + A \mu)$  with  $A$  the mass number, considering that neutron and proton have the same mass. This lead to a small sensitivity  $S = 1/(1 + A\mu)$  since  $A\mu > 1836$ .

Hydrogenlike atoms are not well suited for  $m_p/m_e$  determination. Indeed, to get this ratio at the  $10^{-10}$  level requires experimental measurements and theoretical calculations at the  $5 \times 10^{-14}$  level. The most precise experimental determination of  $1S - 2S$  transition frequency attains the  $4.2 \times 10^{-15}$  accuracy level [21] but unfortunately the theoretical calculation of this transition frequency is limited at 6 kHz i.e.  $2.4 \times 10^{-13}$  accuracy level [23]. In practice, atomic hydrogen is used for Rydberg constant [24, 25], Lamb shift [24, 25] and proton radius [1] determination,  $m_p/m_e$  being an input parameter.

A more complicated but theoretically exploitable system are the hydrogen molecular ions  $H_2^+$  and  $HD^+$  for which highly accurate nonrelativistic energy levels [26, 27] as well as relativistic, QED and hyperfine structure corrections [28] are calculated.

$H_2^+$  can be probed using two photon vibrational transitions in the 9-12  $\mu\text{m}$  domain.

$HD^+$  offers a wider variety of single-photon vibrational or rotational transitions, two-photon vibrational transitions in the 5 to 1  $\mu\text{m}$  domain.

In a diatomic molecule, the vibrational frequency scales as  $\nu_{12} \sim \sqrt{m_e/m_r} R_\infty c$ , where  $m_r = m_p/2$  for  $H_2^+$  and  $m_r = m_p m_d / (m_p + m_d)$  for  $HD^+$ . The sensitivity for vibrational transitions are given in [26] and close to  $S = 1/2$  which is 1000 times larger than in hydrogenlike systems. Spectroscopy at the  $5 \times 10^{-11}$  level, corresponding to 3 kHz at 10  $\mu\text{m}$  or 30 kHz at 1  $\mu\text{m}$ , make it possible to determine  $m_p/m_e$  at the  $10^{-10}$  level.

Rotational transition frequencies in  $HD^+$  scales as  $m_e/m_r R_\infty c$  leading to a sensitivity  $S \approx 1$ . Nevertheless, with rotational transition frequencies,  $5 \times 10^{-11}$  accuracy level corresponds to  $\sim 3$  Hz requiring long interaction times.

Conclusion : The molecular hydrogen ions  $H_2^+$  and  $HD^+$  are the most interesting candidates for the optical measurement of the proton-to-electron mass ratio.

### 1.3.2 Choice of transitions

To determine which transitions in  $H_2^+$  and  $HD^+$  are the most favorable, we first ignore sophisticated effects like the hyperfine structure, the black body radiation, Zeeman splitting ... and we take into consideration only the fundamental questions of laser wavelength and of the transition probability between two rovibrational levels.

Figures 1.2 and 1.3 show the two first Born-Oppenheimer electronic energy curves for  $H_2^+$  and  $HD^+$ . It also shows some bound rovibrational levels supported by the  $1s\sigma_g$  binding curve. The red arrows shows the rovibrational transitions discussed below. The blue/purple arrows show the dissociation process to the dissociative  $2p\sigma_u$  energy curve.

For  $\text{H}_2^+$ , single photon transitions are forbidden by Pauli exclusion principle, only two-photon transitions are allowed<sup>1</sup>. The theoretical calculations of the two-photon probabilities between two rovibrational states  $\{|\nu, J = 0\rangle, |\nu', J = 0\rangle\}$  of  $\text{H}_2^+$  show that the two-photon signals are large only for the transitions with  $|\Delta\nu| = 1$  and dramatically decrease with  $|\Delta\nu|$  [29]. We can naturally extend this conclusion for different values of  $J$ . The  $|\Delta\nu| = 1$  transitions require a laser source in the 8 – 12  $\mu\text{m}$  range. One might think about  $\text{CO}_2$  laser as a two-photon excitation source because it has a line spectrum in the range 9 – 11  $\mu\text{m}$ , but the narrow tuning range makes it difficult to obtain a coincidence between laser line and the wavelength for two-photon transitions. This is the main disadvantage of  $\text{CO}_2$  laser sources. Our group has shown that Quantum Cascade Laser (QCL) phase-locked on a  $\text{CO}_2$  laser with a frequency offset are well suited for  $\text{H}_2^+$  two-photon excitation [30].

Two-photon transitions in  $\text{H}_2^+$  can be probed for any values of the rotational quantum number  $L$  and  $L' = L, L \pm 2$ . For odd values of  $L$ , the total nuclear spin is  $I = 1$  leading to a rich hyperfine structure. For even values of  $L$ ,  $I = 0$  and there is no hyperfine structure. As a consequence, there are less substates and thus larger populations, i.e., larger signals.

Two-photon transition spectra including fine and hyperfine structure has been studied [31] showing that  $L \rightarrow L' = L$  transitions are most favorable. For thermal  $\text{H}_2$  mother molecules, the rotation quantum number is less than 5, so only low  $L$  values are experimentally possible.

Finally, we have chosen to probe the  $|\nu = 0, L = 2\rangle \rightarrow |\nu = 1, L = 2\rangle$  two photon transition at 9.17  $\mu\text{m}$  as shown in Fig. 1.2 because we have a high power QCL ( $\sim 100$  mW) at that wavelength.

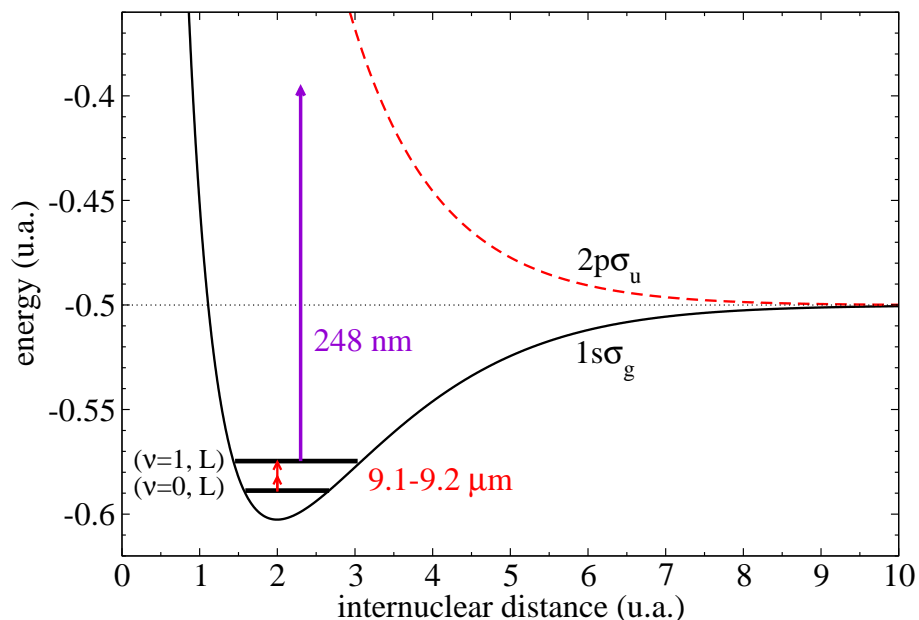


Figure 1.2: Two-photon rovibrational transitions and photodissociative transitions in  $\text{H}_2^+$ . The electronic curves  $1s\sigma_g$  and  $2p\sigma_u$  are calculated by N. Billy.

<sup>1</sup>More informations can be found in the Appendix A

$\text{HD}^+$  candidate possesses a big advantage in comparison with  $\text{H}_2^+$  : single photon transitions are allowed due to the breaking of the internuclear exchange symmetry. Therefore, in the experiment using  $\text{HD}^+$ , both one- and two-photon transitions can be exploited.

At thermal equilibrium, all  $\text{HD}^+$  ions are in the vibrational ground state levels  $|\nu = 0, L = 0, \dots, 5\rangle$ . Although the Franck-Condon factors between two vibrational levels  $\nu$  and  $\nu'$  decrease very quickly with  $\Delta\nu = \nu' - \nu$ , it's possible to saturate overtone transitions with  $\Delta\nu$  up to 8 using standard lasers. The advantage of overtone transitions is to use near IR lasers. These transitions corresponds to large frequencies and for a given resolution  $\Delta\nu$  leads to low relative resolutions.

So far, rovibrational transitions have been observed :

- In Düsseldorf, in the group led by S. Schiller using the  $|\nu = 0, L = 2\rangle \rightarrow |\nu = 4, L = 3\rangle$  transition [32] depicted in Fig. 1.3. They also probed the transition  $|\nu = 0, L = 0\rangle \rightarrow |\nu = 1, L = 1\rangle$  [33].
- In Amsterdam, in the group led by J. C. J. Koelemeij using the  $|\nu = 0\rangle \rightarrow |\nu = 8\rangle$  vibrational transition [34].

The figure 1.3 shows single photon transition for the experiment at Düsseldorf [32].

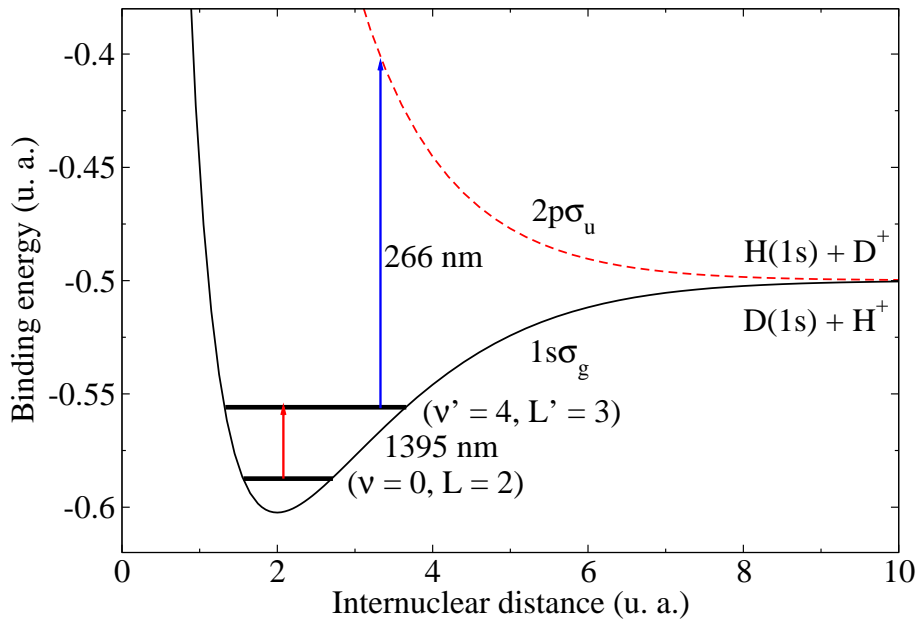


Figure 1.3: Single photon transition in  $\text{HD}^+$  as in [32]. We use the data in [35] to obtain these electronic curves.

## 1.4 Principle of experiment

The principle of direct optical determination of proton-to-electron mass ratio is the following : Using a frequency-stabilized laser to measure the transition frequency  $\nu_{12}$  between to rovibrational state  $|1\rangle$  and  $|2\rangle$  with high precision and using a numerical calculation of

$\nu_{12} = f(R_\infty, \alpha, m_p/m_e, \dots)$  which includes the relativistic and QED corrections, one can determine the mass ratio  $m_p/m_e$  as

$$m_p/m_e = f^{-1}(R_\infty, \alpha, \nu_{12}, \dots) .$$

Determining the proton-to-electron mass ratio  $m_p/m_e$  at the relative uncertainty level of  $10^{-10}$  corresponds to an uncertainty of the transition frequency measurement of about 3 kHz at 32 THz ( $\text{H}_2^+$ ) or 10 kHz at 100 THz ( $\text{HD}^+$ ). The errors in the theoretical calculation which comes from high order QED effects must be also limited to  $10^{-10}$ .

The experimental requirements to achieve  $\text{H}_2^+$  and  $\text{HD}^+$  spectroscopy at the  $10^{-10}$  level with a large signal to noise ratio are :

- Molecular hydrogen ions must be trapped in a small region using linear or hyperbolic Paul trap in order to give  $\mu\text{s}$  interaction time.
- For single photon transition in  $\text{HD}^+$ , Doppler effect, which is given by  $v/\lambda$ , must be strongly reduced below the MHz levels. In other words, the molecular ions must be sympathetically cooled as much as possible using laser cooled atomic ions, since direct laser cooling of hydrogen ions is impossible. For  $\text{H}_2^+$ , two-photon Doppler-free spectroscopy is only sensitive to second order Doppler effect  $-v^2/(2c^2) = -3kT/(2mc^2)$  and the requirement is less stringent.
- An efficient detection method has to be worked out. The only known way to detect the hydrogen molecular ion excited state is selective photodissociation, leading to the REMPD (Resonance-Enhanced MultiPhoton Dissociation) scheme.
- The hydrogen molecular ions have to be prepared with a as large as possible population in the ground state of the transition. Whereas electron impact works well for  $\text{HD}^+$ , it leads to wide-spread rovibrational distribution for  $\text{H}_2^+$  that prevents easily observing a transition. As a consequence, we need a more efficient way to produce  $\text{H}_2^+$ , namely, using REMPI (Resonance-Enhanced MultiPhoton Ionization) method.

I hereafter review the experimental techniques that are used for hydrogen molecular ion spectroscopy.

### 1.4.1 Ion trapping

The principle of a Paul trap is quite simple : One can not create a local minimum of the static electronic potential that verifies the Poisson equation  $\phi(\mathbf{r}) : \Delta\phi(\mathbf{r}) = 0$ . The idea is to rotate one of the saddle point of this potential, to find a local minimum of an effective potential. More precisely, we combine the dc voltages and ac voltages in a particular way to form the quadrupolar potential :

$$\phi(\mathbf{r}, t) = \frac{U_0 + V_0 \cos(\Omega t)}{r_0^2 + 2z_0^2} (x^2 + y^2 - 2z^2) . \quad (1.2)$$

Separating the ion trajectory into small and fast micromotion and a slow and large macromotion, and using an adiabatic approximation one can define an effective potential involving a DC term and a ponderomotive term :

$$\phi_{eff}(\mathbf{r}) = \frac{U_0}{r_0^2 + 2z_0^2}(x^2 + y^2 - 2z^2) + \frac{qV_0^2}{m\Omega^2(r_0^2 + 2z_0^2)^2}(x^2 + y^2 + 4z^2). \quad (1.3)$$

If  $V_0$  is large enough, the effective potential has a local minimum that give the equilibrium position for an ion. In practice, the time-dependent potential as in Eq.1.2 can be created by using a system of electrodes and voltages as shown in Fig.1.4.

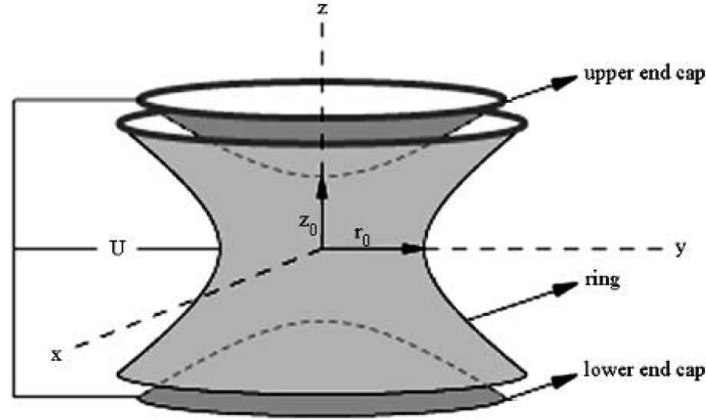


Figure 1.4: Hyperbolic Paul trap.

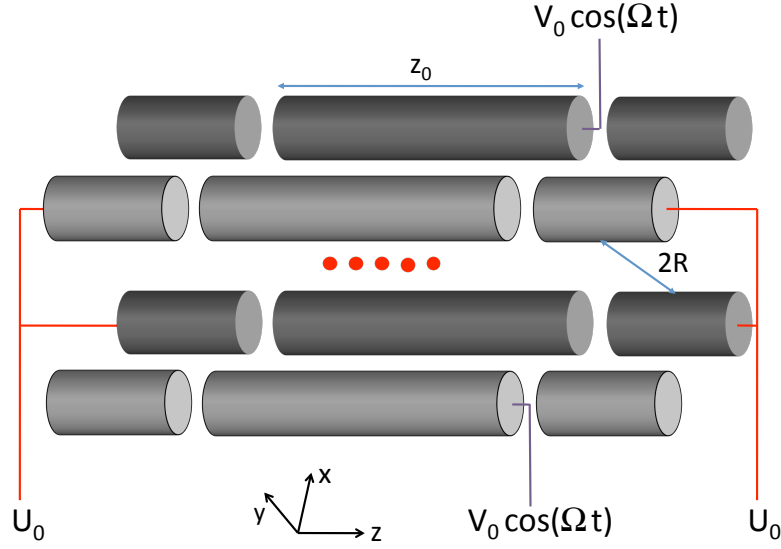
There are many different types of Paul trap whose principle is similar to that of the hyperbolic Paul trap : linear Paul trap, multipole trap, ring trap, ... In the experiment with  $H_2^+$ , at the first try, for the seak of simplicity, we first used the the hyperbolic Paul trap. But this design is not convinient for the future project because it's difficult to add another laser system for the sympathetic cooling. Therefore, we switch to the same design as for the  $HD^+$  experiment : the linear Paul trap. The electrode geometry of linear Paul trap consists of four linear segmented rods as shown in Fig. 1.5.

The radial confinement is due to an ac voltage  $V_0 \cos(\Omega t)$  applied between diagonally opposite rods and the axial confinement is due to a voltage  $U_0$  applied to the end segments of the rods. Near the center of the trap, these voltages create a time-dependent potential given by :

$$\Phi = \Phi_{rf} + \Phi_{dc} = \frac{1}{2}V_0 \cos(\Omega t) \frac{x^2 - y^2}{R^2} + \frac{\kappa U_0}{z_0^2} (z^2 - \frac{1}{2}(x^2 + y^2))$$

where  $R$  is the distance from the axis of the trap to the surface of the electrode,  $z_0$  is the length of the center electrode, and  $\kappa$  is a geometric factor.

The equation of motion of an ion undergoing the electric field  $-\vec{\text{grad}}\Phi$  is described by the Mathieu equation :

Figure 1.5: Linear Paul trap for both  $\text{H}_2^+$  and  $\text{HD}^+$  experiments.

$$\begin{cases} \frac{d^2 x}{d^2 \zeta} + [a_x + 2q_x \cos(2\zeta)]x = 0 \\ \frac{d^2 y}{d^2 \zeta} + [a_y + 2q_y \cos(2\zeta)]y = 0 \\ \frac{d^2 z}{d^2 \zeta} + [a_z + 2q_z \cos(2\zeta)]z = 0 \end{cases} \quad (1.4)$$

where  $\zeta = \Omega t/2$ ,  $a_x = a_y = -\frac{1}{2}a_z = -\frac{4Q\kappa U_0}{mz_0^2 \Omega^2}$ ,  $q_x = -q_y = 2V_0/(\Omega^2 m R^2)$  and  $q_z = 0$ .

If  $a_i < q_i^2 \ll 1$ , the solutions of 1.4 have the following form :

$$u_i(t) = u_{1i} \cos(\omega_i t) \left(1 + \frac{q_i}{2} \cos(\Omega t)\right) .$$

where  $u_i = x, y, z$  and

$$\omega_i = \beta_i \frac{\Omega}{2} \ll \Omega, \quad \beta_i = \sqrt{a_i + \frac{q_i^2}{2}} .$$

From this approximate solution, we can recognize two kinds of motion. The *secular motion* is the oscillation at frequency  $\omega_i$  and the *micromotion* is the oscillation at frequency  $\Omega$ .

In the ideal linear Paul trap, the  $\text{HD}^+$  ions form a string on the trap axis without any radial extent. In the real trap, the presence of stray charges on the electrodes leads to stray dc electric fields  $\vec{E}^{stray}$ , the Mathieu equations are modified as [36] :

$$\begin{cases} \frac{d^2x}{d^2\zeta} + [a_x + 2q_x \cos(2\zeta)]x = \frac{QE_x^{stray}}{m} \\ \frac{d^2y}{d^2\zeta} + [a_y + 2q_y \cos(2\zeta)]y = \frac{QE_y^{stray}}{m} \\ \frac{d^2z}{d^2\zeta} + [a_z + 2q_z \cos(2\zeta)]z = \frac{QE_z^{stray}}{m} \end{cases} \quad (1.5)$$

The solutions of this modified Mathieu equations are :

$$u_i(t) = [u_{0i} + u_{1i} \cos(\omega_i t)] \left(1 + \frac{q_i}{2} \cos(\Omega t)\right)$$

where  $u_i = x, y, z$  and

$$u_{0i} = \frac{Q\vec{E}^{stray}\hat{u}_i}{m\omega_i^2} .$$

The ion is displaced from the axis to the average position  $\vec{u}_0 = u_{0x}\hat{x} + u_{0y}\hat{y} + u_{0z}\hat{z}$  and the additional motion  $(1/2)q_i u_{0i} \cos(\Omega t)$  is called "excess micromotion".

Another sources of excess micromotion are : the phase difference between the ac potentials applied to the diagonally opposite electrodes and the imperfection of linear Paul trap.

### 1.4.2 Molecular Ion sympathetic cooling

Hot molecular ions are very difficult to cool directly with laser due to the complexity of the energy structure and the lack of cycling transitions. We must then use indirect laser cooling called sympathetic cooling. The linear Paul trap will trap both molecular hydrogen ions ( $\text{HD}^+$  or  $\text{H}_2^+$ ) and beryllium ions  $\text{Be}^+$ . Because of its simple energy structure, the  $\text{Be}^+$  ions can be directly laser cooled. Thanks to the Coulombian interaction between the  $\text{Be}^+$  ions and the molecular hydrogen ions ( $\text{HD}^+$  or  $\text{H}_2^+$ ), the molecule ion motion is strongly damped until the  $\text{Be}^+$ /molecular ion system form a mixed Coulomb crystal [37] such as that shown in Fig. 1.6.

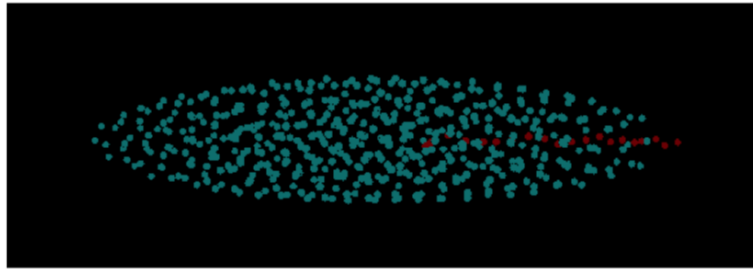


Figure 1.6: Coulomb crystal formed 20 sympathetically cooled  $\text{HD}^+$  ions (red points) and 400 laser-cooled  $\text{Be}^+$  ions (blue points). This image is obtained from our Molecular Dynamics simulation program.

For  $\text{HD}^+$  experiment, cooling is necessary to limit first order Doppler broadening.

L	$P_{\nu=0,L}$
0	0.10
1	0.25
2	0.27
3	0.20
4	0.11
5	0.04

Table 1.1: Population of HD<sup>+</sup> for different rotational quantum number

For H<sub>2</sub><sup>+</sup> experiment, it was believed that ion cooling is not necessary thank to the Doppler-free two-photon spectroscopy. Nevertheless, velocity estimation of hot H<sub>2</sub><sup>+</sup> ion cloud shows that the second-order Doppler effect is about 7 kHz [38] which is larger than the REMPD signal linewidth required to achieve the accuracy level 10<sup>-10</sup> for proton-to-electron mass ratio determination.

Finally, sympathetic cooling by lase-cooled Be<sup>+</sup> ions is unavoidable for hydrogen molecular ion spectroscopy.

### 1.4.3 Ion detection : REMPD

For both molecular hydrogen ions H<sub>2</sub><sup>+</sup> and HD<sup>+</sup>, the linewidth of the excited level is very small, so the transition cannot be observed by fluorescence methods. Since the rovibrational levels are long lived they can be further photodissociated using green to UV lasers. In that case, the transition is observed by Resonance-Enhanced MultiPhoton Dissociation (REMPD).

### 1.4.4 Ion source preparation

The creation of the molecular ion cloud can be done with two different methods. An easy and unexpensive method called "electronic impact" is effective for HD<sup>+</sup> experiments. For H<sub>2</sub><sup>+</sup>, a more involved REMPI method has to be used. I now discuss the ion creation methods.

#### Electronic impact method :

The simplest way to produce ions is electronic impact. The collision between hydrogen molecules H<sub>2</sub> (or HD) in the vacuum chamber and electrons emitted by an electron gun produce hydrogen molecular ions H<sub>2</sub><sup>+</sup> (or HD<sup>+</sup>) in a number of states ( as well as a few proton H<sup>+</sup>, or deuterons D<sup>+</sup>).

The ions produced by this method are not state-selected. For HD<sup>+</sup>, the electron impact leads to a rovibrational distribution that relaxes to thermal equilibrium by fast vibrational relaxation and by black body radiation redistribution among rotational levels. The HD<sup>+</sup> ions are all in the  $\nu = 0$  vibrational level and spread over 5 rotational levels as reported in Tab. 1.1.

The situation for H<sub>2</sub><sup>+</sup> is completely different since all the bound state are metastable. Theoretical and experimental vibrational population are reported in Tab. 1.2.

$\nu$	experiment [39]	theory [40]
0	0.121	0.11916
1	0.193	0.18994
2	0.192	0.18781
3	0.156	0.15173
4	0.115	0.11097
5	0.079	0.07732
6	0.0403	0.05270
7	0.0271	0.03564
8	0.0185	0.02411

Table 1.2: Population of  $\text{H}_2^+$  for different vibrational quantum number

L	relative rotational population
0	11%
1	66 %
2	13 %
3	8 %
4	negligible

Table 1.3: Population of  $\text{H}_2^+$  for different rotational quantum number

The light electron impact process does not significantly modify the rotation of the heavy proton pair in  $\text{H}_2$ <sup>2</sup>. As a consequence, the rotational distribution is simply given by the Boltzmann distribution :

$$P_L \sim (2I + 1)(2L + 1)e^{-\frac{BL(L+1)}{k_B T}}$$

where the rotational constant  $B = 60.8 \text{ cm}^{-1}$ ,  $I$  the total nuclear spin and  $L$  the orbital angular momentum. Therefore, the population of  $\text{H}_2^+$  as a function of  $L$  is given in Tab. 1.3 :

The population of  $|\nu = 0, L = 2\rangle$  is  $0.121 \times 0.13 = 1.6 \%$  only. Taking into account the hyperfine structure with the nuclear spin  $I = 0$  and the electron spin  $s_e = 1/2$ , this level is splitted in a  $J = 3/2$  and a  $J = 5/2$  sublevel with 40% and 60% population respectively, less than 1% of the electron impact produced  $\text{H}_2^+$  ions participate in the REMPD signal.

It is then extremely important to use a state-selective  $\text{H}_2^+$  production method.

### Preparation of $\text{HD}^+$ in the rovibrational ground state :

For the purpose of spectroscopy, the translational temperature of the  $\text{HD}^+$  ion is easily reduced close to the Doppler limit temperature with sympathetic cooling techniques but the internal temperature remains intact and equal to the room temperature  $T \approx 300 \text{ K}$ . Therefore, not all ions are in the rovibrational ground state  $|\nu = 0, L = 0\rangle$ .

<sup>2</sup>This is simply a generalization of the experimental results on the rotational distribution of  $\text{N}_2$  [40, 41].

The spectroscopy of  $\text{HD}^+$  using REMPD doesn't require the preparation of the molecular ions in a particular initial rovibrational state because the BBR will slowly pump this state to keep the internal rotational states at the room temperature. Nevertheless to improve the signal-to-noise ratio, it's interesting to maximize the population of the initial state.

A method of preparation of  $\text{HD}^+$  in the initial state  $|\nu = 0, L = 0\rangle$  worked out in Düsseldorf is presented in [42, 33]. Two lasers at 2.713  $\mu\text{m}$  and 5.485  $\mu\text{m}$  are used to pump  $|\nu = 0, L \neq 0\rangle$  to the excited states  $|\nu = 2, L = 0\rangle$  and  $|\nu = 1, L = 1\rangle$ . Thank to spontaneous emission from the state  $|\nu = 1, L = 1\rangle$  to the ground state  $|\nu = 0, L = 0\rangle$ , the optical pump rate exceed the BBR redistribution rate and therefore, most of the ions are transferred to the ground state. With trapped and translationally sympathetically cooled  $\text{HD}^+$  ions, T. Schneider *et al.* [42] achieve 78 (4)% rovibrational ground state population.

### REMPI for $\text{H}_2^+$ ions :

As emphasized by O'Halloran *et al.* [43], four-photon REMPI (Resonance-Enhanced MultiPhoton Ionization) can be used to produce state-selected  $\text{H}_2^+$  ions in a  $|\nu = 0, L = 0\rangle$  level from room temperature  $\text{H}_2$  molecules. This technique requiring a high power pulsed laser in the 300 nm range is much more involved, and is discussed in chapter 2.

## 1.5 Precision spectroscopy of molecular hydrogen ions : Status

The molecular hydrogen ions  $\text{H}_2^+$  and  $\text{HD}^+$  are the simplest molecules : they consist of only two nuclei and one electron. For this particular simplicity, it has been the object of many theoretical research whereas spectroscopic experimental results are in a very limited number. In this section, i present a brief history of both theoretical and experimental research on this topics and then i discuss the present status of the experiment with  $\text{H}_2^+$  and  $\text{HD}^+$  in three different groups in Paris, Düsseldorf and Amsterdam.

### 1.5.1 Brief history

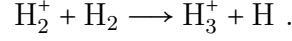
#### Theoretical study :

Because hydrogen molecular ions are the simplest possible molecules and because it's also linked to the famous three-body problem, it has been the subject of many theoretical research. The first theoretical calculation of  $\text{H}_2^+$  was done in 1927 by Øjvind Burrau [44], only one year after the publication of Schrödinger's equation in 1926 [45]. Since then, many different authors have contributed to the energy calculations of hydrogen molecular ions, among them L. Wolniewicz and J. D. Poll [46]; E. A. Colbourn and P. R. Bunker [47], D. M. Bishop [48] ... The complete calculations of bound energy levels of  $\text{HD}^+$  and  $\text{H}_2^+$  were done by R.E. Moss in 1993 [49, 50], including the relativistic and QED corrections at the 0.00003  $\text{cm}^{-1}$  accuracy level.

In 2000, L. Hilico *et al* [26] published very accurate energy calculations of  $\text{H}_2^+$ ,  $\text{D}_2^+$  and  $\text{HD}^+$  by studying the standard three-body problem using the perimetric coordinates and a generalized Hylleraas basis set. Simultaneously, V. I. Korobov worked out an even more precise energy calculation with a different generalized Hylleraas basis [27].

### Experimental study :

Unlike the theoretical aspects, the number of experimental studies on the energy structure of hydrogen molecular ions are very modest<sup>3</sup>. The difficulty in the preparation of a reasonably high density and long lived sample was the main obstacle for the past researches. Indeed, the hydrogen molecular ions repeats themselves and are chemically extremely active and may be destroyed following the reaction :



This reaction proceeds very quickly and keeps  $\text{H}_2^+$  ions at very low density.

I now review the most relevant results :

- In 1968 : Hans G. Dehmelt at University of Washington, USA and coauthors investigated the magnetic resonance transitions among several Zeeman sublevels of  $\text{H}_2^+$  hyperfine states. An external RF magnetic field interacts with electronic magnetic moment  $\mu \propto \vec{S}$  and causes the transition between two hyperfine states. Since the UV photodissociation cross section slightly depends on the hyperfine states, resonances in the photodissociation signal reveals transitions among Zeeman substates. Five transition between hyperfine states  $(K, F_2, F) - (K, F'_2, F')$  with  $K = 1$  [51, 52] were observed (here, we denote  $\vec{K}$  as the rotational angular momentum,  $\vec{F}_2$  as the sum of nuclear and electronic spin, and  $\vec{F} = \vec{K} + \vec{F}_2$ ) :

$$\left(1, \frac{1}{2}, \frac{1}{2}\right) \longleftrightarrow \left(1, \frac{3}{2}, \frac{3}{2}\right) \quad (|\Delta E|/\hbar = 1400.9 \text{ MHz})$$

$$\left(1, \frac{3}{2}, \frac{1}{2}\right) \longleftrightarrow \left(1, \frac{1}{2}, \frac{1}{2}\right) \quad (|\Delta E|/\hbar = 1308.2 \text{ MHz})$$

$$\left(1, \frac{1}{2}, \frac{3}{2}\right) \longleftrightarrow \left(1, \frac{3}{2}, \frac{1}{2}\right) \quad (|\Delta E|/\hbar = 1322.4 \text{ MHz})$$

$$\left(1, \frac{1}{2}, \frac{3}{2}\right) \longleftrightarrow \left(1, \frac{3}{2}, \frac{3}{2}\right) \quad (|\Delta E|/\hbar = 1415.3 \text{ MHz})$$

$$\left(1, \frac{1}{2}, \frac{3}{2}\right) \longleftrightarrow \left(1, \frac{3}{2}, \frac{5}{2}\right) \quad (|\Delta E|/\hbar = 1398.1 \text{ MHz})$$

Using the same idea for para- $\text{H}_2^+$  (nuclear spin  $I = 0$ ), K. B. Jefferts [53] observed the transitions between Zeemann sublevels  $|K = 2; I = 0; F = \frac{5}{2}; M_F = \pm\frac{5}{2}, \pm\frac{1}{2}\rangle$  and  $|K = 2; I = 0; F = \frac{3}{2}; M_F = \pm\frac{3}{2}\rangle$ . K. B. Jefferts improved the experiment and observed 30 transitions between hyperfine levels of  $\text{H}_2^+$  with vibrational quantum number  $\nu = 4 - 8$  and rotational quantum number  $K = 1 - 2$  [54].

---

<sup>3</sup>We don't imply in our discussion the experimental studies on the dynamics of photodissociation of  $\text{H}_2^+$  and  $\text{HD}^+$

$(\nu, N) - (\nu', N')$	observed frequency ( $\text{cm}^{-1}$ )
(1,0)-(0,1)	1869.134
(1,1)-(0,2)	1823.533
(2,1)-(1,0)	1856.778
(3,1)-(2,0)	1761.616
(3,2)-(2,1)	1797.522
(3,1)-(2,2)	1642.108

Table 1.4: Rovibrational transitions in  $\text{HD}^+$  [55]

- In 1976 : W. H. Wing at University of Arizona, USA and coauthors [55] published the first detection of rotation-vibration transitions in  $\text{HD}^+$ . They observed six group of transitions  $(\nu, N) \leftrightarrow (\nu', N')$  with  $\nu, \nu'$  in the range 0 to 3 and  $N, N'$  in the range 0 to 2 (see Tab. 1.4) by means of ion-beam laser-resonance method : An  $\text{HD}^+$  ion beam at several keV energy interacts with a coaxial CO infrared laser beam and the vibrational excitation in  $\text{HD}^+$  is detected through collisions with  $\text{H}_2$  target gas because the charge exchange cross section between  $\text{HD}^+$  and  $\text{H}_2$  depends on the  $\text{HD}^+$  vibrational state. These transitions lying between 1642 and 1869  $\text{cm}^{-1}$  were observed with the relative uncertainty  $\pm 1$  ppm partially resolving the hyperfine structure.
- From 1981 to 1991, A. Carrington *et al.* at University of Southampton, England published a series of articles [56, 57, 58, 59, 60, 61, 62] on experimental and theoretical studies of the transitions between two rovibrational levels of the fundamental electronic curve  $1s\sigma_g$  close to the photodissociation limit of  $\text{HD}^+$ . Their ion-beam laser-resonance method is quite similar to the method of W. H. Wing *et al.* [55] but the rovibrational transitions in  $\text{HD}^+$  were detected by using infrared photodissociation method instead of collisional detection method. They observed rotation-vibration transitions in  $\text{HD}^+$  for  $\nu = 18 - 16$  band [56],  $\nu = 17 - 14$  band [57];  $\nu = 17 - 15$  and  $\nu = 20 - 17$  band [58];  $\nu = 21 - 17$  band [60],  $\nu = 22 - 17$  band [61].
- In 2007 : The group of S. Schiller [32] successfully measured the frequency transition between two rovibrational states  $(\nu, N) : (4, 3) \leftarrow (0, 2)$  of the ground state electronic potential energy curve of  $\text{HD}^+$ . Using a sample of few hundreds sympathetically cooled ions, the Doppler width is reduced and the resolution is improved by order of magnitude to the 2-ppb level i.e  $\sim 150$  times better than the measurement of W. H. Wing *et al* [55].
- In 2012, U. Bressel *et al.* [33] reported the observation of the transition from  $|\nu = 0, N = 0\rangle$  to  $|\nu = 1, N = 1\rangle$  using both the technique presented in [32] and pumping technique [42].
- In 2012, J. C. J. Koelemeij *et al.* [34] at LaserLab used the same technique as in [32] to observe the transition between two rovibrational states  $|\nu = 0, J\rangle$  and  $|\nu' = 8, J'\rangle$

## 1.5.2 Theoretical developments

The proton-to-electron mass ratio determination using  $H_2^+$  or  $HD^+$  spectroscopy relies on highly accurate energy calculations. This theoretical works have been done mainly by V.I. Korobov and our group and it is also useful for a similar experiment on the determination of antiproton-to-electron mass ratio using  $\bar{p}He^+$  antiprotonic helium [63].

### 1.5.2.1 Highly accurate nonrelativistic energy calculations

The proposal of F. Biraben in 1995 to improve the determination of proton-to-electron mass ratio using  $H_2^+$  spectroscopy pushed L. Hilico in collaboration with D. Delande B. Gremaud and N. Billy to recalculate the energy levels of  $H_2^+$ ,  $D_2^+$  and  $HD^+$  with very high accuracy [64, 26].

The idea of the calculation is quite simple : diagonalizing the eigenenergies of the Coulomb three-body Hamiltonian without Born-Oppenheimer approximation :

$$H_0\Psi(1, 2, e^-) = E_0\Psi(1, 2, e^-) ,$$

where, the Hamiltonian is :

$$H_0 = \frac{\mathbf{p}^2}{2} + \frac{\mathbf{P}_1^2}{2M_1} + \frac{\mathbf{P}_2^2}{2M_2} - \frac{1}{r_1} - \frac{1}{r_2} + \frac{1}{R} , \quad (1.6)$$

and the coordinates  $r_1, r_2, R$  are depicted in Fig.1.7.

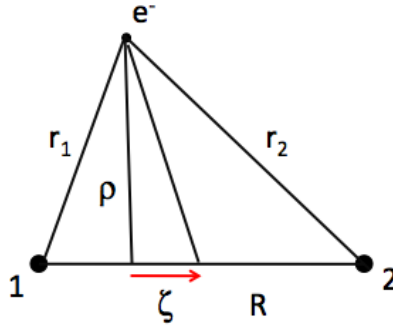


Figure 1.7: Coordinates for the three-body problem.

The eigenenergies can be obtained with high numerical accuracy using a variational method. The approach consists in using the perimetric coordinates defined by :

$$\begin{cases} x = r_1 + r_2 - R \\ y = r_1 - r_2 + R \\ z = -r_1 + r_2 + R \end{cases}$$

and to expand the radial wavefunctions as :

$$\phi(x, y, z) = \sum_{n_x, n_y, n_z} C_{n_x, n_y, n_z} \chi_{n_x}^{(\alpha)}(x) \chi_{n_y}^{(\beta)}(y) \chi_{n_z}^{(\beta)}(z)$$

where  $\chi_n^{(\alpha)}(u) = (-1)^n \sqrt{\alpha} L_n(\alpha u) e^{-\alpha u/2}$  with  $L_n$  the Laguerre polynomials.

The main advantage of this method is that it exploits the dynamical symmetries of the problem, so that the Hamiltonian has strict coupling rules and can be written in the form of a sparse-band matrix. Convergence of the eigenenergies at the  $10^{-13}$  a.u. accuracy level is obtained using double precision arithmetics. However, it becomes inefficient for states with a rotational quantum number  $L \geq 3$ , because the size and width of the matrices increase considerably [65]. Another disadvantage of this method is that it is not adapted for QED correction calculations because the perturbation Hamiltonian are expressed using  $r_1, r_2, R$  and not the perimetric coordinates.

Vladimir I. Korobov at JINR, Dubna, Russia has developed an alternative method using a variation expansion of the wave function on a  $(r_1, r_2, R)$  exponential basis set as :

$$\Psi(1, 2, e^-) = \sum_{i=1}^{\infty} \{U_i \text{Re}[e^{-\alpha_i r_1 - \beta_i r_2 - \gamma_i R}] + W_i \text{Im}[e^{-\alpha_i r_1 - \beta_i r_2 - \gamma_i R}]\} Y_{l_1 l_2}^{LM}$$

In this formula,  $\alpha_i, \beta_i$  and  $\gamma_i$  are complex parameters generated in a quasirandom ways in several intervals to represent the behavior of the wave function at different length scale. Complex parameters are chosen to get oscillatory basis function in order to represent the wave function vibrational behavior.

The variational parameters are the bounds of the intervals.

The Hamiltonian matrix is a full matrix. Convergence at the  $10^{-15}$  to  $10^{-30}$  a.u. levels is obtained using quadruple to octuple precision arithmetics. Such a high precision level is required to get accurate enough eigenvectors for precise evaluation of relativistic, QED and hyperfine structure corrections.

### 1.5.3 Energy corrections

The nonrelativistic energy levels obtained from the Schrödinger equation 1.6 are of orders  $R_\infty \alpha^2$  ( $R_\infty$  is the Rydberg constant and  $\alpha$  is the fine structure constant). The theoretical calculations are useful for the experimental purpose only when the high-order relativistic and radiative energy corrections are included. The corrections are systematically calculated using a series expansion of the binding energy in terms of three small parameters : fine structure constant  $\alpha$ ,  $Z\alpha$  ( $Z$  is the nuclear charge) and electron-to-proton mass ratio  $m/M$ . The powers of  $\alpha$  represent the radiative corrections,  $Z\alpha$  represent the relativistic corrections and  $m/M$  represent the recoil effect. We usually denote the orders of energy corrections as  $R_\infty \alpha^{n_1} (Z\alpha)^{n_2} (m/M)^{n_3}$  (where  $n_1, n_2, n_3 \in \mathbb{N}$ ).

The energy corrections at a given order are obtained by deriving an effective correction Hamiltonian  $H_{eff}$  and by averaging out over an unperturbed wave function. The effective Hamiltonian is obtained in the so called Nonrelativistic Quantum Electrodynamics (NRQED) framework [66, 67].

#### Relativistic correction :

The leading-order relativistic corrections of order  $R_\infty (Z\alpha)^2 \sim \alpha^4$  can be understood as the sum of relativistic corrections for each particle and the Breit-Pauli interaction which is the lowest order in the relativistic corrections to the interaction between two particle (see Fig.1.8).

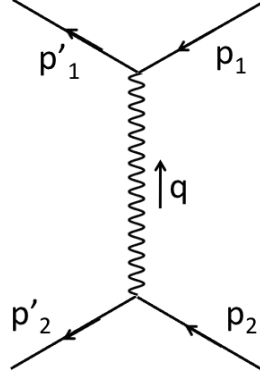


Figure 1.8: The Feynman diagram for the Breit-Pauli interaction. In the nonrelativistic approximation, the interaction between two particles is the well-known Born interaction. The first order correction in the relativistic quantum theory means that two particles exchange a virtual photon.

The Breit-Pauli Hamiltonian for two particles 1 and 2 of momenta  $\vec{p}_1, \vec{p}_2$ ; masses  $m_1, m_2$  and charges  $Z_1, Z_2$  at the relative position  $\vec{r}$  can be written in atomic units as [68] :

$$H_B = H_1^{(0)} + H_2^{(0)} + U_{12} , \quad (1.7)$$

where,

$$H_i^{(0)} = \frac{\vec{p}_i^2}{2m_i} - \frac{\vec{p}_i^4}{8m_i^3 c^2} \quad (\text{with } i = 1, 2) ,$$

and

$$\begin{aligned} U_{12} = U_{12}(\vec{p}_1, \vec{p}_2, \vec{r}) = & \frac{Z_1 Z_2}{r} - \frac{\pi Z_1 Z_2 \alpha^2}{2} \left( \frac{1}{m_1^2} + \frac{1}{m_2^2} \right) \delta(\vec{r}) - \frac{Z_1 Z_2 \alpha^2}{2m_1 m_2 r} \left[ \vec{p}_1 \vec{p}_2 + \frac{(\vec{p}_1 \vec{r})(\vec{p}_2 \vec{r})}{r^2} \right] \\ & - \frac{Z_1 Z_2 \alpha^2}{2m_1^2 r^3} (\vec{r} \times \vec{p}_1) \vec{s}_1 + \frac{Z_1 Z_2 \alpha^2}{2m_2^2 r^3} (\vec{r} \times \vec{p}_2) \vec{s}_2 \\ & - \frac{Z_1 Z_2 \alpha^2}{m_1 m_2 r^3} [(\vec{r} \times \vec{p}_1) \vec{s}_2 - (\vec{r} \times \vec{p}_2) \vec{s}_1] \\ & + \frac{Z_1 Z_2 \alpha^2}{m_1 m_2} \left[ \frac{\vec{s}_1 \vec{s}_2}{r^3} - 3 \frac{(\vec{s}_1 \vec{r})(\vec{s}_2 \vec{r})}{r^5} - \frac{8\pi}{3} \vec{s}_1 \vec{s}_2 \delta(\vec{r}) \right] , \end{aligned}$$

where,  $\vec{s}_1$  and  $\vec{s}_2$  are spins of particle 1 and 2 respectively.

The Breit-Pauli Hamiltonian for a system of three particles is defined as a sum of pairwise interactions. If we denote  $\vec{P}_1, \vec{P}_2, \vec{p}_e$  as momenta and  $\vec{R}_1, \vec{R}_2, \vec{r}_e$  are coordinates of nuclei and electron with respect to the center of mass of a molecular ion and  $\vec{r}_1 = \vec{r}_e - \vec{R}_1, \vec{r}_2 = \vec{r}_e - \vec{R}_2, \vec{R} = \vec{R}_1 - \vec{R}_2$  then we can write the Breit-Pauli Hamiltonian for the three body system as :

$$\mathcal{H}_B = H_1^{(0)} + H_2^{(0)} + H_e^{(0)} + U_{1e}(\vec{P}_1, \vec{p}_e, \vec{r}) + U_{2e}(\vec{P}_2, \vec{p}_e, \vec{r}) + U_{12}(\vec{P}_1, \vec{p}_2, \vec{R}) \quad (1.8)$$

We present this Breit-Pauli Hamiltonian in terms of different corrections as in [69] :

- Relativistic correction for the bound electron :

$$E_{rc}^{(2)} = \alpha^2 \left\langle -\frac{\vec{p}_e^4}{8m_e^3} + \frac{4\pi}{8m_e^2} [Z_1\delta(\vec{r}_1) + Z_2\delta(\vec{r}_2)] \right\rangle$$

- The correction due to the *transverse photon-exchange* :

$$E_{tr-ph}^{(2)} = \frac{\alpha^2 Z_1}{2m_e M_1} \left\langle \frac{\vec{p}_e \vec{P}_1}{r_1} + \frac{\vec{r}_1 (\vec{r}_1 \vec{p}_e) \vec{P}_1}{r_1^3} \right\rangle + \frac{\alpha^2 Z_2}{2m_e M_2} \left\langle \frac{\vec{p}_e \vec{P}_2}{r_2} + \frac{\vec{r}_2 (\vec{r}_2 \vec{p}_e) \vec{P}_2}{r_2^3} \right\rangle - \frac{\alpha^2 Z_1 Z_2}{2M_1 M_2} \left\langle \frac{\vec{P}_1 \vec{P}_2}{R} + \frac{\vec{R} (\vec{R} \vec{P}_1) \vec{P}_2}{r_1^3} \right\rangle$$

- The correction of the relativistic kinetic energy :

$$E_{kin}^{(2)} = -\alpha^2 \left\langle \frac{\vec{P}_1^4}{8M_1^3} + \frac{\vec{P}_2^4}{8M_2^3} \right\rangle$$

- Nuclear spin dependent recoil corrections (only for proton, this term vanishes for deuteron) :

$$E_{Darwin}^{(2)} = \frac{\alpha^2 4\pi Z_p}{8M_p^2} \langle \delta(\vec{r}_p) \rangle$$

- The correction due to the finite size of electric charge radius of nuclei <sup>4</sup> :

$$E_{nuc}^{(2)} = \sum_{i=1,2} \frac{2\pi Z_i (R_i/a_0)^2}{3} \langle \delta(\vec{r}_i) \rangle$$

The complete contribution to the correction of the order  $R_\infty \alpha^2$  is :

$$E_{\alpha^2} = E_{rc}^{(2)} + E_{kin}^{(2)} + E_{tr-ph}^{(2)} + E_{Darwin}^{(2)} + E_{nuc}^{(2)}$$

The higher order relativistic corrections are much more complicated. To calculate the full correction of order  $R_\infty (Z\alpha)^4$  including the recoil terms would already be a difficult task. Fortunately, in view of the targeted accuracy, recoil terms can be neglected and it is enough to consider the relativistic corrections to the bound electron. For example, the relativistic corrections of order  $R_\infty \alpha^4 \sim m_e c^2 \alpha^6$  is obtained by using the Rayleigh-Schrödinger perturbation theory [70]:

$$\Delta E^{(6)} = \langle H'_B Q (E_0 - H_0)^{-1} Q H'_B \rangle + \langle H^{(6)} \rangle \quad (1.9)$$

---

<sup>4</sup>This correction does not come from the Breit-Pauli Hamiltonian but its contribution is also of the order of  $R_\infty \alpha^2$

where  $Q$  is a projector on the subspace orthogonal to the space constituted by unperturbed wavefunctions  $\{\Psi\}$ ,  $H_0$  is defined as :

$$H_0 = \frac{\vec{p}^2}{2m_e} + V, \quad V = -\frac{Z_1\alpha}{r_1} - \frac{Z_2\alpha}{r_2},$$

$H'_B$  is the spin-independent Breit-Pauli interaction :

$$H'_B = -\frac{p^4}{8m_e^3} + \frac{\pi}{2m_e^2}[Z_1\delta(\vec{r}_1) + Z_2\delta(\vec{r}_2)] + \left( Z_1 \frac{[\vec{r}_1 \times \vec{p}]}{2m_e^2 r_1^3} + Z_2 \frac{[\vec{r}_2 \times \vec{p}]}{2m_e^2 r_2^3} \right) \vec{s},$$

and

$$H^{(6)} = \frac{p^6}{16m_e^5} + \frac{(\mathcal{E}_1 + \mathcal{E}_2)^2}{8m_e^3} - \frac{3\pi}{16m_e^4} \{p^2[\rho_1 + \rho_2] + [\rho_1 + \rho_2]p^2\} + \frac{5}{128m_e^4} (p^4V + Vp^4) - \frac{5}{64m_e^4} (p^2Vp^2).$$

We should notice that both terms in Eq. 1.9 are divergent, therefore, a transformation of the spin-independent Breit-Pauli Hamiltonian  $H'_B$  to remove the infinities is necessary.

The complete treatment of relativistic corrections of orders  $R_\infty\alpha^4$  were presented in [70]. The relativistic corrections of order  $R_\infty\alpha^4 m/M$  to the hyperfine structure of  $H_2^+$  were calculated in [71].

### Radiative correction :

The leading  $R_\infty\alpha^3$  order radiative corrections can be expressed as :

$$E_{\alpha^3} = E_{se}^{(3)} + E_{anom}^{(3)} + E_{vp}^{(3)} + E_{tr-ph}^{(3)}$$

where :

- $E_{se}^{(3)}$  is the one-loop self-energy correction ( $R_\infty\alpha^3$ ) :

$$E_{se}^{(3)} = \frac{4\alpha^3}{3m_e^2} \left( -\ln(\alpha^2) - \beta(L, \nu) + \frac{5}{6} - \frac{3}{8} \right) \langle Z_1\delta(\vec{r}_1) + Z_2\delta(\vec{r}_2) \rangle,$$

where,  $\beta(L, \nu)$  is the Bethe logarithm [72] given by :

$$\beta(L, \nu) = \frac{\langle \vec{J}(H_0 - E_0) \ln[(H_0 - E_0)/R_\infty] \vec{J} \rangle}{\langle [\vec{J}, [H_0, \vec{J}]]/2 \rangle}.$$

Here,  $\vec{J} = -\vec{p}_e + \sum_i Z_i \vec{p}_i/M_i$  is the electric current density operator.

- $E_{anom}^{(3)}$  is the correction due to the anomalous magnetic moment ( $R_\infty\alpha^3$ ) :

$$E_{anom}^{(3)} = \frac{\pi\alpha^2}{m_e^2} \left[ \frac{1}{2} \left( \frac{\alpha}{\pi} \right) \right] \langle Z_1\delta(\vec{r}_1) + Z_2\delta(\vec{r}_2) \rangle$$

- $E_{vp}^{(3)}$  is the one-loop vacuum polarization correction ( $R_\infty\alpha^3$ ) :

$$E_{vp}^{(3)} = \frac{4\alpha^3}{3m_e^2} \left( -\frac{1}{5} \right) \langle Z_1\delta(\vec{r}_1) + Z_2\delta(\vec{r}_2) \rangle$$

	H <sub>2</sub> <sup>+</sup>	HD <sup>+</sup>
$\Delta E_{nr}$	65 687 511.0714	57 349 439.9733
$\Delta E_{\alpha^4}$	1091.0400	958.1514
$\Delta E_{\alpha^5}$	-276.5450	-242.1262
$\Delta E_{\alpha^6}$	-1.9969	-1.7481
$\Delta E_{\alpha^7}$	0.129(2)	0.113(2)
$\Delta E_{\alpha^8}$	0.0005	0.0004
$\Delta E_{tot}$	65 688 323.699(2)	57 350 154.364(2)

Table 1.5: Summary contribution to the transition from  $|\nu = 0, L = 0\rangle$  to  $|\nu = 1, L = 0\rangle$  of both H<sub>2</sub><sup>+</sup> and HD<sup>+</sup>

- $E_{tr-ph}^{(3)}$  is the correction due to the one transverse photon exchange ( $R_\infty \alpha^3 m/M$ ) :

$$E_{tr-ph}^{(3)} = \alpha^3 \sum_{i=1,2} \left[ \frac{2Z_i^2}{3m_e M_i} \left( -\ln(\alpha) - 4\beta(L, \nu) + \frac{31}{3} \right) \langle \delta(\vec{r}_i) \rangle - \frac{14Z_i^2}{3m_e M_i} Q(r_i) \right],$$

where  $Q(r)$  is the Araki-Sucher term given by:

$$Q(r) = \lim_{\rho \rightarrow 0} \left\{ \frac{\Theta(r - \rho)}{4\pi r^3} + (\ln(\rho) + \gamma_E) \delta(\vec{r}) \right\}$$

The radiative corrections of order  $R_\infty \alpha^4$ , and leading contributions of order  $R_\infty \alpha^5$  were calculated in the Born-Oppenheimer approximation [69, 70, 73].

The calculation of energy corrections up to the order  $R_\infty \alpha^5$  are necessary for the purpose of experiments. The table 1.5 shows a recent result including energy corrections up to  $R_\infty \alpha^5 \sim m_e \alpha^5$

### 1.5.3.1 Hyperfine structure

The hyperfine structure is the spin dependent part of QED corrections. At the leading order, it's given by Breit-Pauli interaction Hamiltonian. After averaging over spatial variables, the hyperfine interactions can be expressed in terms of an effective spin Hamiltonian. For H<sub>2</sub><sup>+</sup>, we have :

$$H_{hfs} = b_F(\mathbf{I}\mathbf{S}_e) + c_e(\mathbf{L}\mathbf{S}_e) + c_I(\mathbf{L}\mathbf{I}) + \frac{d_2}{(2L-1)(2L+3)} \left[ \frac{1}{3} \mathbf{L}^2 \mathbf{I}^2 - \frac{1}{2} (\mathbf{L}\mathbf{I}) - (\mathbf{L}\mathbf{I})^2 \right] \\ + \frac{d_1}{(2L-1)(2L+3)} \left\{ \frac{2}{3} \mathbf{L}^2 (\mathbf{I}\mathbf{S}_e) - [(\mathbf{L}\mathbf{I})(\mathbf{L}\mathbf{S}_e) + (\mathbf{L}\mathbf{S}_e)(\mathbf{L}\mathbf{I})] \right\},$$

and for HD<sup>+</sup>, we have :

$$\begin{aligned}
H_{hfs} = & E_1(\mathbf{L}\mathbf{s}_e) + E_2(\mathbf{L}\mathbf{I}_p) + E_3(\mathbf{L}\mathbf{I}_d) + E_4(\mathbf{I}_p\mathbf{s}_e) + E_5(\mathbf{I}_d\mathbf{s}_e) \\
& + E_6\{2\mathbf{L}^2(\mathbf{I}_p\mathbf{s}_e) - 3[(\mathbf{L}\mathbf{I}_p)(\mathbf{L}\mathbf{s}_e) + (\mathbf{L}\mathbf{s}_e)(\mathbf{L}\mathbf{I}_p)]\} \\
& + E_7\{2\mathbf{L}^2(\mathbf{I}_d\mathbf{s}_e) - 3[(\mathbf{L}\mathbf{I}_d)(\mathbf{L}\mathbf{s}_e) + (\mathbf{L}\mathbf{s}_e)(\mathbf{L}\mathbf{I}_d)]\} \\
& + E_8\{2\mathbf{L}^2(\mathbf{I}_p\mathbf{I}_d) - 3[(\mathbf{L}\mathbf{I}_p)(\mathbf{L}\mathbf{I}_d) + (\mathbf{L}\mathbf{I}_d)(\mathbf{L}\mathbf{I}_p)]\} \\
& + E_9\left[\mathbf{L}^2\mathbf{I}_d^2 - \frac{3}{2}(\mathbf{L}\mathbf{I}_d) - 3(\mathbf{L}\mathbf{I}_d)^2\right].
\end{aligned}$$

The coefficients involved in those expressions have been determined numerically by Vladimir I. Korobov *et al.* [74, 75].

For  $\text{H}_2^+$ , the leading term is  $b_F(\mathbf{I}\mathbf{S}_e)$ , hence we use the coupling scheme  $\mathbf{F} = \mathbf{I} + \mathbf{S}_e$  and  $\mathbf{J} = \mathbf{L} + \mathbf{F}$  to label the hyperfine states. In  $\text{H}_2^+$ , the total nuclear spin is  $I = 0$  for an even total orbital angular momentum quantum number  $L$  and  $I$  for odd values. In the former case  $F = 1/2$  leading to a singlet  $J = 1/2$  for  $L = 0$  and doublet  $J = L \pm 1/2$  for  $L \geq 1$ . In the later case, the structure is slightly more complicated with  $F = 1/2, 3/2$  leading to a  $J = L \pm 1/2$  doublet and  $J = L \pm 1/2, L \pm 3/2$  multiplet as depicted in the left part of Fig.1.9.

For  $\text{HD}^+$ , the leading term is  $E_4(\mathbf{I}_p\mathbf{S}_e)$  and  $E_5(\mathbf{I}_d\mathbf{S}_e)$ . Hence the coupling scheme is  $\mathbf{F} = \mathbf{I}_p + \mathbf{S}_e$ ,  $\mathbf{S} = \mathbf{F} + \mathbf{I}_d$  and  $\mathbf{J} = \mathbf{L} + \mathbf{S}$ . With  $I_p = 1/2$ ,  $S_e = 1/2$  and  $I_d = 1$ , the hyperfine structure is much more complicated with 4, 10, 12 sublevels for  $L = 0, 1$ , or  $\geq 2$  (see the right part of Fig.1.9).

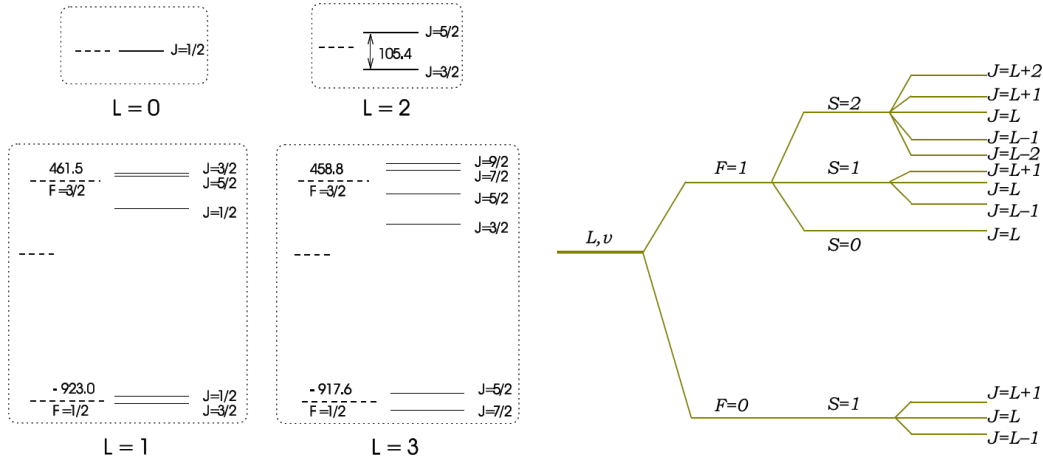


Figure 1.9: Left : Hyperfine structure for the ground state  $\nu = 0$  of  $\text{H}_2^+$ . Right : Hyperfine structure of a rovibrational state of  $\text{HD}^+$  with  $L \geq 2$

### 1.5.3.2 Two-photon transition probability

With  $\text{HD}^+$  ions, single photon spectroscopy is possible and lead to the results already mentioned in Section 1.5.1, with an resolution mainly limited by first order Doppler effect, although the ion temperature is reduced to about 15 mK using sympathetic cooling.

In  $\text{H}_2^+$ , single photon transitions between bound states are not allowed so transition can only be probed using two photon transitions. One great advantage for metrology is that first order Doppler effect is cancelled but with the drawback of low transition probabilities. In 2000, L. Hilico and coauthors showed the feasibility of  $\nu = 0 \rightarrow \nu = 1$  vibrational two-photon transition predicting transition probabilities in the  $1 \text{ s}^{-1}$  range with available lasers near  $9 \mu\text{m}$  [29]. Hyperfine structure of two-photon transition is given in [31].

Doppler-free two-photon spectroscopy has also been theoretically investigated by L. Hilico and J.-Ph. Karr showing that the  $(\nu = 0, N = 0) \rightarrow (\nu' = 2, N' = 0)$  transition (that is very weak in  $\text{H}_2^+$ ) can be strongly enhanced due to a quasi-resonance with the intermediate level  $(\nu_i = 1, N_i = 0)$  [76]. The corresponding wavelength is  $5.368 \mu\text{m}$  is not very convenient from the laser point of view, although quantum cascade lasers are now available. In the chapter 3, I show how we can take advantage of dipole allowed transitions in  $\text{HD}^+$  to perform Doppler-free quasi-degenerate two-photon spectroscopy in the Lamb-Dicke regime.

#### 1.5.4 Status of $\text{H}_2^+$ experiment

With both  $\text{H}_2^+$  and  $\text{HD}^+$ , there is no direct way to observe the excitation of a rovibrational level by fluorescence. The idea that makes it possible to detect the transition is to further bring the excited state to a dissociative state (belonging to the  $2p\sigma_u$  electronic curve of Fig.1.2 or Fig.1.3) leading to photodissociation. The transition is detected by observing a decrease in the trapped ion number after the probing sequence. Such a process is called Resonance Enhanced MultiPhoton Dissociation namely  $2 + 1$  REMPD in  $\text{H}_2^+$ ,  $1 + 1'$  or  $1 + 1' + 1''$  REMPD for single- or two-photon excitation in  $\text{HD}^+$ .

Due to the large number of long lived levels in  $\text{H}_2^+$  and  $\text{HD}^+$ , it is important to prepare highly state-selected ion samples with adapted methods.

A first version of the  $\text{H}_2^+$  spectroscopy experiment was set up and operated in 2008. The signal to noise ratio of the REMPD signal was too low to observe a signal. A careful analysis of the signal and noise, the necessary improvements of the experiment set up were pointed out in [38]. I now briefly describe this first version and discuss the possible improvements.

#### Two-photon sources for $\text{H}_2^+$ experiment :

In the experiment with  $\text{H}_2^+$ , to measure the proton-to-electron mass ratio  $m_p/m_e$  with the relative uncertainty of  $10^{-10}$ , the linewidth of the laser source for the two-photon excitation from the state  $|\nu = 0, L = 2\rangle$  to  $|\nu = 1, L = 2\rangle$  should be a few kHz. This is one of the main challenges of this experiment. The solution for this problem is the QCL laser at  $9.2 \mu\text{m}$ , phase-locked to a single-mode  $\text{CO}_2$  laser as depicted in Fig.1.10.

#### $\text{H}_2^+$ ion source

As mentioned previously, we have two methods for ion production : the electronic impact method and REMPI method.

The 100 eV electron beam emitted from a tungsten filament interacts with residual  $\text{H}_2$  in the high vacuum chamber. This interaction produces mostly  $\text{H}_2^+$  ions and some  $\text{H}^+$

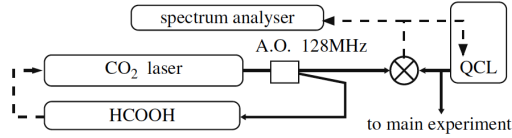


Figure 1.10: Setup of the phase-locked QCL laser for the  $\text{H}_2^+$  experiment.

ions. There are also  $\text{H}_3^+$  ion due to the recombination process between  $\text{H}_2^+$  and  $\text{H}_2$ .

This reaction reduces the trapping time of ion  $\text{H}_2^+$ , therefore, a high vacuum chamber is required.

The big disadvantage of the ion source produced by this method is that the internal state distribution is not well selected. We will return to this in the chapter 2 and explain why this ion source is not well suited for the  $\text{H}_2^+$  experiment.

The Resonance Enhanced Multiphoton Ionization or REMPI method is an alternative way to produce the ion  $\text{H}_2^+$  and it's shown theoretically that this method can be used to produce a highly state-selected ion source.

## Hyperbolic Paul trap

At the beginning of  $\text{H}_2^+$  project, the hyperbolic Paul trap was considered to be good enough for ion trapping. This trap is chosen because of its simplicity and also because it's easier to create the accesses for the ultraviolet laser and infrared laser.

The ion trap is a hyperbolic RF Paul trap (see Fig.1.4) with inner radius  $r_0 = 4.24$  mm and  $z_0 = r_0/\sqrt{2} = 3$  mm, operated using 180 V at 13.3 MHz on the ring electrode, corresponding to a  $q_z = -2q_r = \dots$  stability parameters. A DC voltage  $U_0$  can be added to the RF voltage.

Two pairs of 5 mm in diameter holes are drilled in the ring electrode to shine the IR two photon excitation laser and the UV photodissociation laser. The upper endcap has a hole (1 mm in diameter) for the electron beam, and the lower endcap has a hole (2 mm in diameter) for ion extraction.

The ions are created in-situ by electronic impact on residual  $\text{H}_2^+$  molecules outgassing from the stainless steel electrodes. A cloud of up to few thousand  $\text{H}_2^+$  ions is observed. Only slightly less than 1% of the ions are in the  $(\nu = 0, N = 2, J = 5/2)$  level leading to small spectroscopic signals. The main improvement of the experimental set-up consists in implementing a REMPI state-selected  $\text{H}_2^+$  ion source. The process and the source will be described in chapter 2.

## Ion detection

To study the content of ion cloud trapped inside the hyperbolic Paul trap, by changing the voltages, we can extract the ion cloud inside the hyperbolic Paul trap and accelerate them to the Microchannel plate or MCP detector. Each collision between ion and MCP detector will create a micro electric current and this current will be amplified and detected through an oscilloscope.

The times of flight from the ion trap center to the MCP detector of  $H^+$ ,  $H_2^+$  and  $H_3^+$  are different. Therefore, three types of ions correspond to three different peaks as shown in the fig. 1.11

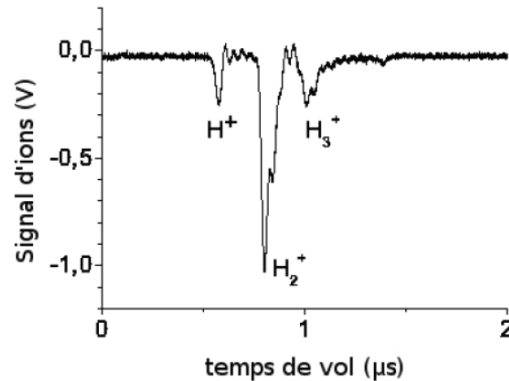


Figure 1.11: Times of flight of different ions  $H^+$ ,  $H_2^+$  and  $H_3^+$

## 2008 experiments

In 2008, after achieving the two-photon source for the high precision spectroscopy of  $H_2^+$  (see [30, 77]), Hilico and colleagues set up the complete experiment system aiming at observing the two-photon transition from  $|\nu = 0, L = 2, J = 5/2\rangle$  to  $|\nu = 1, L = 2, J = 5/2\rangle$ . The details of this experiment can be found in [77, 38], i only give a brief description of the full set-up shown in Fig. 1.12:

*Experimental sequence :*

- The  $H_2^+$  ions are created by electron impact method inside the hyperbolic Paul trap.
- During the whole experiment, the ion cloud is irradiated by a frequency stabilized Quantum Cascade Laser (QCL) at  $9.17 \mu\text{m}$ .
- The ions  $H_2^+$  are photodissociated by a UV laser at 248 nm using a burst of  $N$  UV pulses starting 0.01 s after the end of ion creation.
- Ion extraction and counting, 0.01 s after the last UV pulse.
- The photodissociated ions are detected using a Microchannel Plate detector (MCP detector).

The ions  $H_2^+$  created and trapped inside the hyperbolic Paul trap can reach a number of a few thousands. The decay of ion population doesn't follow a simple exponential law due to collisions between the ions and the residual hydrogen molecules. The decay also depends the increase of pressure (due to electron impact induced outgassing of  $H_2$  from the stainless steel electrodes). The theory that take into account all these effect shows that the ion number  $N$  will decrease as follows :

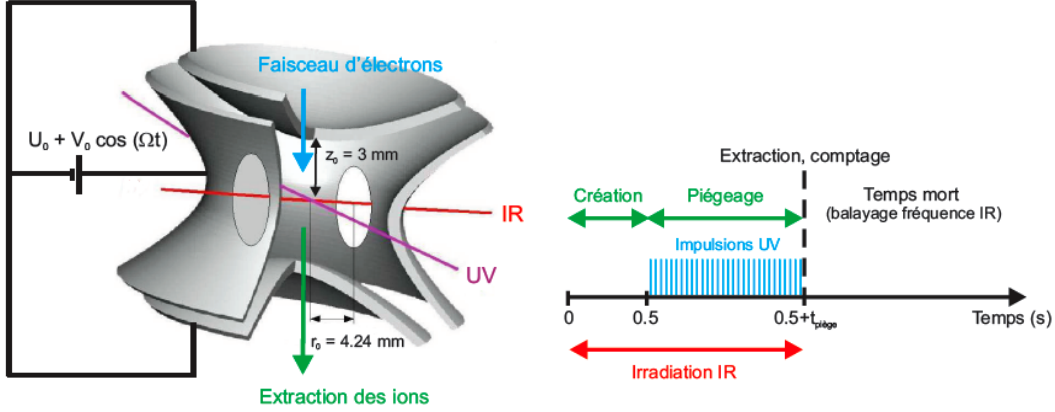


Figure 1.12: Left: Scheme of the hyperbolic Paul trap, the UV and IR lasers and the ion beam. Right : Experimental sequence for REMPD

$$N(t) = N_0 \exp(-\gamma_0 t - (\gamma_1 - \gamma_0)\tau(1 - \exp(-t/\tau))) \quad (1.10)$$

where  $N_0$  is the initial ion number,  $\gamma_0 = 0.073(3) \text{ s}^{-1}$ ,  $\gamma_1 = 0.267(6) \text{ s}^{-1}$  are the loss rates,  $\tau = 4.9(4) \text{ s}$  is the pumping time.

For the detection of the two-photon transition from  $|\nu = 0, L = 2\rangle$  to  $|\nu = 1, L = 2\rangle$ , we combine the infrared laser and ultraviolet laser. The first laser is for the two-photon transition and the second laser is for photodissociation. This technique is known as (2+1) REMPD (Resonance Enhanced MultiPhoton Dissociation) : the UV photon energy is strong enough to break all the ions  $\text{H}_2^+$  in vibrational states  $\nu \geq 1$ . The difference of the numbers of ions in the case with two-photon resonance or two-photon non-resonance will indicate the influence of two-photon transition. In our experiment, the UV laser for the photodissociation is KrF laser at 248 nm up to 100 mJ [30].

In order to compensate the possible drift of the ion number, two successive experimental sequences are needed : one with the IR frequency close to the theoretical transition frequency  $\nu_{th}$ , and another with the IR frequency far away from  $\nu_{th}$ . And the REMPD signal is the normalized difference between the remaining  $\text{H}_2^+$  ion numbers at the end of these two sequences.

For this complete run, no two-photon signal was observed. Figure 1.13 shows the experimental results, and there is no peak around the theoretical values.

The reason behind this failure is that the  $\text{H}_2^+$  ion population produced by the electronic impact is widespread over the rovibrational levels. It has been shown theoretically [40] and experimentally [39] that only 12 % ions  $\text{H}_2^+$  are in the vibrational state  $\nu = 0$ . And because the electronic impact process doesn't influence the rotational population of the initial  $\text{H}_2$  then using the Maxwell-Boltzmann distribution we can estimate that at 300 K, 12 % ions  $\text{H}_2^+$  are in the rotational state  $L = 2$  and 60 % in the hyperfin state  $J = 5/2$ . For the state of interest  $|\nu = 0, L = 2, J = 5/2\rangle$  the population is only  $12\% \times 12\% \times 60\% = 0.86\%$ , this strongly limits the signal-to-noise ratio of the experiment.

The exhaustive analysis of this experimental results and some improvement proposals have been discussed in [38] or [77]. The following Tab. 1.6 summarizes improvements

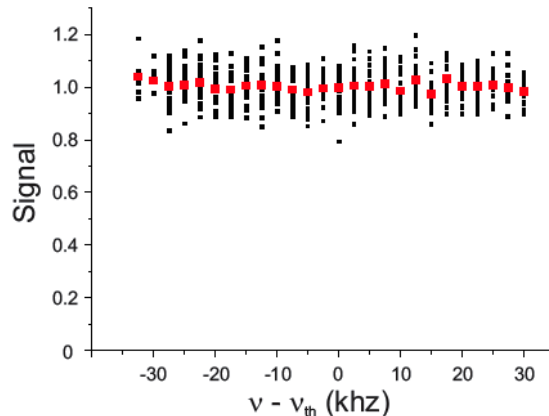


Figure 1.13: Experimental data of the (2+1) REMPD spectroscopy. The QCL laser frequency is tuned around the theoretical value  $\nu_{th} = 32706606500(12)$  kHz. The signal is defined as the ratio between the dissociated fraction in the case where the excitation laser is tuned on or out of resonance. The red squares are the values averaged over the number of runs.

Improvement	Parameters	$t_f$ (s)	SNR
None	-	3.56	0.27
Lifetime (background pressure)	$\gamma_0 = 0.07 \text{ s}^{-1}$	8.63	0.81
Lifetime (pressure + cooling)	$\gamma_0 = 0.01 \text{ s}^{-1}$	13.2	1.1
REMPI production	ro-vibr. populations	3.07	6.3
UV power	$E_{UV} = 114 \text{ mJ}$	2.85	0.31
IR focusing	$\Gamma = 22 \text{ s}^{-1}$	1.90	0.71
IR focusing + cooling	$\Gamma = 66 \text{ s}^{-1}$	1.87	0.72
Linear trap	$\gamma_0 = 0.07 \text{ s}^{-1}, \Gamma = 22 \text{ s}^{-1}$	3.01	1.17
Linear trap + REMPI	$\gamma_0 = 0.07 \text{ s}^{-1}, \Gamma = 22 \text{ s}^{-1} + \text{ro-vibr. populations}$	2.49	25
Linear trap + REMPI + cooling	$\gamma_0 = 0.01 \text{ s}^{-1}, \Gamma = 66 \text{ s}^{-1} + \text{ro-vibr. populations}$	3.23	27

Table 1.6: Proposal of improvements and their effects on the signal-to-noise ratio

and their effect on the signal-to-noise ratio.

From this table, we can see that the most important improvements consists in changing the ion production method. And the solution for the state-selected ion production is the (3 + 1) REMPI (Resonance Enhanced MultiPhoton Ionization) method via the intermediate state  $C \ ^1\Pi_u$  of  $H_2$ . This is the motivation of our research and one of the main topics of my PhD thesis.

## 1.6 Comparison between $\text{H}_2^+$ and $\text{HD}^+$

	$\text{H}_2^+$	$\text{HD}^+$	Comments
State-selected ion production	$\ominus$	$\oplus$	For $\text{H}_2^+$ , the ion production using electronic impact is not well state-selected enough for the two-photon detection, the alternative way for the ion production using REMPI seems very interesting in theory. For $\text{HD}^+$ , the black-body radiation redistribute permanently the population of the rovibrational states, therefore, all populations will contribute to the signal
wavelength	$\oplus$	$\oplus \oplus$	
cooling	$\oplus$	$\oplus$	The sympathetic cooling using $\text{Be}^+$ is slightly more efficient for $\text{H}_2^+$ than $\text{HD}^+$ .
hyperfine structure	$\oplus$	$\ominus$	
natural linewidths	$\oplus$	$\ominus$	in $\text{H}_2^+$ The natural linewidths are extremely small [78] while those of $\text{HD}^+$ are about 10 Hz. Therefore, at the long term, $\text{H}_2^+$ seems to be more interesting than $\text{HD}^+$ .
theoretical calculations	$\oplus$	$\ominus$	
REMPD signal	$\ominus \ominus$	$\oplus$	For $\text{H}_2^+$ : only two-photon excitation is permitted and the two-photon signal is very small. For $\text{HD}^+$ : the single-photon or two-photon excitations are possible.

# Chapter 2

## State-Selected Ion Production by REMPI Method

**Resonance-Enhanced MultiPhoton Ionization** or REMPI process is a multiphoton process used to ionize neutral atoms or molecules through an intermediate (or relay) state.

This technique has been studied and exploited since 1980s by many groups and it's shown that under certain conditions, it serves as an efficient way to make a highly state selected ion source.

In our  $H_2^+$  experiment, the idea of an ion source using REMPI technique came naturally after the failure to observe the REMPD signal of two-photon induced transition in  $H_2^+$  with the ion source using the "traditional" electronic impact method.

This chapter is organized as follows :

- ◆ A brief account of the history on REMPI, the detailed calculation of cross section and branching ratio which is necessary to the  $H_2^+$  experiment.

- ◆ The experimental set-up for the production of  $H_2^+$  ion source using REMPI technique.

### 2.1 Ion source using REMPI technique : Theory

#### 2.1.1 Introduction

Single photon spectroscopy has a long history. It contributed enormously to the development of both fundamental and practical aspects of science. But a single photon transition from one state to another state is unfortunately limited by selection rules and laser wavelength availability. With the development of high-power, pulsed tunable lasers, we can overcome this obstacle by using the (n+m) resonance-enhanced multiphoton ionization or (n+m) REMPI, where n is the number of photon in the transition from the ground state to the intermediate excited state and m is the number of photon in the transition from the intermediate excited state to the ionization continuum state. The selection rules for multiphoton ionization are generally different from those for single-photon transition and we can study the transition between two states that is forbidden for single-photon transition.

The (n+m) REMPI has been extensively studied in the 1980s by many authors for example S.T. Pratt et al. [79] or R.N. Zare et al. [80] ... The authors concentrate the

study of REMPI process on the various diatomic molecules like  $H_2$ , NO, CO,  $N_2$  ... with different combinations of  $m$  et  $n$  (1+1, 2+1, 3+1, 2+2, ...). S.T. Pratt gave an almost exhaustive review of these research in [81].

The (3+1) REMPI process of  $H_2$  via the intermediate state  $C^1\Pi_u$  has also been experimentally studied by S.T. Pratt et al. [79] and by O'Halloran et al. [43].

S. T. Pratt *et al.* considered the photoelectron spectra of  $H_2$  through the excited state  $C^1\Pi_u$  for  $\nu = 0 - 4$ ,  $L = 1$  and showed that the  $H_2^+$  vibrational state distribution follows the Franck-Condon principle.

M. A. O'Halloran *et al.* also considered the same case but with  $L = 2$  and show that the rotational state distribution of the ion  $H_2^+$  is dominated by the channel  $L_+ = L = 2$ . This result is very interesting for us !

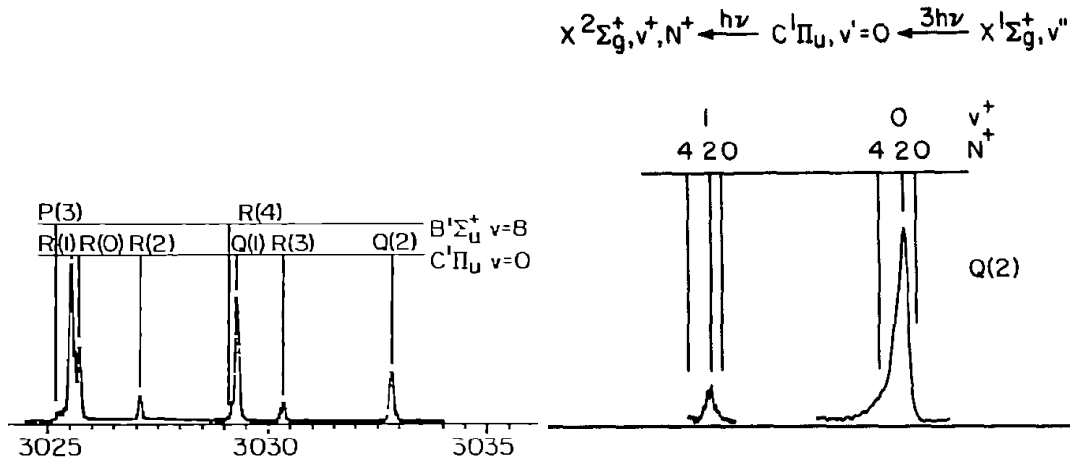


Figure 2.1: Left : (3+1) REMPI signal with different channel and the corresponding wavelength taken from [79]. Right : Rovibrational state distribution of  $H_2^+$  created by the (3+1) REMPI process via the intermediate  $C^1\Pi_u$  state of  $H_2$  taken from [43].

The theoretical study of (n+1) REMPI process and of the selection rules can be found in the articles of S.N. Dixit and V. McKoy [82, 83].

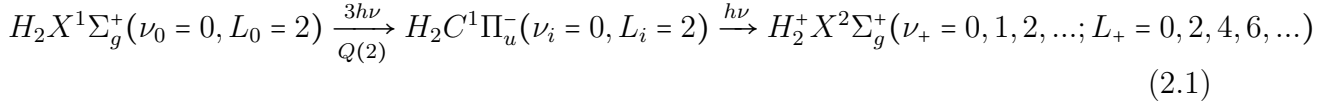
But most of the article are only the proof of concept, as far as i know, no practical applications of this method has been mentioned. In our project, we will use the REMPI method for the practical application : state-selected molecular ion production and measurement of proton-to-electron mass ratio.

### 2.1.2 Vibrational and rotational distribution of $H_2^+$ ions

In this section, we will consider a simple calculation to understand the experimental result in the article of O'Halloran et al. [43] on the rotational distribution of  $H_2^+$   $|\nu_+, L_+\rangle$  in the photoionization of  $H_2$   $C^1\Pi_u$  and predict rotational branching ratios in our case.

The (3 + 1) REMPI process for the state-selected production of  $H_2^+$   $|\nu = 0, L = 2\rangle$ <sup>1</sup>:

<sup>1</sup>The rotational quantum number  $L_+$  of the final state  $|\nu_+, L_+\rangle$  of  $H_2^+$  is an even number due to the symmetry of our system. Both molecules  $H_2$  and  $H_2^+$  possess the exchange symmetry of the nuclei  $P_{12}$ . It's easy to establish a relation between the total parity  $\Pi$ , the electronic parity  $\pi_e$  and  $P_{12}$  as  $Pi = P_{12}\pi_e$ .



The (3+1) REMPI process is a four-photon process from the ground state  $H_2 X^1\Sigma_g^+, \nu_0 = 0, L_0 = 2$  to the ionization continuum state  $H_2^+, \nu_+, L_+$ . This process is illustrated in Fig.2.2. In this figure, we omit the intermediate energy levels whose contribution to the signal is small.

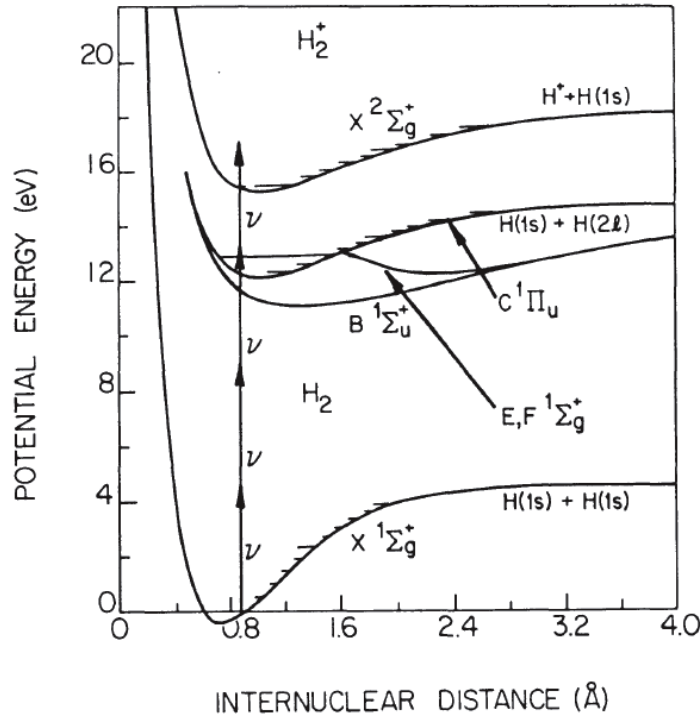


Figure 2.2: Energy level diagram of  $H_2$  relevant to 2.1 [84]

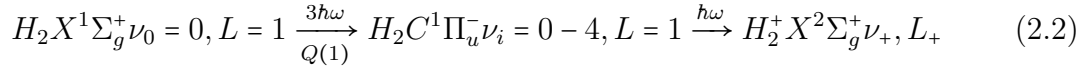
It's very important for our experiment to know the rovibrational distribution of  $H_2^+$  ions from this process. Therefore, we now use both experimental and theoretical results to understand the vibrational and rotational distribution of the final state of the (3+1) REMPI process 2.1.

---

For the states  $X^1\Sigma_g^+$  of  $H_2$  and  $X^2\Sigma_g^+$  of  $H_2^+$ , we have always  $\pi_e = 1$ , and because the electronic dipole-allowed transition respects the conservation of the spins, then  $P_{12}$  is unchanged during the interaction. We have demonstrated that the total parity is changed, and because  $\Pi = (-1)^L$  for both states  $X^1\Sigma_g^+, \nu, L$  of  $H_2$  and  $X^2\Sigma_g^+, \nu, L$  of  $H_2^+$ , then the rotational number of the ion  $H_2^+$  is always even. The reason why the total parity  $\Pi$  is unchanged can be obtained from fact that the operator of the four-photon transition is an even operator but this is only true when we suppose that this transition is allowed.

### 2.1.2.1 Vibrational distribution

S. T. Pratt *et al.* [79] have investigated experimentally the photoelectron spectra for  $H_2$  through the excited state  $C^1\Pi_u$ ,  $\nu = 0 - 4$ ,  $L = 1$  as shown in Fig.2.2.



They showed that the the  $H_2^+$  vibrational state distribution is dominated by the channel  $\nu_+ = \nu_i$  (see Fig.2.3) in accordance with the Franck-Condon principle (see Tab.2.1). For high values of the vibrational quantum number ( for example,  $\nu_i = 4$  ), they observed significant deviations of the experimental results with respect the Franck-Condon principle.

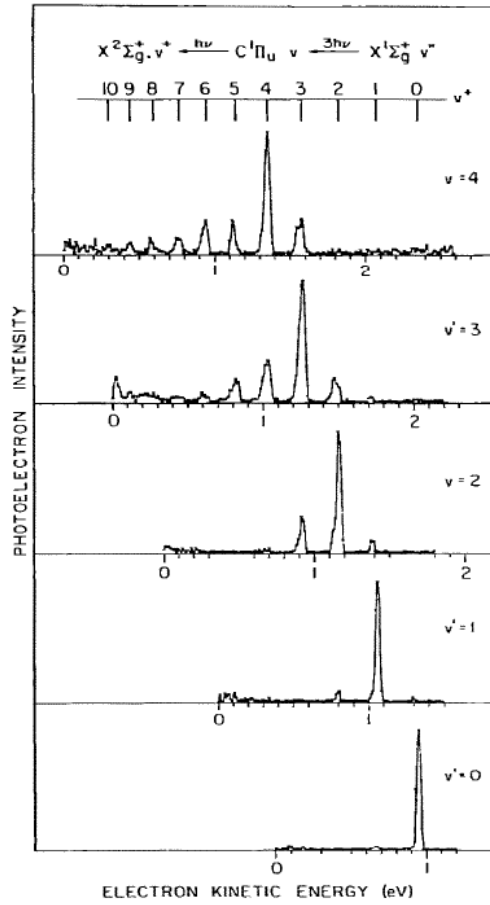


Figure 2.3: Photoelectron spectra of  $H_2$  [79]

The Franck-Condon factors for the transition  $H_2^+ X^2\Sigma_g^+, \nu_+ \leftarrow H_2 C^1\Pi_u, \nu_i$  are maximum for the transition with  $\nu_+ = \nu_i$ . This explains the peak  $\nu_+ = \nu_i$  in the experimental observation but it fails to explain the peaks with  $\nu_+ \neq \nu_i$ .

S. N. Dixit *et al.* [85] proceeded the full consideration of (3+1) REMPI process without Franck-Condon approximation to explain both the central peak at  $\nu_+ = \nu_i$  and small peaks at  $\nu_+ \neq \nu_i$ . Their works give a quite good agreement with the experimental observation but the differences between these theoretical results and the experimental results for the small peaks with  $\nu_+ \neq \nu_i$  and for high values of  $\nu_i$  are large. Another attempt to

$\nu_+$	$\nu_i = 0$	$\nu_i = 1$	$\nu_i = 2$	$\nu_i = 3$	$\nu_i = 4$
0	$9.89 \times 10^{-1}$	$1.10 \times 10^{-2}$	$4.67 \times 10^{-6}$	$1.45 \times 10^{-8}$	$2.26 \times 10^{-9}$
1	$1.06 \times 10^{-2}$	$9.66 \times 10^{-1}$	$2.29 \times 10^{-2}$	$2.04 \times 10^{-5}$	$2.98 \times 10^{-8}$
2	$3.08 \times 10^{-4}$	$2.16 \times 10^{-2}$	$9.43 \times 10^{-1}$	$3.55 \times 10^{-2}$	$6.47 \times 10^{-5}$
3	$1.46 \times 10^{-5}$	$9.98 \times 10^{-4}$	$3.22 \times 10^{-2}$	$9.19 \times 10^{-1}$	$4.80 \times 10^{-2}$
4	$1.04 \times 10^{-6}$	$6.53 \times 10^{-5}$	$2.13 \times 10^{-3}$	$4.16 \times 10^{-2}$	$8.96 \times 10^{-1}$
5	$1.00 \times 10^{-7}$	$5.95 \times 10^{-6}$	$1.82 \times 10^{-4}$	$3.71 \times 10^{-3}$	$4.93 \times 10^{-2}$
6	$1.22 \times 10^{-8}$	$7.24 \times 10^{-7}$	$2.03 \times 10^{-5}$	$3.98 \times 10^{-4}$	$5.69 \times 10^{-3}$
7	$1.87 \times 10^{-9}$	$1.12 \times 10^{-7}$	$2.92 \times 10^{-6}$	$5.42 \times 10^{-5}$	$7.43 \times 10^{-4}$

Table 2.1: Franck-Condon factors for  $\text{H}_2^+ \text{ X } ^2\Sigma_g^+, \nu_+ \leftarrow \text{H}_2 \text{ C}^1\Pi_u, \nu_i$  [79]

$\nu_i$	$\nu_+$	Q(1)	Q(2)
0	0	1.00	1.00
	1	0.10(2)	0.09(2)
1	0	0.09(2)	0.08(4)
	1	1.00	1.00
	2	0.21(3)	0.16(6)
	3	0.06(2)	0.02(4)

Table 2.2: Vibrational branching ratios for the  $\text{H}_2^+ \text{ C } ^1\Pi_u \nu_i \rightarrow \text{H}_2^+ \text{ X } ^2\Sigma_g^+ \nu_+$  ionizing transition [43]

explain this deviation by A. P. Hickman [86] based on a new mechanism where the final step of ionization the excited state  $\text{C } ^1\Pi_u$  of  $\text{H}_2$  is followed by the competition between dissociation of the nuclei (leading to  $\text{H}^* + \text{H}$ ) and electronic autoionization (leading to  $\text{H}_2^+ + \text{e}$ ) [86].

M. A. O'Halloran *et al.* [43] also investigated experimentally the vibrational distribution of the process described in 2.1. They observed that 90% of  $\text{H}_2^+$  is in the vibrational state  $\nu_+ = 0$  as shown in the Fig.2.1 or in the Tab.2.2.

**Conclusion :**

90 %  $\text{H}_2^+$  ions produced by the process 2.4 are in the vibrational state  $|\nu_+ = 0\rangle$

### 2.1.2.2 Rotational distribution

The experimental observation of the REMPI process of Eq. 2.1, by O'Halloran *et al.* is shown in Fig. 2.1. The central peak corresponds to the rovibrational state  $|\nu_+ = 0, L_+ = 2\rangle$ . Most of  $\text{H}_2^+$  ions are in the vibrational state  $|\nu_+ = 0\rangle$  as discussed in the previous paragraph but the distribution of population in the rotational state is not well resolved. In this paragraph, we will proceed the "simple" calculation to better understand the rotational distribution of the signal in Fig. 2.1.

I will use the theoretical foundation of REMPI process in the article of Dixit *et al.* [82] to estimate the rotational distribution of the ions  $\text{H}_2^+$  in the final step of the (3 + 1) REMPI process 2.1. The calculation can be divided in two parts :

- Calculation of the alignment created in the  $\text{C } ^1\Pi_u$   $|\nu_i = 0, L_i = 2\rangle$  state of  $\text{H}_2$  due to three-photon absorption from the  $\text{X } ^1\Sigma_g^+$   $|\nu_0 = 0, L_0 = 2\rangle$  state of  $\text{H}_2$  or more precisely, calculation of the matrix density  $\rho_{ii'} = \langle L_i M_i | \rho | L_i M_{i'} \rangle$  (with  $M_i, M_{i'} = -L_i, -L_i + 1, \dots, L_i - 1, L_i$ ).
- Calculation of the generalized photoionization rate  $\Gamma_{M_{i'} M_i}^{L_i L_+}$  for the ionization step from the intermediate state  $\text{H}_2 \text{ C } ^1\Pi_u$   $|\nu_i = 0, L_i = 2\rangle$  to the final continuum state with  $|\nu_+ = 0, L_+\rangle$  as the rovibrational state of  $\text{H}_2^+$  (the mathematical definition of the photoionization rate will be given latter).

The first part of the calculation is very complicated so i will present only the general results, but i will expose in detail the calculation for the second part and give an estimation of the rotational distribution of  $\text{H}_2^+$ .

If we denote  $P_{L_i L_+}$  the probability that the  $\text{H}_2^+$  ions created by the photoionization of the excited state  $\text{C } ^1\Pi_u$   $|\nu_i = 0, L_i = 2\rangle$  of  $\text{H}_2$  are in the rotational quantum state  $|L_+\rangle$  (the vibrational quantum state is suppose to be always  $|\nu = 0\rangle$ ).

The relation between  $P_{L_i L_+}$ ,  $\rho_{ii'}$  and  $\Gamma_{M_{i'} M_i}^{L_i L_+}$  is :

$$P_{L_i L_+} \propto \sum_{M_i, M_{i'}} \Gamma_{M_{i'} M_i}^{L_i L_+} \rho_{ii'} \quad (2.3)$$

Therefore, to determine the rotational distribution of  $\text{H}_2^+$  created by the process 2.1, we need to calculate both the alignment of the intermediate level  $|L_i, M_i\rangle$  and photoionization rate from this intermediate level to the ionized continuum levels.

### Photoionization rate :

In figure 2.4, i show in detail the most important chanel contributing to the process of Eq.2.1 for linearly polarized light. The relay states for one-photon and two-photon transition from the initial state are simplified to the most resonant states, we omit the relay states like  $\text{I } ^1\Pi_g$ ,  $\text{J } ^1\Sigma_g^+$ . Normally, the intermediate Rydberg state  $\text{H}_2 \text{ C } ^1\Pi_u$  overlaps in energy with the valence state  $\text{H}_2 \text{ B } ^1\Sigma_u^+$ , but by tuning the laser frequency in resonance with the three-photon Q(2) transition line, we are able to eliminate the Rydberg-valence mixing between these two states because the state  $\text{H}_2 \text{ B } ^1\Sigma_u^+$  couples only with the component  $\Pi^+$  but the component  $\Pi^-$  is unaffected.

The diagram is generated by applying succesively the single-photon dipole selection rules for the homonuclear molecules [87]:

$$\Delta L = 0, \pm 1$$

$$\Delta K = 0, \pm 1$$

$$\oplus \leftrightarrow \ominus$$

$$g \leftrightarrow u$$

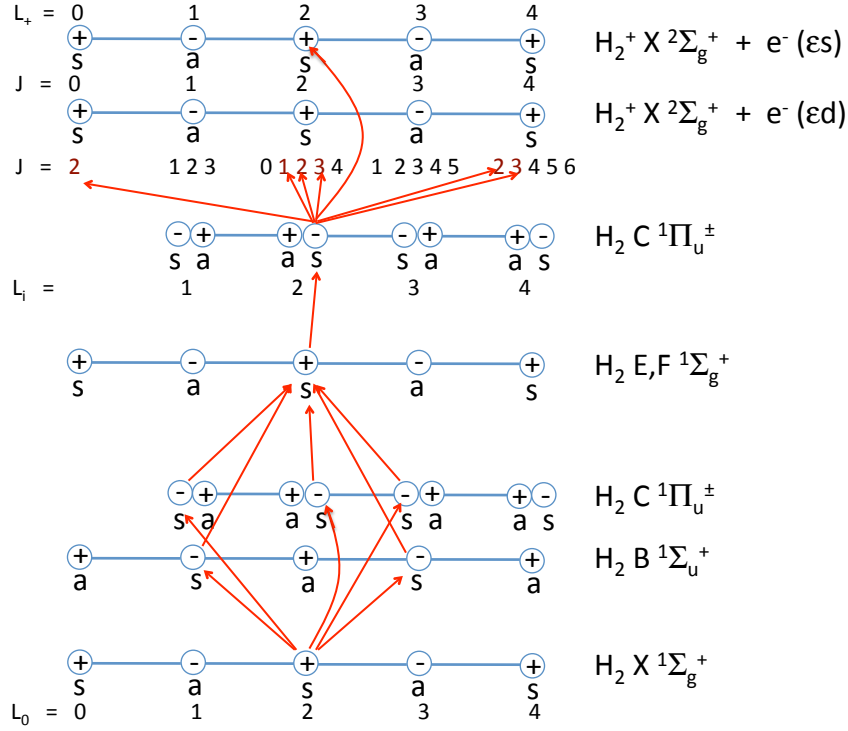


Figure 2.4: Diagram of leading channels for the (3+1) REMPI process of 2.1. The  $\oplus, \ominus$  denote the parity of the total wave function, the  $+, -$  superscripts used in the electronic state labelling denote the parity of the electronic wave function.

$$s \longleftrightarrow s$$

$$a \longleftrightarrow a$$

here,  $s$  and  $a$  denote the symmetry of the total wave function under the exchange of nuclei,  $g$  and  $u$  denote the symmetry of the electronic wave function under the inversion through the origin.

To calculate the alignment or more precisely  $\rho_{ii}$ , we might use the optical Bloch equation to study a three-photon transition from the initial state X  $^1\Sigma_g^+$   $|\nu_0 = 0, L_0 = 2\rangle$  state of H<sub>2</sub> to the C  $^1\Pi_u$   $|\nu_i = 0, L_i = 2\rangle$  state of H<sub>2</sub> as in [82] but in the case of weak field, we can use the Q operator as in the PhD thesis of F. Biraben [88] :

$$Q = \sum_{r,r'} \vec{D}\vec{\epsilon}|r'\rangle \frac{1}{\hbar\Delta\omega'} \langle r'|\vec{D}\vec{\epsilon}|r\rangle \frac{1}{\hbar\Delta\omega} \langle r|\vec{D}\vec{\epsilon} \quad (2.4)$$

where,  $\Delta\omega = \omega_r - \omega_0 - \omega$  and  $\Delta\omega' = \omega'_r - \omega_0 - 2\omega$ .

And we can obtain an expression for  $\rho_{ii}$  as following :

$$\rho_{ii} \propto \sum_{M_0} \left| \sum_{L_1 M_1} \sum_{L_2 M_2} \frac{\langle L_i M_i | \vec{D}\vec{\epsilon} | L_2 M_2 \rangle \langle L_2 M_2 | \vec{D}\vec{\epsilon} | L_1 M_1 \rangle \langle L_1 M_1 | \vec{D}\vec{\epsilon} | L_0 M_0 \rangle}{\hbar\Delta\omega' \hbar\Delta\omega} \right|^2 \quad (2.5)$$

The accurate calculation of this term is very complicated since it requires a precise knowledge of the dipole matrix elements between excited states of  $H_2$  and we will show later that the alignment of the intermediate state don't really have a particular importance in our estimation of the rotational distribution of  $H_2^+$  ions at the final step of the (3+1) REMPI process.

Now, we proceed the second task : the calculation of the generalized photoionization rate  $\Gamma_{M_i' M_i}^{L_i L_+}$ . For the sake of simplicity, in the calculation we use linearly polarized light. Hence, in the absence of other interactions like collisions between molecules, the ionization through each  $|L_i, M_i\rangle$  forms an independant chanel, and we only need to consider the photoionization rate  $\Gamma_{M_i M_i}^{L_i L_+}$  and the population  $\rho_{ii}$ . We also neglect the spin of electron which will restrict our results to Hund's case (b).

In what follows, we use the convention of Wigner D-matrix, angular wave function of the diatomic molecules ... as described in Edmonds' book [89]<sup>2</sup>. We denote the space-fixed frame as  $(x, y, z)$  and body-fixed frame as  $(x', y', z')$ . The primed coordinates refer to the body-fixed frame while the unprimed coordinates refer to the space-fixed frame.

The rate of ejection of a photoelectron in the direction  $(\theta, \phi)$  after ionization of the intermediate state  $|L_i, M_i\rangle$  is:

$$\Gamma_{M_i M_i}^{L_i L_+}(\theta, \phi) = 2\pi\alpha I \sum_{M_+, K_+} |\langle \Psi_{\gamma_+ L_+ M_+ K_+} | D_{\mu_0} | \Psi_{\gamma_i L_i M_i K_i} \rangle|^2 \quad (2.6)$$

where  $\alpha$  is the fine structure constant, the parameter  $I$  denotes the laser intensity ( $W/cm^2$ ). The spherical polar angles  $\theta$  and  $\phi$  are mesured in a spherical coordinate system whose  $z$  axis coincides with the direction of light polarization for linearly polarized light or with the direction of propagation if the light is circularly polarized.  $|\Psi_{\gamma_i L_i M_i K_i}\rangle$  and  $|\Psi_{\gamma_+ L_+ M_+ K_+}\rangle$  are respectively the wave function of the intermediate state and the final continuum ionized state.  $eD_{\mu_0}$  is the total electronic dipole moment.

The wave function for the intermediate state in the Born-Oppenheimer approximation is factorized in the form :

$$|\Psi_{\gamma_i L_i M_i K_i}\rangle = \sqrt{\frac{2L_i + 1}{8\pi^2}} \psi_{\gamma_i}^{(e)}(\{\mathbf{r}'_i\}, R) \chi_{\nu_i}(R) \mathcal{D}_{M_i K_i}^{(L_i)}(\hat{R}) \quad (2.7)$$

where  $\psi_{\gamma_i}^{(e)}$  is the electronic wave function,  $\chi_{\nu_i}(R)$  is the vibrational wave function and  $\mathcal{D}_{M_i K_i}^{(L_i)}(\hat{R})$  is the Wigner D-matrix with total angular momentum  $L_i$ . The projection of  $L_i$  along the  $z$  axis of the space-fixed frame  $L_{iz} = M_i$  and the projection of  $L_i$  along the  $z'$  axis of the body-fixed frame  $L_{iz'} = K_i$ .

The wave function for the final continuum ionized state is :

$$|\Psi_{\gamma_+ L_+ M_+ K_+}\rangle = \sqrt{\frac{2L_+ + 1}{8\pi^2}} \chi_{\nu_+}(R) \mathcal{D}_{M_+ K_+}^{(L_+)}(\hat{R}) \sum_{lm\lambda} i^l e^{-im\phi} Y_{lm}^*(\theta, \phi) (-1)^{m-\lambda} \mathcal{D}_{m\lambda}^{(l)}(\hat{R}) \psi_{\gamma_+}^{(e)}(\{\mathbf{r}'_+\}, R) \quad (2.8)$$

where  $\nu_+$ ,  $L_+$ ,  $M_+$  and  $K_+$  are respectively the ionic vibrational quantum number, its total orbital angular momentum quantum number, the projection of  $\vec{L}$  on the  $z$  axis of

---

<sup>2</sup>The convention used in the book of Edmonds is slightly different in comparison with most of reference books. The author use the "passive rotation" i.e the rotation means the rotation of the coordinate frame, the physical system remains immobile.

the space-fixed frame and the projection of  $\vec{L}$  on the  $\bar{z}$  axis of the body-fixed frame. We denote respectively  $l, m$  and  $\lambda$  the angular momentum quantum number of photoelectron, its projection on the  $z$  axis of the space-fixed frame and its projection on the  $\bar{z}$  axis of the body-fixed frame. The real quantity  $\eta_l$  is the *phase shift* [90],  $\psi_{\gamma_f}^{(e)}(\{\mathbf{r}'_i\}, R)$  is the antisymmetrized electronic wave function including the wave function of the photoelectron and the  $N - 1$  electron wave function for ion.

In the calculation of rotational branching ratio of  $(3 + 1)$  REMPI process, direction of photoelectron in the formula of  $\Gamma_{M_i M_i}^{L_i L_+}(\theta, \phi)$  is a redundant parameter, therefore the photodissociation rates that we want to calculate is defined as follows :

- The partial photoionization rate for different Zeeman sublevels of the intermediate state is obtained by integrating over all direction  $(\theta, \phi)$  of photoelectron :

$$\Gamma_{L_i L_+}(M_i) := \int d\Omega(\theta, \phi) \sum_{K_i} \Gamma_{M_i M_i}^{L_i L_+}(\theta, \phi)$$

- The total photodissociation rate is obtained by summing over all initial Zeeman sublevels the partial photodissociation rate :

$$\begin{aligned} \Gamma_{L_i L_+} &:= \sum_{M_i} \Gamma_{L_i L_+}(M_i) \\ &= \int d\Omega(\theta, \phi) \sum_{M_i K_i} \Gamma_{M_i M_i}^{L_i L_+}(\theta, \phi) \end{aligned}$$

We now proceed some complicated algebraic manipulations to obtain the partial photodissociation rate  $\Gamma_{L_i L_+}(M_i)$  and total photodissociation rate  $\Gamma_{L_i L_+}$

The total electronic dipole moment can be written as:

$$D_{\mu_0} = \frac{4\pi}{3} \sum_{\mu} (-1)^{\mu - \mu_0} \mathcal{D}_{\mu_0 \mu}^{(1)}(\hat{R}) \sum_s r_s Y_{1\mu}(\hat{r}'_s) \quad (2.9)$$

From 2.6, 2.7, 2.8, 2.9, we can rewrite  $\Gamma_{M_i M_i}(\theta, \phi)$  as:

$$\begin{aligned} \Gamma_{M_i M_i}^{L_i L_+}(\theta, \phi) &= 2\pi\alpha I \sum_{M_+ K_+} \left| \sqrt{\frac{4\pi}{3}} \sum_{lm\lambda} \sum_{\mu} \sum_{l_t m_t k_t} (-i)^l e^{im} Y_{lm}(\theta, \phi) (-1)^{\mu - \mu_0 + M_+ - K_+ + m_t - k_t} (2l_t + 1) \right. \\ &\quad \left. \sqrt{(2L_i + 1)(2L_+ + 1)} \begin{pmatrix} L_+ & L_i & l_t \\ -M_+ & M_i & m_t \end{pmatrix} \begin{pmatrix} L_+ & L_i & l_t \\ -K_+ & K_i & k_t \end{pmatrix} \begin{pmatrix} l & 1 & l_t \\ -m & \mu_0 & -m_t \end{pmatrix} \right. \\ &\quad \left. \begin{pmatrix} l & 1 & l_t \\ -\lambda & \mu & -k_t \end{pmatrix} \overline{r_{fi}^{(\mu)}} \right|^2 \end{aligned} \quad (2.10)$$

where

$$\begin{aligned} \overline{r_{fi}^{(\mu)}} &= \int dR \chi_{\nu_+}^*(R) \chi_{\nu_i}(R) r_{fi}^{(\mu)}(R) \\ r_{fi}^{(\mu)}(R) &= \langle \psi_{\gamma_f}^{(e)}(\{\mathbf{r}'_i\}, R) | \sum_s r_s Y_{1\mu}(\hat{r}'_s) | \psi_{\gamma_i}^{(e)}(\{\mathbf{r}'_i\}, R) \rangle \end{aligned}$$

By expanding the square modulus and using  $\int d\Omega Y_{lm}(\theta, \phi) Y_{l'm'}(\theta, \phi)^* = \delta_{ll'} \delta_{mm'}$ , we have :

$$\begin{aligned}
\Gamma_{L_i L_+} &= 2\pi\alpha I \frac{4\pi}{3} (2L_+ + 1)(2L_i + 1) \sum_{M_i K_i} \sum_{M_+ K_+} \sum_{lm} \sum_{\lambda\lambda'} \sum_{\mu\mu'} \sum_{l_t m_t k_t} \sum_{l'_t m'_t k'_t} (-1)^{\mu+\mu'+m_t+m'_t-k_t-k'_t} \\
&\quad (2l_t + 1) \begin{pmatrix} L_+ & L_i & l_t \\ -M_+ & M_i & m_t \end{pmatrix} \begin{pmatrix} L_+ & L_i & l_t \\ -K_+ & K_i & k_t \end{pmatrix} \begin{pmatrix} l & 1 & l_t \\ -m & \mu_0 & -m_t \end{pmatrix} \begin{pmatrix} l & 1 & l_t \\ -\lambda & \mu & -k_t \end{pmatrix} \overline{r_{fi}^{(\mu)}} \\
&\quad (2l'_t + 1) \begin{pmatrix} L_+ & L_i & l'_t \\ -M_+ & M_i & m'_t \end{pmatrix} \begin{pmatrix} L_+ & L_i & l'_t \\ -K_+ & K_i & k'_t \end{pmatrix} \begin{pmatrix} l & 1 & l'_t \\ -m & \mu_0 & -m'_t \end{pmatrix} \begin{pmatrix} l & 1 & l'_t \\ -\lambda' & \mu' & -k'_t \end{pmatrix} \overline{r_{fi}^{(\mu')}}^* \\
&= 2\pi\alpha I \frac{4\pi}{3} (2L_+ + 1)(2L_i + 1) \sum_{M_i K_i} \sum_{M_+ K_+} \sum_{lm} \left| \sum_{\lambda} \sum_{\mu} \sum_{l_t m_t k_t} (-1)^{\mu+m_t-k_t} (2l_t + 1) \right. \\
&\quad \left. \begin{pmatrix} L_+ & L_i & l_t \\ -M_+ & M_i & m_t \end{pmatrix} \begin{pmatrix} L_+ & L_i & l_t \\ -K_+ & K_i & k_t \end{pmatrix} \begin{pmatrix} l & 1 & l_t \\ -m & \mu_0 & -m_t \end{pmatrix} \begin{pmatrix} l & 1 & l_t \\ -\lambda & \mu & -k_t \end{pmatrix} \overline{r_{fi}^{(\mu)}} \right|^2
\end{aligned}$$

### Branching ratio :

Now we will apply the general formula of the photoionization rate for our (3 + 1) REMPI process. We have  $L_i = 2, L_+ = 0, 2, 4, K_i = \pm 1, K_+ = 0$   
For the linearly polarized light, we have  $\mu_0 = 0$  and in general  $\mu = -1, 0, +1$   
The properties of 3-j symbols imply :

$$k_t = -K_i, \lambda = \mu + K_i, m_t = -m = M_+ - M_i$$

The selection rule (Dixit & McKoy [83]) :  $L_+ - L_i + l + p_i + p_+ = \text{odd}$ , so we have  $l = 0, 2, 4, 6, 8$  (in our case,  $l_{max} = 8$ )

The formula for  $\Gamma_{L_i L_+}$  reduces to:

$$\begin{aligned}
\Gamma_{2L_+} &= 2\pi\alpha I \frac{4\pi}{3} .5. (2L_+ + 1) \sum_{M_i = -2}^2 \sum_{K_i = \pm 1} \sum_{M_+ = -L_+}^{L_+} \sum_{l=0,2,4,6,8} \left| \sum_{\mu=-1,0,+1} \sum_{l_t=0}^{10} (-1)^\mu (2l_t + 1) \right. \\
&\quad \begin{pmatrix} L_+ & 2 & l_t \\ -M_+ & M_i & M_+ - M_i \end{pmatrix} \begin{pmatrix} L_+ & 2 & l_t \\ 0 & K_i & -K_i \end{pmatrix} \begin{pmatrix} l & 1 & l_t \\ M_+ - M_i & 0 & M_i - M_+ \end{pmatrix} \\
&\quad \left. \begin{pmatrix} l & 1 & l_t \\ -\mu - K_i & \mu & K_i \end{pmatrix} \overline{r_{fi}^{(\mu)}} \right|^2
\end{aligned}$$

Note that we only need  $(l_t)_{max} = 10$  and  $(l_t)_{min} = 0$  (because of 3-j symbol properties).

The partial photoionization rate for different Zeeman sublevels of the intermediate state is:

$$\begin{aligned}
\Gamma_{2L_+}(M_i) &= 2\pi\alpha I \frac{4\pi}{3} .5. (2L_+ + 1) \sum_{K_i = \pm 1} \sum_{M_+ = -L_+}^{L_+} \sum_{l=0,2,4,6,8} \left| \sum_{\mu=-1,0,+1} \sum_{l_t=0}^{10} (-1)^\mu (2l_t + 1) \right. \\
&\quad \begin{pmatrix} L_+ & 2 & l_t \\ -M_+ & M_i & M_+ - M_i \end{pmatrix} \begin{pmatrix} L_+ & 2 & l_t \\ 0 & K_i & -K_i \end{pmatrix} \begin{pmatrix} l & 1 & l_t \\ M_+ - M_i & 0 & M_i - M_+ \end{pmatrix} \\
&\quad \left. \begin{pmatrix} l & 1 & l_t \\ -\mu - K_i & \mu & K_i \end{pmatrix} \overline{r_{fi}^{(\mu)}} \right|^2
\end{aligned}$$

The population  $N_{L_+}$  of  $\text{H}_2^+$  ions in the rotational state  $|L_+\rangle$  is proportional to the probability  $P_{L_i L_+}$  in the Eq. 2.3, then we have :

$$N_{L_+} \sim \sum_{M_i} \Gamma_{2L_+}(M_i) \rho_{ii}$$

The lower and upper bound of the ratio of populations of two rotational level  $|L\rangle$  and  $|L'\rangle$  are determined using the following inequality:

$$\frac{\min_{M_i} \Gamma_{2L'}(M_i)}{\max_{M_i} \Gamma_{2L}(M_i)} \leq \frac{N_{L'}}{N_L} = \frac{\sum_{M_i} \Gamma_{2L'}(M_i) \rho_{ii}}{\sum_{M_i} \Gamma_{2L}(M_i) \rho_{ii}} \leq \frac{\max_{M_i} \Gamma_{2L'}(M_i)}{\min_{M_i} \Gamma_{2L}(M_i)}$$

Now, we use *Mathematica* and the matrix elements  $r_{fi}^{(\mu)}$  calculated by V. McKoy and K. Wang [91] to calculate these bounds (see Appendix B for the matrix element table and the *Mathematica* program):

◆ For the ratio between the populations in  $|L_+ = 0\rangle$  and  $|L_+ = 2\rangle$  :

$$0 \% \leq \frac{N_0}{N_2} \leq 1.21709 \%$$

◆ For the ratio between the populations in  $|L_+ = 4\rangle$  and  $|L_+ = 2\rangle$  :

$$0.633558 \% \leq \frac{N_4}{N_2} \leq 1.52453 \%$$

If we suppose that the intermediate state  $|L_i, M_i\rangle$  is isotropic i.e the population is equi-distributed between the Zeeman sublevels  $\rho_{ii} = 1/(2L_i + 1)$ , then  $N_{L_+} \sim \sum_{M_i} \Gamma_{2L_+}(M_i) \rho_{ii} \sim \Gamma_{2L_+}$ . Therefore, we can use branching ratio between the photoionization rates  $\Gamma_{2L_+}$  to determine the rotational distribution of population of  $\text{H}_2^+$  as follows :

$$\frac{N_0}{N_2} = \frac{\Gamma_{20}}{\Gamma_{22}} = 0.487294 \%$$

$$\frac{N_4}{N_2} = \frac{\Gamma_{24}}{\Gamma_{22}} = 0.990281 \%$$

**Conclusion :**

97  $\geq$  %  $\text{H}_2^+$  ions produced by the process 2.4 are in the rotational state state  $|L_+ = 2\rangle$

## 2.2 Experimental set-up

In this second part, i will present in details our experiment set-up to produce a source of highly state-selected  $\text{H}_2^+$  ions using the (3+1) REMPI method described in Sect.2.1.

The experiment can be divided into two separate tasks : first task consists in installing and controlling the laser source at 303 nm for the 3+1 REMPI excitation and the second task is to manipulate and transfer the ion beam into the linear Paul trap for the  $\text{H}_2^+$  experiment.

The simplified experimental scheme is described in Fig. 2.5 : the 303 nm photons interact with a  $\text{H}_2$  molecular beam. The  $\text{H}_2^+$  ions created by REMPI process will be pushed by the difference of voltage between two truncated conic electrodes, then will be transferred and controled by the Einzel lenses, deflection systems. The "Gate" valve is used to test the efficiency of REMPI method before transferring the ions into the linear Paul trap through quadrupole guide.

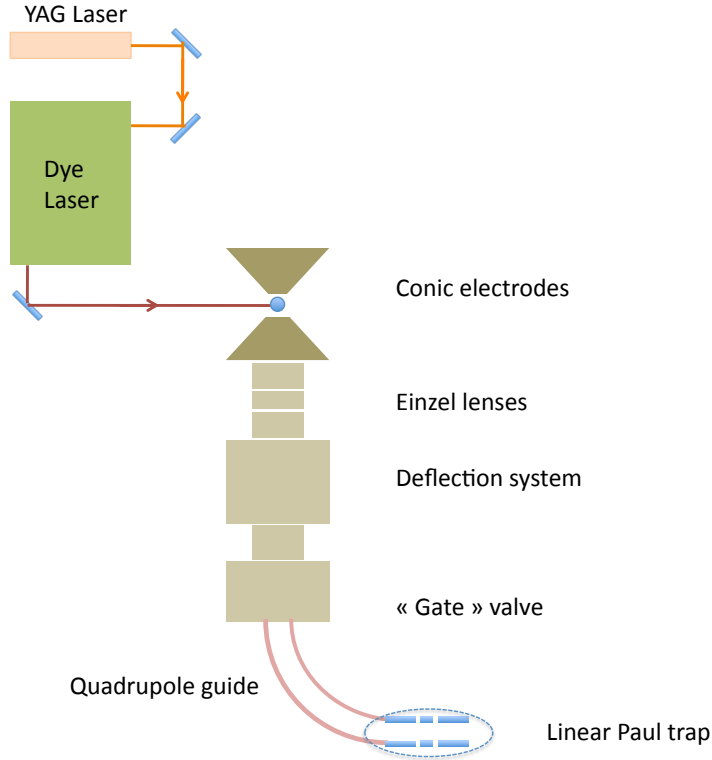


Figure 2.5: The scheme of the experimental setup for REMPI production and two-photon experiment (not to scale).

### 2.2.1 Laser source at 303 nm

For the 303 nm photon source, we follow closely the experiment described in the article of Pratt *et al* [79]. They have observed the (3+1) REMPI signal of  $\text{H}_2$  via  $C^1\Pi_u$  state using a frequency-doubled pulsed dye laser delivering 0.4-1.3 mJ and pumped by a frequency-doubled YAG laser.

In our experiment, we use a Quantel Brilliant frequency-doubled YAG laser at 532 nm, 120 mJ and delivering pulses with a 20 Hz repetition rate to pump a Sirah Cobra frequency-doubled pulsed dye laser. We obtain the photon source at 303 nm with about 4 mJ energy, repetition frequency  $f_{rep} = 20$  Hz.

### 2.2.1.1 Pulsed Dye Laser

The optical system of Sirah pulsed dye laser consists of a resonator, a preamplifier and a remote controlled frequency-doubling system used to convert visible photons to UV photons as depicted in Fig.2.6.

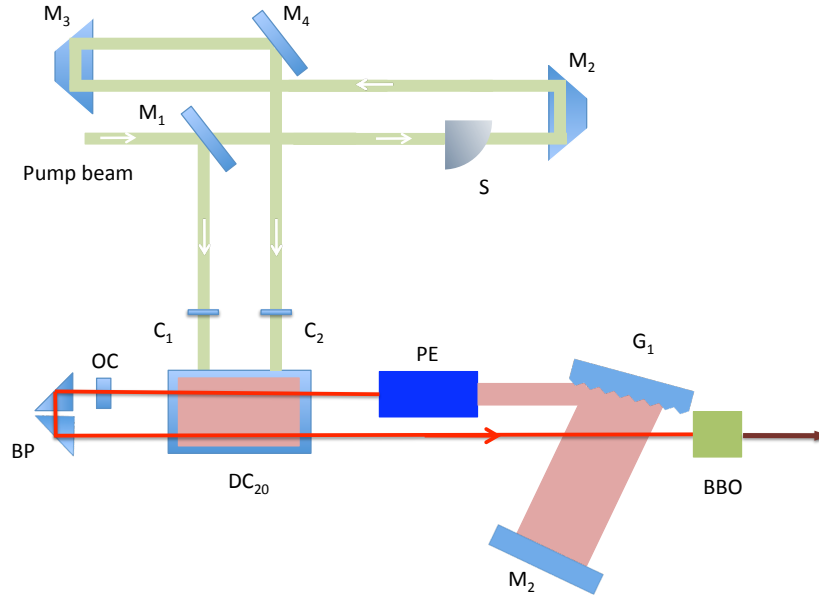


Figure 2.6: Optical set-up for Sirah pulsed dye laser ( $G_1$  - gratings;  $G_2$  - mirror for wavelength tuning;  $PE$  - prism expander;  $DC_{20}$  - dye cell 20 mm;  $OC$  - output coupler;  $BP$  - polarising Brewster plates + reflecting prism;  $M_i$  - mirrors/prisms/beamsplitters for pump beam;  $C_i$  - cylindrical lenses;  $S$  - beam shutter;  $DC$  - doubling crystal)

The resonator is the heart of the laser system, it consists of the output coupler  $OC$ , the dye cell  $DC_{20}$  containing the dye mixture of Rhodamine 640 and Rhodamine 610, the prism expander  $PE$ , the grazing incidence grating  $G_1$  and the Aluminium mirror with protective coating  $G_2$  used for wavelength tuning.

The output of the oscillator is polarized using three Brewster plates and elevated about 1 cm and sent back to the preamplifier zone in the dye cell.

The dye in this system are Rhodamine 610 and Rhodamine 640. The figure 2.8 shows the typical dye gain curves. We can see from this figure that the maximal output of gain curve of Rhodamine 610 is at 600 nm, and Rhodamine 640 at 625 nm. The 606 nm wavelength lies between Rhodamine 610 and Rhodamine 640 ranges, hence the pure Rhodamine can not be efficient at 606 nm, and we need to prepare a mixture of both kinds to get the optimal efficiency at 606 nm.

We measured the laser power with different mixtures of Rhodamine 610 and Rhodamine 640 (figure 2.9), and we found that the laser operate at almost optimal efficiency

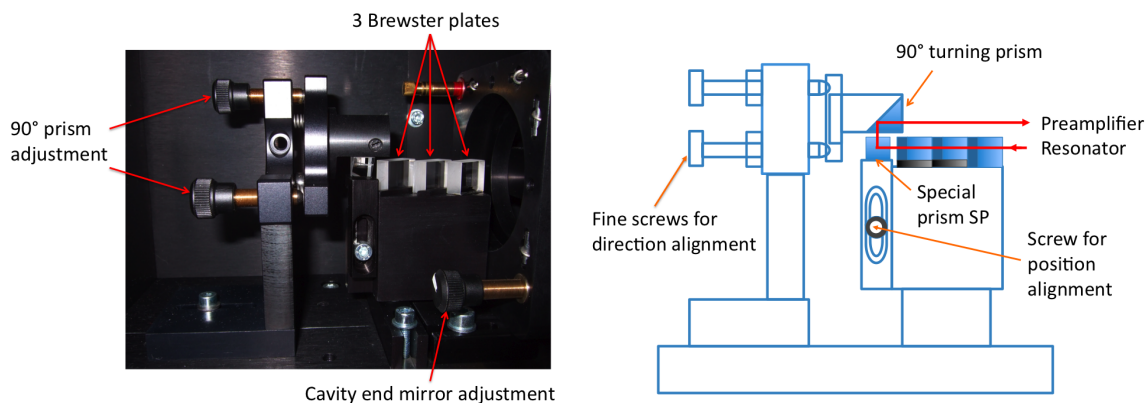


Figure 2.7: Three Brewster plates, special prism and 90 prism

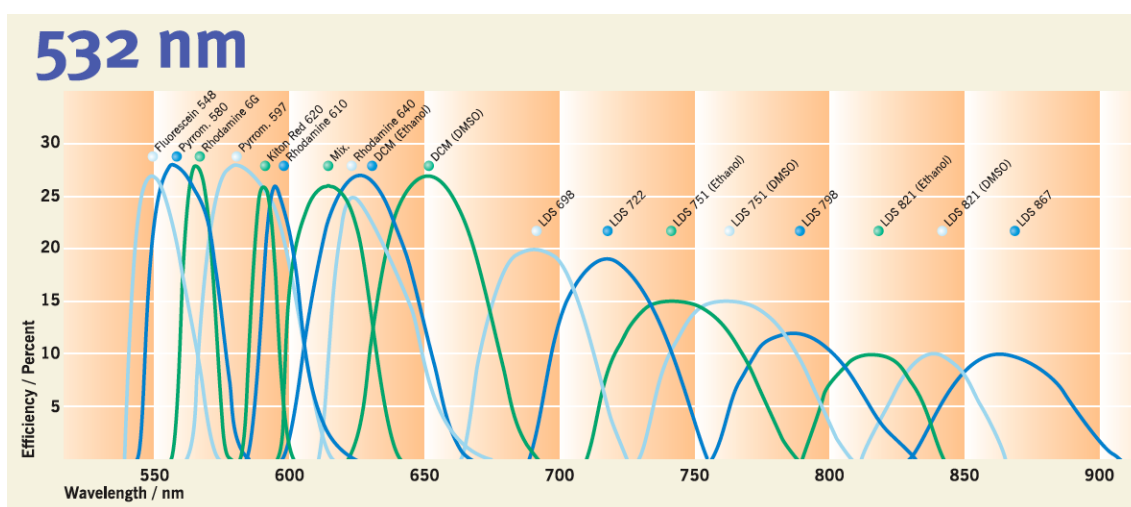


Figure 2.8: Gain curves of different dye/solvent combinatio.

with the mixture of 0.02105 gram/liter of Rhodamine 640 and 0.08914 gram/liter of Rhodamine 610.

### 2.2.1.2 YAG laser

The Nd:YAG frequency-doubled Q-Switched laser at 532 nm, 160 mJ is a commercial laser. It consists of two main parts : the Optical Head and the Power Supply. The Optical Head contains all the necessary components for generating the laser beam and its 2<sup>nd</sup> harmonics. The Power Supply not only provides energy for the laser but also all logical functions necessary to operate the laser.

The pulse energy can be tuned by using the delay between the flash lamp and the Q-Switch trigger. The dependence of output laser power on this time delay is shown in Fig.2.10. For most experiments, we have set  $t_{delay} = 230\mu s$  corresponding to 120 mJ pulses.

The YAG laser provides us a possibility to trigger externally laser pulse. This function

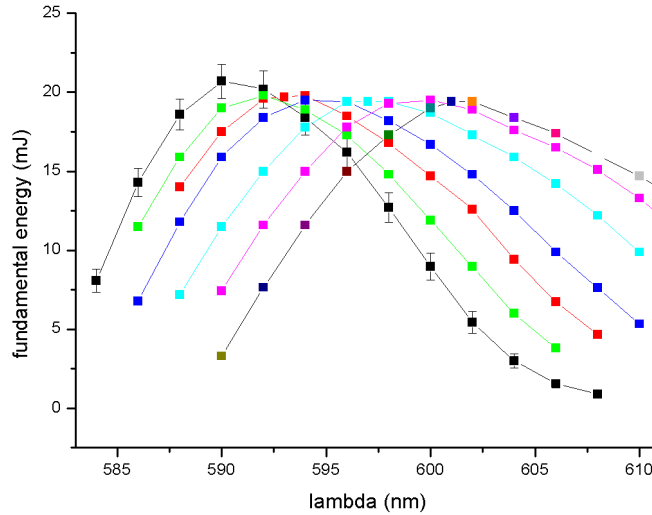


Figure 2.9: The efficient of laser system with different mixtures of Rhodamine 610 and Rhodamine 640

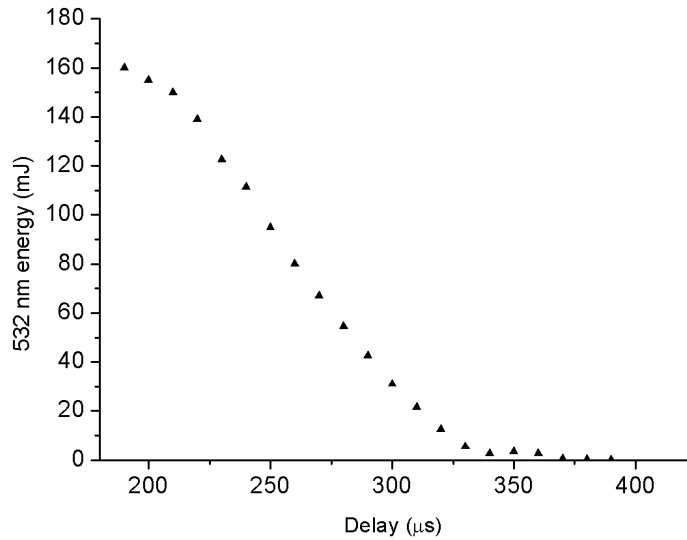


Figure 2.10: YAG laser output power vs delay time

is very useful for the frequency scanning or synchronization with another system. In our experiment, we take the 20 Hz signal from the output of flash lamp and we use a logical function "AND" to combine this signal with the large pulse defining the ion creation time window.

We use the 20 Hz signal produced from this operation to generate a 20 Hz pulse train with time delay  $t_{\text{delay}} = 230 \mu\text{s}$ . This operation is done using the LabVIEW program from Computer and the 8-Channel Counter (see Appendix C). The time delay is an adjustable parameter in LabVIEW program. The 8-Channel Counter serves as a time clock of 20 MHz frequency. When the gate signal indicates the value 1 corresponding to the rising

side of pulse, the LabVIEW program asks the 8-Channel Counter to wait  $t_{delay}$   $\mu s$  before generating the output pulse for the Q-Switch.

Finally, this delayed pulse train will be put at the Q-Switch input gate and the YAG laser is ready for external manipulation.

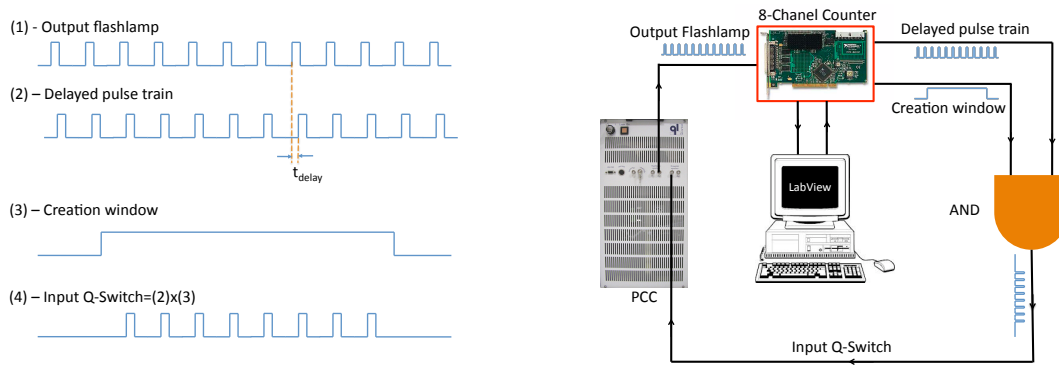


Figure 2.11: Delayed pulse train for Q-Switch trigger

### 2.2.1.3 Optimization of frequency doubler of the Sirah dye laser

The Sirah dye laser is equipped with a Frequency Conversion Unit (denoted briefly as FCU) aiming at frequency double the fundamental dye laser radiation. The FCU consists of a non-linear crystal and a compensator. To tune the laser wavelength, grating  $G_1$  and mirror  $M_2$  are rotated using remote controlled step motors. To achieve optimal UV conversion efficiency, the doubling crystal and compensation prism are rotated synchronously according to an appropriate calibration curve.

In our experiment, we need to maximize the UV output power of laser, then we want to make sure that the previously established calibration curve is optimal even with the actual condition. To establish the calibration curve, we choose a wavelength between 600 nm and 610 nm, and measure the energy variation when the FCU motor position changes and we note the position with the maximal value of energy into table.

## 2.2.2 Automatic scanning of laser wavelength

In the (3+1) REMPI experiment, the laser wavelength has to be scanned around the value 303 nm, we add a subroutine in the LabVIEW program for the automatic scanning of laser wavelength.

With the Sirah dye laser, this task is considerably simplified due to the well-documented book "Programmer's guide to Sirah dye laser" and the Sirah Laser Library VIs. The two most important VIs that we used to read the wavelength value and change to another wavelength is shown in Fig. 2.13:

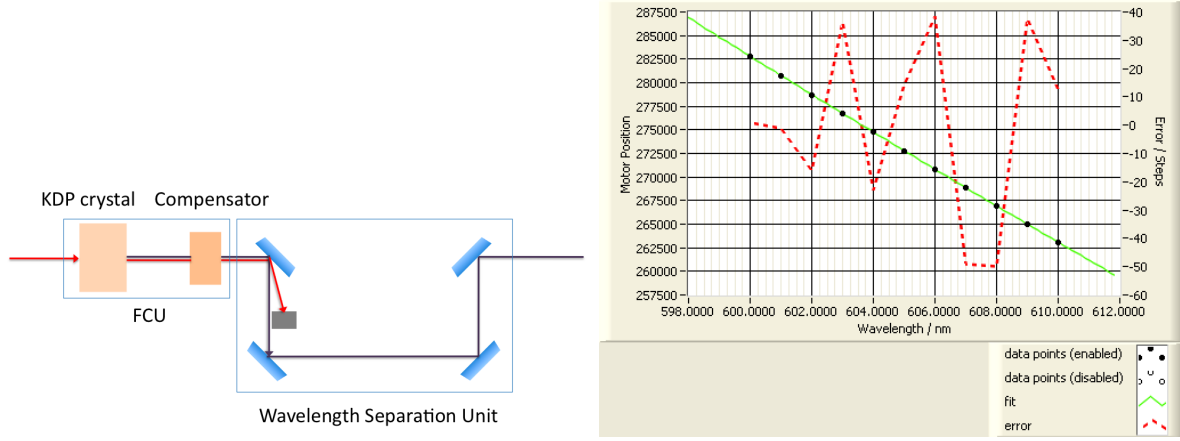


Figure 2.12: Left : Frequency Conversion Unit and Wavelength Separation Unit. Right: Calibration curve

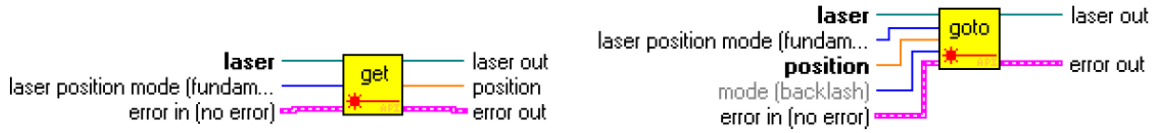


Figure 2.13: Left : "get" function used to read the current emission wavelength of the laser. Right : "goto" function used to set the laser's emission to a wavelength given by the position parameter.

### 2.2.3 Beam shaping

For the  $\text{H}_2^+$  ion production using the (3+1) REMPI method, if we suppose the ionization step is saturated, the dependence of number of  $\text{H}_2^+$  ions  $N$  to the density of  $\text{H}_2$  molecules  $n(x, y, z)$ , laser intensity  $I(x, y, z)$  as:

$$N \sim \iiint_{V_{int}} dx dy dz n(x, y, z) I(x, y, z)^3 \quad (2.11)$$

where  $V_{int}$  is the interaction volume.

We suppose that the output laser follows the well known Gaussian beam which can be described mathematically by [92] :

$$E(x, y, z, t) = \text{Re}\left\{ E_0 \sqrt{\frac{w_{0x}}{w_x(z)} \frac{w_{0y}}{w_y(z)}} e^{-\frac{x^2}{w_x(z)^2} - \frac{y^2}{w_y(z)^2}} e^{ik\left(\frac{x^2}{2R_x(z)} + \frac{y^2}{2R_y(z)}\right)} e^{i(kz - \omega t - \phi)} \right\}$$

where the characteristic beam radii are given by

$$w_x(z) = w_{0x} \sqrt{1 + \frac{z^2}{z_{Rx}^2}}$$

$$w_y(z) = w_{0y} \sqrt{1 + \frac{z^2}{z_{Ry}^2}}$$

and  $E_0$  is linked to the pulse energy  $\mathcal{E}_0$  and beam waists by :

$$E_0^2 \propto \frac{\mathcal{E}_0}{w_{0x} w_{0y}}$$

If we suppose that the interaction region is limited into a cylindrical volume with  $z \in [z_0 - L/2, z_0 + L/2]$  and  $(x, y) \in S \propto w_x(z_0)w_y(z_0)$ , and we suppose the molecular density is quasi-constant  $n(x, y, z) \approx n_0$ , we can rewrite 2.11 as :

$$\begin{aligned} N &\propto \iiint_{V_{int}} dx dy dz n(x, y, z) I(x, y, z)^3 \propto \iiint_{V_{int}} dx dy dz n(x, y, z) |E(x, y, z)|^6 \\ &= \iiint_{V_{int}} dx dy dz n(x, y, z) E_0^6 \left( \sqrt{\frac{w_{0x}}{w_x(z)} \frac{w_{0y}}{w_y(z)}} \right)^6 e^{-\frac{6x^2}{w_x(z)^2}} e^{-\frac{6y^2}{w_y(z)^2}} \\ &\approx \int_{z_0-L/2}^{z_0+L/2} dz \iint dx dy n_0 E_0^6 \left( \frac{w_{0x}}{w_x(z)} \frac{w_{0y}}{w_y(z)} \right)^3 e^{-\frac{6x^2}{w_x(z)^2}} e^{-\frac{6y^2}{w_y(z)^2}} \\ &\approx n_0 L E_0^6 \left( \frac{w_{0x}}{w_x(z_0)} \frac{w_{0y}}{w_y(z_0)} \right)^3 \iint dx dy e^{-\frac{6x^2}{w_x(z_0)^2}} e^{-\frac{6y^2}{w_y(z_0)^2}} \\ &= n_0 L E_0^6 \left( \frac{w_{0x}}{w_x(z_0)} \frac{w_{0y}}{w_y(z_0)} \right)^3 \pi \frac{w_x(z_0)w_y(z_0)}{6} \\ &= \frac{\pi}{6} n_0 L E_0^6 \frac{[w_{0x} w_{0y}]^3}{[w_x(z_0) w_y(z_0)]^2} \end{aligned} \quad (2.12)$$

Therefore, the maximal number of  $H_2^+$  ions created by the (3+1) REMPI process is :

$$N_{max} \propto E_0^6 w_{0x} w_{0y} \propto \frac{\mathcal{E}_0^3}{(w_{0x} w_{0y})^2} \quad (2.13)$$

From Eq.2.12 and Eq.2.13, to increase the number of  $H_2^+$  ions, we need to reduce the size of laser beam at the interaction region, and also change the elliptical form of laser beam to the quasi-circular beam by using the cylindrical lenses.

We saw in the previous sections the optimization of laser pulse energy through the dye concentration, the time delay between flash lamp and Q-Switch, but the laser intensity also depends on the laser beam quality and minimum focus spot size.

The preliminary measurement have shown that the waist of laser beam is far from the mirror  $M$ , then we can approximate that the output laser beam profile is horizontally and vertically linear. We can use the basic optical relations (Table I in the article of Kogelnik and Li [93]) to estimate the distance  $x$  and  $l$  for the cylindrical lenses  $L_1$  and  $L_2$  of focal lengths  $f_1 = -62.6$  mm and  $f_2 = 261$  mm. We choose  $x = 41.5$  cm,  $l = 17.5$  cm.

We need to measure the characteristic beam radii  $w_x(z)$ ,  $w_y(z)$  and the waist  $w_0$  and from this measurement, we can use the cylindrical lenses to reshape the laser beam as we want.

The method that we use to measure  $w(z)$  is quite simple: a razor blade fixed on a translation system will cut step by step the laser beam, and by measurement the

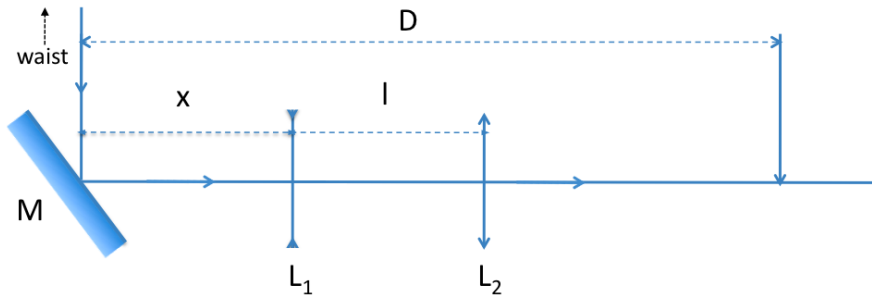


Figure 2.14: Optical set-up for beam shaping

transmitted laser beam energy, we can determine the characteristic beam radius using the following relation :

$$P_m(x) = P_x^0 \left( 1 - \operatorname{erf} \left( \frac{x - x_0}{w_x / \sqrt{2}} \right) \right)$$

$$P_m(y) = P_y^0 \left( 1 - \operatorname{erf} \left( \frac{y - y_0}{w_y / \sqrt{2}} \right) \right)$$

where  $P_m$  is measured values and  $\operatorname{erf}$  is the Gaussian error function.

Figure 2.15 shows the horizontal and vertical profile of UV beam without the cylindrical lenses and the corrected horizontal profile with cylindrical lenses.

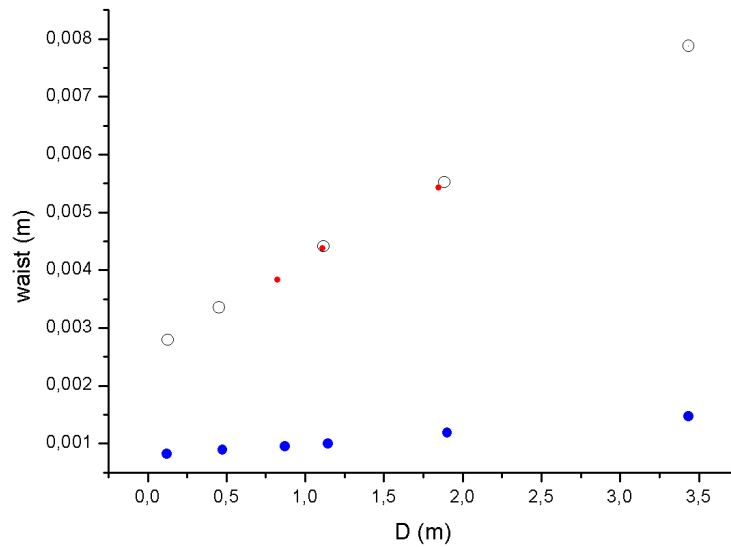


Figure 2.15: Blue circle : Horizontal profile of laser beam without cylindrical lenses; Open circle : Vertical profile; Small red circle : Horizontal profile of laser beam with cylindrical lenses.

## 2.2.4 The ion source

In the previous section, we showed how to maximize the output laser intensity at 303 nm, but as shown in Eq. 2.12, to maximize number of  $H_2^+$  ions, the optimization of the density  $n$  of  $H_2$  molecules in the interaction region is also necessary. This can be done by using a dense molecular beam. This is the main idea of our experimental set-up.

The necessity of a dense molecular beam of  $H_2$  implies that the REMPI ion source must be created outside of the linear Paul trap. If the production of  $H_2^+$  ions are inside the trap, the residual  $H_2$  from the molecular beam will increase considerably the pressure in the vacuum chamber of the trap and reduce the important parameters for the spectroscopy experiment like ion trapping time, number of trapped ions ...

Our experimental set-up for the ion source part is closely inspired by that of Xavier Urbain group at Louvain-la-Neuve, Belgium. Their system can be divided into three parts : the first part is for ion production, the second for ion beam manipulation and the third for ion detection.

The ion production part consists of two electrodes of flat + conic form, a small needle with a 0.3 mm inner diameter used for  $H_2$  injection. The  $H_2$  molecular beam from gas bottle is injected at the center region between two conic electrode through the needle. The molecular jet escaping from the end of needle has a  $\cos(\theta)^5$  distribution with a 60 half angle [94]. In their system, the center of interaction is 2 mm from the end of needle, and the diameter of the interaction volume is 2.6 mm [95].

The  $H_2^+$  ions produced by REMPI process will be pushed into the Einzel lenses and acceleration tube due to the voltage difference between two conic electrode. The Einzel lenses play a similar role as optical lenses, it aims to focus the ion beam from the ion source. The ion beam size is important for the efficiency of ion transportation, ion cooling and metrological experiments. The ions arrive finally at the removable detector through a deflection system.

### Comments :

1. The choice of flat + conic form for two electrode of ion source is due to the form of molecular jet. We want to avoid all possible collisions between  $H_2$  molecules and the electrodes which reduces the efficiency of vacuum pumping.
2. The distance between the laser beam and the end of capillary tube should not exceed 1 mm. Because if the laser beam is too close to the capillary tube, it might interact with the tube and the possible electrons issued from this interaction might collide with hydrogen molecules. This might have some undesirable effect on the ion production by REMPI method.

### 2.2.4.1 Conception

In our experiment, the REMPI ion source created outside of linear Paul ion trap need to be efficiently transferred into the ion trap and also to be efficiently sympathetically cooled by  $Be^+$  Coulomb crystal. Therefore, the experiment design at Louvain-la-Neuve must be modified to well suit our experiment conditions.

### Constraints

For all experimental task : ion production by REMPI method, ion beam manipulation and transportation, ion cooling ..., the  $H_2^+$  ions need to be placed in high vacuum conditions, especially the final task where the ion need to be trapped and cooled down.

The high vacuum chamber reduce the possibility of collisions between residual molecules and the ions. This undesirable collisions decrease considerably the quality of the ion manipulation like ion trapping time, number of  $H_2^+$  ion right before entering into the linear Paul trap....

We divided the system into three regions as shown in Fig. 2.16:

- First region : Two acceleration electrodes, the small capillary tube.
- Second region : The small tube, the einzel lens and the deflection system.
- Third region : The small tube, the rf quadrupole guide and the linear Paul trap.

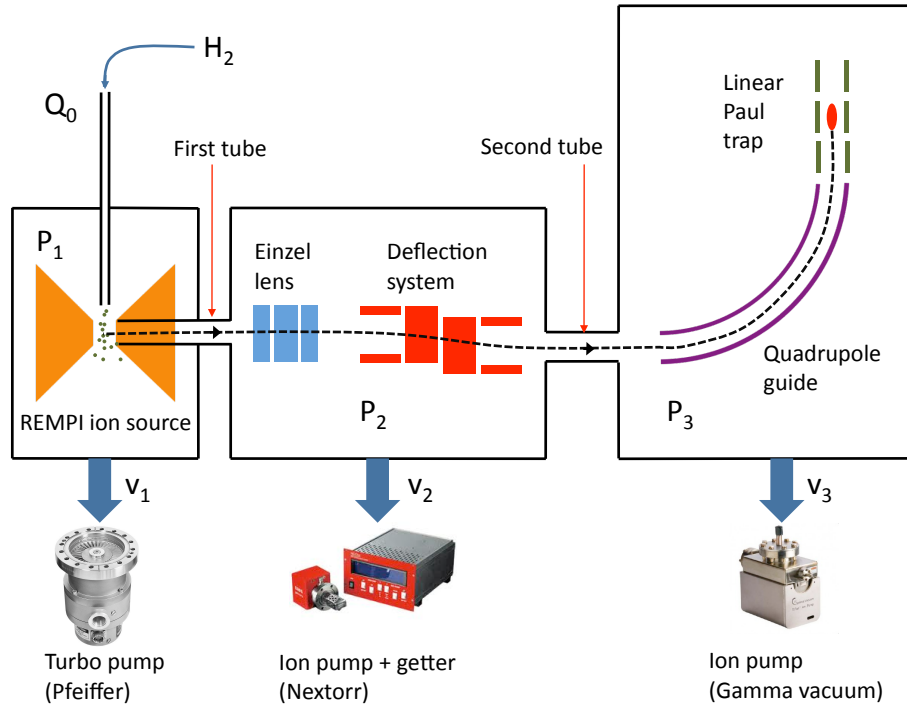


Figure 2.16: Experiment design for REMPI ion source and ion manipulation.  $Q_0$  is the gas flow from the needle;  $P_i$  is the pressure in the vacuum chamber  $i$  ( $i = 1, 2, 3$ );  $v_i$  is the pumping speed of the vacuum pump of the chamber  $i$  ( $i = 1, 2, 3$ );  $L_i, D_i$  the length and diameter of the tube  $i$  ( $i = 1, 2$ )

Each system is placed in a separate vacuum chamber equipped with a vacuum pump. For the first region, we could use the TMH 521P Pfeiffer turbomolecular pump with the pumping speed  $v_1 \sim 300$  ( $l/s$ ). This turbomolecular pump can reduce the pressure in the first vacuum chamber down to  $P_1 \approx Q_0/v_1 \sim 10^{-6}$  mbar ( $Q_0$  is gas flow from the capillary tube). For the second pump, we use a Nextorr D 200-5 SAES pump which is a combination of ion pump technologies and non-evaporable getter (NEG) technologies. The pumping speed of this pump is  $v_2 \sim 100$  ( $l/s$ ). And the third vacuum chamber is equipped with a 75S Titan CV Gamma Vacuum ion pump operated at the pumping speed  $v_3 \sim 65$  ( $l/s$ ). The pressure in the third vacuum should be in the  $10^{-10} - 10^{-11}$  mbar range, therefore, the dimensions of the first and second tube must be well chosen to attain this

pression range. Using the basic formula of conductance in the vacuum technique [96], we can establish a relation between the pressure  $P_1$ ,  $P_3$  and the dimension of two tubes as :

$$P_3 = P_1 \frac{C_2 C_1}{v_3 v_2}$$

where, the conductance of tube  $i$  is given by :

$$C_i \approx 12.1 \sqrt{\frac{29}{2}} \frac{D_i^2}{L_i}$$

( $D_i, L_i$  are diameter and length of tube  $i$  as shown in the Fig. 2.16)

If we choose  $D_1 = D_2 = 2$  mm,  $L_1 = 10$  mm and  $L_2 = 40$  mm, the pressure in the third vacuum chamber is reduced by a factor :

$$\beta = \frac{P_3}{P_1} \approx 5.12 \times 10^{-6}$$

Because the pressure the first chamber is in the  $10^{-6}$  range, the pressure  $P_3$  can reach the necessary pressure for the experiment. Using the similar estimation, we can show that it is very difficult to reach the  $10^{-10} - 10^{-11}$  mbar range of pressure in the last vacuum chamber by using only two vacuum chamber.

The core of our experiment design consists of two acceleration electrodes, a small tube at the end of second acceleration electrode, an Einzel lens for ion beam manipulation, a deflection systems with four horizontal plates and four vertical plates, another tube aiming to reduce the size of ion beam, a rf quadrupole guide which will transfer ions into the linear Paul trap. The complete system (except for the linear Paul trap) is depicted in Fig. 2.17

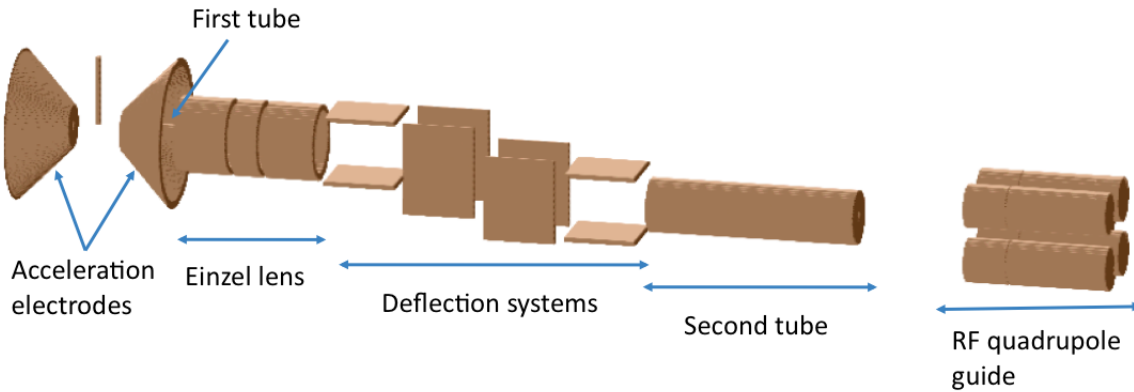


Figure 2.17: Experiment design for REMPI ion source and ion manipulation with SIMION 8

The following sections, i will give more information about each part of this system.

### Ion Source:

For the REMPI experiment, the ion source is based on the model of Louvain. In the experiment at Louvain-le-Neuve, they used a very instense laser (their laser can reach 40 mJ) but our pulsed dye laser power can reach the value of 3 mJ. To increase the number

of molecules in the interaction volume, the laser beam need to be tightly focused using a converging lens, and the focal point must be as close to the end of capillary tube as possible because the hydrogen molecular density decreases with the distance from the tube. For these reasons, the distance between laser beam and the end of the needle is only 1 mm (in the experiment at Louvain, this distance is 2 mm). And we also reduce the size of conic electrodes by a factor 2 in comparison with Louvain's experiment.

### Einzel lens

An einzel lens is a charged particle lens which plays a similar role as a optical lens. The charged particle beam passing through the einzel lens will be focused without changing the energy of the beam. The system consists of three cylindrical electrodes which are symmetrically arranged (Fig. 2.18).

Depending on the polarity of voltage applied between the central electrode, the left electrode and the right electrode, the einzel lens is either converging or diverging. If the voltage applied on the center electrode is  $V_2 \geq 0$ , the that of right and left electrode is 0, we will have a converging lens.

In our experiment design, the electrodes and the voltages applied on each electrode are symmetric in order to conserve the ion energy. By varying the voltage of the central electrode, we can change  $H_2^+$  beam focusig point and change also the transmission rate of the system.

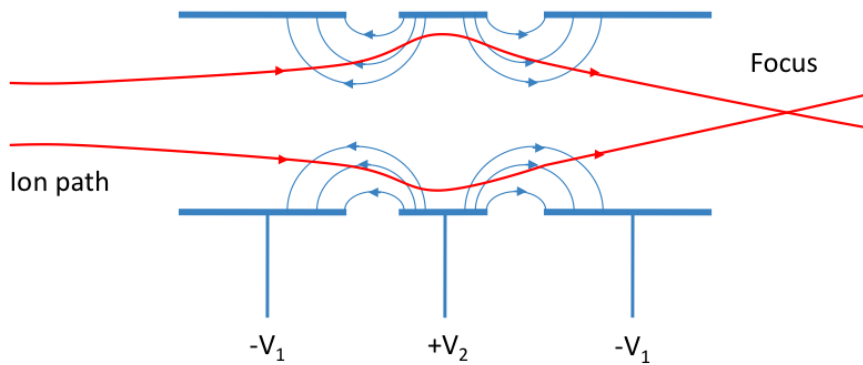


Figure 2.18: Einzel lens

### Deflection system

To increase the efficiency of the vacuum pumping, we need to include the deflection system which separate the neutral molecular beam and charged molecular beam. The neutral molecular beam will stay in the vacuum chamber containing the 8 deflecting plates, only the charged particles will be transferred into the rf quadrupole guide through the second tube which is right after the deflection system.

We need 4 vertical plates for the vertical beam manipulation and 4 horizontal plates for the horizontal manipulation. In principle, only 4 vertical plates are necessary but in practice, the vertical plates are not perfectly parallel, a small deviation between two parallel vertical plates can change considerably the horizontal beam size.

### RF quadrupole guide

Once the ion beam was created, manipulated, it will be transferred to the linear Paul

trap using a rf quadrupole guide. The rf quadrupole guide is necessary because we need to reserve more free space for laser beams like laser cooling of  $Be^+$ , the infrared Fabry-Perot cavity for 2-photon excitation, the UV laser for photodissociation.

The idea of a rf quadrupole guide was used previously by, for example, the group of T. Schaetz ([97, 98, 99]). They used four 90-bent, cylindrical, gold plated copper rods of 2 mm of diameter, 49 mm of length and 35.5 mm of radius of curvature to form a quadrupole guide. The minimal distance between the guide center and the surface of the rods is  $r_0 = 1.2$  mm. The radial confinement is achieved by applying a rf-voltage on each pair of opposite electrodes with a phase difference of  $\pi$ .

In our design, the rf quadrupole guide is made by four 90-bent cylindrical molybdenum rods of 7 mm of diameter, 95.3 mm of radius of curvature and the minimal distance of the center of guide and the rod is 8 mm.

The principle of the rf quadrupole guide is the same as the rf quadrupole trap. The radius of curvature is chosen sufficiently large, so that we can approximate the guide as an assembly of many separate linear quadrupole trap without endcaps. A full theoretical treatment of this system is complicated but a simple approximative solution is possible. Supposing that the radius of curvature of the guide  $R$  is much larger than the distance  $r_0$  from the axis of the guide to the electrodes (see Fig. 2.19). An ion beam arriving at the guide with the velocity  $v_z$  in the axis direction and we suppose that this velocity component remains unchanged in module inside the quadrupole guide but changes in direction due to the electric potential. In the ion frame, this velocity corresponds to a centrifugal force  $\vec{F}_c$  :

$$\vec{F}_c = -m \frac{v_z^2}{R} \hat{x}$$

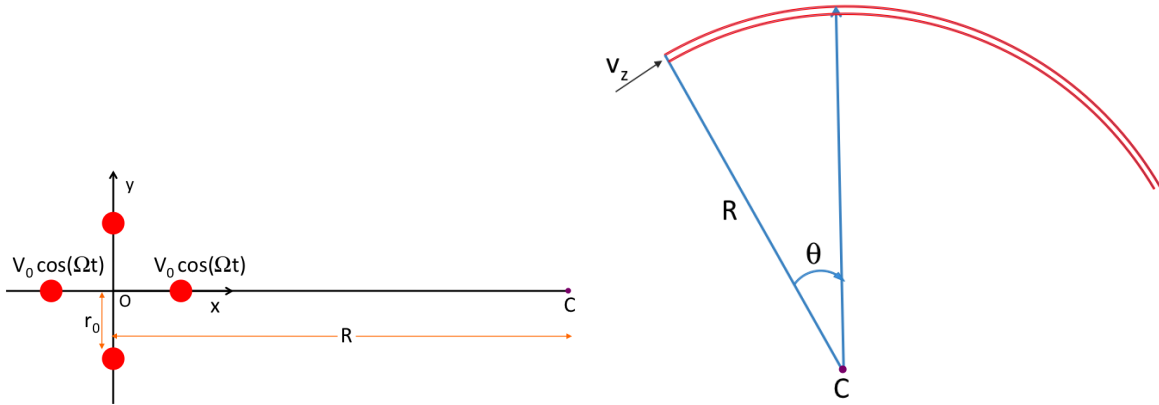


Figure 2.19: The parameters for the quadrupole guide

The electric potential  $\phi(\theta, x, y, t)$  created by the voltages  $V_0 \cos(\Omega t)$  applied on two diagonally opposite electrodes is given by :

$$\phi(\theta, x, y, t) = \frac{x^2 - y^2}{2r_0^2} V_0 \cos(\Omega t)$$

The equation of motion is then :

$$\begin{cases} \frac{d^2x}{dt^2} + 2q_x \cos(2\Omega t) \frac{\Omega^2}{4} x = -\frac{v_z^2}{R} \\ \frac{d^2y}{dt^2} + 2q_y \cos(2\Omega t) \frac{\Omega^2}{4} y = 0 \end{cases} \quad (2.14)$$

where  $q_x = -q_y = \frac{2qV_0}{mr_0^2\Omega^2}$ .

These equations is similar to the modified Mathieu equation for the "excess micromotion" (see Eq. 1.5), therefore the solution is

$$\begin{aligned} x(t) &= [x_0 + x_1 \cos(\omega_x t)] \left(1 + \frac{q_x}{2} \cos(\Omega t)\right) \\ y(t) &= y_1 \cos(\omega_y t) \left(1 + \frac{q_y}{2} \cos(\Omega t)\right) \end{aligned}$$

where  $\omega_x = \omega_y = (1/2\sqrt{2})\Omega q_x$

The ion is displaced from the axis of quadrupole guide by a distance  $x_0$  given by :

$$x_0 = -2 \frac{m^2 r_0^4 \Omega^2}{q^2 V_0^2} \frac{v_z^2}{R}$$

This quantity provides a upper bound limit for the  $v_z$  as :

$$x_0 < r_0 \iff v_z < \frac{qV_0}{\Omega m r_0} \sqrt{\frac{R}{2r_0}}$$

### Linear Paul trap

In the  $H_2^+$  experiment, the linear Paul trap (or quadrupole trap) is used instead of hyperbolic Paul trap as before for two reasons :

1. The experiment requires the sympathetic cooling using laser-cooled  $Be^+$  to limit the influence of second order Doppler effect on the REMPD signal, and because the cooling process requires an elongated atomic cloud, the linear Paul trap is much better suited than the hyperbolic Paul trap.

2. The analysis in [38] shows that the linear Paul trap can increase the signal-to-noise.

In the  $H_2^+$  experiment, we need to obtain a sympathetically cooled  $H_2^+$  ion cloud to reduce the influence of second order Doppler effect, this will be done in collaboration with J. C. Koelemeij at LaserLab, Amsterdam. We will use the same model of linear Paul trap as that of J. Koelemeij at LaserLab, VU, Amsterdam. This linear Paul trap is constituted by two unsegmented rods and two segmented rods as shown in the Fig. 2.20.

#### 2.2.4.2 Ion optical bench test the system with Simion

The conception system has been tested with SIMION 8.0 - an ion optics simulation program. We use this program to calculate the electronic potential of any configuration of electrodes and the ion trajectories in this potential. The electrostatic potential is calculated by solving the Laplace equation using the finite difference technique. The ion's trajectory is calculated by the fourth order Runge-Kutta method.

Because we need a good estimation of number of ions  $H_2^+$  arriving at the final sep i.e the center of the linear Paul trap, in the simulation with SIMION, we must descibre the ion beam  $H_2^+$  in the most correct way as possible.

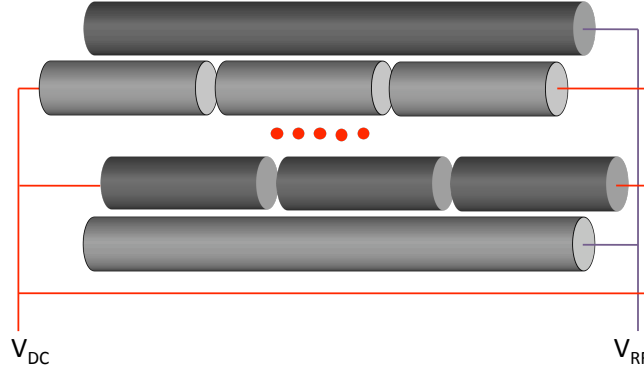


Figure 2.20: The design of the linear Paul trap for both  $\text{H}_2^+$  and  $\text{HD}^+$  experiments.

The ion axial velocity distribution in a effusive molecular beam can be approximated by the well-known results [100]:

$$P(v) \sim v^3 e^{-v^2/\alpha^2}$$

where  $\alpha = \sqrt{2k_B T/m}$ .

The angular distribution of the molecular beam  $\text{H}_2$  as a function of the angle  $\theta$  with respect to the capillary tube is [94]:

$$P(\theta) \sim (\cos(\theta))^5$$

And we suppose that number of ions  $\text{H}_2^+$  produced from the REMPI process is proportional to  $I^3$  where  $I$  is laser intensity i.e the photoionization step - final step of 3+1 REMPI process - is saturated. The laser beam is a gaussian beam with the waist  $w_0 = 0.2$  mm. The origin of coordinate system  $xyz$  is placed at the center of interaction volume as depicted in the figure 2.21

The formula for the distribution of  $\text{H}_2^+$  as a function of  $x, y, z$  can be given by :

$$P(x, y, z) = P(\theta)P_{REMPI} = C \frac{(d-y)^5}{(x^2 + (d-y)^2 + z^2)^{5/2}} \frac{1}{(1 + z^2/z_R^2)^3} e^{-6(x^2+y^2)/(w_0^2(1+z^2/z_R^2))}$$

where  $C$  is a normization constant.

Because the ion velocity direction is given by the ion direction  $(x, y, z)$ , then we only need to simulate the distribution of the amplitude of velocity  $v$  given by the formula  $P(v)$ .

For the simulation of any distribution function, we can use the rejection sampling method [101].

We tested the system with different values of voltage and find the optimal transmission rate of 84% after the first tube and 78% after the second tube. In the ideal condition

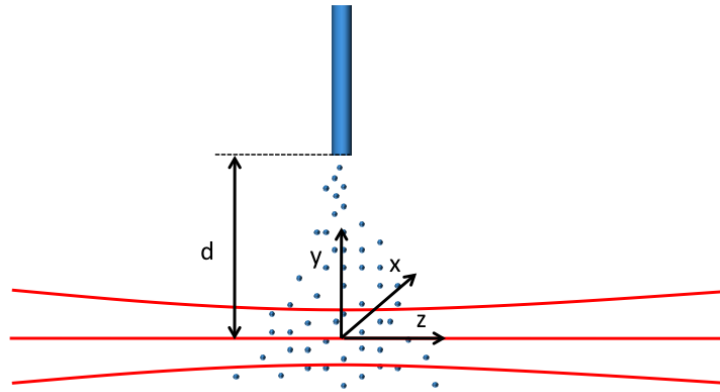


Figure 2.21: Scheme of the interaction region. The distance between the center of interaction i.e the waist and the end of tube is  $d = 1$  mm.

of vacuum chamber, the transmission in the rf quadrupole guide takes place without any loss.

#### 2.2.4.3 Experimental results



# Chapter 3

## Quasi-degenerate two-photon HD<sup>+</sup> spectroscopy in the Lamb-Dicke regime

In this chapter, we will investigate the possibility of Doppler-free spectroscopy for the sympathetically cooled ion HD<sup>+</sup> using quasi-degenerate two-photon transitions. Normally for the Doppler-free spectroscopy, people use the transition with two photons of equal frequency as in our experiment with H<sub>2</sub><sup>+</sup>. For the experiment with HD<sup>+</sup>, the equal-frequency two-photon transition is possible [76], but the difficulty of putting the Fabry-Pérot cavity in the experiment at LaserLab, Amsterdam forces to think about the possibility of unequal-frequency two-photon spectroscopy of cold trapped ion HD<sup>+</sup> without cavity.

### 3.1 Introduction

#### 3.1.1 Two-photon spectroscopy

The idea of two-photon spectroscopy began in 1930 with the theoretical calculation of M. Goeppert-Mayer of the two-photon absorption probability [102]. But because this is a two-photon process, it requires an intense light radiation to observe experimentally the two-photon signal. It was shown theoretically in 1970 by L. S. Vasilenko et al. [103] that the absorption of two photon propagating in two opposite directions can be used to suppress the first order Doppler broadening. And in 1974 by F. Biraben et al. [104] observed the 3S-5S two-photon transition transition in dilute Sodium gas. This method has played an important role in the development of high precision laser spectroscopy.

Here, i present briefly the principle of this experiment: supposing that an atom moving at velocity  $\vec{v}$  interacts with two laser beam of the same frequency  $\omega$  in two opposite directions as depicted in Fig. 3.1.

In the atom frame, the atom interacts with two photon of frequencies  $\omega(1 + \frac{v_z}{c})$  and  $\omega(1 - \frac{v_z}{c})$  respectively. The two-photon resonance condition is given by :

$$\omega_{eg} = \frac{1}{\hbar}(E_e - E_g) = \omega(1 + \frac{v_z}{c}) + \omega(1 - \frac{v_z}{c}) = 2\omega .$$

It does not depend on the atom velocity class and is not affected by Doppler broad-

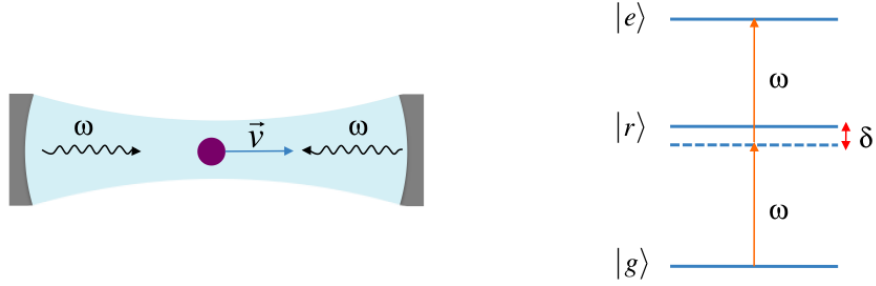


Figure 3.1: Two-photon spectroscopy : experiment arrangement and energy level scheme.

ening to the first order in  $v/c$ . The width of two-photon signal at resonance is therefore of the same order of magnitude as the natural linewidth.

In this two-photon absorption method, to completely suppress the first order Doppler broadening, the directions of two photon must be perfectly opposite. This requirement is usually assured by using a Fabry-Pérot cavity.

The two-photon rate  $\Gamma_{2ph}$  is inversely proportional to the detuning between the laser frequency  $\omega$  and the transition frequency from the ground state  $|g\rangle$  to the intermediate state  $|r\rangle$  as  $\Gamma_{2ph} \sim 1/\delta^2$ [105]. Therefore, in many cases, one need to reduce the detuning  $\delta$  to increase the two-photon signal by means of two photon of different frequencies  $\omega$  and  $\omega'$ . But with this method have two disadvantages :

- The residual Doppler broadening due to  $\omega \neq \omega'$
- The alignment of the directions of two photon can not be done with Fabry-Pérot cavity.

The first disadvantage can be overcome by tuning laser frequency so that the detuning  $\delta$  is of the same order of magnitude as the natural linewidth of the intermediate level  $|r\rangle$ . The first transition is resonant with a particular velocity class, and the two-photon transition is therefore Doppler-free [106]. But this method works only in gas phase where the motion of particle is rectilinear between collisions.

But the second disadvantage is unavoidable !

### 3.1.2 Lamb-Dicke regime

In a dilute gas, the signal of single-photon transition is always broadened by the Doppler effect. But for strongly confined particles, Doppler-free signal is observable if the amplitude of vibration of particles is much smaller than the wavelength of the laser light. This is known as the Lamb-Dicke regime.

To understand this effect, we consider the emission spectroscopy of a two-level atom trapped in a harmonic potential  $V(\vec{r}) = \frac{1}{2}m\Omega_{vib}^2\vec{r}^2$ . We denote the two internal levels as  $|g\rangle$  and  $|e\rangle$ . The external motion of particle is described by the Hamiltonian  $H = \frac{\vec{p}^2}{2m} + V(\vec{r})$ . For a harmonic potential  $V(\vec{r})$ , the eigenvectors  $\{|\nu\rangle\}$  of  $H$  form an orthonormal basis. The coupling between the trapped atom and the electromagnetic radiation in the electric dipole approximation is given by  $V_{int} = -\vec{D}\vec{E} \sim (\vec{D}\vec{\epsilon})e^{-i\vec{k}\vec{r}}$ .

In the "dressed atom" picture, the atomic state is described by  $|a\rangle \otimes |\nu\rangle = |a, \nu\rangle$  where  $|a\rangle$  is the internal state, and  $|\nu\rangle$  is the external states. For the spontaneous emission from  $|e\rangle$  to  $|g\rangle$ , the atom emit a photon of frequency  $\omega_{eg} + \Delta\nu\Omega_{vib}$ . The fluorescence is then a structure of sidebands regularly separated by  $\Omega_{vib}$ .

In the interaction picture, the amplitude of each sideband is given by [107]:

$$\langle g, \nu', \vec{k} \vec{\epsilon} | V_{int} | e, \nu, 0 \rangle \sim \langle g | \vec{D} \vec{\epsilon} | e \rangle \langle \nu' | e^{-i\vec{k}\vec{r}} | \nu \rangle .$$

In the Lamb-Dicke regime, we have  $\vec{k}\vec{r} \ll 1$ , then  $\langle \nu' | e^{-i\vec{k}\vec{r}} | \nu \rangle = \delta_{\nu'\nu}$ . The central band is much more intense than the sidebands. This central band corresponds exactly to the emission frequency  $\omega_{eg}$  of an at rest atom.

### 3.1.3 HD<sup>+</sup> spectroscopy : limits of single-photon transition method

In the high precision spectroscopy of molecular hydrogen ions, HD<sup>+</sup> possesses an interesting property that H<sub>2</sub><sup>+</sup> don't have : The transition between two rovibrational states of the fundamental potential energy curve  $X^2\Sigma^+$  is dipole-allowed. One might say that with the development of laser cooling method, it's not a big deal to trap and to cool down the ions HD<sup>+</sup> and that with single-photon spectroscopy, the desired relative uncertainty of proton-to-electron mass ratio of  $10^{-10}$  is attainable. In this section, i will explain why with this method, it's difficult to achieve that objective.

The idea of single-photon spectroscopy of HD<sup>+</sup> have been pioneered by the group at Dusseldorf lead by S. Schiller. In 2007, they reported the measurement of the transition frequency between the rovibrational state  $|\nu = 0, N = 2\rangle$  and  $|\nu = 4, N = 3\rangle$  with the relative uncertainty of  $2.3 \cdot 10^{-9}$  [32]. In their experiment, the molecular hydrogen ions HD<sup>+</sup> are sympathetically cooled down to the temperature  $T = 53(8)$  mK by a  $Be^+$  Coulomb crystal. This temperature corresponds to the Doppler width  $\Gamma_D = 20.3(1.4)$  MHz. For this reason, they observe only two resolved hyperfine components around the unperturbed value  $\nu_d$  of the frequency transition from  $|\nu = 0, N = 2\rangle$  to  $|\nu = 4, N = 3\rangle$  as shown in Fig.2 of [32].

The natural questions rise from this result : How far this method can go to get a better resolution ? Which method would allow to obtain the spectrum with well resolved hyperfine structures ?

To answer this question, we examine the absolute uncertainty and relative uncertainty of this measurement. The absolute uncertainty is the single-photon Doppler broadening  $\Gamma = \nu_d \bar{v} / c$  where  $\bar{v} \sim \sqrt{k_B T}$  is the averaged velocity of HD<sup>+</sup> ions. Then we have :

$$\Gamma_D \sim \nu_d \sqrt{k_B T} .$$

And the relative uncertainty is given by

$$\eta = \frac{\Delta\nu_d}{\nu_d} = \frac{\Gamma_D}{\nu_d} \sim \sqrt{k_B T} .$$

This relation shows that the relative uncertainty is independent of  $\nu_d$  and limited by the temperature  $T$  for one photon transitions.

Here, we list some possible improvements to obtain a better resolution and to reduce the relative uncertainty with one photon transitions :

- To achieve the spectrum of better resolved hyperfine structure i.e the better absolute uncertainty, we can choose a transition between two state  $(\nu, N)$  and  $(\nu', N')$  so that the transition frequency  $\nu_d$  is much smaller. But the relative uncertainty remains unchanged ! And another disadvantage is that when two level are very close, the populations of two level are very similar, hence to obtain the signal by  $(1 + 1)$  REMPD method, one must transfer the population of upper level to the lower level by using the sophisticated Black-Body Radiation (BBR) pumping method [33].<sup>1</sup>
- One can use the cooling technique to reduce the temperature  $T$  of  $\text{HD}^+$  ions, the absolute and relative uncertainty are then reduced. But the temperature  $T$  is limited by the Doppler temperature  $T_{Doppler} = \hbar\Gamma/2k_B$  of the laser cooling of  $\text{Be}^+$  ions. In theory,  $T_B = 0.5$  mK but in practice, the minimal measured temperature is 5 – 10 mK.
- If the confinement by the trap is increased to reach the Lamb-Dicke regime then the Doppler-free spectroscopy is possible [32]. This method requires very high secular frequencies for resolved sideband cooling to reach the Lamb-Dicke regime. Hence, one need to switch the traditional hyperbolic or linear Paul trap to microtraps. This is a big experimental challenge !

To overcome the limits of one-photon transition method, J.C.J Koelemeij comes up with the idea of the combination of spectroscopy of two quasi-degenerate photons and the sympathetic cooling of ions : In two-photon transition with wave vectors  $\vec{k}$  and  $\vec{k}'$ , the ions can "feel" as single photon transition with the effective wave vector  $\vec{k}_{eff} = \vec{k} + \vec{k}'$ . The effective wavelength is therefore much larger than the wavelenths of two photons, and for that reason, with the sympathetic cooling, we can easily reach the Lamb-Dicke regime for the two-photon transition. The complete theoretical treatment of this theory is explained in the following article.

---

<sup>1</sup>We should also note that when reducing the transition frequency  $\nu_d$ , one might have the possibility to attain the Lamb-Dicke regime and the  $\text{HD}^+$  spectroscopy is therefore Doppler-free, both relative and absolute uncertainty are improved.

**Two-photon spectroscopy of trapped HD<sup>+</sup> ions in the Lamb-Dicke regime**Vu Quang Tran,<sup>1</sup> Jean-Philippe Karr,<sup>1,2</sup> Albane Douillet,<sup>1,2</sup> Jeroen C. J. Koelemeij,<sup>3</sup> and Laurent Hilico<sup>1,2</sup><sup>1</sup>Laboratoire Kastler Brossel UMR 8552, UPMC, CNRS, ENS, C 74, Université Pierre et Marie Curie 4 place Jussieu, 75252 Paris, France<sup>2</sup>Département de Physique, Université d'Evry Val d'Essonne, Rue du père André Jarlan, 91025 Evry cedex, France<sup>3</sup>LaserLab, VU University, De Boelelaan 1081, 1081 HV Amsterdam, The Netherlands

(Received 22 July 2013; published 24 September 2013)

We study the feasibility of nearly degenerate two-photon rovibrational spectroscopy in ensembles of trapped, sympathetically cooled hydrogen molecular ions using a resonance-enhanced multiphoton dissociation (REMPD) scheme. Taking advantage of quasicoincidences in the rovibrational spectrum, the excitation lasers are tuned close to an intermediate level to resonantly enhance two-photon absorption. Realistic simulations of the REMPD signal are obtained using a four-level model that takes into account saturation effects, ion trajectories, laser frequency noise, and redistribution of population by blackbody radiation. We show that the use of counterpropagating laser beams enables optical excitation in an effective Lamb-Dicke regime. Sub-Doppler lines having widths in the 100-Hz range can be observed with good signal-to-noise ratio for an optimal choice of laser detunings. Our results indicate the feasibility of molecular spectroscopy at the  $10^{-14}$  accuracy level for improved tests of molecular QED, a new determination of the proton-to-electron mass ratio, and studies of the time (in)dependence of the latter.

DOI: [10.1103/PhysRevA.88.033421](https://doi.org/10.1103/PhysRevA.88.033421)

PACS number(s): 33.80.Rv, 33.80.Wz, 37.10.Pq, 37.10.Ty

**I. INTRODUCTION**

Most high-precision measurements in atomic or molecular physics rely on laser spectroscopy in dilute gases. Several methods have been developed to suppress Doppler line broadening and reach natural linewidth or laser-width limited resolutions, such as saturated absorption [1–3] or Doppler-free two-photon spectroscopy [4–7]. Resonantly enhanced two-photon absorption using two lasers of unequal frequencies tuned close to an intermediate level was also studied both theoretically and experimentally [8–10]; sequential two-photon absorption at exact resonance was shown to provide both maximum transition rates and Doppler-free spectra. Indeed, the photon absorbed in the first transition selects a velocity class from which the second absorption occurs without Doppler broadening.

One of the most successful methods to suppress the Doppler effect is single-photon absorption on trapped species in the Lamb-Dicke regime where the confinement length is smaller than the wavelength. This condition is easily satisfied in ion traps in the microwave domain, which has allowed high-precision hyperfine structure measurements in many ionic species [11–13] and the development of microwave frequency standards [14–16]. The Lamb-Dicke regime is much more challenging to achieve in the optical domain [17,18]. It requires tight confinement of laser-cooled ions and has been obtained only with small ion numbers, i.e., single ions or ion strings located on the axis of a linear trap.

We address here the specific case of molecular ions, where high-resolution infrared spectroscopy opens the way to many interesting applications such as tests of QED [19,20] or parity violation [21], measurement of nucleus-to-electron mass ratios [22,23], and studies of their variation in time [24–26]. Studies on small ion numbers in the Lamb-Dicke regime raise additional problems due to the difficulty of preparing and controlling the internal state of molecules. So far, the best resolutions have been obtained with ensembles of sympathetically cooled molecular ions [27,28]. Temperatures

of a few tens of mK are typically achieved, which corresponds to a Doppler broadening of several MHz, well above the natural linewidths of excited rovibrational states.

To circumvent this limitation, degenerate Doppler-free two-photon spectroscopy is a natural solution [29,30]. However, relatively high field intensities are generally required to achieve a substantial transition rate, and this approach often implies installing a high-finesse enhancement cavity in the vacuum chamber [31]. For the sake of experimental convenience and universality, a sub-Doppler spectroscopic scheme that would be free of this requirement is highly desirable.

In this paper, we analyze theoretically the resonantly enhanced two-photon excitation of trapped molecular ions with nearly degenerate counterpropagating laser fields, which is made possible by quasicoincidences in the rovibrational spectrum. Near-resonant excitation of an intermediate level warrants sufficient transition rates with moderate laser power; in addition, two-photon absorption takes place in the Lamb-Dicke regime, due to the effective wavelength associated with simultaneous absorption of one photon from each field. The proposed scheme thus combines advantages of the resonant enhancement already evidenced in neutral gases, and of the Lamb-Dicke effect that has been exploited in microwave spectroscopy of trapped ions.

As a first application, we focus on hydrogen molecular ions. These simple systems enable highly precise comparisons between measured transition frequencies and theoretical predictions. Current efforts to evaluate hyperfine structure [19] and QED corrections [20] in H<sub>2</sub><sup>+</sup> or HD<sup>+</sup> are expected to improve the theoretical accuracy beyond 0.1 ppb, allowing for stringent tests of QED and for an improved determination of the proton-to-electron mass ratio (presently known to 0.41 ppb accuracy [32]). The high  $Q$  factor of rovibrational lines also opens the way to searches for possible time variations of fundamental constants [24,25] and “fifth forces” [33] with improved sensitivity. Experimental studies on sympathetically

cooled  $\text{HD}^+$  ions [28,34], using single-photon rovibrational transitions detected by  $(1 + 1')$  resonance-enhanced multiphoton dissociation (REMPD), are so far limited to the ppb level, mainly by the Doppler broadening. As we show, this limitation can be overcome by several orders of magnitude in the proposed experiment.

The paper is organized as follows. In Sec. II, we describe the proposed  $(1 + 1' + 1'')$  REMPD experimental scheme and discuss all the frequency scales in the problem. The theoretical model of REMPD is introduced in Sec. III. We model the molecule-light interaction as a three-level system which interacts coherently with the two laser fields and take dissociation into account by introducing a noncoherent coupling to a fourth level. Our treatment furthermore includes the motional degrees of freedom of the molecules. The dynamics of the entire system are captured within a set of optical Bloch equations (OBEs), which are solved to predict the dissociated ion fraction monitored in the experiment. In Sec. IV, we first numerically solve the model in the ideal case of a single ion undergoing a pure harmonic motion in order to highlight the main features of the signal and evidence the Lamb-Dicke effect. Realistic ion motion obtained from molecular ion dynamics simulations is then incorporated in the model, and optimal conditions for the experiment in terms of laser detunings, which are found markedly different from the gas case [9], are determined. We show that under these conditions, an approximate model of the two-photon transition rate can be used, and its validity range is assessed by comparing to the exact OBE model. The power shift and broadening is analyzed, as well as the effect of laser frequency noise. Finally, in Sec. V, in order to obtain realistic estimates of the expected REMPD signal strength, we simulate the dynamics of the total number of  $\text{HD}^+$  ions taking into account the REMPD rates as well as the redistribution of rotational population induced by blackbody radiation (BBR).

## II. TWO-PHOTON TRANSITIONS IN $\text{HD}^+$ AND FREQUENCY SCALES OF THE PROBLEM

The permanent electric dipole moment of  $\text{HD}^+$  allows rovibrational transitions within the electronic ground state. Weak vibrational overtone transitions exist only by virtue of the anharmonicity of the  $\text{HD}^+$  bond. Two-photon vibrational transitions are possible, but require a quasiresonance with an intermediate level to achieve sufficiently high transition rates. Using the extensive set of accurate rovibrational level energies obtained by Moss [35], an analysis of intermediate level energy mismatch reveals two interesting transitions:  $(v = 0, L = 1) \rightarrow (v = 1, L = 0) \rightarrow (v = 2, L = 1)$  at  $5.37 \mu\text{m}$  [30] (energy mismatch,  $\Delta E = 6.18 \text{ cm}^{-1}$ ) and  $(v = 0, L = 3) \rightarrow (v = 4, L = 2) \rightarrow (v = 9, L = 3)$  at  $1.44 \mu\text{m}$  ( $\Delta E = 6.84 \text{ cm}^{-1}$ ). In the following, we consider the latter, whose wavelength is more convenient for laser stabilization and absolute frequency measurements.

Throughout the paper, the values of various parameters are taken from the  $\text{HD}^+$  spectroscopy experiment developed by the Amsterdam team and described in [34]. A set of about 100  $\text{HD}^+$  ions is sympathetically cooled by  $1\text{--}2 \times 10^3$  laser-cooled  $\text{Be}^+$  ions to about 10 mK. The  $(1 + 1' + 1'')$  REMPD experiment proposed here consists in driving a quasidanger-

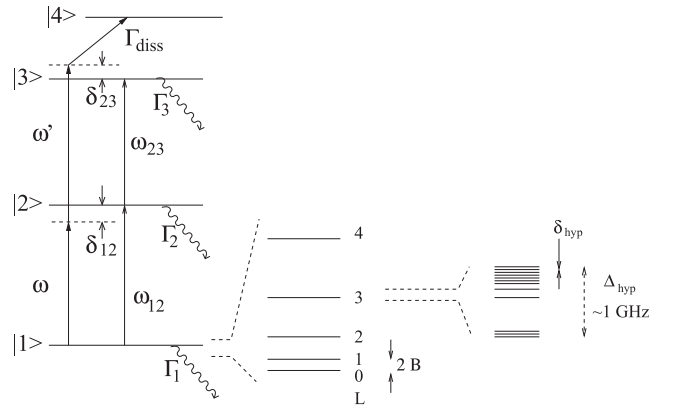


FIG. 1. Sketch of the  $\text{HD}^+$  energy levels involved in the proposed REMPD experiment. (Left) Vibrational structure. Couplings by laser fields and spontaneous relaxation are respectively indicated by straight and zigzag arrows. (Center) Rotational structure. (Right) Hyperfine structures (not to scale).

ate two-photon overtone transition using counterpropagating beams. The  $v = 9$  level is efficiently photodissociated using a 532-nm laser beam. Two-photon excitation and subsequent dissociation lead to loss of  $\text{HD}^+$  ions from the trapped ensemble. This loss is observed by comparing the number of  $\text{HD}^+$  ions before and after REMPD, which is deduced from the fluorescence photons emitted by the laser-cooled  $\text{Be}^+$  ions while heating the ion ensemble through resonant excitation of the  $\text{HD}^+$  motion [36]. The detection noise typically observed in the experiment limits the minimum detectable dissociated  $\text{HD}^+$  fraction to a few percent.

Figure 1 shows the structure of  $\text{HD}^+$  energy levels involved in the REMPD scheme. The kets  $|1\rangle$ ,  $|2\rangle$ , and  $|3\rangle$  denote the levels  $(v = 0, L = 3, F, S, J_1)$ ,  $(v = 4, L = 2, F, S, J_2)$ , and  $(v = 9, L = 3, F, S, J_3)$ , where  $(F, S, J)$  are hyperfine quantum numbers according to the coupling scheme detailed below. The vibrational structure (with intervals of about 60 THz) sets the larger frequency scale in the experiment, followed by the rotational constant ( $B \approx 700 \text{ GHz}$ ). The resonant angular frequencies are  $\omega_{12}/2\pi = 207.838 \text{ THz}$  and  $\omega_{23}/2\pi = 207.427 \text{ THz}$ , leading to a small two-photon transition mismatch  $\omega_{12} - \omega_{23} = 410 \text{ GHz}$  ( $13.7 \text{ cm}^{-1}$ ), i.e., 0.2% in relative value. The rovibrational states have small natural widths  $\Gamma_1/2\pi = 0.037 \text{ Hz}$ ,  $\Gamma_2/2\pi = 9.2 \text{ Hz}$ , and  $\Gamma_3/2\pi = 13.1 \text{ Hz}$  [37].

We use the standard spin-coupling scheme  $\mathbf{F} = \mathbf{I}_p + \mathbf{S}_e$ ,  $\mathbf{S} = \mathbf{F} + \mathbf{I}_d$ ,  $\mathbf{J} = \mathbf{S} + \mathbf{L}$  [38]. For a given rovibrational level, the hyperfine structure spreads over  $\Delta_{\text{hyp}} \approx 1 \text{ GHz}$ , the smallest interval between two hyperfine sublevels being  $\delta_{\text{hyp}} \approx 8 \text{ MHz}$  for the  $v = 0, L = 3$  level [38]. The Zeeman structure is discussed in Appendix A. In the Amsterdam experimental setup, the magnetic field can be reduced to values as low as 20 mG, resulting in a Zeeman splitting  $\delta_Z$  smaller than 10 Hz for the best suited lines, due to an almost perfect compensation of Zeeman shifts. Assuming the laser linewidth is larger than the Zeeman splitting, all the Zeeman components can be addressed simultaneously. That is why the Zeeman structure is not considered in our model.

The two-photon transition is driven by two lasers of angular frequencies  $\omega$  and  $\omega'$  close to the single-photon transition frequencies  $\omega_{12}$  and  $\omega_{23}$ , respectively. The transitions lie in the 1.4- $\mu\text{m}$  range and can be driven by frequency-stabilized diode lasers. Using transition moments calculated with the approach of [39], the achievable laser intensities, i.e., about  $20 \text{ mW}/(0.1 \text{ mm})^2$ , can be translated into maximum values for the Rabi frequencies  $\Omega_{12}/2\pi$  or  $\Omega_{23}/2\pi$  that exceed 100 kHz.

In the linear rf Paul trap, the HD<sup>+</sup> molecular ions are embedded in a Be<sup>+</sup> Coulomb crystal [40,41]. As part of a complex mechanical system, each HD<sup>+</sup> ion oscillates around its equilibrium position with oscillation frequencies in the kHz to MHz ranges and amplitudes in the  $\mu\text{m}$  range. Velocities can typically reach 5 m/s (see Appendix B), resulting in a single-photon Doppler effect  $\Gamma_D$  in the 5 MHz range that clearly dominates the single-photon transition width. The values of the laser detunings  $\delta_{12} = \omega - \omega_{12}$  and  $\delta_{23} = \omega' - \omega_{23}$  with respect to  $\Gamma_D$  determine the dynamics of the system: instantaneous two-photon transitions will dominate if  $\delta_{12} > \Gamma_D$ , while in the opposite case sequential transitions will also take place.

With a counterpropagating two-photon excitation scheme, the effective wavelength  $\lambda_{\text{eff}} = 2\pi c/|\omega_{12} - \omega_{23}|$  is about 500 times larger than the single-photon wavelength, i.e., 0.7 mm. Since the ion motional amplitude  $a$  is about  $1 \mu\text{m}$ , the Lamb-Dicke parameter  $\eta = a/\lambda_{\text{eff}} \approx 0.014$  is much smaller than unity, leading to a Doppler-free signal, as evidenced in Sec. IV.

The REMP process involves a photodissociation step from level |3) using a 532-nm cw laser with a maximum intensity of  $140 \text{ W}/\text{cm}^2$ , corresponding to a photodissociation rate  $\Gamma_{\text{diss}} = 5000 \text{ s}^{-1}$ . In the following, we use  $\Gamma_{\text{diss}} = 200 \text{ s}^{-1}$ , which is still much larger than the natural decay rate and sufficient to detect the REMP signal [34].

The laser linewidths  $\Gamma_L$  may range from hundreds of kHz down to the Hz level depending on the laser frequency stabilization scheme. In case of imperfect stabilization,  $\Gamma_L$  may be comparable to the Rabi frequencies and strongly affect the two-photon transition rate and linewidth, which requires taking laser frequency noise into account.

At thermal equilibrium at room temperature, most of the HD<sup>+</sup> population is concentrated in the  $v = 0, 0 \leq L \leq 5$  levels [42]. Blackbody radiation permanently redistributes the populations among those levels with transition rates  $\Gamma_{\text{BBR}}$  in the  $0.1 \text{ s}^{-1}$  range [39], the smallest frequency scale of the problem.

To summarize, the different rates follow the hierarchy

$$\begin{aligned} \Gamma_{\text{BBR}} &\ll \delta_Z, \Gamma_{1,2,3} \leq \Gamma_{\text{diss}}, \Gamma_L \leq \Omega_{12} \approx \Omega_{23} \\ &\ll \Gamma_D \sim \delta_{12} \sim \delta_{23} \leq \delta_{\text{hyp}} \\ &\ll \Delta_{\text{hyp}} \ll |\omega_{12} - \omega_{23}| < B \ll \omega_{12}, \omega_{23}. \end{aligned} \quad (1)$$

This analysis shows that the different hyperfine components of the two-photon transition can be considered to be well isolated and that it is appropriate to study the two-photon transition rate using a three-level ladder system. It also shows that one can distinguish two different time scales for the population evolution: a fast one due to laser couplings and spontaneous relaxation and a much slower one due to BBR population redistribution. As a consequence, in a very good approximation, the REMP process can be studied

in two steps. The first step evaluates the short-term ( $\approx 1 \text{ s}$ ) time evolution of a three-level system under laser excitation and spontaneous decay to obtain the effective two-photon excitation and REMP rates (Secs. III and IV). In the second step, the long-term evolution of the total number of HD<sup>+</sup> ions is studied, taking into account the REMP rate obtained in the first step, and the redistribution of rotational-state population by BBR (Sec. V).

### III. REMP MODEL

We consider the three-level ladder structure shown in Fig. 1. For states |2) and |3), the relaxation by spontaneous emission mainly populates rovibrational levels with  $v' = v - 1$ . The spontaneous emission cascade, coupled to BBR redistribution, can, of course, ultimately populate the  $v = 0, L = 3$  state, but this happens on much longer time scales with respect to laser excitation, dissociation, and spontaneous decay. We thus treat the three-level system as an open system, and postpone the analysis of BBR redistribution to Sec. V. While levels |1) and |2) have natural widths  $\Gamma_1$  and  $\Gamma_2$ , level |3) relaxes through spontaneous emission with a natural width  $\Gamma_3$  and through dissociation with a rate  $\Gamma_{\text{diss}}$ , resulting in an effective width  $\Gamma_3^{\text{eff}} = \Gamma_3 + \Gamma_{\text{diss}}$ . We introduce a fourth virtual level |4) whose population represents the photodissociated fraction. The coupling to level |4) is an irreversible process.

The ions are excited by two counterpropagating beams of angular frequencies  $\omega$  and  $\omega'$  close to the resonant frequencies  $\omega_{12}$  and  $\omega_{23}$ . The corresponding electric field is given by

$$\mathbf{E}(\mathbf{r}, t) = E\boldsymbol{\epsilon}e^{-i[\omega t - \mathbf{k}\cdot\mathbf{r} + \varphi(t)]} + E'\boldsymbol{\epsilon}'e^{-i[\omega' t - \mathbf{k}'\cdot\mathbf{r} + \varphi'(t)]} + \text{c.c.}, \quad (2)$$

where  $\varphi(t)$  and  $\varphi'(t)$  describe laser phase noise, and  $E, E'$  and  $\boldsymbol{\epsilon}, \boldsymbol{\epsilon}'$  stand for the field amplitudes and polarization states, respectively.

Following the lines of [43], the density matrix  $\varrho(\mathbf{r}, t)$  obeys the OBEs  $\frac{d}{dt}\varrho(\mathbf{r}, t) = \frac{1}{i\hbar}[H, \varrho(\mathbf{r}, t)] + \dot{\varrho}_{\text{relax}}$ , where the total time derivative is written as  $\frac{d}{dt} = \frac{\partial}{\partial t} + \mathbf{v} \cdot \nabla$ . Applying the rotating wave approximation, we set

$$\begin{aligned} \varrho_{ii} &= \rho_{ii}, \quad i = 1, \dots, 4, \quad \varrho_{12} = \rho_{12}(t)e^{-i[\omega t - \mathbf{k}\cdot\mathbf{r}(t)]}, \\ \varrho_{23} &= \rho_{23}(t)e^{-i[\omega' t - \mathbf{k}'\cdot\mathbf{r}(t)]}, \quad \varrho_{13} = \rho_{13}(t)e^{-i[(\omega + \omega')t - (\mathbf{k} + \mathbf{k}')\cdot\mathbf{r}(t)]}, \end{aligned} \quad (3)$$

and we obtain

$$\begin{aligned} \dot{\rho}_{11} &= -\Gamma_1\rho_{11} + i(\Omega_{12}\rho_{21} - \Omega_{12}^*\rho_{12}), \\ \dot{\rho}_{22} &= -\Gamma_2\rho_{22} + i(\Omega_{12}^*\rho_{12} - \Omega_{12}\rho_{21} + \Omega_{23}\rho_{32} - \Omega_{23}^*\rho_{23}), \\ \dot{\rho}_{33} &= -(\Gamma_3 + \Gamma_{\text{diss}})\rho_{33} + i(\Omega_{23}^*\rho_{23} - \Omega_{23}\rho_{32}), \\ \dot{\rho}_{44} &= \Gamma_{\text{diss}}\rho_{33}, \\ \dot{\rho}_{12} &= \{i[\delta_{12} - \mathbf{k} \cdot \dot{\mathbf{r}}(t)] - \gamma_{12}\}\rho_{12} \\ &\quad + i[\Omega_{12}(\rho_{22} - \rho_{11}) - \Omega_{23}^*\rho_{13}], \\ \dot{\rho}_{13} &= \{i[\delta_{12} + \delta_{23} - (\mathbf{k} + \mathbf{k}') \cdot \dot{\mathbf{r}}(t)] - \gamma_{13}\}\rho_{13} \\ &\quad + i(\Omega_{12}\rho_{23} - \Omega_{23}\rho_{12}), \\ \dot{\rho}_{23} &= \{i[\delta_{23} - \mathbf{k}' \cdot \dot{\mathbf{r}}(t)] - \gamma_{23}\}\rho_{23} \\ &\quad + i[\Omega_{23}(\rho_{33} - \rho_{22}) + \Omega_{12}^*\rho_{13}], \end{aligned} \quad (4)$$

where the Rabi frequencies are  $\Omega_{12} = \mathbf{d}_{12} \cdot \boldsymbol{\epsilon} E e^{i\varphi(t)}/\hbar$  and  $\Omega_{23} = \mathbf{d}_{23} \cdot \boldsymbol{\epsilon}' E' e^{i\varphi'(t)}/\hbar$  with the dipole moment matrix elements  $\mathbf{d}_{ij} = \langle i|\mathbf{d}|j\rangle$ . The coherences relaxation rates are  $\gamma_{12} = (\Gamma_1 + \Gamma_2)/2$  and  $\gamma_{13} = (\Gamma_1 + \Gamma_3 + \Gamma_{\text{diss}})/2$ . The photodissociated fraction  $\rho_{44}$  is proportional to the time integral of the upper level population  $\rho_{33}(t)$ .

The Doppler effect appears in the terms  $\mathbf{k} \cdot \dot{\mathbf{r}}(t)$  and  $\mathbf{k}' \cdot \dot{\mathbf{r}}(t)$  in the evolution equations of  $\rho_{12}$  and  $\rho_{23}$ . Suppression of the Doppler effect occurs in the  $\rho_{13}$  evolution equation in the case of counterpropagating beams of nearly equal frequencies for which  $\mathbf{k} + \mathbf{k}' \approx \mathbf{0}$ . In the following, the laser direction is assumed parallel to the linear trap axis  $z$ , so that the Doppler effect in Eq. (4) reduces to  $\mathbf{k} \cdot \dot{\mathbf{r}}(t) = k \dot{z}(t)$  and  $\mathbf{k}' \cdot \dot{\mathbf{r}}(t) = -k' \dot{z}(t)$ . This assumption furthermore justifies ignoring effects of ion micromotion at the rf trap frequency. A detailed discussion of micromotion effects is postponed to Sec. IV D4.

At first glance, the largest REMPD signal could be expected for the doubly resonant configuration,  $\delta_{12} = -\delta_{23} = 0$ , as in a thermal gas [9]. However, if the detunings are smaller than (or comparable to) the single-photon Doppler width, sequential absorption of photons  $\omega$  and  $\omega'$  through level  $|2\rangle$  can compete with the Doppler-free signal. The main objective of this paper is to determine the experimental conditions under which one can obtain sub-Doppler REMPD signals with the largest signal-to-noise ratio; in particular, to determine the optimal single-photon detunings  $\delta_{12}$  and  $\delta_{23}$ , taking into account realistic ion trajectories and laser phase noise.

Since under those conditions the OBE cannot be solved in a closed form, we integrate them numerically between  $t = 0$  and  $t = t_{\text{max}}$ . We use a fourth-order Runge-Kutta method with a short enough time step ( $10^{-9}$  to  $5 \times 10^{-8}$  s) to well represent the relevant characteristic frequencies of the problem. The initial conditions are  $\rho_{11} = 1$ , and zero for all the other density matrix elements. Since we consider an open three-level system, the stationary solution is not relevant. The populations and coherences only have a transient behavior and vanish for long times. The signal, i.e., the dissociated fraction, is given by  $\rho_{44}^\infty = \rho_{44}(t \rightarrow \infty)$ ; the integration time  $t_{\text{max}}$  has to be chosen long enough to get a precise estimate of  $\rho_{44}^\infty$ .

## IV. RESULTS

The REMPD signal given by the dissociated fraction  $\rho_{44}$  is first studied in Sec. IV A in the simple case of noiseless lasers and of a single molecular ion with a harmonic motion to characterize sideband effects and identify the Lamb-Dicke regime. In Sec. IV B, we come to a more realistic model by including actual ion trajectories to simulate the experimental signal and determine optimal conditions for REMPD signal observation. The OBE results are compared to a simple rate equation model introduced in Sec. IV C. Finally, we evaluate light shifts and power broadening and analyze the effects of laser phase noise in Sec. IV D.

### A. Single-frequency oscillating ion

Here, we consider a single ion oscillating with an angular frequency  $\Omega_{\text{vibr}}$  and velocity amplitude  $\tilde{v}$ . Figure 2 (Fig. 3) shows the typical time evolution of the populations  $\rho_{11}$ ,

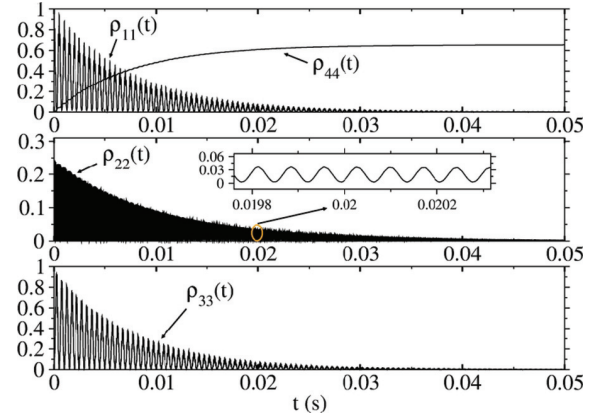


FIG. 2. (Color online) Time evolution of the populations in the case of a single ion undergoing pure harmonic motion along the  $z$  axis.  $\Omega_{\text{vibr}} = 2\pi \times 600$  kHz; velocity amplitude,  $\tilde{v} = 1$  m/s,  $\Omega_{12} = \Omega_{23} = 2\pi \times 5$  kHz; small detuning,  $\delta_{12} = -\delta_{23} = 2\pi \times 10$  kHz; integration time step,  $10^{-9}$  s.

$\rho_{22}$ , and  $\rho_{33}$ , as well as the dissociated fraction  $\rho_{44}$  in the case of an ion with a pure oscillatory motion for opposite small (large) detunings of 10 kHz (5 MHz) as compared to the single-photon Doppler width  $\tilde{v}/\lambda = 714$  kHz. The other parameters of the calculation (see figure captions) correspond to the typical values used throughout the paper. Although the final dissociated fractions  $\rho_{44}$  are comparable, the two figures corresponds to completely different conditions.

For small detunings, two-photon excitation is a sequential process involving a large intermediate state population  $\rho_{22}$ .  $\rho_{11}$  and  $\rho_{33}$  ( $\rho_{22}$ ) exhibit strong oscillations at 2 kHz (12 and 14 kHz), see Fig. 2. We have checked that those evolution frequencies are consistent with the generalized Rabi frequencies that can be determined by solving the OBE analytically for an ion at rest [ $\dot{\mathbf{r}}(t) = \mathbf{0}$ ].

In the large detuning regime (Fig. 3),  $\rho_{22}$  always remains negligible, and level  $|3\rangle$  is directly excited from level  $|1\rangle$  by a two-photon process. Comparing the time scales in Figs. 2 and 3, one can see that the two-photon process is much slower than the low-detuning sequential process; nonetheless, it also leads to a large dissociated fraction after a long-enough

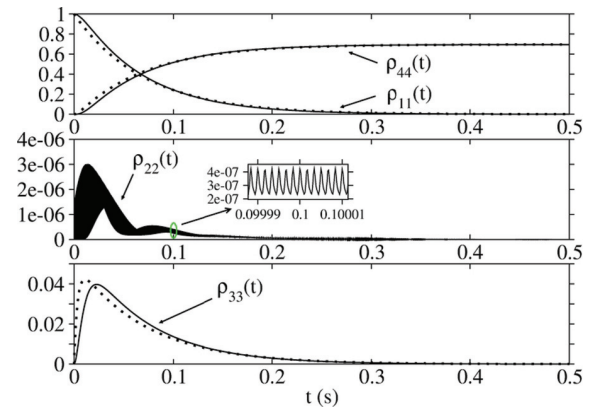


FIG. 3. (Color online) Same as Fig. 2 but with a large detuning  $\delta_{12} = -\delta_{23} = 2\pi \times 5$  MHz. Dotted lines are obtained from Eq. (6) without adjustable parameter.

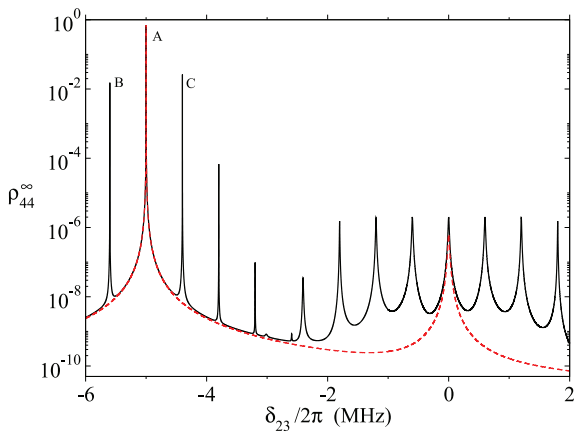


FIG. 4. (Color online) Photodissociated fraction as a function of  $\delta_{23}$ . Red dashed line, ion at rest. Black solid line, oscillating ion with  $\Omega_{\text{vibr}}/2\pi = 600$  kHz,  $\tilde{v} = 1$  m/s. Parameters:  $\Omega_{12} = \Omega_{23} = 2\pi \times 5$  kHz,  $\delta_{12}/2\pi = 5$  MHz. Time step:  $5 \times 10^{-8}$  s,  $t_{\text{max}} = 0.5$  s.

time. The behavior of  $\rho_{11}$  and  $\rho_{44}$  in Fig. 3 is very close to exponential decay, which will make it possible to describe the evolution by an effective REMP rate. The apparent thickness of the  $\rho_{22}$  curve is due to fast modulation at the ion oscillation frequency.

We now analyze the REMP signal  $\rho_{44}^{\infty}$  as a function of  $\delta_{23}$  for a (fixed) large detuning  $\delta_{12}$ . Figure 4 shows the spectrum for an oscillating ion with  $\Omega_{\text{vibr}} = 2\pi \times 600$  kHz and  $\tilde{v} = 1$  m/s (the red dashed line is obtained for an ion at rest for comparison). It exhibits two groups of peaks having a sideband structure, in which the sidebands are generated by the Doppler effect due to the ion oscillation, leading to a comb of lines separated by  $\Omega_{\text{vibr}}$ . They correspond to two different processes.

The right part of Fig. 4, centered at  $\delta_{23} = 0$ , corresponds to sequential excitation. Since the detuning  $\delta_{12}$  is large as compared to the single-photon Doppler width, sequential excitation is inefficient, leading to very small dissociated fractions of the order of  $10^{-6}$ . In its rest frame, the oscillating ion sees phase-modulated laser spectra with a modulation index of  $2\pi\tilde{v}/(\lambda\Omega_{\text{vibr}}) = 1.16$ , leading to three significant sidebands on each side of the carrier, explaining the broad signal sideband structure.

The left part of Fig. 4, centered at the two-photon resonance  $\delta_{23} = -\delta_{12}$ , is the signal due to instantaneous two-photon excitation. It exhibits an intense narrow peak as well as sidebands. However, the sidebands are much smaller than the carrier and drop off very rapidly with sideband order, evidencing the Lamb-Dicke regime. In order to get a more quantitative understanding, we varied the ion oscillation frequency  $\Omega_{\text{vibr}}$  for a given velocity amplitude ( $\tilde{v} = 1$  m/s) and determined the two-photon transition rate  $\Gamma_{2\text{ph}}$  by fitting the decay of  $\rho_{11}(t)$  with Eq. (6) (see Sec. IV C) for the carrier and first sidebands of the two-photon signal (peaks A, B, and C in Fig. 4). Figure 5 shows  $\Gamma_{2\text{ph}}$  versus  $\Omega_{\text{vibr}}$ . Red solid lines are obtained from the model given in Appendix D [Eqs. (C2) and (C3)]. In Eq. (C3), the effective quantum number  $n$  depends on  $\Omega_{\text{vibr}}$  through the relationship  $(n + 1/2)\hbar\Omega_{\text{vibr}} \approx m\tilde{v}^2/2$ , and we used  $s = 0, \pm 1$  for the carrier A and sidebands B and C, respectively. Both approaches are in good agreement and demonstrate that the system is deep in the Lamb-Dicke regime.

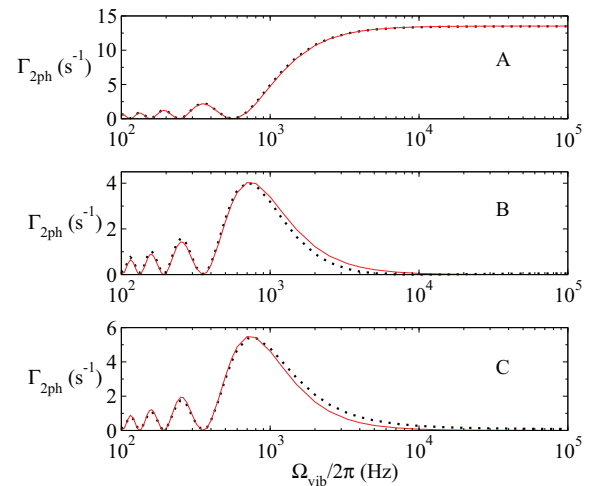


FIG. 5. (Color online) Black dotted curves, two-photon transition rates on the carrier (A) and first sidebands (B), (C) of the two-photon resonance versus the oscillation frequency, obtained by solving the OBE for a harmonic oscillation. Red solid curves, same, but obtained using Eqs. (C2) and (C3) of Appendix C. Parameters:  $\delta_{12}/2\pi = 5$  MHz,  $\Omega_{12} = \Omega_{23} = 2\pi \times 5$  kHz,  $\tilde{v} = 1$  m/s. Time step:  $10^{-9}$  s,  $t_{\text{max}} = 1$  s.

To conclude on the spectrum of Fig. 4, let us stress again the important differences with respect to the gas case. In a dilute gas, the velocity can be considered as constant during the interaction with light; as a result, sequential transitions are Doppler-free because the first transition selects a velocity class [9]. This effect does not take place in ion traps, where the ion velocities oscillate with time, and sequential transitions are Doppler-broadened. On the contrary, instantaneous transitions which are Doppler-free in ion traps due to the Lamb-Dicke effect, exhibit residual Doppler broadening in a gas.

Figure 6 shows the signal at two-photon resonance as a function of the Rabi frequencies  $\Omega_{12}$  and  $\Omega_{23}$ , assuming that

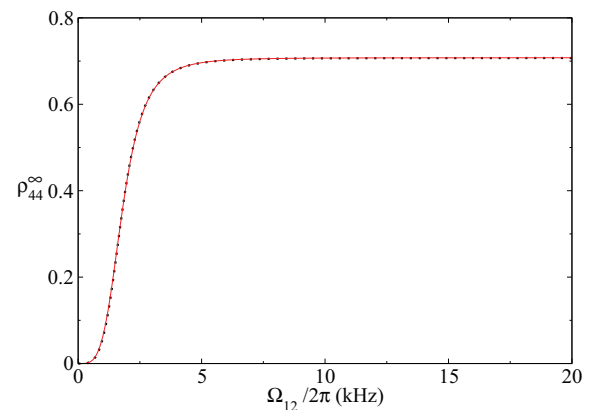


FIG. 6. (Color online) Photodissociated fraction versus Rabi frequencies for a detuning  $\delta_{12} = -\delta_{23} = 2\pi \times 5$  MHz.  $\Omega_{\text{vibr}} = 2\pi \times 600$  kHz,  $\tilde{v} = 1$  m/s.  $\Omega_{12}$  and  $\Omega_{23}$  are taken as equal. The red solid line corresponds to the prediction of Eq. (8), and the dotted curve is obtained by solving the OBE with a time step of  $10^{-8}$  s, and  $t_{\text{max}} = 10$  s.

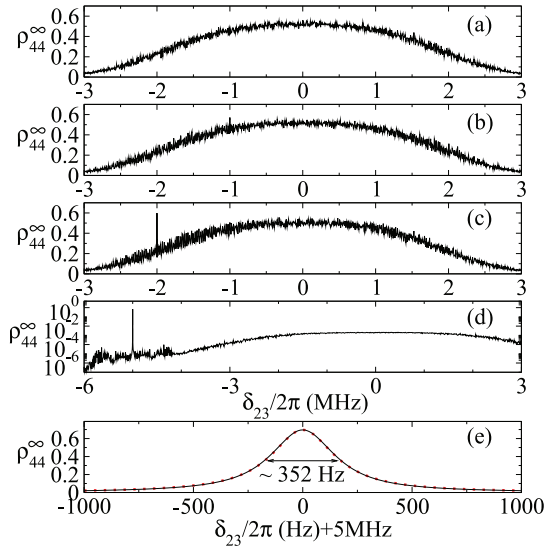


FIG. 7. (Color online) (a)–(d) Dissociated fraction as a function of  $\delta_{23}$  for four values of  $\delta_{12}/2\pi$ : 0, 1, 2, and 5 MHz. (e) Magnification of the Doppler-free peak for  $\delta_{12}/2\pi = 5$  MHz; the solid line is obtained from Eq. (8). The simulations are performed for 20  $\text{HD}^+$  ions in a  $400\text{-Be}^+$  ion cloud. Parameters:  $\Omega_{12} = \Omega_{23} = 2\pi \times 5$  kHz; time step,  $10^{-8}$  s,  $t_{\text{max}} = 0.5$  s for (a)–(d) and 10 s for (e).

they are equal. The saturation intensity (for which the signal is equal to half its maximum value) is found to correspond to Rabi frequencies of about 2 kHz, in excellent agreement with the rate equation model of Sec. IV C [Eq. (9)]. For most of the calculations hereafter, the Rabi frequencies are set to 5 kHz to achieve large signals.

### B. Real ion motion

In this section, we come to a more realistic description of the REMP dynamics by inserting into the OBE ion trajectories obtained by numerically simulating the motion of 20  $\text{HD}^+$  ions sympathetically cooled by 400  $\text{Be}^+$  ions (Appendix B). The dissociated fraction is computed for each trajectory and the results are averaged. Figure 7 shows the dissociated fraction  $\rho_{44}$  as a function of detuning  $\delta_{23}$  for  $\delta_{12} = 0, 1, 2,$  and 5 MHz. For small detunings,  $\rho_{44}$  is dominated by the sequential contribution, leading to a wide Doppler-broadened spectrum which obscures the Doppler-free instantaneous two-photon signal. For detunings larger than the single-photon Doppler width, the sequential contribution strongly decreases and the narrow Doppler-free peak dominates.

The sequential contribution thus appears as a noise floor that limits the visibility of the Doppler-free signal. In order to determine how close to the resonance the detuning can be set, we compare the Doppler-free signal to the sequential contribution by plotting in Fig. 8 the top of the Doppler-free peak and the estimated “noise floor” due to the sequential signal. The results show that an optimal visibility of the Doppler-free signal is achieved for detunings around 5 MHz, which corresponds to the maximum single-photon Doppler shift experienced by the ions.

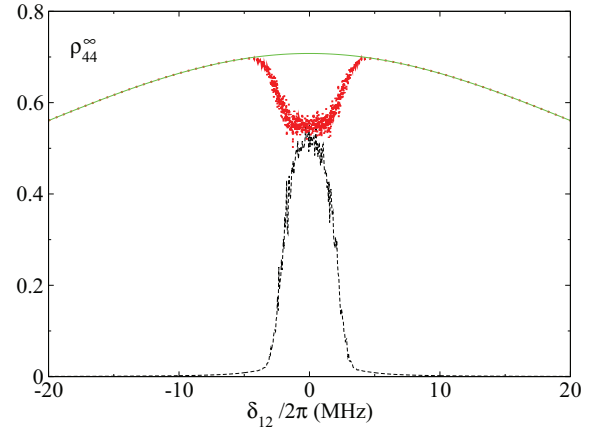


FIG. 8. (Color online) (Red dotted) Photodissociated fraction  $\rho_{44}$  as a function of the detuning  $\delta_{12}$  at two-photon resonance ( $\delta_{23} = -\delta_{12}$ ) obtained by solving the OBE. (Black dashed) Photodissociated fraction due to sequential two-photon excitation (“noise floor”), which we evaluate at the pedestal of the Doppler-free peak. The green solid curve is obtained from Eq. (8). Parameters:  $\Omega_{12} = \Omega_{23} = 2\pi \times 5$  kHz; time step  $10^{-8}$  s,  $t_{\text{max}} = 2$  s.

### C. Rate equation model

The analysis of the signal predicted by solving numerically the OBE showed that the optimum value of the detuning is slightly larger than the Doppler width. In that case, the population of level  $|2\rangle$  always remains negligible, and the OBE describing the evolution of the three-level system in interaction with the laser fields can be simplified by introducing the two-photon transition probability  $\Gamma_{2\text{ph}}$  between levels  $|1\rangle$  and  $|3\rangle$  (see Appendix C). The time evolution of the populations  $\rho_{11}, \rho_{33},$  and  $\rho_{44}$  can then be described by a simple rate equation model. Introducing  $\Gamma_3^{\text{eff}} = \Gamma_3 + \Gamma_{\text{diss}}$ , the rate equations are written

$$\begin{aligned} \frac{d\rho_{11}}{dt} &= -(\Gamma_{2\text{ph}} + \Gamma_1)\rho_{11}, & \frac{d\rho_{33}}{dt} &= \Gamma_{2\text{ph}}\rho_{11} - \Gamma_3^{\text{eff}}\rho_{33}, \\ \frac{d\rho_{44}}{dt} &= \Gamma_{\text{diss}}\rho_{33}, \end{aligned} \quad (5)$$

where, in order to simplify the expressions, we have replaced  $\rho_{11} - \rho_{33}$  by  $\rho_{11}$  in the first two equations. This approximation is justified for large detunings, since  $\rho_{33}$  then remains much smaller than  $\rho_{11}$ . The solution corresponding to  $\rho_{11}(0) = 1$  and  $\rho_{33}(0) = \rho_{44}(0) = 0$  reads

$$\begin{aligned} \rho_{11}(t) &= e^{-(\Gamma_1 + \Gamma_{2\text{ph}})t}, \\ \rho_{33}(t) &= \frac{\Gamma_{2\text{ph}}}{\Gamma_3^{\text{eff}} - \Gamma_1 - \Gamma_{2\text{ph}}} \left( e^{-(\Gamma_1 + \Gamma_{2\text{ph}})t} - e^{-\Gamma_3^{\text{eff}}t} \right), \\ \rho_{44}(t) &= \frac{\Gamma_{\text{diss}}\Gamma_{2\text{ph}}}{\Gamma_3^{\text{eff}}(\Gamma_1 + \Gamma_{2\text{ph}})} - \frac{\Gamma_{\text{diss}}\Gamma_{2\text{ph}}}{\Gamma_3^{\text{eff}} - \Gamma_1 - \Gamma_{2\text{ph}}} \\ &\quad \times \left( \frac{e^{-(\Gamma_1 + \Gamma_{2\text{ph}})t}}{\Gamma_1 + \Gamma_{2\text{ph}}} - \frac{e^{-\Gamma_3^{\text{eff}}t}}{\Gamma_3^{\text{eff}}} \right). \end{aligned} \quad (6)$$

Dotted lines in Fig. 3 are plotted from Eq. (6). They compare very well with the numerical result obtained with an oscillating ion in the large detuning limit, indicating that the instantaneous two-photon contribution is insensitive to the ion motion as

expected in the Lamb-Dicke regime. The long-term behavior of  $\rho_{44}$  is given by

$$\rho_{44}^{\infty} = \frac{\Gamma_{\text{diss}}\Gamma_{2\text{ph}}}{(\Gamma_3 + \Gamma_{\text{diss}})(\Gamma_1 + \Gamma_{2\text{ph}})}. \quad (7)$$

If  $\Gamma_{2\text{ph}} \gg \Gamma_1$  we have simply  $\rho_{44}^{\infty} \approx \Gamma_{\text{diss}}/(\Gamma_3 + \Gamma_{\text{diss}})$ . Indeed, in that case, direct losses from level |1) are negligible as compared to excitation to level |3), and  $\rho_{44}^{\infty}$  is given by the branching ratio between dissociation and natural relaxation.

In the general case, replacing  $\Gamma_{2\text{ph}}$  with the expression given by Eq. (C5), we obtain an expression for the photodissociated fraction that is valid in the Lamb-Dicke regime:

$$\rho_{44}^{\infty} = \frac{\Gamma_{\text{diss}}}{\Gamma_1} \frac{\Omega_{12}^2 \Omega_{23}^2}{\delta_{12}^2} \frac{1}{\delta_{13}^2 + \frac{(\Gamma_3^{\text{eff}})^2}{4} + \frac{\Gamma_3^{\text{eff}}}{\Gamma_1} \frac{\Omega_{12}^2 \Omega_{23}^2}{\delta_{12}^2}}. \quad (8)$$

Figure 6, showing  $\rho_{44}^{\infty}$  versus the Rabi frequencies, is obtained for an oscillating ion in the large detuning limit. Again, the results of Eq. (8) closely match the OBE numerical model.

The saturation Rabi frequency, defined as the Rabi frequency product  $\Omega_{12}\Omega_{23}$  for which  $\rho_{44}^{\infty} = \Gamma_{\text{diss}}/2\Gamma_3^{\text{eff}}$ , is given by

$$\Omega_{12}\Omega_{23} = \delta_{12} \sqrt{\frac{\Gamma_1}{\Gamma_3^{\text{eff}}} [\delta_{13}^2 + (\Gamma_3^{\text{eff}})^2/4]}, \quad (9)$$

which reduces to  $\Omega_{12}\Omega_{23} = \delta_{12}\sqrt{\Gamma_1\Gamma_3^{\text{eff}}}/2$  on two-photon resonance.

Comparing the green solid line in Fig. 8 with the red line representing the solution of the OBE shows that the rate equation model accurately predicts  $\rho_{44}^{\infty}$  for detunings larger than the Doppler width, but as expected, fails for small detunings. Finally, the Doppler-free line obtained by solving the OBE and shown in Fig. 7(e) has a Lorentzian shape of amplitude 0.7 and FWHM 352 Hz, in excellent agreement with the predictions of Eq. (8), giving 0.71 for the amplitude and 354 Hz for the width.

#### D. Systematic shifts and line broadening

In this section, we study the main effects that may perturb the Doppler-free REMP signal, i.e., light shifts, power broadening, and laser frequency noise. Only the large-detuning limit will be studied, and numerical results obtained from the OBE will be compared with predictions of the simple analytical model developed in Sec. IV C.

##### 1. Light shifts

The light shift experienced by the lower and upper levels |1) and |3) are given by  $+\Omega_{12}^2/\delta_{12}$  and  $-\Omega_{23}^2/\delta_{23}$ , respectively [44,45]. Close to the two-photon resonance defined by  $\delta_{12} = -\delta_{23}$ , both shifts have the same sign, leading to a compensated light shift for the transition frequency:

$$\Delta_{LS} = (\Omega_{23}^2 - \Omega_{12}^2)/\delta_{12}. \quad (10)$$

As was shown in Sec. IV B, the optimal value of the detuning  $\delta_{12}$  is of the order of the Doppler width (a few MHz), whereas the Rabi frequencies are of a few kHz. Therefore, the light shift typically amounts to a few Hz, i.e., a relative shift of about  $10^{-14}$  on the transition frequency. Moreover, laser intensities

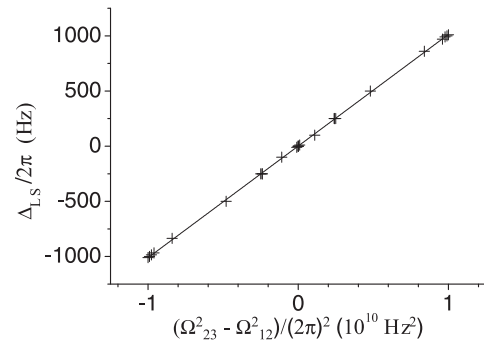


FIG. 9. Crosses, light shift of the two-photon resonance versus Rabi frequencies. The two-photon resonance is located by finding the maximum of the Doppler-free peak [see Fig. 7 (e)]. Solid line, linear fit giving a slope of  $1.011(2) \cdot 10^{-7}$  Hz/(Hz)<sup>2</sup>. Parameters:  $\delta_{12} = 10$  MHz; time step,  $10^{-8}$  s,  $t_{\text{max}} = 0.5$  s.

can be chosen in order to get equal Rabi frequencies, thus canceling the light shifts.

In Fig. 9, the position  $\delta_{23}$  of the two-photon peak is plotted versus  $\Omega_{23}^2 - \Omega_{12}^2$  for a fixed detuning  $\delta_{12} = 10$  MHz. It has a linear dependence with a slope of  $1.011(2) \cdot 10^{-7}$  Hz/(Hz)<sup>2</sup>, in good agreement with Eq. (10), which predicts  $10^{-7}$  Hz/(Hz)<sup>2</sup>.

##### 2. Power broadening

A simple expression of the power broadening is easily deduced from Eq. (8). Figure 10 compares the broadening predicted by Eq. (8) to a more precise calculation from the numerical solution of the OBE. The inset shows that there is excellent agreement at low intensity. For very large Rabi frequencies, the numerically obtained power broadening is smaller than expected from Eq. (8). This discrepancy stems from the fact that Eq. (8) is obtained using Eq. (C5) for  $\Gamma_{2\text{ph}}$ , which is valid if  $\Gamma_{2\text{ph}} \ll \Gamma_3^{\text{eff}}$  but not for large laser fields.

As already mentioned in Sec. IV B, the FWHM of the two-photon peak for the laser intensities used throughout the paper ( $\Omega_{12} = \Omega_{23} = 2\pi \times 5$  kHz, signalled by a vertical

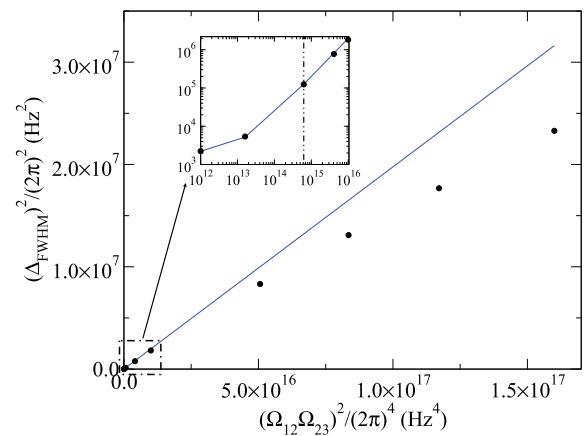


FIG. 10. (Color online) Squared width (FWHM) of the Doppler-free peak versus Rabi frequencies. The solid line is obtained from Eq. (8). The vertical dashed line in the inset corresponds to the typical Rabi frequencies used throughout the paper, i.e.,  $\Omega_{12} = \Omega_{23} = 2\pi \times 5$  kHz. Parameters:  $\delta_{12} = 5$  MHz; time step,  $10^{-8}$  s,  $t_{\text{max}} = 20$  s.

dashed line in the inset of Fig. 10), is 354 Hz [see Fig. 7(e)], while the prediction of Eq. (8) is 351 Hz. Thus, power broadening significantly degrades the resolution with respect to the effective linewidth  $\Gamma_3^{\text{eff}} = 45$  Hz. Lower intensities can be used to improve the resolution, at the cost of a slightly reduced signal-to-noise ratio.

### 3. Laser frequency noise

The analysis of light shifts and power broadening shows that REMPD spectroscopy at the sub-kHz level is feasible. In this section, we discuss the effect of the laser width on the signal, using both numerical solutions of OBE and an analytical model.

So far, we have assumed noiseless laser fields by setting  $\varphi(t) = \varphi'(t) = 0$  in Eq. (2). This means that the two laser fields are supposed to be perfectly phase locked. The discussion in Sec. II shows that laser linewidths cannot always be neglected as compared to Rabi frequencies and level widths. The REMPD experiment involves frequency controlled diode laser sources, which have a Lorentzian line shape. In order to include the laser frequency noise into the model, two independent noisy phases  $\varphi(t)$  and  $\varphi'(t)$  are numerically generated as centered Gaussian stationary processes with the desired shape and width [46,47] as explained in Appendix D, and used as inputs in the OBE (4). For both lasers the phase noise bandwidth  $B$  is chosen to be 100 kHz and the width  $\Delta_{\text{FWHM}}$  is varied from a few Hz to 30 kHz.

The effect of laser phase noise on two-photon transition rates is theoretically addressed in [48]. For two uncorrelated phases  $\varphi(t)$  and  $\varphi'(t)$ , formula (C4) is modified into

$$\Gamma_{2\text{ph}} = \frac{\Omega_{12}^2 \Omega_{23}^2}{\delta_{12}^2 \delta_{13}^2} \frac{\Gamma_3^{\text{eff}} + 2\Delta_{\text{FWHM}}}{(\Gamma_3^{\text{eff}} + 2\Delta_{\text{FWHM}})^2 / 4}. \quad (11)$$

Just like Eq. (C4), the above expression is valid in the large-detuning limit  $\delta_{12} > \Gamma_D$ . In Fig. 11, we plot  $\Gamma_{2\text{ph}}$  versus  $\Delta_{\text{FWHM}}$  assuming both lasers have the same width. Numerical results from the OBE are in very good agreement with Eq. (11),

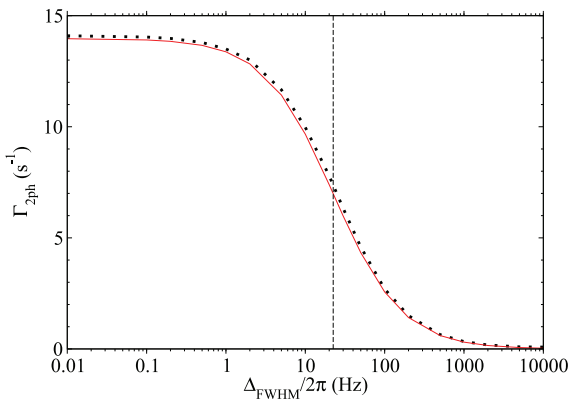


FIG. 11. (Color online) Two-photon transition rate versus the laser width (assuming a Lorentzian spectrum). The black dotted curve is obtained by integrating the OBE with a time step of  $10^{-8}$  and  $t_{\text{max}} = 0.5$  s. The red solid line is obtained from Eq. (11). The dashed vertical line corresponds to  $\Delta_{\text{FWHM}} = \Gamma_3^{\text{eff}}/2$ . Parameters:  $\Omega_{12} = \Omega_{23} = 2\pi \times 5$  kHz,  $\delta_{12} = -\delta_{23} = 2\pi \times 5$  MHz.

and show that it is desirable to have laser widths smaller than the effective width  $\Gamma_3 + \Gamma_{\text{diss}}$  of the upper level in order not to limit the two-photon transition rate, as well as the resolution.

### 4. Effects of micromotion

In a Paul trap, the ions undergo micromotion driven by the rf field at the ion location  $(x, y, z)$ . In this section, we evaluate the magnitude of the micromotion in the linear trap described in [34] to show that it has a negligible impact on the two-photon line shape and that the associated second-order Doppler effect does not limit the expected resolution.

The linear trap geometry is defined by an effective inner radius  $r_0 = 3.5$  mm and is operated using a rf voltage  $V_0 = 270$  V at  $\Omega_{\text{rf}} = 2\pi \times 13.3$  MHz, resulting in a  $\omega_r = 2\pi \times 0.9$  MHz  $\text{HD}^+$  radial trap frequency. The micromotion amplitude  $\delta\mathbf{r}$  is linked to the rf field  $\mathbf{E}_{\text{rf}}$  by  $\delta\mathbf{r} = -q\mathbf{E}_{\text{rf}}/(m\Omega_{\text{rf}}^2)$ . The leading components of the rf field are  $\mathbf{E}_{\text{rf}} = (-V_0 x/r_0^2, V_0 y/r_0^2, E_{\text{rf},z}) \cos(\Omega_{\text{rf}}t)$ . The radial components correspond to the trap's quadrupolar field. The axial component is a worst case value, obtained using a finite difference analysis (SIMION software) to model the actual trap potential taking into account the maximum possible deviation of end cap electrodes from the ideal geometry;  $E_{\text{rf},z}$  is less than 100 V/m over the ion cloud extension. However, trap imperfections, rf phase differences on the trap electrodes, and stray electric fields may lead to excess micromotion, which in turn can give rise to second-order Doppler shifts of the observed transition frequency, as well as additional sideband features in the spectrum [49,50]. Stray electric fields may be compensated by applying voltages on the trap electrodes to position the  $\text{Be}^+$  and  $\text{HD}^+$  ion clouds symmetrically with respect to the trap axis. From the applied voltages and the trap geometry, the residual stray field amplitude is estimated to be smaller than 7.3 V/m. The maximum radial displacement  $r_{\text{max}}^{\text{rad}}$  is obtained by balancing the stray electric force  $qE_{\text{stray}}$  with the ponderomotive force  $m\omega_r^2 r_{\text{max}}^{\text{rad}}$ , leading to  $r_{\text{max}}^{\text{rad}} = qE_{\text{stray}}/(m\omega_r^2) = 7.3 \mu\text{m}$  and maximum radial rf field components of 114 V/m. The maximum axial and radial micromotion amplitudes  $\delta x$ ,  $\delta y$ , and  $\delta z$  are all less than  $0.5 \mu\text{m}$ , much smaller than the effective transition wavelength. Furthermore, the ion trap was designed such that rf phase differences do not exceed 3 mrad. For the above trap parameters, this implies a maximum micromotion amplitude due to rf phase differences of  $0.4 \mu\text{m}$  [49].

Micromotion might lead to sidebands in the two-photon excitation spectrum, located  $\pm 13.3$  MHz from the main spectral feature. Nevertheless, under the present conditions, the modulation index  $|(\mathbf{k} - \mathbf{k}') \cdot \delta\mathbf{r}| < 0.007$  is very small, leading to strongly suppressed sidebands, justifying ignoring micromotion in the interaction model.

Although the micromotion amplitude is small, the associated velocity amplitude is large and second-order Doppler shift and broadening have to be evaluated. It is given by  $\delta f/f = -\langle v(t)^2 \rangle / (2c^2)$ . For micromotion with amplitude  $\delta\mathbf{r} = 0.9 \mu\text{m}$ , it is given by  $-(\delta\mathbf{r})^2 \Omega_{\text{rf}}^2 / (4c^2) = -1.5 \times 10^{-14}$ . Including rf phase differences, the shift may reach  $-1.8 \times 10^{-14}$  corresponding to less than 4 Hz on individual laser frequencies. This is much smaller than the expected two-photon linewidth and cannot hinder the two-photon line

observation. Nevertheless, careful micromotion compensation is necessary to reach the  $10^{-14}$  accuracy level.

### V. INFLUENCE OF BBR ON REMPD AND SIGNAL STRENGTH

In the preceding sections, the photodissociated fraction was interpreted as the spectroscopic signal of interest. However, in previous experiments spectroscopic signals were obtained by comparing the initial number of trapped HD<sup>+</sup> ions,  $N_i$ , to the remaining number of HD<sup>+</sup> ions after REMPD,  $N_f$ , by constructing a signal  $s = (N_i - N_f)/N_i$  [27,34]. Obviously, the finite size of the trapped HD<sup>+</sup> samples may lead to additional saturation effects. It should also be noted that before REMPD, most of the HD<sup>+</sup> ions are in states other than  $v = 0, L = 3$  as the ambient BBR (temperature  $T = 300$  K) distributes population over rotational states with  $L = 0$  to  $L = 6$  [42]. Each rotational level is furthermore split into 4 ( $L = 0$ ), 10 ( $L = 1$ ), or 12 ( $L \geq 2$ ) hyperfine states. As a consequence, only a few percent of the HD<sup>+</sup> ions may be found to be in a particular hyperfine state. For example, 2.6% of the HD<sup>+</sup> ions are in the favored initial hyperfine state with  $(v, L) = (0, 3)$  and  $(F, S, J) = (1, 2, 5)$  (see Appendix B). At first glance, one would therefore not expect to achieve a signal  $s$  larger than 0.026, which is barely above the noise background observed by Koелеmeij *et al.* [27]. However, for REMPD durations on the order of 1 s or longer, redistribution of population by BBR becomes an important factor, as this takes place on a similar time scale. In fact, BBR will continue to refill the initial state population while it is being depleted via REMPD, thereby enhancing the signal  $s$ . To estimate the expected signal strength, we treat the interaction of the ensemble of HD<sup>+</sup> ions with BBR and the REMPD lasers in the form of Einstein rate equations, which we integrate over the REMPD duration,  $t$ , to obtain  $s(t)$ . Here we introduce two simplifying assumptions. First, the REMPD process is considered sufficiently efficient so that no spontaneous emission from high vibrational states occurs. Second, all HD<sup>+</sup> ions are considered to be in states with  $v = 0$  and  $L = 0, \dots, 5$  (we ignore the population in  $L = 6$ , which is less than 2%). Taking hyperfine structure into account, the rate equations read

$$\begin{aligned} \frac{d}{dt} \rho_{\alpha L} = & \sum_{\alpha'} [A_{\alpha L}^{\alpha' L+1} + B_{\alpha L}^{\alpha' L+1} W(\omega_{\alpha L}^{\alpha' L+1}, T)] \rho_{\alpha' L+1} \\ & + \sum_{\alpha'} B_{\alpha L}^{\alpha' L-1} W(\omega_{\alpha L}^{\alpha' L-1}, T) \rho_{\alpha' L-1} \\ & - \sum_{\alpha'} [A_{\alpha L}^{\alpha' L} + B_{\alpha L}^{\alpha' L} W(\omega_{\alpha L}^{\alpha' L}, T)] \rho_{\alpha L} \\ & - \sum_{\alpha'} B_{\alpha L}^{\alpha' L} W(\omega_{\alpha L}^{\alpha' L}, T) \rho_{\alpha L} - \delta_{\alpha\alpha_0} \delta_{LL_0} \Gamma_{2\text{ph}} \rho_{\alpha L}. \end{aligned} \quad (12)$$

Here, the hyperfine populations  $\rho$  are labeled with the hyperfine index  $\alpha \equiv (F, S, J)$ . Transition frequencies are written as  $\omega_{\alpha L}^{\alpha' L'}$ , where the upper and lower indices refer to the upper and lower levels, respectively. The BBR spectral energy density at temperature  $T$  is denoted as  $W(\omega, T)$ . The hyperfine state subject to REMPD at rate  $\Gamma_{2\text{ph}}$  is labeled by  $\alpha_0$  and  $L_0$ . Introducing the equivalent notation  $A_{ij} = A_j^i = A_{\alpha' L'}^{\alpha L}$  (and

likewise for  $B_{ij}$  and  $\omega_{ij}$ ), the rate coefficients for spontaneous emission from an upper state  $i$  to a lower state  $j$  are written as

$$A_{ij} = \frac{\omega_{ij}^3}{3\pi\epsilon_0\hbar c^3} \frac{\mathcal{S}_{ij}}{2J_i + 1} \mu_{ij}^2. \quad (13)$$

The radial dipole matrix elements  $\mu_{ij}$  are those presented previously in Ref. [39], and the hyperfine line strengths  $\mathcal{S}_{ij}$  are derived in a similar fashion as in Refs. [51,52]. The calculation of  $\mathcal{S}_{ij}$  involves hyperfine eigenvectors, which are obtained by diagonalization of an effective spin Hamiltonian [38]. Spin coefficients for  $v = 0, L = 0, \dots, 4$  are taken from [38], and extrapolation of these coefficients results in a set of spin coefficients for  $v = 0, L = 5$ . Likewise, the rate coefficients for stimulated emission and stimulated absorption are

$$B_{ij} = \frac{\pi^2 c^3}{\hbar \omega_{ij}^3} A_{ij} \quad (14)$$

and

$$B_{ji} = \frac{2J_i + 1}{2J_j + 1} B_{ij}, \quad (15)$$

respectively. After integrating Eq. (12) to obtain  $\rho_{\alpha L}(t)$  as a function of the REMPD duration  $t$ , the signal  $s(t)$  becomes

$$s(t) = \frac{\sum_{\alpha, L} \rho_{\alpha L}(0) - \rho_{\alpha L}(t)}{\sum_{\alpha, L} \rho_{\alpha L}(0)}. \quad (16)$$

Here, the initial distribution of populations  $\rho_{\alpha L}(0)$  is assumed to be a thermal distribution corresponding to the temperature of the BBR (which is assumed to be 300 K here).

We compute signal strengths for the conditions of Fig. 11, and for a laser linewidth of 10 Hz, for which the REMPD rate is about  $10 \text{ s}^{-1}$ . The result for the transition starting from the hyperfine level with  $(F, S, J) = (1, 2, 5)$  is shown in Fig. 12. Different time scales can be identified in the growth of  $s(t)$ . After 0.2 s, nearly all the population in the initial state  $(F, S, J) = (1, 2, 5)$  is dissociated, and the signal

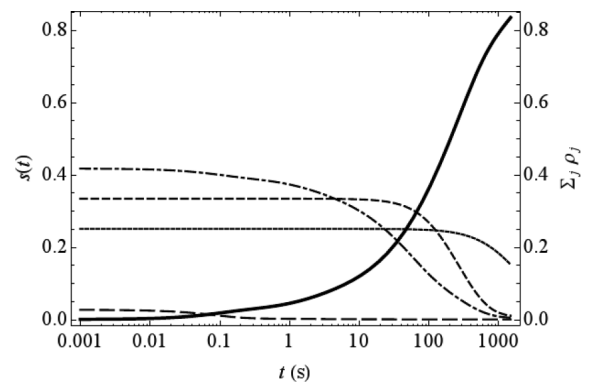


FIG. 12. Log-linear plot of the signal strength  $s(t)$  as a function of REMPD duration  $t$ , for two-photon transitions starting from the hyperfine state with  $(L, F, S, J) = (3, 1, 2, 5)$  (solid curve) in  $v = 0$ . Shown as well are populations of certain “spin classes” (rightmost vertical axis). Long-dashed curve, population in  $(L, F, S, J) = (3, 1, 2, 5)$ ; dash-dotted curve, sum over  $L, J$  of all population in states with  $F = 1, S = 2$ ; short-dashed curve, sum over  $L, S, J$  of all population in states with  $F = 1, S \neq 2$ ; dotted curve, sum over  $L, S, J$  of all population in states with  $F = 0$ .

corresponds to the initial hyperfine state population of 0.026. After  $t = 0.2$  s, BBR continues to replenish population from states with  $L \neq 3$  [and with primarily  $(F, S) = (1, 2)$ ] through allowed electric-dipole transitions. Transitions between states with equal  $F$  but different  $S$  are only allowed by virtue of hyperfine mixing and therefore are considerably weaker; transitions between states with different  $F$  are even less allowed. The former become important after  $t = 100$  s, when most  $\text{HD}^+$  ions with  $(F, S) = (1, 2)$  have been dissociated, whereas the latter start to dominate the dissociation dynamics only after  $t = 700$  s when most  $\text{HD}^+$  ions with  $F = 1$  have been depleted. The population dynamics are illustrated by the curves in Fig. 12.

For efficient data acquisition, it is important to find the optimum REMP duration. Figure 12 shows that longer durations lead to larger signals. On the other hand, shorter durations allow more data points to be acquired within a given amount of time,  $T_{\text{exp}}$ , which can be averaged to improve the signal-to-noise ratio. The optimum duration depends also on the overhead per data point (e.g., time needed to expunge the remaining  $\text{HD}^+$  ions from the trap, and reload a fresh sample of  $\text{HD}^+$  ions for the next REMP cycle). We define a figure of merit for the signal quality,  $\mathcal{L}$ , obtainable given a total time  $T_{\text{exp}}$ , REMP duration  $t$  and the overhead,  $t_{\text{oh}}$ , as follows. The number of experiments that can be done is  $N_{\text{exp}} = \lfloor T_{\text{exp}}/(t + t_{\text{oh}}) \rfloor$ , where  $\lfloor \cdot \rfloor$  denotes the floor. Assuming the signal-to-noise ratio improves as  $\sqrt{N_{\text{exp}}}$ , our figure of merit becomes

$$\mathcal{L}(t) = s(t)\sqrt{N_{\text{exp}}} = s(t)\sqrt{\lfloor T_{\text{exp}}/(t + t_{\text{oh}}) \rfloor}. \quad (17)$$

$\mathcal{L}(t)$  is plotted for  $T_{\text{exp}} = 3600$  s and for various values of  $t_{\text{oh}}$  in Fig. 13. Typically,  $t_{\text{oh}}$  is 30–60 s, for which we find an optimum REMP duration of  $\sim 100$  s. In this case, we find from Fig. 12 that about 35% of the  $\text{HD}^+$  ions are dissociated. We point out that this is much larger than the 1%–2% measurement noise observed by Koelemeij *et al.* [27]. A spectral line shape consisting of at least 20 data points may therefore be obtained with a good signal-to-noise ratio within the course of 1 h.

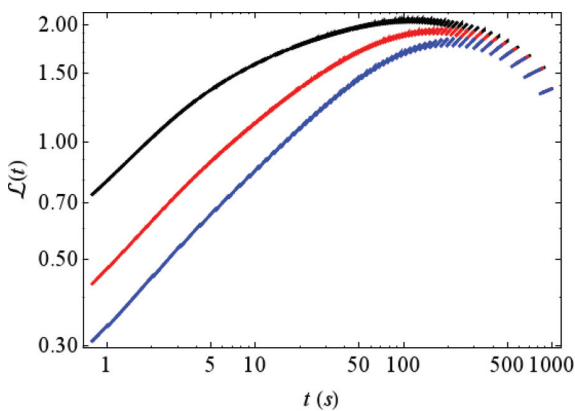


FIG. 13. (Color online) Figure-of-merit function  $\mathcal{L}$  as a function of REMP duration  $t$ , and for various values of the overhead  $t_{\text{oh}}$ .  $T_{\text{exp}} = 3600$  s. Uppermost black curve,  $t_{\text{oh}} = 10$  s; middle red curve,  $t_{\text{oh}} = 30$  s; lowermost blue curve,  $t_{\text{oh}} = 60$  s. In all cases, the optimum REMP duration is near 100 s.

## VI. CONCLUSION

We have shown that Doppler-free signals can be observed on trapped  $\text{HD}^+$  ions by nearly degenerate two-photon spectroscopy, taking advantage of a quasiharmonic three-level ladder in the rovibrational spectrum. The suppression of the Doppler effect, due to an effective Lamb-Dicke regime with respect to the simultaneous absorption of counterpropagating photons, opens the way to high-resolution spectroscopy at the natural width limit. Numerical simulations of the REMP signal, taking into account saturation effects, realistic ion trajectories and laser phase noise, allowed us to determine the optimal laser detunings, which are slightly larger than the single-photon Doppler width. In this large-detuning limit, the population of the intermediate state may be neglected, and a simplified model of the two-photon transition rate was shown to be in excellent agreement with our numerical results. Finally, BBR redistribution among rovibrational and hyperfine levels was taken into account to get realistic estimates of experimental signal strengths.

With the parameters used in the paper, the predicted linewidth of 350 Hz is dominated by power broadening. It may be reduced to about 100 Hz by using lower intensities, at the cost of a slight diminution of the signal-to-noise ratio. The line center may eventually be determined with about 5 Hz accuracy, corresponding to a relative accuracy of  $1 \times 10^{-14}$ . Other systematic effects such as quadrupolar shifts, light shifts by cooling and dissociation lasers, BBR shifts, Stark shifts due to stray electric fields and ac Zeeman shifts are estimated to be below  $10^{-15}$ , as discussed in a recent study [53].

Potential applications of the proposed spectroscopic method include improved tests of QED [19,20], an improved determination of the proton-to-electron mass ratio [22,23], as well as studies of its time variation [24] and searches for possible fifth forces [33].

For the rovibrational levels of  $\text{HD}^+$  selected in this study, the mismatch of the intermediate state is only 0.2% of the one-photon frequency, leading to a long effective wavelength  $\lambda_{\text{eff}} = 0.7$  mm. It is worth noting that the effective Lamb-Dicke regime could still be reached with significantly higher frequency mismatch, possibly up to 10% for excitation wavelengths in the micron range ( $\lambda_{\text{eff}} \sim 10 \mu\text{m}$ ). This means that the proposed method has potential for application to many other molecular (or even atomic) ions, since the existence of such quasicoincidences is quite probable in a rich rovibrational spectrum characterized by a quasiharmonic vibrational ladder. In the case of  $\text{HD}^+$ , two other promising transitions are worth pointing out:  $v = 0, L = 3$  to  $v = 12, L = 3$  via  $v = 5, L = 2$ , with wavelengths near  $1.18 \mu\text{m}$ , and  $v = 0, L = 4$  to  $v = 16, L = 4$  via  $v = 6, L = 3$  near  $1.01 \mu\text{m}$  [35]. Finally, the proposed method could also be extended to multiphoton transitions in a configuration where the laser wave vectors nearly add up to zero [54].

## ACKNOWLEDGMENTS

V.Q.T. would like to acknowledge Ile de France region for his Ph.D. grant. J.C.J.K. would like to acknowledge the Netherlands Organisation for Scientific Research (NWO) and the Dutch Foundation for Fundamental Research on Matter

TABLE I. Zeeman shift of the magnetic sublevels  $M_J = -J$  (upper lines) and  $M_J = J$  (lower lines) in a 0.02-G field (in kHz), for all hyperfine sublevels  $(F, S, J)$  of the rovibrational states involved in the two-photon transition under study. The most Zeeman-insensitive transitions are highlighted by bold characters.

$v$	$L$	$(F, S) = (0, 1)$			(1, 0)	(1, 1)			(1, 2)				
		$J = 4$	$J = 3$	$J = 2$	$J = 3$	$J = 4$	$J = 3$	$J = 2$	$J = 5$	$J = 4$	$J = 3$	$J = 2$	$J = 1$
0	3	6.8549	3.8100	-0.1054	17.8049	- <b>18.0662</b>	-18.6888	16.9358	- <b>27.9358</b>	-22.2457	-16.7916	-7.4441	<b>14.0003</b>
		-6.8564	-3.8111	0.1047	-17.8098	- <b>18.0652</b>	18.6893	-16.9470	<b>27.9358</b>	22.2423	16.7889	7.4388	- <b>14.0137</b>
9	3	6.1161	2.9767	-0.9929	14.5500	- <b>18.0820</b>	-16.3205	15.6554	- <b>27.9391</b>	-21.5026	-15.0863	-5.2879	<b>13.9928</b>
		-6.1179	-2.9776	0.9928	-14.5592	- <b>18.0807</b>	16.3231	-15.6716	<b>27.9391</b>	21.4959	15.0801	5.2771	- <b>14.0167</b>

(FOM) for support. The authors acknowledge the COST action MP1001 *Ion Traps for Tomorrow Applications* (IOTA).

### APPENDIX A: HD<sup>+</sup> ZEEMAN EFFECT

As discussed in Sec. II, it is preferable to address simultaneously all Zeeman components of the two-photon transition in order to get sufficiently large signals. In the Amsterdam experiment, a static  $B$  field is used to define a quantization axis and cool Be<sup>+</sup> ions with a single circularly polarized laser beam [34]. Experimental investigation showed that the minimal  $B$  field value that still enables efficient cooling is about 0.02 G. The Zeeman splitting of the two-photon transition in such a field thus sets a lower limit for the width of the line shape, which may be broadened as required by control of  $\Gamma_{\text{diss}}$  and the linewidth of the excitation lasers. It is therefore desirable to select a hyperfine component having a low Zeeman effect in order to minimize line broadening and maximize the two-photon transition rate for a given laser intensity. In view of this, it is important to evaluate the Zeeman splitting of the  $(v = 0, L = 3) \rightarrow (v = 9, L = 3)$  two-photon transition, accounting for the hyperfine structure, so as to (i) select the most promising hyperfine component and (ii) determine the optimal dissociation rate and laser linewidth accordingly.

Following the approach of Ref. [52], we write the effective spin Hamiltonian for an HD<sup>+</sup> ion in a rovibrational state  $(v, L)$ , with an external magnetic field  $\mathbf{B}$  oriented along the  $z$  axis,

$$H_{\text{eff}}^{\text{tot}} = H_{\text{eff}}^{\text{hfs}} + E_{10}(\mathbf{L} \cdot \mathbf{B}) + E_{11}(\mathbf{S}_p \cdot \mathbf{B}) + E_{12}(\mathbf{S}_d \cdot \mathbf{B}) + E_{13}(\mathbf{S}_e \cdot \mathbf{B}), \quad (\text{A1})$$

where  $H_{\text{eff}}^{\text{hfs}}$  is the effective spin Hamiltonian in the absence of magnetic field derived in [38], and

$$E_{10} = -\mu_B \sum_i \frac{Z_i m_e}{m_i} \frac{\langle vL || L || vL \rangle}{\sqrt{L(L+1)(2L+1)}}, \quad (\text{A2a})$$

$$E_{11} = -\frac{e\mu_p}{m_p c} = -4.2577 \text{ kHz G}^{-1}, \quad (\text{A2b})$$

$$E_{12} = -\frac{e\mu_d}{2m_d c} = -0.6539 \text{ kHz G}^{-1}, \quad (\text{A2c})$$

$$E_{13} = \frac{e\mu_e}{m_e c} = 2.8024953 \text{ MHz G}^{-1}, \quad (\text{A2d})$$

where 2010 CODATA values of fundamental constants were used. The value of  $E_{10}$  is calculated using nonrelativistic variational wave functions [55]. We obtain  $E_{10} = -0.55792 \text{ kHz G}^{-1}$  for the  $(v = 0, L = 3)$  level, in

agreement with Table 1 of [52], and  $E_{10} = -0.50281 \text{ kHz G}^{-1}$  for the  $(v = 9, L = 3)$  level.

In the presence of a magnetic field, the hyperfine states of HD<sup>+</sup> labeled with  $F$ ,  $S$ , and  $J$  (see Sec. II) are split into sublevels distinguished by the quantum number  $M_J$ . We diagonalize the Hamiltonian (A2) for  $M_J = \pm J$  and  $B = 0.02 \text{ G}$ , in order to obtain the Zeeman shifts  $\Delta E^{vLFSJM_J} = E^{vLFSJM_J}(B) - E^{vLFSJM_J}(0)$ . Results are given in Table I.

It appears that some of the hyperfine components connecting homologous spin states [i.e., states with the same  $(F, S, J)$ ] benefit from a strong cancellation of Zeeman shifts. This occurs for  $(F, S, J) = (1, 1, 4)$ ,  $(1, 2, 5)$ , and  $(1, 2, 1)$ , where the Zeeman splitting is, respectively, of 31.3, 6.6, and 4.5 Hz at 0.02 G. In the last two cases, the Zeeman structure is hidden within the natural linewidth of the transition and does not limit the resolution in any way. The most favorable component is  $(F, S, J) = (1, 2, 5)$  since this hyperfine level has the highest population, making it possible to get a stronger REMPD signal. There is only one dipole-allowed intermediate level for the two-photon transition, namely the  $(v = 4, L = 2)$ ,  $(F, S, J) = (1, 2, 4)$  level, so that the three-level approximation introduced in Sec. II is well justified in this case.

### APPENDIX B: TRAPPED ION DYNAMICS

In order to get a realistic description of the sympathetically cooled HD<sup>+</sup> ion velocities, we use a homemade simulation code taking into account the time-dependent trapping force, the Coulomb interaction, and the laser cooling process (recoil due to absorption and emission of individual photons) [56,57]. The laser-cooled ions are described as two-level atomic systems with a transition width  $\Gamma_{\text{Be}^+} = 19.4 \text{ MHz}$ .

We assume a perfect linear quadrupolar Paul trap geometry with  $r_0 = 3.5 \text{ mm}$ . The rf frequency  $\Omega_{\text{rf}}$  is  $2\pi \times 13.3 \text{ MHz}$  and the rf voltage amplitude is  $V_0 = 270 \text{ V}$ . The stability parameter for the radial confinement is  $q = 0.2$  for HD<sup>+</sup> and 0.067 for <sup>9</sup>Be<sup>+</sup>. A harmonic axial static potential provides axial confinement, with a trap frequency  $\omega_z/2\pi = 100 \text{ kHz}$  for Be<sup>+</sup> ions and 173 kHz for HD<sup>+</sup> ions. The Coulomb interaction between the ions, which is responsible for the sympathetic cooling, is taken into account without any approximations.

The Newton equations of motion are numerically integrated using a fixed-step leap-frog algorithm [58]. The time step  $\delta t = 2 \times 10^{-10} \text{ s}$  is chosen short enough to well represent the rf field, Coulomb collisions and laser absorption and emission cycles so as to get converged results for simulation times up to 20 ms.

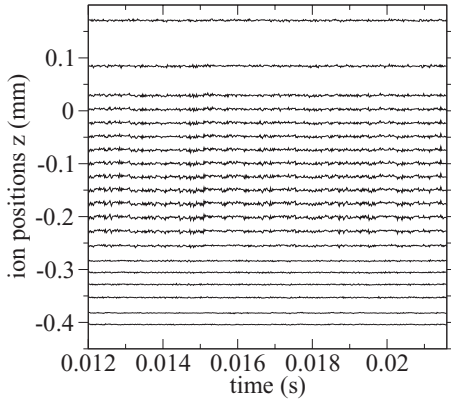


FIG. 14. Typical axial trajectories around their equilibrium position for 20 sympathetically cooled  $\text{HD}^+$  ions in a 400- $\text{Be}^+$ -ion Coulomb crystal. Laser cooling conditions: detuning,  $\delta_L = -\Gamma_{\text{Be}^+}$ ; saturation parameter,  $I/I_{\text{sat}} = 1.5$ .

The laser interaction is described in terms of absorption, spontaneous, or stimulated emission processes, thus including saturation effects. The laser beam has a wavelength  $\lambda = 313.13$  nm and a  $\text{TEM}_{00}$  Gaussian profile with a waist  $w_0 = 1$  mm much larger than the ion cloud size. It is assumed to be perfectly aligned with the trap axis. The laser intensity  $I$  and laser detuning  $\delta_L$  are chosen close to optimal cooling conditions ( $\delta_L = -\Gamma_{\text{Be}^+}$ , and  $I = I_{\text{sat}}/2$ , where  $I_{\text{sat}}$  is the saturation intensity). At each time step, and for each laser-cooled ion in the ground state, the absorption probability is evaluated at the ion location and compared to a uniform random number generator between 0 and 1. In case an absorption occurs, the ion velocity is altered by a kick  $\hbar\mathbf{k}/m$ , where  $\mathbf{k}$  is the photon wave vector. For laser-cooled ions in the excited state, the spontaneous (stimulated) emission is treated in a similar way but with a  $\hbar\mathbf{k}/m$  velocity kick with a uniformly randomized direction (a  $-\hbar\mathbf{k}/m$  velocity kick) [57,59].

A simulation is run in the following way. Ion position and velocities are randomized in a cylindrical volume around the trap center with a temperature  $T \approx 10$  K. During the first 0.2 ms of the simulation, a huge drag force is applied to reach the Coulomb crystal regime where each ion oscillates around an equilibrium position. Then, the laser interaction is turned on and the ion cloud relaxes to its equilibrium temperature which is usually reached after 0.8 ms. Ion positions and velocities, mean secular kinetic energies, potential, and Coulomb energies are periodically stored with a period of  $4 \times 10^{-8}$  s. With a pure sample of laser-cooled ions, we have checked that the ion cloud equilibrium temperature corresponds to the Doppler limit  $k_B T = \hbar\Gamma_{\text{Be}^+}/2$  in the optimal cooling conditions.

Figure 14 shows typical axial ( $z$  axis) trajectories for 20  $\text{HD}^+$  ions that are sympathetically cooled by 400  $\text{Be}^+$  ions. The ions are nearly equally spaced and shifted in the direction of the incoming  $\text{Be}^+$  cooling laser. The axial motion amplitude is in the  $\mu\text{m}$  range and the maximum axial velocities are of the order of 5 m/s. This gives a maximum Doppler effect  $v/\lambda \approx 3.5$  MHz at the wavelength of the two-photon excitation lasers  $\lambda = 1.44 \mu\text{m}$ . The Doppler shift is larger than the oscillation frequencies, indicating that in the ion rest frame, the ions see motional sidebands with high modulation indexes. Figure 15

shows the axial velocity spectrum for each ion. Depending on the ion position within the cloud, the ion motion can be close to a pure harmonic motion or have a complex spectrum. This explains why the REMPD signal has to be averaged over the different ion trajectories.

### APPENDIX C: TWO-PHOTON TRANSITION PROBABILITY

We here consider a trapped particle with a three-level internal structure, undergoing one-dimensional harmonic motion at frequency  $\Omega_{\text{vibr}}$ . The external degree of freedom is described quantum-mechanically and labeled by the vibrational quantum number  $n$ . Following time-dependent second-order perturbation theory, the two-photon transition rate between states  $|1, n_1\rangle$  and  $|3, n_3\rangle$  is given by

$$\Gamma_{2\text{ph}} = \left| \sum_{n_2=0}^{\infty} \frac{\Omega_{12}\Omega_{23}\langle n_3|e^{-ik'z}|n_2\rangle\langle n_2|e^{ikz}|n_1\rangle}{[\delta_{12} - i\frac{\Gamma_2}{2} + (n_1 - n_2)\Omega_{\text{vibr}}]} \right|^2 \times \frac{\Gamma_3^{\text{eff}}}{[\delta_{13} + (n_1 - n_3)\Omega_{\text{vibr}}]^2 + \frac{(\Gamma_3^{\text{eff}})^2}{4}}. \quad (\text{C1})$$

Assuming the detuning  $\delta_{12}$  is much larger than both the intermediate level width and the vibration frequency and summing over  $n_2$ , the first term in Eq. (C1) can be simplified, leading to

$$\Gamma_{2\text{ph}} = \frac{|\Omega_{12}\Omega_{23}\langle n_3|e^{i\delta k z}|n_1\rangle|^2}{\delta_{12}^2} \times \frac{\Gamma_3^{\text{eff}}}{[\delta_{13} + (n_1 - n_3)\Omega_{\text{vibr}}]^2 + \frac{(\Gamma_3^{\text{eff}})^2}{4}}. \quad (\text{C2})$$

The denominator of the second factor shows that the two-photon transition probability exhibits sidebands separated by  $\Omega_{\text{vibr}}$ . The amplitudes of the sidebands are given by the matrix element  $\langle n_3|e^{i\delta k z}|n_1\rangle$  [60–62] with

$$|\langle n+s|e^{i\eta(a+a^\dagger)}|n\rangle| = e^{-\eta^2/2} \eta^{|s|} \sqrt{\frac{n_{<}!}{n_{>}!}} L_{n_{<}}^{|s|}(\eta^2), \quad (\text{C3})$$

where  $n_{<}$  and  $n_{>}$  are the lesser and greater of  $n$  and  $n+s$ , and  $\eta = \delta k \sqrt{\hbar/(2m\Omega_{\text{vibr}})}$ .  $L_n^s$  are the generalized Laguerre polynomials, and  $a$  and  $a^\dagger$  are the annihilation and creation operators, respectively, associated with the harmonic confinement. In the Lamb-Dicke regime where the oscillation amplitude is much smaller than the effective wavelength  $2\pi/\delta k$ , this matrix element is  $\approx \delta_{n_1, n_3}$  and the two-photon rate further simplifies to

$$\Gamma_{2\text{ph}} = \frac{\Omega_{12}^2 \Omega_{23}^2}{\delta_{12}^2} \frac{\Gamma_3^{\text{eff}}}{\delta_{13}^2 + \frac{(\Gamma_3^{\text{eff}})^2}{4}}. \quad (\text{C4})$$

On two-photon resonance where  $\delta_{13} = 0$ , it is given by

$$\Gamma_{2\text{ph}} = \frac{\Omega_{12}^2 \Omega_{23}^2}{\delta_{12}^2} \frac{4}{\Gamma_3^{\text{eff}}}. \quad (\text{C5})$$

### APPENDIX D: LASER PHASE NOISE SIMULATION

In this appendix, we describe the phase noise generator we have implemented to simulate the laser Lorentzian line

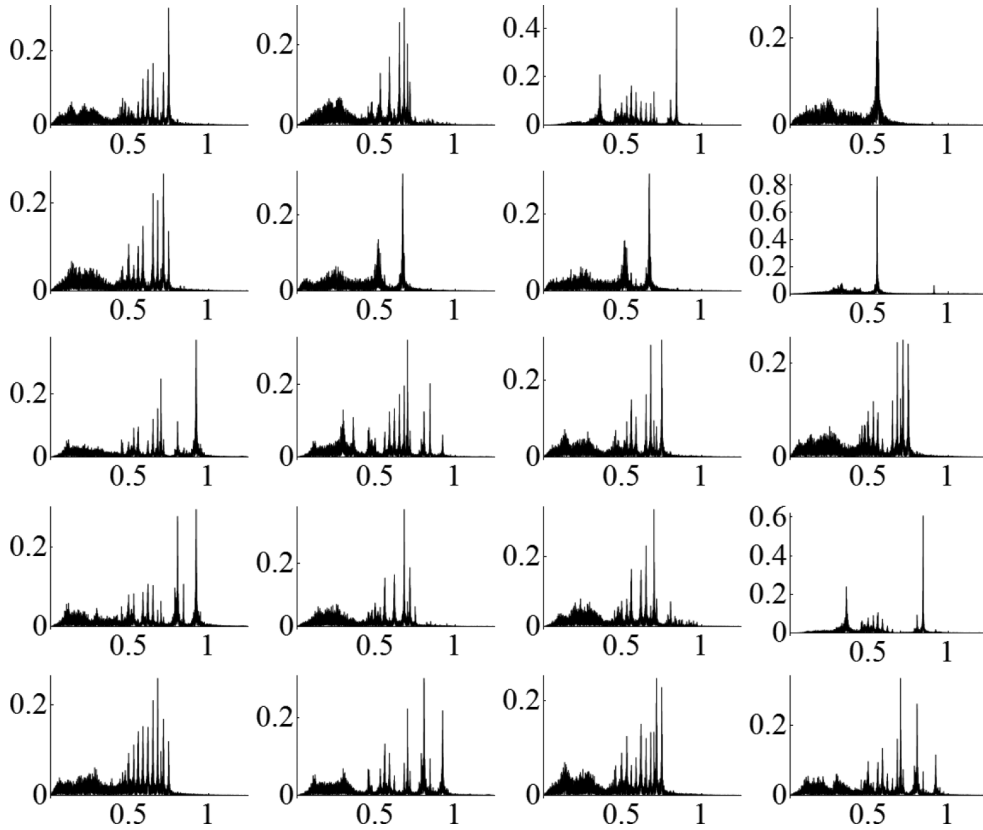


FIG. 15. Spectrum of the velocity amplitudes obtained by FFT from the trajectories shown in Fig. 14. Horizontal scale is in MHz, vertical scale is in (m/s)/ $\sqrt{\text{Hz}}$ .

shape. Let  $f(t)$  denote the instantaneous laser frequency, and  $\delta f$  the laser frequency noise. It is linked to the laser phase noise by  $\delta f = \frac{1}{2\pi} \frac{d\varphi(t)}{dt}$ . Laser phase noise  $\varphi(t)$  is usually depicted as a centered stationary Gaussian process with a white frequency noise (single sided) spectral density  $S_{\delta f}(\omega)$  in a bandwidth  $2\pi B$  [46]. The variance of the laser frequency noise is given by  $\langle(\delta f)^2\rangle = BS_{\delta f}(\omega)$ . The laser linewidth  $\Delta_{\text{FWHM}}$  is defined by the full width at half maximum of the hypothetical beat-note spectrum of the laser with a perfect noiseless laser. It can be expressed in an integral form as a function of  $S_{\delta f}(\omega)$  [46]. If  $\langle(\delta f)^2\rangle \ll B^2$ , the line shape is Lorentzian with  $\Delta_{\text{FWHM}} = \pi S_{\delta f}(\omega)$ . If  $\langle(\delta f)^2\rangle \gg B^2$ , the line shape is Gaussian with  $\Delta_{\text{FWHM}} = 2\sqrt{2 \ln 2} \sqrt{S_{\delta f} B}$ . For intermediate cases, the linewidth was evaluated by numerical computation of an integral, leading to an empirical interpolating formula [47],

$$\Delta_{\text{FWHM}} = S_{\delta f} \frac{\sqrt{8 \ln 2 B / S_{\delta f}}}{\left(1 + \frac{8 \ln 2 B}{\pi^2 S_{\delta f}}\right)^{1/4}}. \quad (\text{D1})$$

The frequency noise and phase noise spectral densities are linked by  $S_{\delta f}(\omega) = \left(\frac{\omega}{2\pi}\right)^2 S_{\varphi}(\omega)$  so a white frequency noise in a bandwidth  $B$  corresponds to a  $1/\omega^2$  phase noise spectral density with  $0 < \omega \leq 2\pi B$ . The Wiener-Khinchin theorem states that  $S_{\varphi}(\omega) = |\tilde{\varphi}(\omega)|^2$ , where  $\tilde{\varphi}$  is the Fourier transform of  $\varphi(t)$ . Therefore, the desired laser phase noise can be obtained

by randomly generating the Fourier components  $\tilde{\varphi}(\omega)$  and performing an inverse fast Fourier transform.

The discretization is done in the following way. The simulation duration  $T$  and the integration time step  $\delta t$  sets the number  $N = T/\delta t$  of  $\varphi$  values  $\varphi_j = \varphi(j\delta t)$ . It also sets the maximum Fourier frequency  $f_{\text{max}} = 1/2\delta t$  and the frequency resolution  $1/T$ . The corresponding Fourier frequencies and

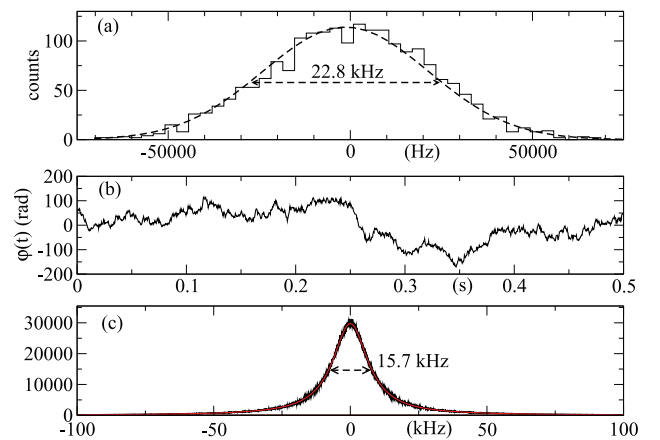


FIG. 16. (Color online) (a) Histogram of the instantaneous frequency  $f(t)$  at time  $t = 0$  for 2000 realizations of the phase noise. (b) a single realization of  $\varphi(t)$ . (c) Black, averaged laser line shape for the 2000 phase noise realizations. Red, Lorentzian fit.

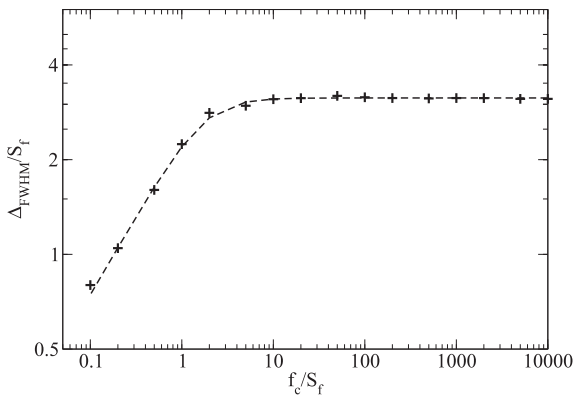


FIG. 17. Comparison of the laser FWHM (crosses) with the empirical formula (dashed line) given in Eq. (D1).

discretized Fourier components are  $\omega_j = 2\pi j/T$  and  $\tilde{\varphi}_j$ , with  $-N/2 \leq j \leq N/2$ . The maximum Fourier frequency has to be larger than the noise bandwidth, i.e.,  $B < \delta t/2$ . The phase noise discretized Fourier components are randomly generated following  $\tilde{\varphi}(\omega_j) = \frac{K}{\omega_j} e^{i\phi_j}$  for  $0 < j \leq BT$  and set to 0 for  $j = 0$  and  $BT < j \leq N/2$ . Since the phase noise is a real process, the negative frequency Fourier components are equal

to the positive ones; hence,  $\tilde{\varphi}_{-j} = \tilde{\varphi}_j^*$ . To generate a random phase noise, the complex argument of the Fourier components  $\phi_j$  is uniformly randomized between 0 and  $2\pi$ . The noise level  $K$  is linked to the variance of the laser frequency noise by  $K = \sqrt{S_{\delta f} f_{\max}}$ . Finally, the FFT of the phase noise components is computed using the FFTW3 FORTRAN subroutine library to obtain the time-dependent phase noise that is used by the OBE numerical solver.

Figure 16(a) shows the histogram of the instantaneous frequency  $f(t)$  obtained for 2000 realizations of the noise process with  $T = 0.5$  s,  $\delta t = 4 \times 10^{-7}$  s,  $S_{\delta f} = 5000$  Hz<sup>2</sup>/Hz, and  $B = 100$  kHz. A Gaussian fit gives a 22.8-kHz standard deviation in agreement with  $\sqrt{S_{\delta f} B} = 22.4$  kHz. Figure 16(b) shows a realization of  $\varphi(t)$  and Fig. 16(c) shows the average line shape of the beat note. The Lorentzian width is 15.7 kHz, in perfect agreement with  $\pi S_{\delta f}$ . We have varied the frequency noise spectral density  $S_{\delta f}$  from 10 to  $10^6$  Hz<sup>2</sup>/Hz and determined the FWHM of the line. Figure 17 shows that it follows the empirical formula and thus the expected linewidth behavior.

Finally, to generate laser phase noise with a Lorentzian line shape, one has to fulfill the conditions  $B \gg 6S_{\delta f}$  and choose  $S_{\delta f} = \Delta_{\text{FWHM}}/\pi$ , so the noise bandwidth must obey  $B \gg 6/\pi \Delta_{\text{FWHM}}$ .

- 
- [1] Ch. J. Bordé, C. R. Acad. Sc. Paris **271**, 371 (1970).  
 [2] P. W. Smith and T. W. Hänsch, *Phys. Rev. Lett.* **26**, 740 (1971).  
 [3] T. W. Hänsch, M. D. Levenson, and A. M. Schawlow, *Phys. Rev. Lett.* **27**, 707 (1971).  
 [4] L. S. Vasilenko, V. P. Chebotaev, and A. V. Shishaev, *Pis'ma Zh. Eksp. Teor. Fiz.* **12**, 161 (1970) [*JETP Lett.* **12**, 113 (1970)].  
 [5] B. Cagnac, G. Grynberg, and F. Biraben, *J. Phys. (Paris)* **34**, 845 (1973).  
 [6] F. Biraben, B. Cagnac, and G. Grynberg, *Phys. Rev. Lett.* **32**, 643 (1974).  
 [7] M. D. Levenson and N. Bloembergen, *Phys. Rev. Lett.* **32**, 645 (1974).  
 [8] J. E. Bjorkholm and P. F. Liao, *Phys. Rev. Lett.* **33**, 128 (1974).  
 [9] J. E. Bjorkholm and P. F. Liao, *Phys. Rev. A* **14**, 751 (1976).  
 [10] T. T. Grove, V. Sanchez-Villicana, B. C. Duncan, S. Maleki, and P. L. Gould, *Phys. Scr.* **52**, 271 (1995).  
 [11] E. N. Fortson, F. G. Major, and H. G. Dehmelt, *Phys. Rev. Lett.* **16**, 221 (1966).  
 [12] C. B. Richardson, K. B. Jefferts, and H. G. Dehmelt, *Phys. Rev.* **165**, 80 (1968).  
 [13] G. Werth, *Phys. Scr.*, T **59**, 206 (1995).  
 [14] P. T. H. Fisk, *Rep. Prog. Phys.* **60**, 761 (1997).  
 [15] E. A. Burt, W. A. Diener, and R. L. Tjoelker, *IEEE Trans. Ultrason. Ferroelectr. Freq. Control* **55**, 2586 (2008).  
 [16] Y.-Y. Jau, H. Partner, P. D. D. Schwindt, J. D. Prestage, J. R. Kellogg, and N. Yu, *Appl. Phys. Lett.* **101**, 253518 (2012).  
 [17] W. Neuhauser, M. Hohenstatt, P. Toschek, and H. Dehmelt, *Phys. Rev. Lett.* **41**, 233 (1978).  
 [18] J. C. Bergquist, W. M. Itano, and D. J. Wineland, *Phys. Rev. A* **36**, 428 (1987).  
 [19] V. I. Korobov, L. Hilico, and J.-Ph. Karr, *Phys. Rev. A* **79**, 012501 (2009).  
 [20] V. I. Korobov, L. Hilico, and J.-Ph. Karr, *Phys. Rev. A* **87**, 062506 (2013).  
 [21] A. Borschevsky, M. Ilias, V. A. Dzuba, K. Beloy, V. V. Flambaum, and P. Schwerdtfeger, *Phys. Rev. A* **86**, 050501 (2012).  
 [22] W. H. Wing, G. A. Ruff, W. E. Lamb, Jr., and J. J. Spezeski, *Phys. Rev. Lett.* **36**, 1488 (1976).  
 [23] B. Roth, J. Koelemeij, S. Schiller, L. Hilico, J.-Ph. Karr, V. I. Korobov, and D. Bakalov, in *Precision Physics of Simple Atoms and Molecules*, edited by S. Karshenboim, Lectures Notes in Physics, Vol. 745 (Springer-Verlag, Berlin, Heidelberg, 2008), p. 205.  
 [24] S. Schiller and V. I. Korobov, *Phys. Rev. A* **71**, 032505 (2005).  
 [25] V. V. Flambaum and M. G. Kozlov, *Phys. Rev. Lett.* **99**, 150801 (2007).  
 [26] A. Shelkovich, R. J. Butcher, C. Chardonnet, and A. Amy-Klein, *Phys. Rev. Lett.* **100**, 150801 (2008).  
 [27] J. C. J. Koelemeij, B. Roth, A. Wicht, I. Ernsting, and S. Schiller, *Phys. Rev. Lett.* **98**, 173002 (2007).  
 [28] U. Bressel, A. Borodin, J. Shen, M. Hansen, I. Ernsting, and S. Schiller, *Phys. Rev. Lett.* **108**, 183003 (2012).  
 [29] L. Hilico, N. Billy, B. Grémaud, and D. Delande, *J. Phys. B* **34**, 491 (2001).  
 [30] J.-Ph. Karr, S. Kilic, and L. Hilico, *J. Phys. B* **38**, 853 (2005).  
 [31] J.-Ph. Karr, F. Bielsa, A. Douillet, J. Pedregosa Gutierrez, V. I. Korobov, and L. Hilico, *Phys. Rev. A* **77**, 063410 (2008).  
 [32] P. J. Mohr, B. N. Taylor, and D. B. Newell, *Rev. Mod. Phys.* **84**, 1527 (2012).  
 [33] E. J. Salumbides, J. C. J. Koelemeij, J. Komasa, K. Pachucki, K. S. E. Eikema, and W. Ubachs, *Phys. Rev. D* **87**, 112008 (2013).

- [34] J. C. J. Koelemeij, D. W. E. Noom, D. de Jong, M. A. Haddad, and W. Ubachs, *Appl. Phys. B* **107**, 1075 (2012).
- [35] R. E. Moss, *Mol. Phys.* **78**, 371 (1993).
- [36] B. Roth, J. C. J. Koelemeij, H. Daerr, and S. Schiller, *Phys. Rev. A* **74**, 040501(R) (2006).
- [37] Z. Amitay, D. Zajfman, and P. Forck, *Phys. Rev. A* **50**, 2304 (1994).
- [38] D. Bakalov, V. I. Korobov, and S. Schiller, *Phys. Rev. Lett.* **97**, 243001 (2006).
- [39] J. C. J. Koelemeij, *Phys. Chem. Chem. Phys.* **13**, 18844 (2011).
- [40] M. Drewsen, I. Jensen, J. Lindballe, N. Nissen, R. Martinussen, A. Mortensen, P. Staantum, and D. Voigt, *Int. J. Mass Spectrom.* **229**, 83 (2003).
- [41] P. Blythe, B. Roth, U. Frohlich, H. Wenz, and S. Schiller, *Phys. Rev. Lett.* **95**, 183002 (2005).
- [42] J. C. J. Koelemeij, B. Roth, and S. Schiller, *Phys. Rev. A* **76**, 023413 (2007).
- [43] T. Hänsch and P. Toschek, *Z. Phys.* **236**, 213 (1970).
- [44] P. F. Liao and J. E. Bjorkholm, *Phys. Rev. Lett.* **34**, 1 (1975).
- [45] R. Salomaa, *J. Phys. B* **10**, 3005 (1977).
- [46] D. S. Elliott, R. Roy, and S. J. Smith, *Phys. Rev. A* **26**, 12 (1982).
- [47] G. Di Domenico, S. Schilt, and P. Thomann, *Appl. Opt.* **49**, 4801 (2010).
- [48] B. R. Mollow, *Phys. Rev.* **175**, 1555 (1968).
- [49] D. J. Berkeland, J. D. Miller, J. C. Bergquist, W. M. Itano, and D. J. Wineland, *J. Appl. Phys.* **83**, 5025 (1998).
- [50] K. Pyka, N. Herschbach, J. Keller, and T. E. Mehlstäubler, *Appl. Phys. B* (2013), doi: 10.1007/s00340-013-5580-5.
- [51] J. J. Spezeski, Ph.D. thesis, Yale University, 1977.
- [52] D. Bakalov, V. I. Korobov, and S. Schiller, *J. Phys. B* **44**, 025003 (2011).
- [53] D. Bakalov and S. Schiller [Appl. Phys. B (to be published)].
- [54] F. Biraben, G. Grynberg, M. Bassini, and B. Cagnac, *Phys. Rev. Lett.* **37**, 283 (1976).
- [55] J.-Ph. Karr, V. I. Korobov, and L. Hilico, *Phys. Rev. A* **77**, 062507 (2008).
- [56] S. Schiller and C. Lämmerzahl, *Phys. Rev. A* **68**, 053406 (2003).
- [57] J. B. Wübbena, S. Amairi, O. Mandel, and P. O. Schmidt, *Phys. Rev. A* **85**, 043412 (2012).
- [58] L. Verlet, *Phys. Rev.* **159**, 98 (1967).
- [59] B. Cagnac and J. C. Pebay-Peroula, *Physique Atomique* (Dunod, Paris, 1982), Tome 2.
- [60] D. Leibfried, R. Blatt, C. Monroe, and D. J. Wineland, *Rev. Mod. Phys.* **75**, 281 (2003).
- [61] D. J. Wineland and W. M. Itano, *Phys. Rev. A* **20**, 1521 (1979).
- [62] K. E. Cahill and R. J. Glauber, *Phys. Rev.* **177**, 1857 (1969).

## 3.2 Complementary informations to the article

### 3.2.1 Hyperfine structure of two-photon transition

The more complete picture of two-photon transition can be shown as in Fig.3.2. The electric dipole-allowed transition don't change the spin states, therefore we have the selection rules :  $\Delta S = 0$  and  $\Delta F = 0$ . The two-photon transitions between two rovibrational state  $(\nu, L) = (0, 3)$  and  $(\nu', L') = (9, 3)$  can be divided into four groups corresponding to  $(F, S) : \{(0, 1), (1, 0), (1, 1), (1, 2)\}$ .

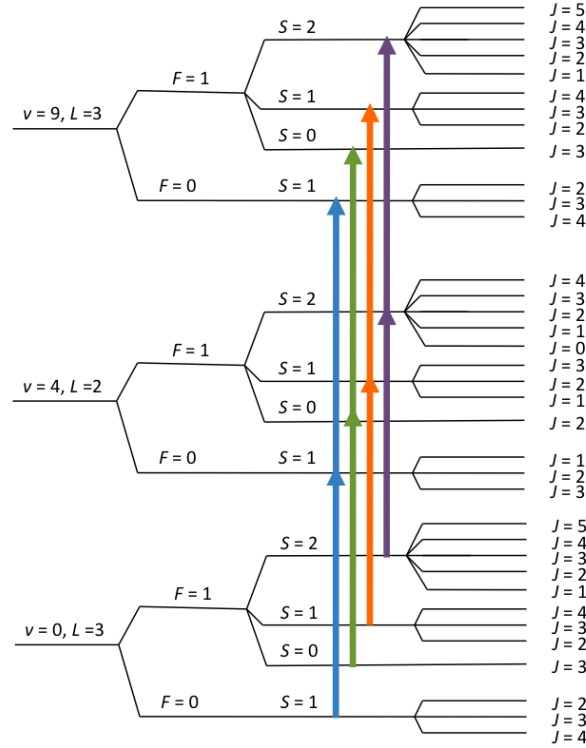


Figure 3.2: Four groups of two-photon transition corresponding to  $(F, S) : \{(0, 1), (1, 0), (1, 1), (1, 2)\}$ .

The Zeeman splitting is also an important factor of this experiment. The laser cooling of  $\text{Be}^+$  ions requires a magnetic field for the definition of quantification axis. The magnetic field strength must be controlled so that the population of all Zeeman substates will be excited by the laser field. In the experiment at Amsterdam, the values of magnetic field strength can be reduced to  $\sim 20$  mG. And the Zeeman splitting corresponding to this value is 10 Hz. Supposing that the laser linewidth is larger than the Zeeman splitting, then all Zeeman substates will be excited by laser field and the contributions of different substates are considered equivalent. In the numerical calculation we omit this Zeeman substates and we will return to this after the theoretical treatment.

### 3.2.2 Physical interpretation of Bloch equations

:

First of all, when talking about two-photon transition for  $|1\rangle$  to  $|3\rangle$ , we should distinguish two possibilities :

1. The ion absorbs the first photon  $\omega$  for the transition from  $|1\rangle$  to  $|2\rangle$ , then it will absorb the second photon  $\omega'$  for the transition from  $|2\rangle$  to  $|3\rangle$ . The state  $|2\rangle$  is populated ( by  $\omega$ ) and depopulated by  $\omega'$  ( we suppose that there is no saturation). This two-photon transition is called "sequential transition".

2. The ion absorbs simultaneously two photon  $\omega$  and  $\omega'$  for the transition from  $|1\rangle$  to  $|3\rangle$  without populating the intermediate state  $|2\rangle$ . This transition is called "direct two-photon transition" or "two-photon transition" if it's not necessary to distinguish with the "sequential transition".

The influence of the sequential transition and direct two-photon transition on the REMPD signal depends on the detuning  $\delta_{12}$ . If the detuning  $\delta_{12} \lesssim \Gamma_2$ , the sequential transition will dominate but if  $\delta_{12} \gg \Gamma_2$ , then the direct two-photon transition dominates.

The negative value of trace of  $\rho(\mathbf{r}, t)$  implies all the populations in the level  $|1\rangle$ ,  $|2\rangle$ ,  $|3\rangle$  will disappear after a while to the fictive state  $|4\rangle$  or other states of  $\text{HD}^+$ . The appearance of  $\mathbf{k}\dot{\mathbf{r}}$  and  $\mathbf{k}'\dot{\mathbf{r}}'$  in the previous system of differential equations represents the Doppler effect. The coherent relaxation term  $\rho_{13}(t)$  is responsible for the direct two-photon excitation. If  $\mathbf{k} + \mathbf{k}' = 0$ , the equation of evolution of  $\rho_{13}$  is independent of ion velocity, the two-photon signal is now Doppler-free. But the problem of our interest is : if  $\mathbf{k} + \mathbf{k}' \approx 0$ , the ion motion is considered as a pure harmonic oscillation i.e  $\dot{\mathbf{r}}(t) = \mathbf{v}_{max} \cos(\Omega_{vib}t)$ , can we obtain the Doppler-free REMPD signal ?

### 3.2.3 Molecular Dynamics simulation of trapped $\text{HD}^+$ ions :

We will use the molecular dynamics (MD) simulations to obtain a more realistic description of trajectories, velocities, ... of  $\text{HD}^+$  ions. The data from this MD simulations will be used for the realistic treatment of the REMPD signal.

The idea of the MD simulation is to solve numerically the second Newton's equation for  $N_{SC}$  sympathetically cooled ions and  $N_{LC}$  laser-cooled ions taking into account the actual trap forces and Coulomb repulsion.

$$m_k \frac{d^2}{dt^2} \mathbf{r}_k = \mathbf{F}_k(\mathbf{r}_1, \dots, \mathbf{r}_N, \mathbf{v}_1, \dots, \mathbf{v}_N, t) ,$$

where  $N = N_{SC} + N_{LC}$ ,  $k = 1, \dots, N$  and

$$\mathbf{F}_k = \mathbf{F}_k^{trap} + \mathbf{F}_k^{Coulomb} + \mathbf{F}_k^{laser} ,$$

with  $\mathbf{F}_k^{trap}$  is the time-dependent trapping force given by

$$\mathbf{F}_k^{trap}(x, y, z, t) = \frac{q_k}{d^2} (U_0 + V_0 \cos(\Omega_{vib}t)) (-x\hat{\mathbf{x}} + y\hat{\mathbf{y}}) + \frac{1}{2} m_k \omega_z^2 (x\hat{\mathbf{x}} + y\hat{\mathbf{y}} - 2z\hat{\mathbf{z}}) .$$

The Coulomb force  $\mathbf{F}_k^{Coulomb}$  which is responsible for the sympathetic cooling of  $\text{HD}^+$

$$\mathbf{F}_k^{Coulomb} = \sum_{\substack{j=1 \\ j \neq k}}^N \frac{e^2}{4\pi\epsilon_0} \frac{\mathbf{r}_k - \mathbf{r}_j}{|\mathbf{r}_k - \mathbf{r}_j|^3},$$

and the laser force which is responsible for the cooling of Be<sup>+</sup> ions is modeled in terms of absorption, spontaneous or stimulated emission processes including saturation effects. This force can be interpreted in two different ways : one by the drag force  $\mathbf{F}_k^{laser} = -\alpha\mathbf{v}_k$  and another by a stochastic process where the absorption, spontaneous emission and stimulated emission process at each time step occurs with the probabilities given by Einstein equations of radiation and these processes will change the ion velocity a quantity  $\hbar\mathbf{k}/m$  where  $\mathbf{k}$  is the wave vector of photon.

The second Newton's equation for the system of  $N$  ions can be rewritten in the following form :

$$\frac{d}{dt}\mathbf{V} = \mathbf{F},$$

where  $\mathbf{V} = (V_1, V_2, \dots, V_N)^t$  with  $V_k = (x_k, y_k, z_k, v_{kx}, v_{ky}, v_{kz})^t$  and  $\mathbf{F} = (F_1, F_2, \dots, F_N)^t$  with  $F_k = (v_{kx}, v_{ky}, v_{kz}, F_{kx}, F_{ky}, F_{kz})^t$ .

This first order differential equation can be solved numerically using 4<sup>th</sup> order Runge-Kutta method or fixed step leap-frog method.

Temperature is a very important parameter to characterize the ion clouds inside the ion trap. This temperature  $T$  is also called "secular" temperature because it is defined from the secular energy  $E_{secular}$  of the ion cloud :

$$E_{secular} = \frac{3}{2}k_B T = \frac{1}{2} \sum_{k=1}^N m_k (\langle v_{kx}^2 \rangle + \langle v_{ky}^2 \rangle + \langle v_{kz}^2 \rangle),$$

where  $\langle \dots \rangle$  denotes the time average over one period of RF field.

In the mixed Coulomb crystal constituted by Be<sup>+</sup> and HD<sup>+</sup> ions, the temperatures of each species are not necessarily the same. We then need to define the temperatures of Be<sup>+</sup> ions and that of HD<sup>+</sup> ions as follows:

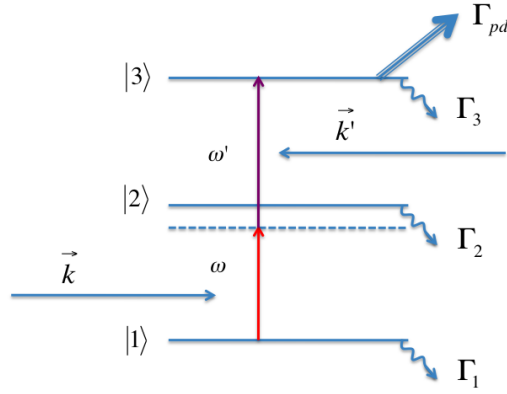
$$T_{Be^+} = \frac{m_{Be^+}}{3k_B} \sum_{k=1}^{N_{Be^+}} (\langle v_{kx}^2 \rangle + \langle v_{ky}^2 \rangle + \langle v_{kz}^2 \rangle),$$

$$T_{HD^+} = \frac{m_{HD^+}}{3k_B} \sum_{k=1}^{N_{HD^+}} (\langle v_{kx}^2 \rangle + \langle v_{ky}^2 \rangle + \langle v_{kz}^2 \rangle).$$

### 3.2.4 Dressed atom approach

In this section, we propose a different approach of this problem. The idea of these calculations was based on the previous work of B. Cagnac et al. [105] which is valid for the gas phase. Now we will generalize this calculations for the systems of strongly confined particles.

We consider a three-level system  $|1\rangle, |2\rangle, |3\rangle$  with the natural linewidth  $\Gamma_1, \Gamma_2, \Gamma_3^{eff} = \Gamma_3 + \Gamma_{pd}$  respectively interacting with two photon  $(\omega, \vec{k})$  et  $(\omega', \vec{k}')$  as depicted in Fig. 3.3.

Figure 3.3: Schema of the three-level ion  $\text{HD}^+$  with two lasers

In our problem, three systems are present : lasers, ion  $\text{HD}^+$  and vacuum. The coupling between the ion  $\text{HD}^+$  and the vacuum leads to spontaneous emission. This effect is taken into account by adding the imaging part  $\frac{1}{2}i\Gamma_j$  to each level energy  $E_j$  ( $j = 1, 2, 3$ ). Because  $\Gamma_1 \ll \Gamma_2, \Gamma_3$ , we can omit  $\Gamma_1$  in our calculations. With these assumptions, we only need to consider the interaction between the lasers and the  $\text{HD}^+$  ion. We suppose that the laser with  $\omega$  are responsible only for the transition between level 1 and 2 and the laser with  $\omega'$  for level |2> and |3>. Ion's motion is considered be an harmonic oscillation along  $z$  axis at frequency  $\Omega_{vib}$ . It's equivalent to say that the ion  $\text{HD}^+$  is trapped in a harmonic potential  $\frac{1}{2}m\Omega_{vib}^2 z^2$  with  $m$  is the mass of  $\text{HD}^+$ .

The total hamiltonian of the system  $\{\text{HD}^+ + \omega + \omega'\}$  is :

$$H = H_0 + V_{IL} + V'_{IL} = H_{ion}^{internal} + H_{ion}^{external} + H_L + H'_L + V_{IL} + V'_{IL} ,$$

where :

The internal and external hamiltonian of  $\text{HD}^+$  are:

$$H_{ion}^{internal} = E_1|1\rangle\langle 1| + (E_2 + \frac{1}{2}i\hbar\Gamma_2)|2\rangle\langle 2| + (E_3 + \frac{1}{2}i\hbar\Gamma_3^{eff})|3\rangle\langle 3| ,$$

and,

$$H_{ion}^{external} = \frac{\vec{P}_z^2}{2m} + \frac{1}{2}m\Omega_{vib}^2 z^2 .$$

The hamiltonian of two monomode laser fields are :

$$H_L = \hbar\omega\hat{a}^\dagger\hat{a} \text{ and } H'_L = \hbar\omega'\hat{a}'^\dagger\hat{a}' .$$

and the couplings between two lasers and  $\text{HD}^+$  is:

$$V_{IL} = -\vec{D}\vec{E}_L \text{ and } V'_{IL} = -\vec{D}'\vec{E}'_L .$$

with  $\vec{D}$  and  $\vec{D}'$  the electric dipole moment,  $E_L$  and  $E'_L$  the electromagnetic field. The expressions for the electric dipole moment and the quantized form of these fields are written as following:

$$\vec{D} = \vec{d}|2\rangle\langle 1| + h.c \text{ and } \vec{D}' = \vec{d}'|3\rangle\langle 2| + h.c ,$$

$$\vec{E}_L = E_L \vec{\epsilon} \hat{e}^{i\vec{k}\vec{r}} + h.c \text{ and } \vec{E}'_L = E'_L \vec{\epsilon}' \hat{e}'^{i\vec{k}'\vec{r}} + h.c ,$$

where the amplitudes of these fields  $E_L = i\sqrt{\frac{\hbar\omega}{2\epsilon_0 L^3}}$  and  $E'_L = i\sqrt{\frac{\hbar\omega'}{2\epsilon_0 L^3}}$ , then

$$V_{IL} = -\vec{D}\vec{E}_L \approx (-\vec{d}\vec{\epsilon}E_L)|2\rangle\langle 1|\hat{a}e^{ikz} + h.c = i\alpha_{12}|2\rangle\langle 1|\hat{a}e^{ikz} + h.c ,$$

$$V'_{IL} = -\vec{D}'\vec{E}'_L \approx (-\vec{d}'\vec{\epsilon}'E'_L)|3\rangle\langle 2|\hat{a}'e^{-ik'z} + h.c = i\alpha'_{23}|3\rangle\langle 2|\hat{a}'e^{-ik'z} + h.c .$$

We can rewrite the external hamiltonian of the ion  $\text{HD}^+$  as :

$$H_{ion}^{external} = \hbar\Omega_{vib}(\hat{a}_\nu^\dagger \hat{a}_\nu + \frac{1}{2}) .$$

We suppose the laser fields with  $\omega$  and  $\omega'$  have  $n$  and  $n'$  photons respectively, so :

$$H_L|n\rangle = (n + \frac{1}{2})\hbar\omega|n\rangle \text{ and } H'_L|n'\rangle = (n' + \frac{1}{2})\hbar\omega'|n'\rangle ,$$

and for  $H_{ion}^{external}$  we also have :

$$H_{ion}^{external}|\nu\rangle = (\nu + \frac{1}{2})\hbar\Omega_{vib}|\nu\rangle .$$

The eigenstate of  $H_0$  is  $|j\rangle|n_j\rangle|n'_j\rangle|\nu_j\rangle$  or simply  $|j, n_j, n'_j, \nu_j\rangle$  with eigenenergy :

$$E_j^{total} = E_j + \frac{1}{2}i\hbar\Gamma_j + (n_j + \frac{1}{2})\hbar\omega + (n'_j + \frac{1}{2})\hbar\omega' + (\nu_j + \frac{1}{2})\hbar\Omega_{vib} ,$$

with  $j = 1, 2, 3; n, n', \nu \in \mathbb{N}$  ( $\Gamma_1$  is supposed to be negligible)

### 3.2.4.1 Two-photon rate

To obtain the two-photon rate, we calculate the eigenstate  $\overline{|1, n_1, n'_1, \nu_1\rangle}$  of  $H$  by using the perturbation theory up to the second order.

$$\overline{|1, n_1, n'_1, \nu_1\rangle} = |1, n_1, n'_1, \nu_1\rangle + \sum_{\nu_2=0}^{\infty} A_{\nu_2}|2, n_1 - 1, n'_1, \nu_2\rangle + \sum_{\nu_3=0}^{\infty} \sum_{\nu_2=0}^{\infty} B_{\nu_2\nu_3}|3, n_1 - 1, n'_1 - 1, \nu_3\rangle ,$$

with

$$A_{\nu_2} = \frac{i\alpha_{12}\sqrt{n_1}\langle \nu_2|e^{ikz}|\nu_1\rangle}{\delta_{12} - i\frac{\Gamma_2}{2} + (\nu_1 - \nu_2)\Omega_{vib}} ,$$

and

$$B_{\nu_2\nu_3} = -\frac{\alpha_{12}\alpha_{23}\sqrt{n_1 n'_1}\langle \nu_3|e^{-ik'z}|\nu_2\rangle\langle \nu_2|e^{ikz}|\nu_1\rangle}{(\delta_{12} - i\frac{\Gamma_2}{2} + (\nu_1 - \nu_2)\Omega_{vib})(\delta_{13} - i\frac{\Gamma_3^{eff}}{2} + (\nu_1 - \nu_3)\Omega_{vib})} .$$

So the probability for a system in the state  $\overline{|1, n_1, n'_1, \nu_1\rangle}$  to appear in the level  $|3\rangle$  (for fixed values of  $\nu_1$  and  $\nu_3$ ) is :

$$p_{13} = \left| \sum_{\nu_2=0}^{\infty} B_{\nu_2\nu_3} \right|^2 .$$

The probability per unit of time for a system in the state  $|3\rangle$  disappears is  $\Gamma_3^{eff}$ , so the two-photon rate is :

$$\Gamma_{2ph} \approx p_{13} \Gamma_3^{eff} = \left| \sum_{\nu_2=0}^{\infty} \frac{\alpha_{12} \alpha_{23} \sqrt{n_1 n'_1} \langle \nu_3 | e^{-ik'z} | \nu_2 \rangle \langle \nu_2 | e^{ikz} | \nu_1 \rangle}{(\delta_{12} - i\frac{\Gamma_2}{2} + (\nu_1 - \nu_2)\Omega_{vib})(\delta_{13} - i\frac{\Gamma_3^{eff}}{2} + (\nu_1 - \nu_3)\Omega_{vib})} \right|^2 \Gamma_3^{eff} .$$

In the numerical simulation, we use the classical form of laser fields

$$\vec{E}_L = E_L \vec{e} e^{-i(\omega t - \vec{k}\vec{r})} + c.c ,$$

$$\vec{E}'_L = E'_L \vec{e}' e^{-i(\omega' t - \vec{k}'\vec{r})} + c.c .$$

So the Rabi frequency is defined as  $\Omega_{12} = \frac{dE_L}{\hbar}$ ,  $\Omega_{23} = \frac{d'E'_L}{\hbar}$ . The laser intensity is given by  $I = \frac{1}{2}c\epsilon_0(2E_L)^2 = 2c\epsilon_0(E_L)^2$ , but we also have  $I = \frac{P}{L^2}$  with  $P$  is laser power, we can deduce the total number of photon  $n$  as :

$$n\hbar\omega = L^3 \frac{P}{L^2 c} = 2\epsilon_0 E_L^2 L^3 ,$$

then, we have

$$\alpha_{12} \sqrt{n} = (-\vec{d}\vec{e}) \sqrt{\frac{n\hbar\omega}{2\epsilon_0 L^3}} = (-\vec{d}\vec{e}) E_L = \Omega_{12} .$$

And in the same way, we also have

$$\alpha_{23} \sqrt{n'} = (-\vec{d}'\vec{e}') E'_L = \Omega_{23} .$$

We can rewrite the two-photon rate as

$$\Gamma_{2ph} = \left| \sum_{\nu_2=0}^{\infty} \frac{\Omega_{12} \Omega_{23} \langle \nu_3 | e^{-ik'z} | \nu_2 \rangle \langle \nu_2 | e^{ikz} | \nu_1 \rangle}{(\delta_{12} - i\frac{\Gamma_2}{2} + (\nu_1 - \nu_2)\Omega_{vib})} \right|^2 \frac{\Gamma_3^{eff}}{(\delta_{13} + (\nu_1 - \nu_3)\Omega_{vib})^2 + \frac{(\Gamma_3^{eff})^2}{4}} .$$

If  $|\delta_{12}| \gg \Omega_{vib}$  we can simplify the formula of  $\Gamma_{2ph}$  as (using  $\sum_{\nu_2=0}^{\infty} |\nu_2\rangle \langle \nu_2| = \mathbb{I}$ ) :

$$\Gamma_{2ph} = \frac{|\Omega_{12} \Omega_{23} \langle \nu_3 | e^{i\delta kz} | \nu_1 \rangle|^2}{\delta_{12}^2} \frac{\Gamma_3^{eff}}{(\delta_{13} + (\nu_1 - \nu_3)\Omega_{vib})^2 + \frac{(\Gamma_3^{eff})^2}{4}} .$$

So we can observe a series of sidebands regularly separated by  $\Omega_{vib}$

In the Lamb-Dicke regime, we have  $\langle \nu_3 | e^{i\delta kz} | \nu_1 \rangle = \delta_{\nu_3\nu_1}$  leading to:

$$\Gamma_{2ph} = \frac{\Omega_{12}^2 \Omega_{23}^2}{\delta_{12}^2} \frac{\Gamma_3^{eff}}{\delta_{13}^2 + \frac{(\Gamma_3^{eff})^2}{4}} .$$

We observe only the central signal and the Doppler effect is completely suppressed.

### 3.2.4.2 ac Stark shift

We use again the second order perturbation theory to calculate the energy  $\overline{E}_j^{total}$  of level  $|j, n_j, n'_j, \nu_j\rangle$  ( $j=1,2,3$ ). The direct calculations give us the energy  $\overline{E}_j^{total}$  and from that we can deduce the ac Stark shift of level  $|j\rangle$  due to the interactions with laser fields.

- ac Stark shift of level  $|1\rangle$ :

$$\begin{aligned} \delta E_1 &:= \overline{E}_1^{total} - E_1^{total} \\ &= \sum_{k \neq 1} \sum_{n_k} \sum_{n'_k} \sum_{\nu_k} \frac{|\langle k, n_k, n'_k, \nu_k | V_{IL} + V'_{IL} | 1, n_1, n'_1, \nu_1 \rangle|^2}{E_1^{total} - E_k^{total}} \\ &= \sum_{\nu_2} \frac{\hbar |\Omega_{12}|^2 \langle \nu_1 | e^{-ikz} | \nu_2 \rangle \langle \nu_2 | e^{ikz} | \nu_1 \rangle}{\delta_{12} - \frac{1}{2} i \Gamma_2 + (\nu_1 - \nu_2) \Omega_{vib}} \\ &\underset{|\delta_{12}| \gg \Omega_{vib}}{\approx} \frac{|\Omega_{12}|^2}{\hbar \delta_{12}}. \end{aligned}$$

- ac Stark shift of level  $|2\rangle$ :

$$\begin{aligned} \delta E_2 &:= \overline{E}_2^{total} - E_2^{total} \\ &= \sum_{k \neq 2} \sum_{n_k} \sum_{n'_k} \sum_{\nu_k} \frac{|\langle k, n_k, n'_k, \nu_k | V_{IL} + V'_{IL} | 2, n_2, n'_2, \nu_2 \rangle|^2}{E_2^{total} - E_k^{total}} \\ &= \sum_{\nu_3} \frac{\hbar |\Omega_{23}|^2 \langle \nu_2 | e^{ik'z} | \nu_3 \rangle \langle \nu_3 | e^{-ik'z} | \nu_2 \rangle}{\delta_{23} + \frac{1}{2} i (\Gamma_2 - \Gamma_3) + (\nu_2 - \nu_3) \Omega_{vib}} + \sum_{\nu_1} \frac{\hbar |\Omega_{12}|^2 \langle \nu_2 | e^{ikz} | \nu_1 \rangle \langle \nu_1 | e^{-ikz} | \nu_2 \rangle}{-\delta_{12} + \frac{1}{2} i \Gamma_2 + (\nu_2 - \nu_1) \Omega_{vib}} \\ &\underset{|\delta_{12}| \gg \Omega_{vib}}{\approx} \frac{\hbar |\Omega_{23}|^2}{\delta_{23}} - \frac{\hbar |\Omega_{12}|^2}{\delta_{12}}. \end{aligned}$$

- ac Stark shift of level  $|3\rangle$ :

$$\begin{aligned} \delta E_3 &:= \overline{E}_3^{total} - E_3^{total} \\ &= \sum_{k \neq 3} \sum_{n_k} \sum_{n'_k} \sum_{\nu_k} \frac{|\langle k, n_k, n'_k, \nu_k | V_{IL} + V'_{IL} | 3, n_3, n'_3, \nu_3 \rangle|^2}{E_3^{total} - E_k^{total}} \\ &= \sum_{\nu_2} \frac{\hbar |\Omega_{23}|^2 \langle \nu_3 | e^{-ik'z} | \nu_2 \rangle \langle \nu_2 | e^{ik'z} | \nu_3 \rangle}{-\delta_{23} + \frac{1}{2} i (\Gamma_3 - \Gamma_2) + (\nu_3 - \nu_2) \Omega_{vib}} \\ &\underset{|\delta_{23}| \gg \Omega_{vib}}{\approx} -\hbar \frac{\Omega_{23}^2}{\delta_{23}}. \end{aligned}$$

*Remarks :*

All the calculations presented above are valid only for the case when  $\delta_{12} \gg \Omega_{vib}$  and  $\Gamma_{2ph} \ll \Gamma_3^{eff}$

### 3.2.5 Comparison of two approaches

In this section, we give some of the numerical results to confirm the validity of the theoretical calculations. They were obtained from the numerical resolution of the optical Bloch equations as described previously.

Figure 3.4 compares the results for  $\Gamma_{2ph}$  obtained from two different approaches : numerical calculation with optical Bloch equation and analytical calculation with dressed atom method as a function of  $(\Omega_{12}\Omega_{23})^2$  :

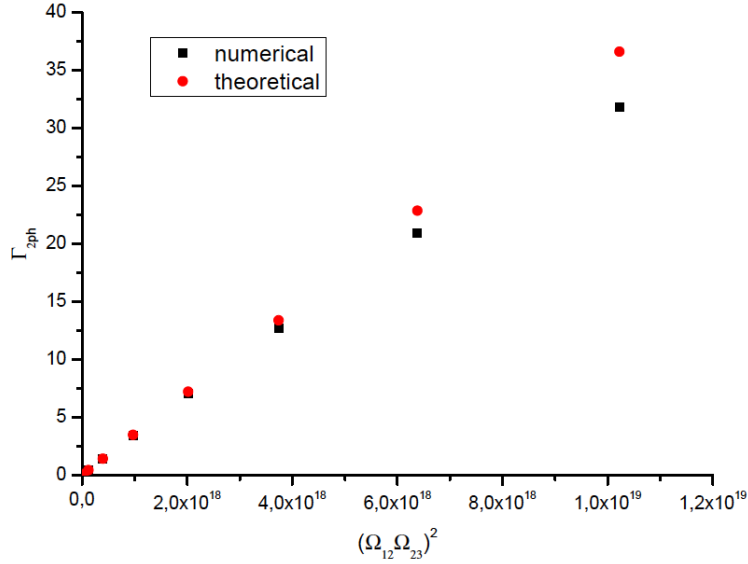


Figure 3.4: Two-photon rate  $\Gamma_{2ph}$  as a function of  $(\Omega_{12}\Omega_{23})^2$ . The ion's motion is harmonic with  $\Omega_{vib} = 600$  kHz,  $v_0 = 0.1$  m/s and  $\delta_{12} = 10$  MHz.

We can see that when  $\Gamma_{2ph} < 0.1 * \Gamma_3^{eff}$ , the theoretical formula for  $\Gamma_{2ph}$  holds true.

#### 3.2.5.1 Analytical formula for $\rho_{44}$

In the article, to calculate  $\rho_{44}$ , we used the following rate equations with the assumption that the  $\rho_{33}$  is much smaller than  $\rho_{11}$  :

$$\begin{cases} \frac{d\rho_{11}}{dt} = -(\Gamma_{2ph} + \Gamma_1)\rho_{11} \\ \frac{d\rho_{33}}{dt} = \Gamma_{2ph}\rho_{11} - (\Gamma_3 + \Gamma_{pd})\rho_{33} \\ \frac{d\rho_{44}}{dt} = \Gamma_{pd}\rho_{33} \end{cases}$$

If we don't use the assumption  $\rho_{11} \gg \rho_{33}$ , the rate equation should be modified as follows :

$$\begin{cases} \frac{d\rho_{11}}{dt} = -(\Gamma_{2ph} + \Gamma_1)(\rho_{11} - \rho_{33}(t)) \\ \frac{d\rho_{33}}{dt} = \Gamma_{2ph}(\rho_{11} - \rho_{33}) - (\Gamma_3 + \Gamma_{pd})\rho_{33} \\ \frac{d\rho_{44}}{dt} = \Gamma_{pd}\rho_{33} \end{cases}$$

With the initial conditions :  $\rho_{11}(0) = 1, \rho_{33}(0) = 0, \rho_{44}(0) = 0$ , we have

$$\begin{pmatrix} \rho_{11}(t) \\ \rho_{33}(t) \end{pmatrix} = C(\alpha_+ e^{\lambda_+ t} - \alpha_- e^{\lambda_- t}),$$

$$\text{where } C = \frac{\Gamma_{2ph}}{\sqrt{(\Gamma_3^{eff} - \Gamma_1)^2 + 4\Gamma_{2ph}^2}},$$

$$\lambda_{\pm} = \frac{1}{2} \left( -\Gamma_3 - \Gamma_1 - 2\Gamma_{2ph} \pm \sqrt{(\Gamma_3^{eff} - \Gamma_1)^2 + 4\Gamma_{2ph}^2} \right),$$

and

$$\alpha_{\pm} = \left( \frac{\Gamma_3 - \Gamma_1 \pm \sqrt{(\Gamma_3^{eff} - \Gamma_1)^2 + 4\Gamma_{2ph}^2}}{2\Gamma_{2ph}} \right).$$

The photodissociated fraction  $\rho_{44}(t)$  is :

$$\rho_{44}(t) = \Gamma_{pd} C \left( \frac{1}{\lambda_-} - \frac{1}{\lambda_+} + \frac{1}{\lambda_+} e^{\lambda_+ t} - \frac{1}{\lambda_-} e^{\lambda_- t} \right),$$

when  $t \rightarrow \infty$ , we have :

$$\rho_{44}^{\infty} = \Gamma_{pd} C \frac{\lambda_+ - \lambda_-}{\lambda_- \lambda_+} = \frac{\Gamma_{2ph} \Gamma_{pd}}{\Gamma_1 \Gamma_3^{eff} + \Gamma_1 \Gamma_{2ph} + \Gamma_3^{eff} \Gamma_{2ph}}.$$

Because  $\Gamma_1 \Gamma_{2ph} \ll \Gamma_3^{eff} \Gamma_{2ph}, \Gamma_1 \Gamma_3^{eff}$ , then the calculation of  $\rho_{44}^{\infty}$  with the assumption  $\rho_{11} \gg \rho_{33}$  is a good approximation.

### 3.2.5.2 Laser phase noise influence

We suppose that the diode lasers for two-photon excitation have the Lorentzian line shape of withs  $\Delta_{FWHM}$  and  $\Delta'_{FWHM}$  and can be mathematically expressed in the following form:

$$\mathbf{E}(\mathbf{r}, t) = E(t)\boldsymbol{\epsilon} + E'(t)\boldsymbol{\epsilon}' = E\boldsymbol{\epsilon}e^{-i(\omega t - \mathbf{k}\mathbf{r} + \phi(t))} + E'\boldsymbol{\epsilon}'e^{-i(\omega' t - \mathbf{k}'\mathbf{r} + \phi'(t))} + c.c., \quad (3.1)$$

where  $\phi(t) = \int_0^t d\tau \Delta\omega(\tau)$  and  $\phi'(t) = \int_0^t d\tau \Delta\omega'(\tau)$  and  $\Delta\omega(t)$  and  $\Delta\omega'(t)$  are two independent stationary joint Gaussian random processes i.e  $\langle \Delta\omega(t)\Delta\omega(t') \rangle = \Delta_{FWHM}\delta(t-t')$ ,  $\langle \Delta\omega'(t)\Delta\omega'(t') \rangle = \Delta'_{FWHM}\delta(t-t')$  and  $\langle \Delta\omega(t)\Delta\omega'(t') \rangle = 0$ . The  $\langle \dots \rangle$  denotes an ensemble averaging process and  $\delta(t)$  is the Dirac delta function.

The influence of laser phase noise on two-photon spectroscopy has been well studied both theoretically [109, 110] and experimentally [111]. These researches showed that the linewidth of two-photon signal scales four times the laser linewidth for two completely correlated photons. In our case, two photons are from two different lasers and hence we suppose that these photons are completely uncorrelated. The extension of theoretical results in [109] to our case can be done straightforwardly without any difficulty. We can establish a relation between the two-photon transition rate and laser field correlation function as follows:

$$\Gamma_{2ph} = 2|g(\omega)|^2 \left[ \int_{-\infty}^{\infty} dt e^{2i\omega_3 t - \Gamma_3^{eff}|t|} G^{(2)}(-t, -t, t, t) \right],$$

where, the laser field correlation function is defined as:

$$G^{(2)}(t'_1, t'_2, t_1, t_2) = \langle E'^*(t'_1) E^*(t'_2) E(t_1) E(t_2) \rangle,$$

and,

$$g(\tilde{\omega}) = \frac{1}{\hbar^2} \frac{d'd}{\omega - \omega_{21} + i\epsilon}$$

(with,  $d = \mathbf{d}_{12}\epsilon$  and  $d' = \mathbf{d}_{23}\epsilon'$ ).

The field correlation function  $G^{(2)}$  can be calculated as follows :

$$\begin{aligned} G^{(2)}(-t, -t, t, t) &= |E|^2 |E'|^2 e^{-2i(\omega+\omega')t} \times \langle e^{i[\phi'(-t)+\phi(-t)-\phi'(t)-\phi(t)]} \rangle \\ &= |E|^2 |E'|^2 e^{-2i(\omega+\omega')t} \times e^{\frac{1}{2}[\phi'(-t)+\phi(-t)-\phi'(t)-\phi(t)]^2} . \end{aligned}$$

Because,

$$\begin{aligned} \langle \phi(t)^2 \rangle &= \Delta_{\text{FWHM}} t \\ \langle \phi'(t)^2 \rangle &= \Delta'_{\text{FWHM}} t \\ \langle \phi(t_1)\phi(t_2) \rangle &= \Delta_{\text{FWHM}} \min\{t_1, t_2\} \\ \langle \phi'(t_1)\phi'(t_2) \rangle &= \Delta'_{\text{FWHM}} \min\{t_1, t_2\} \end{aligned}$$

then we have :

$$G^{(2)}(-t, -t, t, t) = |E|^2 |E'|^2 e^{-2i(\omega+\omega')t} e^{-(\Delta_{\text{FWHM}}+\Delta'_{\text{FWHM}})|t|} .$$

We can rewrite the two-photon transition rate as:

$$\begin{aligned} \Gamma_{2ph} &= 2 |g(\omega) EE'|^2 \left[ \int_{-\infty}^{\infty} dt e^{2i\omega_{31}t - \Gamma_3^{eff}|t|} e^{-2i(\omega+\omega')t} e^{-(\Delta_{\text{FWHM}}+\Delta'_{\text{FWHM}})|t|} \right] \\ &= 2 \frac{\Omega_{12}^2 \Omega_{23}^2}{\delta_{12}^2} \left[ \int_{-\infty}^{\infty} dt e^{-2i\delta_{31}t - (\Gamma_3^{eff} + \Delta_{\text{FWHM}} + \Delta'_{\text{FWHM}})|t|} \right] \end{aligned}$$

Because,  $\int_{-\infty}^{\infty} dt e^{-iat - b|t|} = 2b/(a^2 + b^2)$ , hence we have:

$$\Gamma_{2ph} = \frac{\Omega_{12}^2 \Omega_{23}^2}{\delta_{12}^2} \frac{\Gamma_2^{eff} + \Delta_{\text{FWHM}} + \Delta'_{\text{FWHM}}}{\delta_{31}^2 + (\Gamma_3^{eff} + \Delta_{\text{FWHM}} + \Delta'_{\text{FWHM}})^2/4} .$$

If  $\Delta_{\text{FWHM}} = \Delta'_{\text{FWHM}}$ , then :

$$\Gamma_{2ph} = \frac{\Omega_{12}^2 \Omega_{23}^2}{\delta_{12}^2} \frac{\Gamma_2^{eff} + 2\Delta_{fwhm}}{\delta_{31}^2 + (\Gamma_3^{eff} + 2\Delta_{\text{FWHM}})^2/4} . \quad (3.2)$$

### 3.2.5.3 Misalignment of two counterpropagating lasers

For two-photon spectroscopy using two quasi-degenerate photons, we cannot use the Fabry-Pérot cavity for laser alignment. This task must be done by hand i.e. using a system of mirrors and diaphragms to get the light trajectory of the first laser and then the second laser must be positioned following the previously-measured configuration of diaphragms. Laser alignment by hand cannot completely eliminate the eventual misalignment between two counterpropagating laser beams of wave vector  $\vec{k}$  and  $\vec{k}'$ . We represent the misalignment of two lasers by an angle  $\theta$  as shown in Fig. 3.5.

The effective Lamb-Dicke regime state that : the first order Doppler effect can be suppressed if the following condition holds true :



Figure 3.5: Misalignment of two counterpropagating lasers

$$|(\vec{k} - \vec{k}') \cdot \vec{r}| \ll 1 . \quad (3.3)$$

The ion motional amplitude  $a$  is about  $1 \mu\text{m}$  in all directions. Therefore, if we project the condition 3.3 onto the parallel and perpendicular direction to  $\vec{k}$ , we have :

$$|(\vec{k} - \vec{k}')_{\parallel} \vec{r}_{\parallel}| \sim |k - k' \cos(\theta)|a \approx |k - k' + k' \frac{\theta^2}{2}|a \ll 1 ,$$

$$|(\vec{k} - \vec{k}')_{\perp} \vec{r}_{\perp}| \sim k' \sin(\theta)a \approx k\theta a \ll 1 .$$

The first condition depends on  $\theta^2$  and the second on  $\theta$ , we then only concern about the second relation. Because  $k \approx k' \approx 4.35 \times 10^6 \text{ m}^{-1}$  and  $a \sim 1 \mu\text{m}$ , the second condition can be rewritten as:

$$4.35 \times \theta \ll 1 .$$

The maximal value of  $\theta$  is estimated as follows :

$$4.35 \times \theta_{max} \approx 0.1 \quad \text{or, equivalently} \quad \theta_{max} \approx 0.023 \text{ rad} .$$

This constraint seem not to be a big deal in the experiment.

# Chapter 4

...

My PhD thesis is constituted by both theoretical and experimental aspects of the high precision spectroscopy of hydrogen molecular ions  $\text{H}_2^+$  and  $\text{HD}^+$ . The ultimate goal of this research is to improve the precision of the present value of proton-to-electron mass ratio  $m_p/m_e$  to the level of uncertainty of 0.1 ppb by using a radically different method : laser spectroscopy. The measurement of this mass ratio is also useful for a new determination of fine structure constant  $\alpha$  and also for the quest of variation in time of fundamental constants.

The first topic of this thesis consists of the theoretical study of the state-selected ion production using REMPI method and the experimental realization of this ion source. This state-selected ion source is one of main steps for the observation of two-photon transition signal in the experiment with  $\text{H}_2^+$ . My theoretical study in collaboration with V. McKoy at Caltech, USA showed that the  $\text{H}_2^+$  ions produced by the (3+1) REMPI method via the excited state  $\text{C } ^1\Pi_u \nu = 0, L = 2$  of  $\text{H}_2$  are  $90\% \times 97\%$  in the state  $|\nu_+ = 0, L_+ = 2\rangle$ . This ion source will increase the signal-to-noise ratio of the REMPD signal by a factor of 24 in comparison with that of an ion source produced by the electronic impact method. The experimental realization consists of installing and optimizing a laser system at 303 nm for the (3+1) REMPI process. (to be completed)

The second topic of this thesis is a theoretical study of the feasibility of the nearly-degenerate two-photon spectroscopy in the Lamb-Dicke regime. This work aims to improve the present results of the spectroscopy of  $\text{HD}^+$  using single-photon transitions. The experimental results of the single-photon spectroscopy of  $\text{HD}^+$  ions are very remarkable but still limited by the Doppler broadening. With this new method, this Doppler effect is shown to be completely suppressed. The REMPD signal linewidth is shown to be in the range of 100 Hz and the laser power broadening is the main cause of this linewidth. The molecular spectroscopy at the accuracy level of  $10^{-14}$  could be possible with this method.



# Appendix A

## Notes on $H_2^+$

I want to place in this appendix some basic informations about  $H_2^+$ . It is based mainly on [26, 112].

### A.1 Exact three-body problem

The molecular hydrogen ion  $H_2^+$  is a standard three-body problem with two protons and one electron. Let's denote the positions of two protons and one electron respectively as  $\vec{R}_1, \vec{R}_2, \vec{R}_3$  and thanks to the translation invariance of the system, we can define new coordinates as [26]:

$$\begin{aligned}\vec{R}_G &= \frac{m_p \vec{R}_1 + m_p \vec{R}_2 + m_e \vec{R}_3}{2m_p + m_e} \\ \vec{R} &= \vec{R}_1 - \vec{R}_2 \\ \vec{r} &= \frac{\vec{R}_1 + \vec{R}_2}{2} - \vec{R}_3\end{aligned}$$

then the Hamiltonian of  $H_2^+$  is

$$H = \frac{\vec{p}^2}{2} + \frac{1}{m_p}(\vec{P}^2 + \frac{\vec{p}^2}{4}) - \frac{1}{\|\vec{R}/2 + \vec{r}\|} - \frac{1}{\|\vec{R}/2 - \vec{r}\|} + \frac{1}{R}$$

This Hamiltonian commutes with the  $z$ -projection of total orbital angular momentum  $\vec{L}$  and its square. Therefore, we can use the two corresponding quantum number  $L$  and  $M$  to label the eigenstate  $\psi^{space}$  of  $H$  as  $\psi_{LM}^{space}(1, 2, e^-)$ .

We denote the nuclear spins as  $\vec{I}_1, \vec{I}_2$  and the total nuclear spin as  $\vec{I} = \vec{I}_1 + \vec{I}_2$ . The total nuclear spin state is either singlet  $|I = 0\rangle$  or triplet  $|I = 1\rangle$ .

There're two exact discrete symmetries in  $H_2^+$ : The total parity  $\Pi$  and the internuclear exchange symmetry  $P_{12}$ . Note that in the Born-Oppenheimer approximation, we have an additional symmetry  $\pi_e$  - the electronic parity.

The Hamiltonian  $H$  of the system commutes with the total parity operator  $\Pi$  and the internuclear exchange operator  $P_{12}$ . Therefore, the atomic state  $\psi_{LM}^{space}$  can be classified as even/odd (depending on the value of parity  $\Pi$ ) and symmetric/antisymmetric (depending on the value of  $P_{12}$ ). We choose the notations  $e/o$  for an even/odd state and  $1/3$  for the

symmetric/antisymmetric state. The reason for the notation  $1/3$  is that if we write the total wavefunction  $\psi(1, 2, e^-) = \psi_{LM}^{space}(1, 2, e^-) \otimes \psi^{spin}(1, 2, e^-)$ , the action of internuclear exchange operator can be expressed as (Pauli principle):

$$P_{12}\psi(1, 2, e^-) = -\psi(1, 2, e^-)$$

therefore,

$$(P_{12}\psi_{LM}^{space}(1, 2, e^-)) \otimes (P_{12}\psi^{spin}(1, 2, e^-)) = -\psi_{LM}^{space}(1, 2, e^-) \otimes \psi^{spin}(1, 2, e^-)$$

If the spacial wavefunction  $\psi_{LM}^{space}$  is symmetric i.e.  $P_{12}\psi_{LM}^{space}(1, 2, e^-) = +\psi_{LM}^{space}(1, 2, e^-)$  then we must have  $P_{12}\psi^{spin}(1, 2, e^-) = -\psi^{spin}(1, 2, e^-)$ . This corresponds to the nuclear singlet state  $|I = 0\rangle$ .

If the spacial wavefunction  $\psi_{LM}^{space}$  is antisymmetric i.e.  $P_{12}\psi_{LM}^{space}(1, 2, e^-) = -\psi_{LM}^{space}(1, 2, e^-)$  then  $P_{12}\psi^{spin}(1, 2, e^-) = +\psi^{spin}(1, 2, e^-)$ . This corresponds to the nuclear triplet state  $|I = 0\rangle$ .

Now, for a quantum state obtained from the exact three-body problem, we can label as  $^{2I+1}L^\Pi$  with  $I = 0, 1$  and  $\Pi = e/o$ . And if  $L = 0, 1, 2, 3, \dots$ , the states are labelled as  $S, P, D, F, \dots$  respectively.

## A.2 Born-Oppenheimer approximation

The Born-Oppenheimer (BO) approximation is the widely used method in the molecular physics. In this approximation, because the nuclear motion is very slow with respect of the electronic motion, the electronic wavefunction is calculated with fixed nuclei.

This approximation is included here to give a good picture of the energy levels obtained from the exact three-body problem. In the BO picture, we have another symmetry : the electronic parity  $\pi_e$  or  $u/g$  symmetry. We also have another quantum number  $\Lambda$  - the projection of total orbital angular momentum on the internuclear axis.

In [26], N. Billy used the spheroidal coordinates to solve the three-body problem in the frame of Born-Oppenheimer approximation :

$$\eta = \frac{r_1 - r_2}{R} \longleftrightarrow \text{quantum number } n_\eta$$

$$\xi = \frac{r_1 + r_2}{R} \longleftrightarrow \text{quantum number } n_\xi$$

where  $r_1, r_2$  are the distance between electron and the protons and  $R$  is the distance between two protons.

We can only use the three quantum number  $(n_\eta, n_\xi, \Lambda)$  to describe the electronic potential curves in Fig.A.1.

For the electronic potential curve  $(0, 0, 0)$  (or  $1s\sigma_g$ ), the electronic parity of all bound states is even ( $\pi_e = +1$ ).

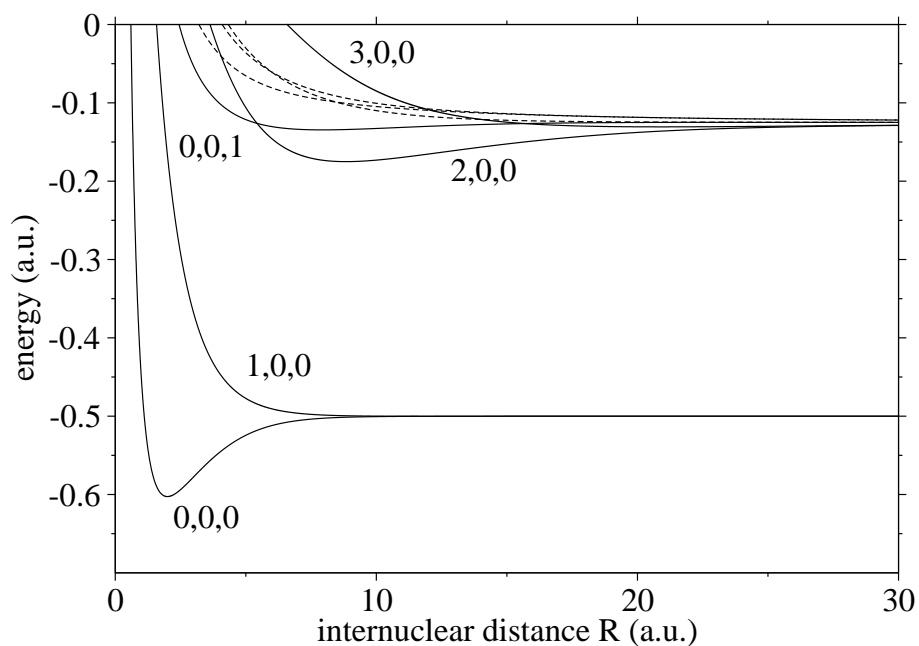


Figure A.1: Electronic potential curves for  $\text{H}_2^+$  ion. These curves are obtained by N. Billy by using the the spheroidal coordinates for the three-body problem in the frame of Born-Oppenheimer approximation. We denote these curves by the molecular quantum numbers  $(n_\eta, n_\xi, \Lambda)$  as in [26]: the curve  $(0, 0, 0)$  corresponds to the usual notation  $1s\sigma_g$ ;  $(1, 0, 0)$  corresponds to  $2p\sigma_u$ ;  $(2, 0, 0)$  corresponds to  $2d\sigma_g$ ,  $(0, 0, 1)$  corresponds to  $2p\pi_u$  and  $(3, 0, 0)$  corresponds to  $4f\sigma_u$ . The dashed lines are dissociative curves.

### A.3 Two-photon transitions

In this section, we consider only the exact bound states  $\{^{2I+1}L^\Pi\}$  which corresponds to the Born-Oppenheimer bound states of the electronic ground-state  $1s\sigma_g$ .

From the numerical resolution of the exact three-body problem, we can establish the relation between the (spacial) parity  $\Pi$  and the total orbital angular momentum  $L$  as  $\Pi = (-1)^L$ . Therefore, we have the following relations between  $L$  and the total nuclear spin:

$$L \text{ even} \longleftrightarrow \psi \text{ is symmetric} \longleftrightarrow \text{nuclear singlet } |I = 0\rangle$$

$$L \text{ odd} \longleftrightarrow \psi \text{ is antisymmetric} \longleftrightarrow \text{nuclear triplet } |I = 1\rangle$$

Because the dipole-allowed transitions don't have any effect on the nuclear spin state, it doesn't change the even/odd characteristics of the spacial wavefunction. And for single-photon transitions happen between two rovibrational states, we have the selection rule  $\Delta L = \pm 1$ . Therefore, the single-photon transition is forbidden with  $H_2^+$ . But two-photon transition is possible because of the selection rule  $\Delta L = 0, \pm 2$ .

# Appendix B

## *Mathematica* program for the calculation of rotational distribution of $\text{H}_2^+$ ions

I put in this appendix the *Mathematica* program (with detailed comments) for the calculation of photoionization rate in the (3+1) REMPI process of  $\text{H}_2^+$  using  $\text{C } ^1\Pi_u$  as the intermediate state.

### B.1 Table of matrix elements

In the calculation of rotational distribution, the branching ratio of photoionization rate is a good estimation of the distribution. This simple estimation requires by the matrix element  $\overline{r_{fi}^{(\mu)}}$  which is difficult to calculate, therefore, we ask V. McKoy from California Institute of Technology to compute the values of the matrix elements. And in collaboration with K. Wang, V. McKoy "reactivated" his numerical programs and gave us the following matrix element table.

The matrix elements are of the form  $\overline{r_{if}^{(\mu)}} = a[l, \text{lambda}, \mu]$  but in the theoretical formula of the photoionization rate, we use a different form  $\overline{r_{fi}^{(\mu)}}$ . Therefore, in the detailed calculation, we need to use the relation :

$$\overline{r_{fi}^{(\mu)}} = (-1)^\mu \left( r_{if}^{(-\mu)} \right)^* = (a[l, \mu + K_i, -\mu])^*$$

```
Table[a[l, lambda, mu], {l, 0, 8, 2}, {lambda, -2, 2, 1}, {mu, -1, 1, 1}];
Do[a[l, lambda, mu] = 0, {l, 0, 8, 2}, {lambda, -2, 2, 1}, {mu, -1, 1, 1}];
a[0, 0, 1] = 0.66608176*10^-01 - 0.45545183*10^-01*I;
a[0, 0, -1] = 0.66608176*10^-01 - 0.45545183*10^-01*I;
a[2, 0, 1] = 0.24339734*10^-01 + 0.74708328*10^-01*I;
a[2, 0, -1] = 0.24339734*10^-01 + 0.74708328*10^-01*I;
```

```

a[4, 0, 1] = 0.33303681*10^-02 - 0.85166318*10^-03*I;
a[4, 0, -1] = 0.33303681*10^-02 - 0.85166318*10^-03*I;
a[6, 0, 1] = -0.82545075*10^-05 - 0.53025578*10^-05*I;
a[6, 0, -1] = -0.82545075*10^-05 - 0.53025578*10^-05*I;
a[8, 0, 1] = -0.39864528*10^-07 + 0.11560013*10^-06*I;
a[8, 0, -1] = -0.39864528*10^-07 + 0.11560013*10^-06*I;
a[2, 1, 0] = -0.35457090*10^-01 - 0.11673052*10^+00*I;
a[2, -1, 0] = -0.35457090*10^-01 - 0.11673052*10^+00*I;
a[4, 1, 0] = -0.51802038*10^-02 + 0.12849222*10^-02*I;
a[4, -1, 0] = -0.51802038*10^-02 + 0.12849222*10^-02*I;
a[6, 1, 0] = 0.13050755*10^-04 + 0.87100443*10^-05*I;
a[6, -1, 0] = 0.13050755*10^-04 + 0.87100443*10^-05*I;
a[8, 1, 0] = 0.15713649*10^-07 - 0.22234012*10^-08*I;
a[8, -1, 0] = 0.15713649*10^-07 - 0.22234012*10^-08*I;
a[2, 2, -1] = 0.40091280*10^-01 + 0.22570294*10^+00*I;
a[2, -2, 1] = 0.40091280*10^-01 + 0.22570294*10^+00*I;
a[4, 2, -1] = 0.51101781*10^-02 - 0.13381141*10^-02*I;
a[4, -2, 1] = 0.51101781*10^-02 - 0.13381141*10^-02*I;
a[6, 2, -1] = -0.11696503*10^-04 - 0.82474889*10^-05*I;
a[6, -2, 1] = -0.11696503*10^-04 - 0.82474889*10^-05*I;
a[8, 2, -1] = 0.53323919*10^-08 + 0.31278493*10^-08*I;
a[8, -2, 1] = 0.53323919*10^-08 + 0.31278493*10^-08*I;

```

## B.2 Photoionization rate

The key quantity to calculate is the total photodissociation rate from the intermediate level to the continuum level to determine the rotational state distribution of the final state of ions  $\text{H}_2^+$

$$\Gamma_{L_i L_+} = 2\pi\alpha I \frac{4\pi}{3} (2L_+ + 1)(2L_i + 1) \sum_{M_i K_i} \sum_{M_+ K_+} \sum_{lm} \left| \sum_{\lambda} \sum_{\mu} \sum_{l_t m_t k_t} (-1)^{\mu+m_t-k_t} (2l_t + 1) \right. \\ \left. \begin{pmatrix} L_+ & L_i & l_t \\ -M_+ & M_i & m_t \end{pmatrix} \begin{pmatrix} L_+ & L_i & l_t \\ -K_+ & K_i & k_t \end{pmatrix} \begin{pmatrix} l & 1 & l_t \\ -m & \mu_0 & -m_t \end{pmatrix} \begin{pmatrix} l & 1 & l_t \\ -\lambda & \mu & -k_t \end{pmatrix} \overline{r_{fi}^{(\mu)}} \right|^2$$

In the Mathematica program, we use the reduced formula of the total photodissociation rate defined as :

$$\bar{\Gamma}_{L_+} = (2L_+ + 1) \sum_{M_i K_i} \sum_{M_+ K_+} \sum_{lm} \left| \sum_{\lambda} \sum_{\mu} \sum_{l_t m_t k_t} (-1)^{\mu+m_t-k_t} (2l_t + 1) \right. \\ \left. \begin{pmatrix} L_+ & L_i & l_t \\ -M_+ & M_i & m_t \end{pmatrix} \begin{pmatrix} L_+ & L_i & l_t \\ -K_+ & K_i & k_t \end{pmatrix} \begin{pmatrix} l & 1 & l_t \\ -m & \mu_0 & -m_t \end{pmatrix} \begin{pmatrix} l & 1 & l_t \\ -\lambda & \mu & -k_t \end{pmatrix} \overline{r_{fi}^{(\mu)}} \right|^2$$

Now, we apply this general formula for our (3+1) REMPI process in  $\text{H}_2^+$  with  $\text{C } ^1\Pi_u$  as the intermediate state. Firstly, we have :

- $L_i = 2; L_+ = 0, 2, 4; K_i = \pm 1$  and  $K_+ = 0$
- For the sake of simplicity, we consider the laser field as linearly polarized, therefore  $\mu_0 = 0$

- The properties of 3-j symbols imply that :  $k_t = -K_i; \lambda = \mu + K_i; m_t = -m = M_+ - M_i$
- The selection rules for (3+1) REMPI process imply :  $l = 0, 2, 4, 6, 8$  (we limit the maximal value of  $l = 8$  because the matrix elements are very small for large  $l$ )

The reduced photodissociate rate for (3+1) REMPI case is :

$$\bar{\Gamma}_{L_+} = (2L_+ + 1) \sum_{M_i=-2}^2 \sum_{K_i=\pm 1} \sum_{M_+=-L_+}^{L_+} \sum_{l=0,2,4,6,8} \left| \sum_{\mu=-1,0,+1} \sum_{l_t=0}^{10} (-1)^\mu (2l_t + 1) \cdot \begin{pmatrix} L_+ & 2 & l_t \\ -M_+ & M_i & M_+ - M_i \end{pmatrix} \begin{pmatrix} L_+ & 2 & l_t \\ 0 & K_i & -K_i \end{pmatrix} \begin{pmatrix} l & 1 & l_t \\ M_+ - M_i & 0 & M_i - M_+ \end{pmatrix} \begin{pmatrix} l & 1 & l_t \\ -\mu - K_i & \mu & K_i \end{pmatrix} \overline{r_{fi}^{(\mu)}} \right|^2$$

To estimate the validity of rotational state distribution based on the total photodissociation rate, we need to calculate the photodissociation rate of different values of  $M_i$  :

$$\bar{\Gamma}_{L_+}(M_i) = (2L_+ + 1) \sum_{K_i=\pm 1} \sum_{M_+=-L_+}^{L_+} \sum_{l=0,2,4,6,8} \left| \sum_{\mu=-1,0,+1} \sum_{l_t=0}^{10} (-1)^\mu (2l_t + 1) \cdot \begin{pmatrix} L_+ & 2 & l_t \\ -M_+ & M_i & M_+ - M_i \end{pmatrix} \begin{pmatrix} L_+ & 2 & l_t \\ 0 & K_i & -K_i \end{pmatrix} \begin{pmatrix} l & 1 & l_t \\ M_+ - M_i & 0 & M_i - M_+ \end{pmatrix} \begin{pmatrix} l & 1 & l_t \\ -\mu - K_i & \mu & K_i \end{pmatrix} \overline{r_{fi}^{(\mu)}} \right|^2$$

In the following we will use the notations GammaA and GammaB instead of  $\bar{\Gamma}_{L_+}(M_i)$  and  $\bar{\Gamma}_{L_+}$  respectively.

The partial photodissociation rate :

```
GammaA[Lp_, Mi_] := (2 Lp + 1)*
Sum[Abs[Sum[(2*lt + 1)*
  ThreeJSymbol[{Lp, -Mp}, {2, Mi}, {lt, Mp - Mi}]*
  ThreeJSymbol[{Lp, 0}, {2, Ki}, {lt, -Ki}]*
  ThreeJSymbol[{1, Mp - Mi}, {1, 0}, {lt, Mi - Mp}]*
  ThreeJSymbol[{1, -mu - Ki}, {1, mu}, {lt, Ki}]*
  Conjugate[a[1, mu + Ki, -mu]], {mu, -1, 1, 1}, {lt, 0, 10,
  1}]]^2, {1, 0, 8, 2}, {Mp, -Lp, Lp, 1}, {Ki, -1, 1, 2}];
```

The total photodissociation rate :

```
GammaB[Lp_] := Sum[GammaA[Lp, Mi], {Mi, -2, 2, 1}];
```

### B.3 Rotational distribution of $H_2^+$ ions

We denote  $N_{L_+}$  as the population of  $H_2^+$  in the rotational state  $|L_+\rangle$ , we have :

$$N_{L_+} \sim \sum_{M_i=2}^2 \bar{\Gamma}_{L_+}(M_i) \rho_{ii}$$

where  $\rho_{ii}$  is the population in the rovibrational state  $|L_i, M_i\rangle$ . The accurate determination of  $\rho_{ii}$  is complicated because the dipole moments which involve in the three-photon transition from the ground state to the intermediate state are very difficult to calculate. But as we will see later, this complicated calculation is unnecessary.

Assuming that the intermediate state is isotropic i.e  $\rho_{ii} = 1/(2L_i + 1)$ , then

$$N_{L_+} \sim \sum_{M_i} \bar{\Gamma}_{L_+}(M_i) \rho_{ii} = \bar{\Gamma}_{L_+}$$

The rotational distribution of population is :

$$\{N_0/N_2, N_4/N_2\} = \{\text{GammaB}[0]/\text{GammaB}[2], \text{GammaB}[4]/\text{GammaB}[2]\}$$

```
In[31] := {GammaB[0]/GammaB[2], GammaB[4]/GammaB[2]}
Out[31] = {0.00487294, 0.00990281}
```

If we don't want to use the hypothesis of isotropy of the intermediate state, we need to calculate the partial photodissociation rate for different values of  $M_i$ , then we will estimate the boundary of the rotational distribution of population of  $H_2^+$ .

For  $L_+ = 0$  we have :

```
In[32] := {GammaA[0,-2], GammaA[0,-1], GammaA[0,0], GammaA[0,1], GammaA[0,2]}
Out[32] = {0.0000513398, 0.000012835, 0., 0.000012835, 0.0000513398}
```

For  $L_+ = 2$  we have :

```
In[33] := {GammaA[2,-2], GammaA[2,-1], GammaA[2,0], GammaA[2,1], GammaA[2,2]}
Out[33] = {0.00631746, 0.00474305, 0.00421824, 0.00474305, 0.00631746}
```

For  $L_+ = 4$  we have :

```
In[34] := {GammaA[4,-2], GammaA[4,-1], GammaA[4,0], GammaA[4,1], GammaA[4,2]}
Out[34]= {0.0000400248,0.0000582374,0.0000643083,0.0000582374,0.0000400248}
```

The lower and upper limits of population distribution are determined using the following relation :

$$\frac{\min_{M_i} \{\bar{\Gamma}_{L'}(M_i)\}}{\max_{M_i} \{\bar{\Gamma}_L(M_i)\}} \leq \frac{N_{L'}}{N_L} = \frac{\sum_{M_i} \bar{\Gamma}_{L'}(M_i) \rho_{ii}}{\sum_{M_i} \bar{\Gamma}_L(M_i) \rho_{ii}} \leq \frac{\max_{M_i} \{\bar{\Gamma}_{L'}(M_i)\}}{\min_{M_i} \{\bar{\Gamma}_L(M_i)\}}$$

Then, we have :

$$0 \% \leq \frac{N_0}{N_2} \leq 1.21709 \%$$

and

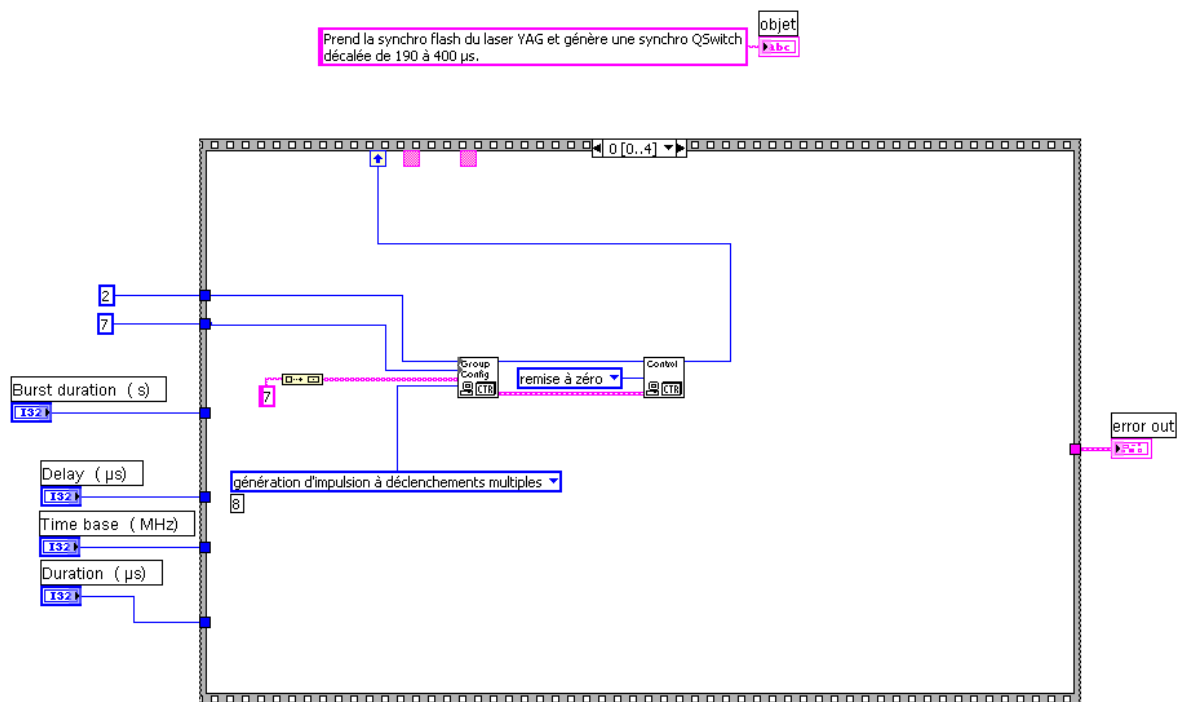
$$0.633558 \% \leq \frac{N_4}{N_2} \leq 1.52453 \%$$

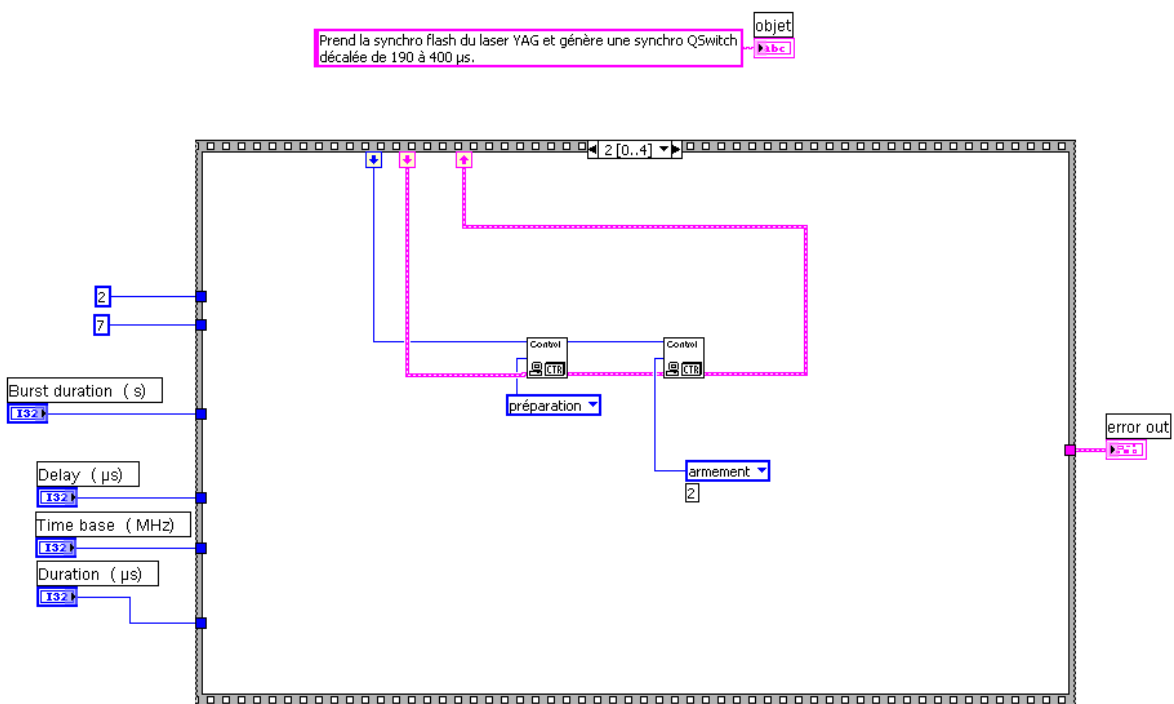
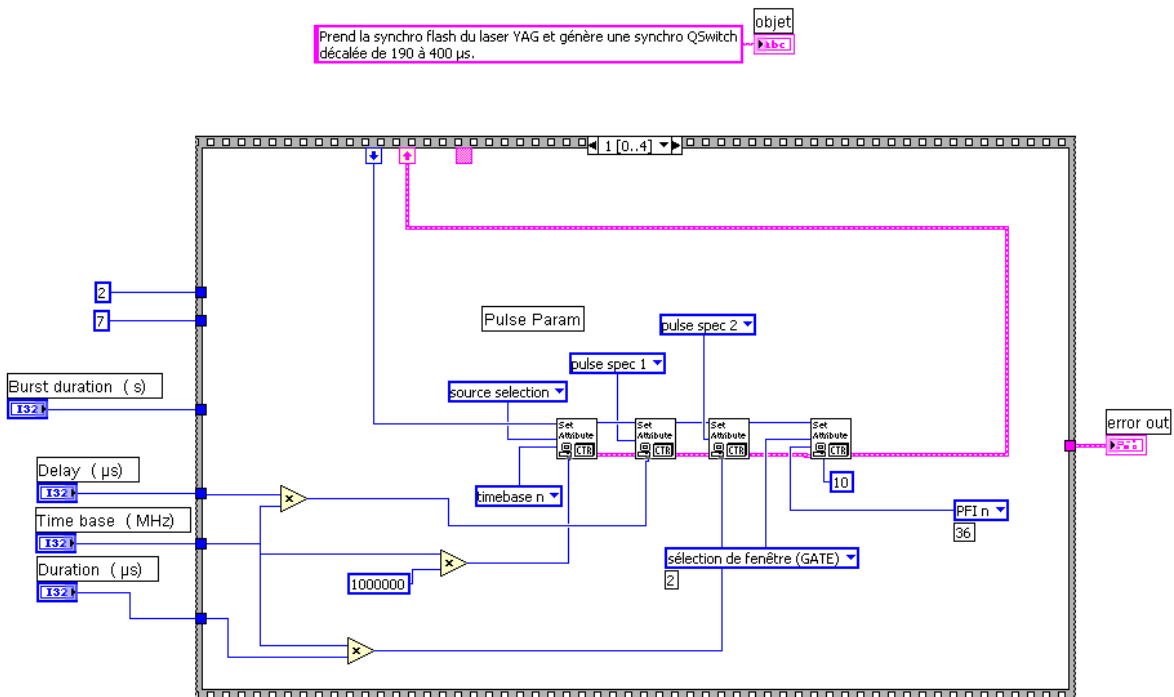
These inequalities confirm that most of ions  $H_2^+$  created by the (3+1) REMPI process via  $C^1\Pi_u$  are in the rotational state  $L_+ = 2$



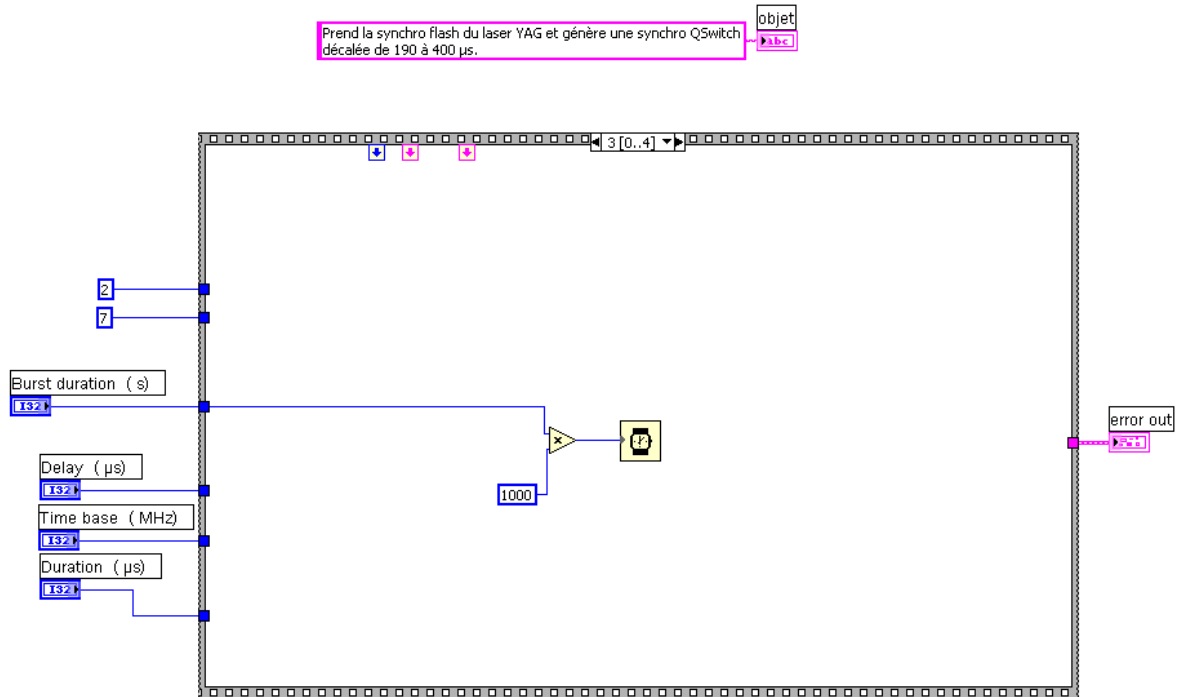
# Appendix C

## LabVIEW program for the external trigger of YAG laser

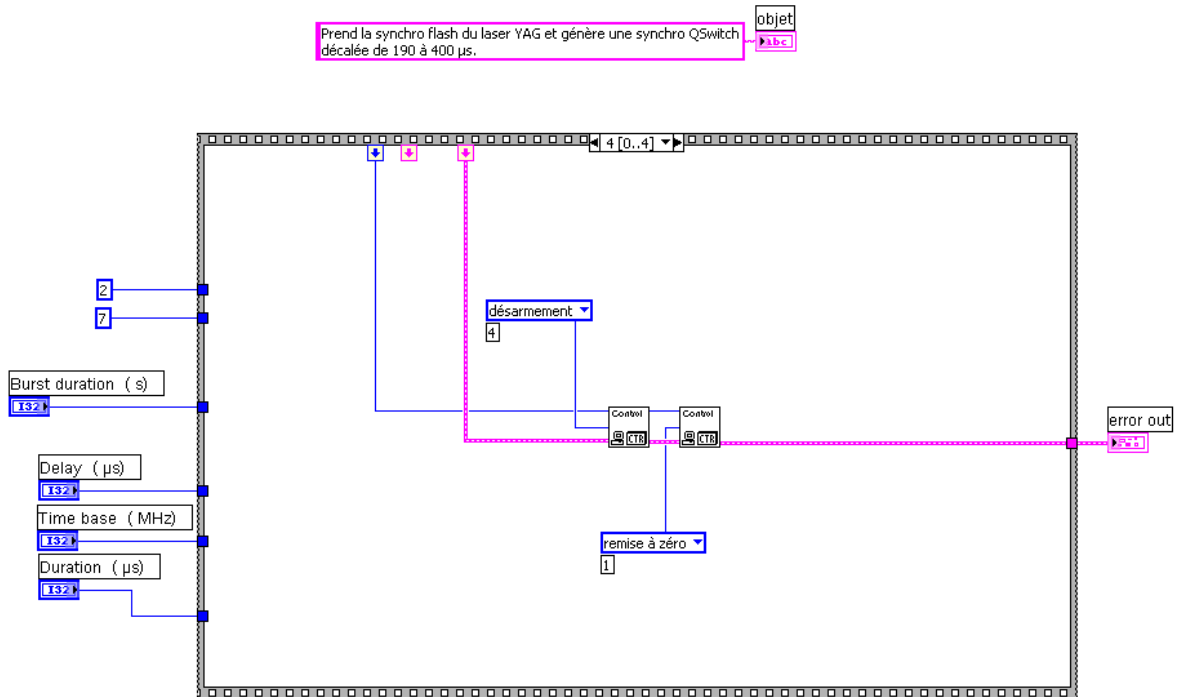




Prend la synchro flash du laser YAG et génère une synchro QSwitch décalée de 190 à 400  $\mu$ s.



Prend la synchro flash du laser YAG et génère une synchro QSwitch décalée de 190 à 400  $\mu$ s.





# Appendix D

## Notes on Diatomic Molecules

### D.1 Born-Oppenheimer approximation for diatomic molecules

The Born-Oppenheimer approximation method is ubiquitous in molecular physics. The main idea of this approximation is that the nuclear motion is much slower than the motion of electrons, therefore, in the theoretical treatment of molecular system, one can separate the nuclear motions and the electronic motions.

In this appendix, i want to discuss the Born-Oppenheimer (BO) approximation into the diatomic molecular physics which have a particular interest in the thesis.

We consider a diatomic molecule with two nuclei  $A$ ,  $B$  and  $N$  electrons as depicted in Fig.D.1

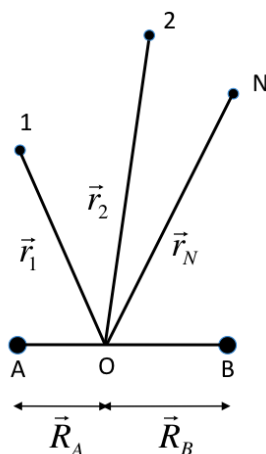


Figure D.1: Diatomic molecule :  $\vec{R}_A = \vec{OA}$ ,  $\vec{R}_B = \vec{OB}$ ,  $\vec{r}_i = \vec{Oi}$  ( $i = 1, 2, \dots, N$ )

The total Hamiltonia of this system can be written as :

$$H = T_N + T_e + V$$

where

◆  $T_N$  is the nuclear kinetic Hamiltonian :

$$T_N = -\frac{\hbar^2}{2\mu}\Delta_R = -\frac{\hbar^2}{2\mu}\left(\frac{1}{R^2}\frac{\partial}{\partial R}R^2\frac{\partial}{\partial R} - \frac{\vec{N}^2}{\hbar^2R^2}\right)$$

with  $\mu = M_A M_B / (M_A + M_B)$  the reduced mass of two nuclei and

$$\vec{N}^2 = -\hbar^2\left(\frac{1}{\sin(\Theta)}\frac{\partial}{\partial\Theta}\frac{\partial}{\partial\Theta} + \frac{1}{\sin(\Theta)^2}\right)$$

◆  $T_e$  is the electronic kinetic Hamiltonian :

$$T_e = \sum_{i=1}^N -\frac{\hbar^2}{2m_e}\Delta_{r_i}$$

◆  $V$  is the total Coulombian potential :

$$V(\vec{R}, \vec{r}_1, \vec{r}_2, \dots, \vec{r}_N) = \frac{Z_A Z_B e^2}{4\pi\epsilon_0 R} - \sum_{i=1}^N \left( \frac{Z_A e^2}{4\pi\epsilon_0 |\vec{r}_i - \vec{R}_A|} + \frac{Z_B e^2}{4\pi\epsilon_0 |\vec{r}_i - \vec{R}_B|} \right) + \sum_{i>j} \frac{e^2}{4\pi\epsilon_0 |\vec{r}_i - \vec{r}_j|}$$

For a given position  $\vec{R}$ , we want to study the electronic motion in the potential created by two nuclei. We define the electronic Hamiltonian as <sup>1</sup>  $H_e = T_e + V$ . A set of eigenfunctions  $\{\Phi_q\}_q$  with eigenenergies  $\{E_q(R)\}$  ( $q = 1, 2, \dots, N$ ) of this Hamiltonian constitute an orthogonal basis. The total wavefunction of the diatomic molecule can be decomposed in this basis as :

$$\Psi(\vec{R}, \vec{r}_1, \dots, \vec{r}_N) = \sum_q F_q(\vec{R})\Phi_q(\vec{R}, \vec{r}_1, \dots, \vec{r}_N)$$

The Schrödinger equation can be expressed as:

$$(T_N + H_e)\Psi(\vec{R}, \vec{r}_1, \dots, \vec{r}_N) = E\Psi(\vec{R}, \vec{r}_1, \dots, \vec{r}_N)$$

or equivalently

$$\sum_q (T_N + H_e - E)F_q(\vec{R})\Phi_q(\vec{R}, \vec{r}_1, \dots, \vec{r}_N) = 0$$

and we can obtain a set of equation as:

$$\sum_q \langle \Phi_s | T_N + H_e - E | \Phi_q \rangle F_q(\vec{R}) = 0$$

with  $s = 1, 2, \dots, N$ .

or equivalently

$$\sum_q \langle \Phi_s | -\frac{\hbar^2}{2\mu}\frac{1}{R^2}\frac{\partial}{\partial R}R^2\frac{\partial}{\partial R} + \frac{\vec{N}^2}{2\mu R^2} | \Phi_q \rangle F_q(\vec{R}) + (E_s(R) - E)F_q(\vec{R}) = 0$$

with  $s = 1, 2, \dots, N$ .

---

<sup>1</sup>In this case, the Coulombian interaction between two nuclei  $A$  and  $B$  :  $Z_A Z_B e^2 / 4\pi\epsilon_0 R$  is only a constant.

Up to now, we don't make any approximation and the Born-Oppenheimer approximation which consider the nuclear motion is much slower than the electronic motions is introduced to simplify the previous equations. The direct implication of this approximation is that the electronic wavefunction  $\Phi_q(\vec{R}, \vec{r}_1, \dots, \vec{r}_N)$  is insensitive to changes in the nuclear positions and velocities. Therefore, we have

$$\left| \frac{\partial}{\partial R} \Phi_q \right| \ll \left| \frac{\partial}{\partial R} F_q \right|$$

And we obtain the Schrödinger's equation for the diatomic molecular system in BO approximation <sup>2</sup>:

$$\left( -\frac{\hbar^2}{2\mu} \frac{1}{R^2} \frac{\partial}{\partial R} R^2 \frac{\partial}{\partial R} + \frac{\langle \Phi_s | \vec{N}^2 | \Phi_s \rangle}{2\mu R^2} + E_s(R) - E \right) F_s(\vec{R}) = 0 \quad (\text{D.1})$$

with  $s = 1, 2, \dots, N$ .

The electronic eigenenergies  $E_s(R)$  are also named the electronic potentials. The dependence of  $E_s$  on the internuclear distance  $R$  is represented by the electronic potential curves. An example of electronic potential curves of  $\text{H}_2^+$  is depicted in Fig. A.1 of appendix A.

## D.2 Symmetries in the diatomic molecules

The symmetries play an important role in molecular physics, especially the diatomic molecular physics. Its help us to understand the energy structure and classify the energy levels.

In molecular physics, people usually use two reference frame to represent the molecules : the space-fixed frame  $Oxyz$  (or labo-fixed frame) and the body-fixed frame  $O\bar{x}\bar{y}\bar{z}$ . The internuclear vector  $\vec{BA}$  is often chosen as the  $\bar{z}$ -axis.

A scheme of different angular momenta is depicted in Fig. D.2 with  $\vec{N}$  the nuclear orbital angular momentum,  $\vec{L}$  the total orbital electric angular momentum and,  $\vec{K}$  the total orbital angular momentum. The influence of spins of electron and nuclei will be considered later.

We always have the fundamental symmetries  $[K^2, H] = 0$  and  $[K_z, H] = 0$  that give us two quantum number  $K$  and  $M_K$ . But in the Born-Oppenheimer picture, the electronic Hamiltonian  $H_e = T_e + V$  is invariant under the rotation about the internuclear  $\bar{z}$ -axis, then we have:

$$[H_e, L_{\bar{z}}] = 0$$

This symmetry give us a supplementary quantum number  $\Lambda$  defined as  $L_{\bar{z}}\Phi_s = \pm\hbar\Lambda\Phi_s$  with  $\Lambda = 0, 1, 2, \dots$ . This quantum numbers are used to label the corresponding quantum states : if  $\Lambda = 0, 1, 2, 3, \dots$ , we have the quantum states  $\Sigma, \Pi, \Delta, \Phi, \dots$  respectively.

<sup>2</sup>In the Born-Oppenheimer approximation, we retain only the term with  $q = s$ . To understand this, we must write  $\vec{N}^2 = \vec{K}^2 + \vec{L}^2 - 2\vec{K}\vec{L}$  and using  $\vec{K}^2\Psi = K(K+1)\Psi$ ,  $L_{\bar{z}}\Phi_q = \pm\Lambda\Phi_q$  to calculate the expectation value of  $\vec{N}^2$

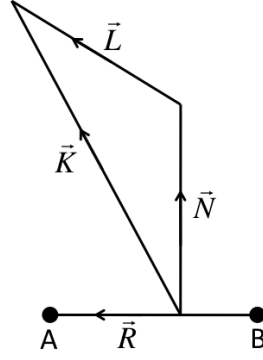


Figure D.2: Angular momentum vectors for diatomic molecules

Another important symmetry for diatomic molecules in the BO picture is : the electronic Hamiltonian is invariant under the reflection in all planes containing the internuclear axis. We denote the operator of reflection as  $A_{\bar{y}}$ , then we have  $[A_{\bar{y}}, H_e] = 0$ . We also have <sup>3</sup>:

$$\{A_{\bar{y}}, L_{\bar{z}}\} = 0$$

The operator  $A_{\bar{y}}$  converts the wavefunction with  $\Lambda$  to another wavefunction with  $-\Lambda$ . The electronic states with  $\Lambda \neq 0$  are thus doubly degenerate. But the  $\Sigma$ -states are non-degenerate and since  $A_{\bar{y}}^2 = \mathbb{I}$ , then we need to distinguish two different types of  $\Sigma$ -states :  $\Sigma^+$  and  $\Sigma^-$ .

In the case of homonuclear diatomic molecules like  $H_2$ ,  $O_2$ ,  $N_2$  ..., we have an extra symmetry : the electronic Hamiltonian is invariant under the reflection at the midpoint between two nuclei. This symmetry divides the electronic wavefunction into two classes : even states ( or gerade states or briefly  $g$  states) and odd states (ungerade states or briefly  $u$  states).

We want to rewrite the Schrödinger's equation D.1 based on the new symmetries. It's easy to see that  $K_{\bar{z}} = L_{\bar{z}}$  and the action of  $K_{\bar{z}}$  on the total wavefunction  $\Psi_s = F_s(\vec{R})\Phi_s(\vec{R}, \vec{r}_1, \dots, \vec{r}_N)$  is:

$$K_{\bar{z}}\Psi_s = K_{\bar{z}}F_s\Phi_s = F_sK_{\bar{z}}\Phi_s = F_sL_{\bar{z}}\Phi_s = \pm\hbar\Lambda F_s\Phi_s = \pm\hbar\Lambda\Psi_s$$

Using the relation  $\vec{N}^2 = (\vec{K} - \vec{L})^2 = \vec{K}^2 + \vec{L}^2 - 2\vec{K}\vec{L}$ , we can evaluate the expectation of  $\vec{N}^2$  in D.1 as :

$$\frac{1}{2\mu R^2}\langle\Phi_s|\vec{N}^2|\Phi_s\rangle F_s(\vec{R}) = \frac{\hbar^2}{2\mu R^2}(K(K+1) - \Lambda^2)F_s(\vec{R}) + \frac{1}{2\mu R^2}\langle\Phi_s|L_{\bar{x}}^2 + L_{\bar{y}}^2|\Phi_s\rangle F_s(\vec{R})$$

In this calculation, we use the result  $\langle\vec{K}\vec{L}\rangle = \langle K_{\bar{z}}L_{\bar{z}}\rangle$ .

The Schrödinger's equation D.1 is then rewritten as :

<sup>3</sup>We need to use the analytical formula of  $L_{\bar{z}} = -i\hbar(\bar{x}\partial/\partial\bar{y} - \bar{y}\partial/\partial\bar{x})$  and direct calculations to understand this relation

$$\left( -\frac{\hbar^2}{2\mu} \frac{1}{R^2} \frac{\partial}{\partial R} R^2 \frac{\partial}{\partial R} + \frac{K(K+1)}{2\mu R^2} + E'_s(R) - E \right) F_s(\vec{R}) = 0$$

where  $E'_s(R) = E_s(R) - \frac{\Lambda^2 \hbar^2}{2\mu R^2} + \frac{1}{2\mu R^2} \langle \Phi_s | L_x^2 + L_y^2 | \Phi_s \rangle$   
 The we will use the decomposition of wave function as:

$$F_s(\vec{R}) = \frac{1}{R} \mathcal{F}_{\nu K}^s(R) {}^\Lambda \mathcal{H}_{KM_K}(\Theta, \Phi)$$

and the total wavefunction is then:

$$\Psi_s = \frac{1}{R} \mathcal{F}_{\nu K}^s(R) {}^\Lambda \mathcal{H}_{KM_K}(\Theta, \Phi) \Phi_s(R, \bar{x}_i, \bar{y}_i, \bar{z}_i)$$

Because the reduce mass  $\mu$  is much larger than the electron mass  $m_e$ , then we can suppose  $E'_s \approx E_s$ , the Schrödinger equation for the radial wave function of diatomic molecules in Born-Oppenheimer approximation:

$$\left( -\frac{\hbar^2}{2\mu} \frac{d^2}{dR^2} + \frac{K(K+1)}{2\mu R^2} + E_s(R) - E \right) \mathcal{F}_{\nu K}^s(R) = 0 \quad (\text{D.2})$$

The angular wave function must satisfy the following equations <sup>4</sup>:

$$\left[ \frac{\partial^2}{\partial \Theta^2} + \cot(\Theta) \frac{\partial}{\partial \Theta} - \frac{1}{\sin^2 \Theta} (M_K - \Lambda \cos(\Theta))^2 - \Lambda^2 \right] {}^\Lambda \mathcal{H}_{KM_K}(\Theta, \Phi) = K(K+1) {}^\Lambda \mathcal{H}_{KM_K}(\Theta, \Phi) \quad (\text{D.3})$$

$$-i \frac{\partial}{\partial \Phi} [{}^\Lambda \mathcal{H}_{KM_K}(\Theta, \Phi)] = M_K \exp(iM_K \Phi) \quad (\text{D.4})$$

### D.3 Rotational and vibrational energies

In the equation D.2, if the electronic potential  $E_s(R)$  have a minimum at  $R_0$ , then we have

$$E_s(R) \approx E_s(R_0) + \frac{1}{2} \mu \omega_0^2 (R - R_0)^2 \quad \text{with} \quad \omega_0^2 = \frac{1}{\mu} \left. \frac{d^2 E_s}{dR^2} \right|_{R_0}$$

where  $E_s(R_0)$  is the minimum of the electronic potential  $E_s(R)$ , and  $(1/2)\mu\omega_0^2(R - R_0)^2$  represents the vibration of nuclei at the equilibrium point.

We also develop the rotational energy in D.2 at  $R_0$  as :

$$E_r = \frac{\hbar^2}{2\mu} \frac{K(K+1)}{R^2} \approx \frac{\hbar^2}{2\mu} \frac{K(K+1)}{R_0^2} = BK(K+1) \quad \text{with} \quad B = \frac{\hbar^2}{2\mu R_0^2}$$

The equation D.2 at the equilibrium point is :

$$\left( -\frac{\hbar^2}{2\mu} \frac{d^2}{dR^2} + \frac{1}{2} \mu \omega_0^2 (R - R_0)^2 + BK(K+1) + E_s(R_0) - E_{s,\nu K} \right) \mathcal{F}_{\nu K}^s(R) = 0$$

---

<sup>4</sup>To establish these equations, we use :  $\vec{K}^2 \Psi_s = \hbar^2 K(K+1) \Psi_s$  and  $K_z \Psi_s = \hbar M_K \Psi_s$

	H <sub>2</sub>	N <sub>2</sub>	O <sub>2</sub>
$E_s(R_0)$ (eV)	4.7	7.5	5.2
$\omega_0$ (eV)	0.54	0.29	0.20
$10^3 B$ (eV)	7.6	0.25	0.18

Table D.1: Values of  $E_s(R_0)$ ,  $\omega_0$  and  $B$  for different diatomic molecules

Therefore, the energies in the diatomic molecules can be expressed as a sum of rotational energies  $E_r = BK(K + 1)$  and vibrational energies  $E_v = \hbar\omega_0(\nu + 1/2)$  :

$$E_{s,\nu K} = E_s(R_0) + BK(K + 1) + \hbar\omega_0(\nu + \frac{1}{2})$$

We denote  $\Delta E_v$  the interval between two vibrational levels and  $\Delta E_r$  the interval between two rotational levels. For a given electric potential curve  $E_s(R)$ ,  $\Delta E_v \sim \omega_0 \sim 1/\sqrt{\mu}$ ,  $\Delta E_r \sim B \sim 1/\mu$  and  $E_s(R_0)$  however is independent of  $\mu$ . Because the mass ratio  $m_e/\mu$  between electron and reduced mass of nuclei is very small, therefore :

$$|E_s(R_0)| \gg |\Delta E_v| \gg |\Delta E_r| \quad (\text{D.5})$$

Different values of these quantities are shown in Table D.1 for different diatomic molecules [113].

In the Fig. D.3, we show a typical rovibrational structure of diatomic molecules.

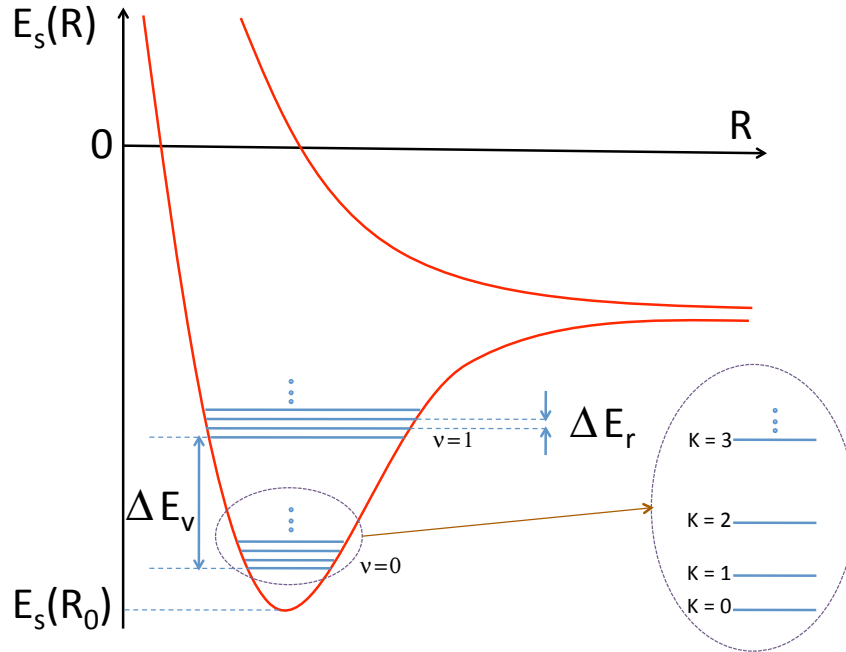


Figure D.3: The vibrational and rotational energy levels corresponding to D.5

## D.4 Hund's cases

In the previous discussion of the energy structure, symmetries ... , the influence of electronic spins is omitted <sup>5</sup>. Taking into account this influence is a very complicated problem but in the limits of strong or weak couplings between angular momenta and spins, the problem can be considerably simplified.

For atomic systems, the electronic Hamiltonian is invariant for rotation about any axis containing the nucleus, but for the diatomic molecules, the electronic system is symmetric only with the rotation about the internuclear axis. Therefore, only the projection of the electronic orbital angular momentum on the internuclear axis is a constant of motion.

We define the electrostatic energy  $\Delta E$  to define the coupling between the electrostatic field created by two nuclei and the electronic motion. Because of this interaction, the electrons move about the internuclear axis and their angular momentum projection  $\Lambda$  on the internuclear axis is used to describe the energy structure.

The coupling between the total electronic spin  $\vec{S}$  and the total electronic orbital angular momentum  $\vec{L}$  is described as : the electrons moving in the electric field created by two nuclei will produce a magnetic field  $B \sim \Lambda$  in the symmetric direction (i.e the internuclear axis). This magnetic field will interact with the electronic spin by means of magnetic moment  $\mu_{\vec{z}} \sim \Sigma$  ( $\Sigma$  is the projection of spin  $\vec{S}$  on the internuclear axis). Therefore, the coupling between the electronic spin and the total electronic orbital angular momentum is given by  $E_{so} \sim \Lambda\Sigma$  or more generally:

$$E_{so} = \bar{A}\vec{L}\vec{S}$$

To characterize the amplitude of this coupling, we define  $A = \bar{A}\hbar^2$

The rotation of two nuclei also creates a magnetic field which interacts with electronic spin. The coupling between the nuclear angular momentum  $\vec{N}$  and the electronic spin  $\vec{S}$  is :

$$E_{sr} = \bar{\gamma}\vec{N}\vec{S}$$

The amplitude of this coupling is  $\bar{\gamma} \sim B = \hbar^2/(2\mu R_0^2)$

By comparing these three coupling amplitudes  $|\Delta E|, |A|$  and  $B$ , we can define the different cases of Hund.

### D.4.1 Hund's case (a) : $|\Delta E| \gg |A| \gg B$

In the Hund's case (a), the electronic orbital angular momentum  $\vec{L}$  is strongly coupled to the internuclear axis by means of the strong axial field created by two nuclei and the electronic spin  $\vec{S}$  is also strongly coupled to  $\vec{L}$ . Therefore, the electronic spin interacts strongly with the internuclear axis.

The projections of  $\vec{L}$  and  $\vec{S}$  on the internuclear axis are thus well defined quantum numbers  $\Lambda$  and  $\Sigma$  respectively. A scheme of the coupling between different angular momenta is depicted in Fig. [D.4](#)

---

<sup>5</sup>Nuclear spin have a very small effect on the energy level

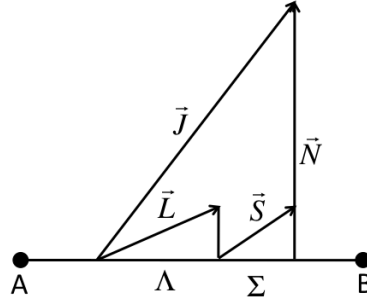


Figure D.4: Angular momenta for Hund's case (a)

In the Hund's case (a), the total wavefunction is an eigenfunction of  $J_z$  with the eigenvalue  $\Omega = \pm\Lambda + \Sigma$ . An we can find out a common basis for a set of operators  $\{\vec{S}^2, S_z, L_z, \vec{J}^2, J_z\}$  and we denote this basis as  $\{|S, \Sigma, \pm\Lambda, J, \Omega, M_J\rangle\}$ .

The energy structure is give by:

$$E_{s,\nu K\Omega} = E_s(R_0) + A\Lambda\Sigma + \hbar\omega_0\left(\nu + \frac{1}{2}\right) + B(J(J+1) - \Omega^2)$$

and we classify the different molecular states by  $^{2S+1}\Lambda_\Omega$

#### D.4.2 Hund's case (b) : $|\Delta E| \gg B \gg |A|$

In this case, the electronic orbital angular momentum  $\vec{L}$  is still strongly coupled to the internuclear axis but the electronic spin  $\vec{S}$  is weakly coupled to  $\vec{L}$  and therefore, also weakly coupled to the internuclear axis.

A scheme of coupling between different angular momenta is described in Fig. D.5.

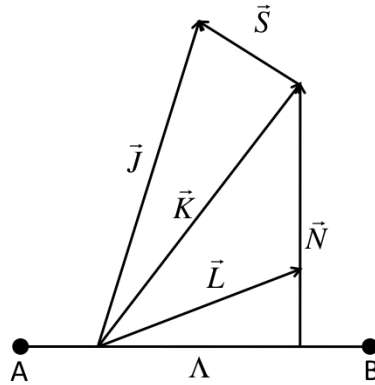


Figure D.5: Angular momenta for Hund's case (b)

In the Hund's case (b), there's a common basis for a set of operators  $\{\vec{S}^2, \vec{K}^2, K_z, \vec{J}^2, J_z\}$  and we denote this basis as  $\{|S, K, \pm\Lambda, J, M_J\rangle\}$ .

The expression for energy in this case is:

$$E_{s,\nu K} = E_s(R_0) + \hbar\omega_0\left(\nu + \frac{1}{2}\right) + BK(K+1) + \gamma[J(J+1) - K(K+1) - S(S+1)]$$

where  $\gamma = \bar{\gamma}\hbar^2$

**D.4.3 Hund's case (c) :**  $|A| \gg |\Delta E| \gg B$

**D.4.4 Hund's case (d) :**  $B \gg |\Delta E| \gg |A|$

**D.4.5 Hund's case (e) :**  $|A| \gg B \gg |\Delta E|$



# Appendix E

## Multiphoton transition in Lamb-Dicke regime

### E.1 Introduction

In this section, we generalize the previous results for the quasi-degenerate two-photon transition to the problem of N-photon excitation of strongly confined particles. I will use some of simple calculations to show that: if the laser detunings for each intermediate step is largrer than the corresponding single photon Doppler broadening, and the effective wavelength of N photon transition is much larger than the vibration amplitude of particles, then the N-photon absorption is a Doppler-free process.

The experiments using N-photon Doppler free spectroscopy with  $N \geq 3$  photons are very rare. The article of Cagnac-Grynberg-Biraben [105] showed theoretically that one can reach the Doppler free spectroscopy regime with  $N$  photons if the sum of  $N$  photon momenta is zero. But it's very difficult to set up a configuration where the sum of  $N$  photon impulsions is really zero. For that reason, with N-photon spectroscopy, the first-order Doppler effect can not be fully eliminated and the measurement at the natural linewidth accuracy can not be achieved with this method.

In 1976, G. Grynberg *et al.* [114] set up an experiment and suscessfully observed the three-photon Doppler free spectroscopy in thermal sodium gas. They used only two lasers : one at a fixed frequency  $\nu_1$  and the other one is tunable and they scanned the frequency  $\nu_2$  of this laser to observe the Doppler-free signal. The sodium atom absorbs two photon at frequency  $\nu_1$  but in two different directions  $\vec{k}_1$  and  $\vec{k}'_1$  and one photon ( $\nu_2, \vec{k}_2$ ) for the transition from the ground state  $3S_{1/2}$  to the excited state  $3P_{1/2}$ . If  $\vec{k}_1 + \vec{k}'_1 + \vec{k}_2 = 0$ , they can observe the Doppler-free three-photon transition. In their experimental conditions, the Doppler broadening is expected in the order of 1000 MHz, but the observed transition signals have 60 MHz width which is larger than the natural linewidth of the excited level  $\approx 10$  MHz. Therefore, we can conclude that the transition signals are strongly influenced by the residual Doppler effect.

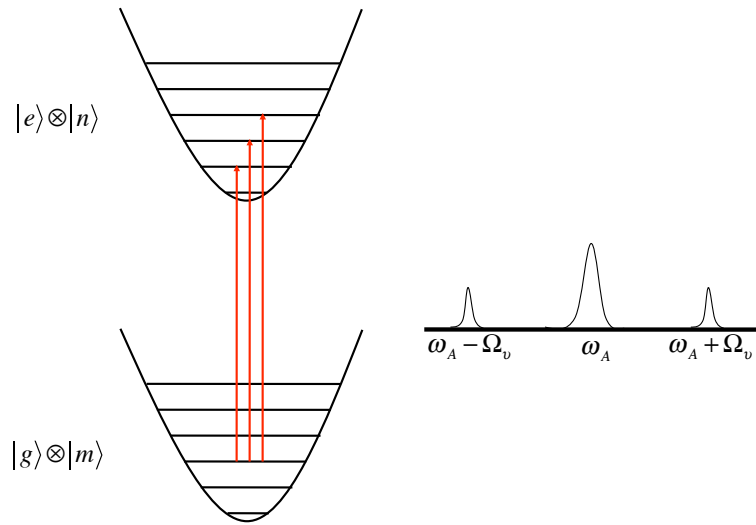


Figure E.1: Left : Single-photon transition from the ground state  $|g\rangle$  to the excited state  $|e\rangle$  of a trapped particles. Right : Sideband structure for the case of strongly confined particle

## E.2 Single-photon transition or Lamb-Dicke regime

Single-photon transition in the two-level atom is a standard problem. It can be found in many (under)graduate textbooks, for example "Optique Quantique 2" of A. Aspect and P. Grangier [115]. The transition rate for an immobile atom is given by

$$R \sim \frac{I}{\delta^2 + \Gamma^2/4}$$

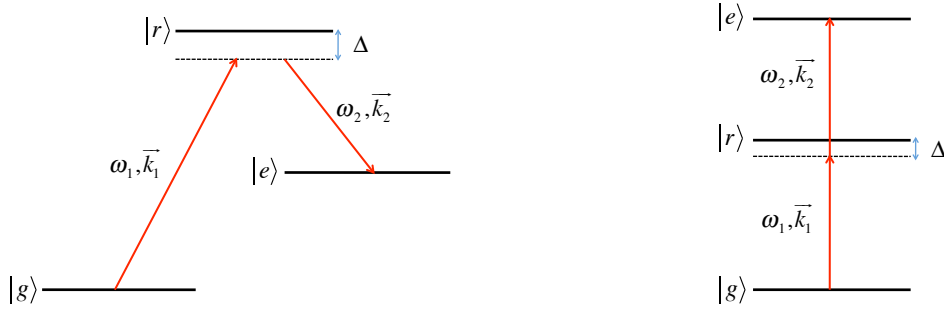
where  $I$  is the laser intensity,  $\delta = \omega_L - \omega_A$  is the laser detuning and  $\Gamma$  is the natural linewidth of the excited level.

The linewidth of the signal of single photon transition is then given by the natural linewidth  $\Gamma$ . But in the case of a cloud of thermal gas, the linewidth of the signal is replaced by the Doppler linewidth  $\Delta_D$  as

$$\Delta_D = \sqrt{\frac{8kT \ln(T)}{m} \frac{\omega_L}{c}}$$

In the case of trapped particles, the problem is also well studied but for a better understanding of multiphoton case, i will put here the key ideas.

Consider a very simple case of single-photon transition between two states of a two-level atom trapped in a harmonic potential  $V(z) = (1/2)m\Omega_\nu z^2$ . In the dressed atom picture, the state of particle is combined of internal atomic state  $\{|g\rangle, |e\rangle\}$  and the vibrational quantum state  $\{|n\rangle\}_n$ . Therefore, the transition between the ground state and the excited state can take place in many different ways as described in the Fig. E.1.

Figure E.2: Left :  $\Lambda$ -configuration. Right : Ladder configuration

If we tune the laser frequency as  $\omega_L = \omega_A + n\Omega_\nu$  (with  $n \in \mathbb{N}$ ) and observe the resonance, we obtain the sideband structure as in the left figure of E.1.

The transition rate  $R$  for the case of weak laser intensity is :

$$R \sim \frac{I}{(\delta - (n_e - n_g)\Omega_\nu)^2 + \Gamma^2/4} \cdot |\langle n_e | \exp(-ikz) | n_e \rangle|^2$$

In case of strong confinement of particle or mathematically  $k\langle z \rangle \ll 1$  the sideband structure disappears. This is the well-known Lamb-Dicke regime.

## E.3 Two-photon transition

For the two-photon transition in the three level system  $\{|e\rangle, |r\rangle, |g\rangle\}$ , we have two possible configuration (see E.2) :  $\Lambda$ -configuration and ladder configuration.

The two-photon transition rate for an immobile atom or thermal gas is a standard problem which has been studied by many authors, for example, B. Cagnac *et al.* [105].

Now, we consider that the particles are trapped in an harmonic potential as before  $V(z) = m\Omega_\nu z^2/2$  and the two photons are noted as  $\{\omega_1, \vec{k}_1\}$  and  $\{\omega_2, \vec{k}_2\}$ .

### E.3.1 $\Lambda$ -configuration

In this configuration, the atom absorb a photon  $\{\omega_1, \vec{k}_1\}$  and emit a photon  $\{\omega_2, \vec{k}_2\}$  through the stimulated emission process.

In case of  $\Lambda$ -configuration, the transition rate  $R$  is given by :

$$R \sim \left| \sum_{r, n_r} \frac{\langle e, n_e | \vec{D} \tilde{e}^{-ik_2 z} | r, n_r \rangle \langle r, n_r | \vec{D} \tilde{e}^{ik_1 z} | g, n_g \rangle}{\delta_{rg} - (n_r - n_g)\Omega_\nu} \right|^2$$

$$\stackrel{\Delta \gg \Omega_\nu}{\sim} \frac{I_1 I_2}{\Delta} \langle n_e | e^{i(k_1 - k_2)z} | n_g \rangle$$

where  $I_1$  and  $I_2$  are laser intensities of laser field 1 and 2 respectively.

If the atom is strongly confined in the trap i.e  $|k_1 - k_2|\langle z \rangle \ll 1$  then the sideband structure will disappear. The system is now in the Lamb-Dicke regime with a new characteristic parameter  $\eta = \delta k \cdot \langle z \rangle$ .

**Comment:**

In the  $\Lambda$ -configuration (or Raman configuration), if the detuning  $\Delta$  is very large, the two-photon transition from  $|g\rangle$  to  $|e\rangle$  of an immobile system is reduced to the single-photon transition of two-level atom with the effective Rabi frequency as:

$$\bar{\Omega} = -\frac{\Omega_1\Omega_2^*}{\Delta}$$

But for trapped ion, we need to include the influence of the harmonic potential, the effective Rabi frequency is therefore modified as :

$$\bar{\Omega}_{n',n} = -\frac{\Omega_1\Omega_2^*}{\Delta} \langle n' | e^{i\eta(\hat{a}+\hat{a}^\dagger)} | n \rangle$$

### E.3.2 Ladder configuration

The two-photon transition in this ladder configuration this the theme of the Chapter 3 of thesis.

The two-photon transition rate of two copropagating photons is :

$$R \sim \left| \sum_{r,n_r} \frac{\langle e, n_e | \vec{D} \vec{\epsilon} e^{ik_2 z} | r, n_r \rangle \langle r, n_r | \vec{D} \vec{\epsilon} e^{ik_1 z} | g, n_g \rangle}{\delta_{rg} - (n_r - n_g)\Omega_\nu} \right|^2$$

$$\stackrel{\Delta \gg \Omega_\nu}{\sim} \frac{I_1 I_2}{\Delta} \langle n_e | e^{i(k_1+k_2)z} | n_g \rangle$$

The Lamb-Dicke parameter  $\eta = (k_1 + k_2)\langle z \rangle$

The two-photon transition rate of two counterpropagating photons is :

$$R \sim \left| \sum_{r,n_r} \frac{\langle e, n_e | \vec{D} \vec{\epsilon} e^{-ik_2 z} | r, n_r \rangle \langle r, n_r | \vec{D} \vec{\epsilon} e^{ik_1 z} | g, n_g \rangle}{\delta_{rg} - (n_r - n_g)\Omega_\nu} \right|^2$$

$$\stackrel{\Delta \gg \Omega_\nu}{\sim} \frac{I_1 I_2}{\Delta} \langle n_e | e^{i(k_1-k_2)z} | n_g \rangle$$

The Lamb-Dicke parameter  $\eta = \delta k \langle z \rangle$

## E.4 Dressed atom approach

The N-photon transition from the ground state  $|g\rangle$  to the excited state  $|e\rangle$  is described in the figure E.3. We note N photons as  $\{\omega_1, \omega_2, \dots, \omega_N\}$ , the intermediate states as  $\{|1\rangle |2\rangle, \dots, |N-1\rangle\}$ . We suppose that the photon with frequency  $\omega_i$  is responsible only for the transition between state  $|i-1\rangle$  and  $|i\rangle$ .

The particle's motion is supposed to be harmonic oscillation around a fixed position i.e the particules is confined in a harmonic potential of form  $\frac{1}{2}m\Omega^2 r^2$ . To include the ion vibration in our calculation, for each atomic state  $|i\rangle$  we associate with a vibrational state

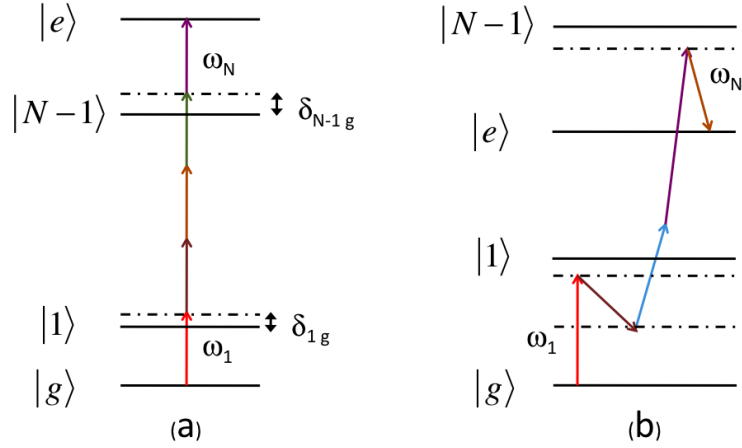


Figure E.3: N-photon transition configuration. (a) : ladder configuration. (b) : random configuration

$|\nu_i\rangle$ , and we have a new quantum state  $|i, \nu_i\rangle$ . And we rewrite the N-photon excitation process as in the following sequence :

$$|g, \nu_0\rangle \xrightarrow{\omega_1} |1, \nu_1\rangle \xrightarrow{\omega_2} \dots \xrightarrow{\omega_{N-1}} |N-1, \nu_{N-1}\rangle \xrightarrow{\omega_N} |e, \nu_N\rangle \quad (\text{E.1})$$

We will use an approach which is similar to that in [105]. The Hamiltonian of the system "Ion + photons" is given by :

$$H = H_0 + V = H_{ion}^{int} + H_{ion}^{ext} + \sum_n H_n^L + \sum_n V_n$$

where,

the internal Hamiltonian of ion is :

$$H_{ion}^{int} = E_g |g\rangle\langle g| + \sum_{j=1}^{N-1} (E_j + \frac{1}{2}i\hbar\Gamma_j) |j\rangle\langle j| + (E_e + \frac{1}{2}i\hbar\Gamma_e) |e\rangle\langle e|$$

the external Hamiltonian of ion is :

$$H_{ion}^{ext} = \frac{P_z^2}{2m} + \frac{1}{2}m\Omega_\nu^2 z^2 = \hbar\Omega_\nu (\hat{a}_\nu^\dagger \hat{a}_\nu + \frac{1}{2})$$

the Hamiltonian of laser fields of frequencies  $\omega_n$  ( $n = 1, \dots, N$ ) is

$$H_n^L = \hbar\omega_n \hat{a}_n^\dagger \hat{a}_n$$

and the laser-ion couplings are given by:

$$V_n = -\vec{D}\vec{E}_n \approx (-\vec{d}\vec{\epsilon}E_L) |n\rangle\langle n-1| \hat{a}_n e^{ik_n z} + h.c = i\alpha_{n-1n} |n\rangle\langle n-1| \hat{a}_n e^{ik_n z} + h.c$$

For the unperturbed Hamiltonian, the eigenstates  $|j, \nu_j, n_1, \dots, n_N\rangle$  (with  $j = g, e, 1, \dots, N$ ) correspond to the eigenenergies

$$E_j^{total} = E_j + \frac{1}{2}i\hbar\Gamma_j + \sum_{k=1}^N (n_k + \frac{1}{2})\hbar\omega_k + (\nu_j + \frac{1}{2})\hbar\Omega_\nu$$

Using the  $N^{th}$ -order perturbation theory to calculate the eigenstates  $\overline{|j, \nu_j, n_1, \dots, n_N\rangle}$ , we can deduce the N-photon transition rate for trapped particles as:

$$\begin{aligned} \Gamma_N &= \frac{\Gamma_e}{(\delta_{eg} - (\nu_N - \nu_0)\Omega)^2 + \Gamma_e^2/4} \\ &\quad \cdot \left| \langle e, \nu_N, n_1 - 1, \dots, n_N - 1 | V_N \frac{1}{E_g - H_0} \dots V_2 \frac{1}{E_g - H_0} V_1 | g, \nu_0, n_1, \dots, n_N \rangle \right|^2 \\ &= \frac{\Gamma_e}{(\delta_{eg} - (\nu_N - \nu_0)\Omega)^2 + \Gamma_e^2/4} \\ &\quad \cdot \left| \sum_{\nu_1, \dots, \nu_{N-1}} \langle e, \nu_N, n_1 - 1, \dots, n_N - 1 | V_N | N - 1, \nu_{N-1}, n_1 - 1, \dots, n_{N-1} - 1, n_N \rangle \right. \\ &\quad \cdot \frac{1}{\delta_{N-1g} - (\nu_{N-1} - \nu_0)\Omega + i\Gamma_{N-1}/2} \\ &\quad \cdot \langle N - 1, \nu_{N-1}, n_1 - 1, \dots, n_{N-1} | V_{N-1} | N - 2, \nu_{N-2}, n_1 - 1, \dots, n_{N-1}, n_N \rangle \\ &\quad \left. \dots \frac{1}{\delta_{1g} - (\nu_1 - \nu_0)\Omega + i\Gamma_1/2} \langle 1, \nu_N, n_1 - 1, n_2, \dots, n_N | V_1 | g, \nu_0, n_1, \dots, n_N \rangle \right|^2 \\ &= \Omega_{eN-1}^2 \Omega_{N-1N-2}^2 \dots \Omega_{1g}^2 \cdot \frac{\Gamma_e}{(\delta_{eg} - (\nu_N - \nu_0)\Omega)^2 + \Gamma_e^2/4} \\ &\quad \cdot \left| \sum_{\nu_1, \dots, \nu_{N-1}} \frac{\langle \nu_N | e^{i\vec{k}_N \vec{r}} | \nu_{N-1} \rangle \langle \nu_{N-1} | \dots | \nu_1 \rangle \langle \nu_1 | e^{i\vec{k}_1 \vec{r}} | \nu_0 \rangle}{(\delta_{N-1g} - (\nu_{N-1} - \nu_0)\Omega + i\Gamma_{N-1}/2) \dots (\delta_{1g} - (\nu_1 - \nu_0)\Omega + i\Gamma_1/2)} \right|^2 \end{aligned}$$

if the laser detunings  $\delta_{ig} \gg (\nu_i - \nu_0)\Omega$  for  $i = 1, \dots, N - 1$ , we will have a simple formula:

$$\Gamma_N = \frac{\Omega_{eN-1}^2 \dots \Omega_{1g}^2}{\delta_{N-1g}^2 \dots \delta_{1g}^2} \cdot \frac{\Gamma_e}{(\delta_{eg} - (\nu_N - \nu_0)\Omega)^2 + \Gamma_e^2/4} \langle \nu_N | e^{i(\vec{k}_1 + \dots + \vec{k}_N) \vec{r}} | \nu_0 \rangle$$

in the Lamb-Dicke regime i.e  $(\sum_{j=1}^N \vec{k}_j) \cdot \vec{r} \ll 1$ , then we have :

$$\Gamma_N = \frac{\Omega_{eN-1}^2 \dots \Omega_{1g}^2}{\delta_{N-1g}^2 \dots \delta_{1g}^2} \cdot \frac{\Gamma_e}{\delta_{eg}^2 + \Gamma_e^2/4}$$

And using again the second-order perturbation theory to calculate the eigenenergies  $\overline{E_j^{total}}$  of the unperturbed Hamiltonian  $H$ , we also obtain the ac Stark shifts as in the case of two-photon:

$$\begin{aligned} \delta E_g &\approx \overline{E_g^{total}} - E_g^{total} = \hbar \frac{\Omega_{g1}^2}{\delta_{g1}} \\ \delta E_j &\approx \overline{E_j^{total}} - E_j^{total} = \hbar \frac{\Omega_{j,j+1}^2}{\delta_{j,j+1}} - \hbar \frac{\Omega_{j-1,j}^2}{\delta_{j-1,j}} \end{aligned}$$

$$\delta E_e \approx \overline{E}_e^{total} - E_e^{total} = -\hbar \frac{\Omega_{N-1,e}^2}{\delta_{N-1,e}}$$

with  $j = 1, 2, \dots, N-1$

**Conclusion :**

In the N-photon spectroscopy, if we choose the laser detunings  $\delta_{jg} \gg k_j v_0$ ,  $j = 1, \dots, N-1$  and a configuration where  $(\sum_{j=1}^N \vec{k}_j) \cdot \vec{r} \ll 1$  (Lamb-Dicke regime) then the Doppler effect on the signal can be fully eliminated.

## E.5 Evolution operator approach

In the calculation of N-photon transition rate, we can use the evolution operator formalism instead of  $N^{th}$ -perturbation theory as follows:

We will use the notation of unperturbed Hamiltonian  $H_0$ , laser-ion coupling  $V$  as above. The evolution operator in the interaction picture is given by :

$$U(T) = \mathcal{T} \left( e^{-\frac{i}{\hbar} \int_0^T V(t) dt} \right) = \sum_{N=0}^{\infty} U^{(N)}(T)$$

where  $\mathcal{T}$  is the time-ordering operator,

$V(t)$  is the laser-ion couplings in the interaction picture :

$$V(t) = e^{-\frac{i}{\hbar} H_0 t} V e^{\frac{i}{\hbar} H_0 t} = \sum_{n=1}^N V_n(t)$$

and

$$\begin{aligned} U^{(N)}(T) &= \left( -\frac{i}{\hbar} \right)^N \frac{1}{N!} \int_0^T \dots \int_0^T \mathcal{T} [V(t_1) \dots V(t_N)] dt_1 \dots dt_N \\ &= \left( -\frac{i}{\hbar} \right)^N \int_0^T \dots \int_0^T \theta(t_N - t_{N-1}) \dots \theta(t_2 - t_1) V(t_1) \dots V(t_N) dt_1 \dots dt_N \end{aligned}$$

Hence, the amplitude of  $N$ -photon transition from  $|i\rangle = |g, \nu_0, n_1, \dots, n_N\rangle$  to  $|f\rangle = |e, \nu_N, n_1 - 1, \dots, n_N - 1\rangle$  is:

$$\begin{aligned} \langle f | U^{(N)}(T) | i \rangle &= \left( -\frac{i}{\hbar} \right)^N \int_0^T \dots \int_0^T \theta(t_N - t_{N-1}) \dots \theta(t_2 - t_1) \times \\ &\quad \times \langle e, \nu_N, n_1 - 1, \dots, n_N - 1 | V(t_1) \dots V(t_N) | g, \nu_0, n_1, \dots, n_N \rangle \end{aligned}$$

Because the N-photon transition follows the order as described in [E.1](#), then we can rewrite the amplitude as:

$$\begin{aligned}
\langle f|U^{(N)}(T)|i\rangle &= \left(-\frac{i}{\hbar}\right)^N \sum_{\nu_{N-1}} \cdots \sum_{\nu_1} \int_0^T \cdots \int_0^T \theta(t_N - t_{N-1}) \cdots \theta(t_2 - t_1) \cdot \\
&\cdot \langle e, \nu_N, n_1 - 1, \dots, n_N - 1 | V_N(t_N) | N - 1, \nu_{N-1}, n_1 - 1, \dots, n_{N-1} - 1, n_N \rangle \cdot \\
&\cdot \langle N - 1, \nu_{N-1}, n_1 - 1, \dots, n_{N-1} - 1, n_N | V_{N-1}(t_{N-1}) | N - 2, \nu_{N-2}, n_1 - 1, \dots, n_{N-2} - 1, n_{N-1}, n_N \rangle \cdot \\
&\cdots \\
&\cdot \langle e, \nu_1, n_1 - 1, n_2 \cdots, n_N | V_1(t_1) | g, \nu_0, n_1, \dots, n_N \rangle
\end{aligned}$$

For the sake of simplicity, we omit the spontaneous effects in the calculations. This effect will be included at the final consideration in the phenomenological way.

Using the following relation :

$$H_0|j, \nu_j, n_1, \dots, n_N\rangle = (E_j + \sum_{k=1}^N (n_k + \frac{1}{2})\hbar\omega_k + (\nu_j + \frac{1}{2})\hbar\Omega_\nu)|j, \nu_j, n_1, \dots, n_N\rangle$$

we have <sup>1</sup>

$$\begin{aligned}
\langle f|U^{(N)}(T)|i\rangle &= \left(-\frac{i}{\hbar}\right)^N \sum_{\nu_{N-1}} \cdots \sum_{\nu_1} \int_0^T \cdots \int_0^T dt_1 \cdots dt_N \theta(t_N - t_{N-1}) \cdots \theta(t_2 - t_1) \times \\
&\times e^{i(-\delta_{e,N-1} + (\nu_e - \nu_{N-1})\Omega_\nu)t_N} \langle e, \nu_e, n_N - 1 | V_N | N - 1, \nu_{N-1}, n_N \rangle \times \\
&\times e^{i(-\delta_{N-1,N-2} + (\nu_{N-1} - \nu_{N-2})\Omega_\nu)t_{N-1}} \langle N - 1, \nu_{N-1}, n_{N-1} - 1 | V_{N-1} | N - 2, \nu_{N-2}, n_{N-1} \rangle \times \\
&\times \cdots \times \\
&\times e^{i(-\delta_{1g} + (\nu_1 - \nu_g)\Omega_\nu)t_1} \langle 1, \nu_1, n_1 - 1 | V_1 | g, \nu_0, n_1 \rangle
\end{aligned}$$

where  $\delta_{j,j-1} = \omega_j - (E_j - E_{j-1})/\hbar$  the detuning of  $j^{th}$  photon.

To calculate this integral, we use the following relation :

$$\theta(t) = \frac{i}{2\pi} \int_{-\infty}^{\infty} d\omega \frac{e^{-i\omega t}}{\omega + i\epsilon}$$

therefore,

$$\begin{aligned}
\langle f|U^{(N)}(T)|i\rangle &= \sum_{\nu_{N-1}} \cdots \sum_{\nu_1} \int_0^T \cdots \int_0^T dt_1 \cdots dt_N \int \cdots \int d\tilde{\omega}_{N-1} \cdots d\tilde{\omega}_1 \times \\
&\times g_{\nu_{N-1}, \dots, \nu_1}(\tilde{\omega}_{N-1}, \dots, \tilde{\omega}_1) \\
&\times \{\exp[i(-\delta_{e,N-1} - \tilde{\omega}_{N-1} + (\nu_e - \nu_{N-1})\Omega_\nu)t_N]\} \times \\
&\times \exp[i(-\delta_{N-1,N-2} + \tilde{\omega}_{N-1} - \tilde{\omega}_{N-2} + (\nu_{N-1} - \nu_{N-2})\Omega_\nu)t_{N-1}] \times \\
&\times \cdots \times \\
&\times \exp[i(-\delta_{21} + \tilde{\omega}_2 - \tilde{\omega}_1 + (\nu_2 - \nu_1)\Omega_\nu)t_2] \times \\
&\times \exp[i(-\delta_{1g} + \tilde{\omega}_1 + (\nu_1 - \nu_g)\Omega_\nu)t_1] \}
\end{aligned}$$

where

---

<sup>1</sup>Here, we keep only the laser modes that couple with the corresponding transitions

$$g_{\nu_{N-1}, \dots, \nu_1}(\tilde{\omega}_{N-1}, \dots, \tilde{\omega}_1) = \left(-\frac{i}{\hbar}\right)^N \left(\frac{i}{2\pi}\right)^{N-1} \frac{\langle V_N \rangle \dots \langle V_1 \rangle}{(\tilde{\omega}_{N-1} + i\epsilon) \dots (\tilde{\omega}_1 + i\epsilon)}$$

By changing the variables as:

$$\tilde{\Omega}_1 = -\delta_{1g} + \tilde{\omega}_1 + (\nu_1 - \nu_g)\Omega_\nu$$

$$\tilde{\Omega}_2 = -\delta_{21} + \tilde{\omega}_2 - \tilde{\omega}_1 + (\nu_2 - \nu_1)\Omega_\nu$$

...

$$\tilde{\Omega}_{N-1} = -\delta_{N-1, N-2} + \tilde{\omega}_{N-1} - \tilde{\omega}_{N-2} + (\nu_{N-1} - \nu_{N-2})\Omega_\nu$$

the transition amplitude is rewritten as

$$\begin{aligned} \langle f|U^{(N)}(T)|i\rangle &= \sum_{\nu_{N-1}} \dots \sum_{\nu_1} \int_0^T \dots \int_0^T dt_1 \dots dt_N \int \dots \int d\tilde{\Omega}_{N-1} \dots d\tilde{\Omega}_1 \times \\ &\quad \times g_{\nu_{N-1}, \dots, \nu_1} \left( \sum_{n=1}^{N-1} \tilde{\Omega}_n + \delta_{N-1, g} - (\nu_{N-1} - \nu_g)\Omega_\nu, \dots, \tilde{\Omega}_1 + \delta_{1g} - (\nu_1 - \nu_g)\Omega_\nu \right) \\ &\quad \times \left\{ \exp[i(-\delta_{e,g} - (\tilde{\Omega}_{N-1} + \dots + \tilde{\Omega}_1) + (\nu_e - \nu_g)\Omega_\nu)t_N] \times \right. \\ &\quad \times \exp[i\tilde{\Omega}_{N-1}t_{N-1}] \times \dots \times \exp[i\tilde{\Omega}_2t_2] \times \exp[i\tilde{\Omega}_1t_1] \left. \right\} \\ &= (2\pi)^{N-1} \sum_{\nu_{N-1}} \dots \sum_{\nu_1} g_{\nu_{N-1}, \dots, \nu_1} (\delta_{N-1, g} - (\nu_{N-1} - \nu_g)\Omega_\nu, \dots, \delta_{1g} - (\nu_1 - \nu_g)\Omega_\nu) \times \\ &\quad \times \int_0^T dt_N \exp[i(-\delta_{e,g} + (\nu_e - \nu_g)\Omega_\nu)t_N] \end{aligned}$$

The probability of the transition from ground state  $|g\rangle$  to the excited state  $|e\rangle$  at time  $T$  is:

$$\begin{aligned} P_N(T) &= |\langle f|U^{(N)}(T)|i\rangle|^2 \\ &= (2\pi)^{2N-2} \left| \sum_{\nu_{N-1}, \dots, \nu_1} g_{\nu_{N-1}, \dots, \nu_1} (\delta_{N-1, g} - (\nu_{N-1} - \nu_g)\Omega_\nu, \dots, \delta_{1g} - (\nu_1 - \nu_g)\Omega_\nu) \right|^2 \\ &\quad \times \int_0^T \int_0^T dt_N dt'_N \exp[i(-\delta_{e,g} + (\nu_e - \nu_g)\Omega_\nu)t_N] \times \exp[-i(-\delta_{e,g} + (\nu_e - \nu_g)\Omega_\nu)t'_N] \end{aligned}$$

The double integrals can be evaluated as follows:

$$\begin{aligned} I &= \int_0^T \int_0^T dt_N dt'_N \exp[i(-\delta_{e,g} + (\nu_e - \nu_g)\Omega_\nu)t_N] \times \exp[-i(-\delta_{e,g} + (\nu_e - \nu_g)\Omega_\nu)t'_N] \\ &= \int_{-t'_N}^{T-t'_N} \int_0^T dt_N dt'_N \exp[i(-\delta_{e,g} + (\nu_e - \nu_g)\Omega_\nu)t_N] \\ &\approx T \int_{-\infty}^{\infty} dt \exp[i(-\delta_{e,g} + (\nu_e - \nu_g)\Omega_\nu)t] \end{aligned}$$

Then, the N-photon transition rate is given by:

$$\begin{aligned} W_N &:= P(T)/T \\ &= \left| \left(-\frac{i}{\hbar}\right)^N \sum_{\nu_{N-1}, \dots, \nu_1} \frac{\langle V_N \rangle \dots \langle V_1 \rangle}{(\delta_{N-1, g} - (\nu_{N-1} - \nu_g)\Omega_\nu + i\epsilon) \dots (\delta_{1g} - (\nu_1 - \nu_g)\Omega_\nu + i\epsilon)} \right|^2 \times \\ &\quad \times \int_{-\infty}^{\infty} dt \exp[-i(\delta_{e,g} - (\nu_e - \nu_g)\Omega_\nu)t] \end{aligned}$$

If we take into account the effect of spontaneous emissions, the previous formula will be modified as:

$$\begin{aligned}
W_N &= \left| \left( -\frac{i}{\hbar} \right)^N \sum_{\nu_{N-1}, \dots, \nu_1} \frac{\langle V_N \rangle \cdots \langle V_1 \rangle}{(\delta_{N-1,g} - (\nu_{N-1} - \nu_g)\Omega_\nu + i\Gamma_{N-1}) \cdots (\delta_{1g} - (\nu_1 - \nu_g)\Omega_\nu + i\Gamma_1)} \right|^2 \times \\
&\times \int_{-\infty}^{\infty} dt \exp[-i(\delta_{e,g} - (\nu_e - \nu_g)\Omega_\nu)t + \frac{1}{2}\Gamma_e|t|] \\
&= \left| \left( -\frac{i}{\hbar} \right)^N \sum_{\nu_{N-1}, \dots, \nu_1} \frac{\langle V_N \rangle \cdots \langle V_1 \rangle}{(\delta_{N-1,g} - (\nu_{N-1} - \nu_g)\Omega_\nu + i\Gamma_{N-1}) \cdots (\delta_{1g} - (\nu_1 - \nu_g)\Omega_\nu + i\Gamma_1)} \right|^2 \times \\
&\times \frac{\Gamma_e}{(\delta_{e,g} - (\nu_e - \nu_g)\Omega_\nu)^2 + \Gamma_e^2/4}
\end{aligned}$$

We found the same result as that obtained from the N-order perturbation theory.

# References

- [1] Randolph Pohl, Aldo Antognini, François Nez, Fernando D. Amaro, François Biraben, João M. R. Cardoso, Daniel S. Covita, Andreas Dax, Satish Dhawan, Luis M. P. Fernandes, Adolf Giesen, Thomas Graf, Theodor W. Hänsch, Paul Indelicato, Lucile Julien, Cheng-Yang Kao, Paul Knowles, Eric-Olivier Le Bigot, Yi-Wei Liu, José A. M. Lopes, Livia Ludhova, Cristina M. B. Monteiro, Franoise Mulhauser, Tobias Nebel, Paul Rabinowitz, Joaquim M. F. dos Santos, Lukas A. Schaller, Karsten Schuhmann, Catherine Schwob, David Taqqu, João F. C. A. Veloso, and Franz Kottmann. The size of the proton. *Nature*, 466(7303):213–216, 2010.
- [2] Aldo Antognini, François Nez, Karsten Schuhmann, Fernando D. Amaro, François Biraben, João M. R. Cardoso, Daniel S. Covita, Andreas Dax, Satish Dhawan, Marc Diepold, Luis M. P. Fernandes, Adolf Giesen, Andrea L. Gouvea, Thomas Graf, Theodor W. Hänsch, Paul Indelicato, Lucile Julien, Cheng-Yang Kao, Paul Knowles, Franz Kottmann, Eric-Olivier Le Bigot, Yi-Wei Liu, José A. M. Lopes, Livia Ludhova, Cristina M. B. Monteiro, Franoise Mulhauser, Tobias Nebel, Paul Rabinowitz, Joaquim M. F. dos Santos, Lukas A. Schaller, Catherine Schwob, David Taqqu, João F. C. A. Veloso, Jan Vogelsang, and Randolph Pohl. Proton structure from the measurement of 2s-2p transition frequencies of muonic hydrogen. *Science*, 339(6118):417–420, 2013.
- [3] M. Fischer, N. Kolachevsky, M. Zimmermann, R. Holzwarth, Th. Udem, T. W. Hänsch, M. Abgrall, J. Grünert, I. Maksimovic, S. Bize, H. Marion, F. Pereira Dos Santos, P. Lemonde, G. Santarelli, P. Laurent, A. Clairon, C. Salomon, M. Haas, U. D. Jentschura, and C. H. Keitel. New limits on the drift of fundamental constants from laboratory measurements. *Phys. Rev. Lett.*, 92:230802, Jun 2004.
- [4] C. W. Chou, D. B. Hume, J. C. J. Koelemeij, D. J. Wineland, and T. Rosenband. Frequency comparison of two high-accuracy  $al^+$  optical clocks. *Phys. Rev. Lett.*, 104:070802, Feb 2010.
- [5] R. Le Targat, L. Lorini, Y. Le Coq, M. Zawada, J. Guna, M. Abgrall, M. Gurov, P. Rosenbusch, D. G. Rovera, B. Nagrny, R. Gartman, P. G. Westergaard, M. E. Tobar, M. Lours, G. Santarelli, A. Clairon, S. Bize, P. Laurent, P. Lemonde, and J. Lodewyck. Experimental realization of an optical second with strontium lattice clocks. *Nat Commun*, 4, 2010.
- [6] Thomas Beier, Hartmut Häffner, Nikolaus Hermanspahn, Savely G. Karshenboim, H.-Jürgen Kluge, Wolfgang Quint, Stefan Stahl, José Verdú, and Günther Werth. New determination of the electron’s mass. *Phys. Rev. Lett.*, 88:011603, Dec 2001.

- [7] Andreas Wicht, Joel M Hensley, Edina Sarajlic, and Steven Chu. A preliminary measurement of the fine structure constant based on atom interferometry. *Physica Scripta*, 2002(T102):82, 2002.
- [8] Rym Bouchendira, Pierre Cladé, Saïda Guellati-Khélifa, François Nez, and François Biraben. New determination of the fine structure constant and test of the quantum electrodynamics. *Phys. Rev. Lett.*, 106:080801, Feb 2011.
- [9] S. Schiller and V. Korobov. Tests of time independence of the electron and nuclear masses with ultracold molecules. *Phys. Rev. A*, 71:032505, Mar 2005.
- [10] Jean-Philippe Uzan. The fundamental constants and their variation: observational and theoretical status. *Rev. Mod. Phys.*, 75:403–455, Apr 2003.
- [11] X. Calmet and H. Fritzsch. The cosmological evolution of the nucleon mass and the electroweak coupling constants. *The European Physical Journal C - Particles and Fields*, 24(4):639–642, 2002.
- [12] Paul Langacker, Gino Segrè, and Matthew J. Strassler. Implications of gauge unification for time variation of the fine structure constant. *Physics Letters B*, 528(12):121 – 128, 2002.
- [13] A. Shelkovernikov, R. J. Butcher, C. Chardonnet, and A. Amy-Klein. Stability of the proton-to-electron mass ratio. *Phys. Rev. Lett.*, 100:150801, Apr 2008.
- [14] Lowell S. Brown and Gerald Gabrielse. Geonium theory: Physics of a single electron or ion in a penning trap. *Rev. Mod. Phys.*, 58:233–311, Jan 1986.
- [15] Jr. Robert S. Van Dyck, Dean L. Farnham, Steven L. Zafonte, and Paul B. Schwinberg. High precision penning trap mass spectroscopy and a new measurement of the proton’s “atomic mass”. *AIP Conference Proceedings*, 457(1):101–110, 1999.
- [16] A. Solders, I. Bergström, Sz. Nagy, M. Suhonen, and R. Schuch. Determination of the proton mass from a measurement of the cyclotron frequencies of  $d^+$  and  $H_2^+$  in a penning trap. *Phys. Rev. A*, 78:012514, Jul 2008.
- [17] H. Häffner, T. Beier, N. Hermanspahn, H.-J. Kluge, W. Quint, S. Stahl, J. Verdú, and G. Werth. High-accuracy measurement of the magnetic moment anomaly of the electron bound in hydrogenlike carbon. *Phys. Rev. Lett.*, 85:5308–5311, Dec 2000.
- [18] R. S. Van Dyck and P. B. Schwinberg. Preliminary proton/electron mass ratio using a compensated quadrupole penning trap. *Phys. Rev. Lett.*, 47:395–398, Aug 1981.
- [19] D. J. Wineland, J. J. Bollinger, and Wayne M. Itano. Laser-fluorescence mass spectroscopy. *Phys. Rev. Lett.*, 50:628–631, Feb 1983.
- [20] Sven Sturm, Anke Wagner, Birgit Schabinger, and Klaus Blaum. Phase-sensitive cyclotron frequency measurements at ultralow energies. *Phys. Rev. Lett.*, 107:143003, Sep 2011.

- [21] Christian G. Parthey, Arthur Matveev, Janis Alnis, Birgitta Bernhardt, Axel Beyer, Ronald Holzwarth, Aliaksei Maistrou, Randolph Pohl, Katharina Predehl, Thomas Udem, Tobias Wilken, Nikolai Kolachevsky, Michel Abgrall, Daniele Rovera, Christophe Salomon, Philippe Laurent, and Theodor W. Hänsch. Improved measurement of the hydrogen  $1s - 2s$  transition frequency. *Phys. Rev. Lett.*, 107:203001, Nov 2011.
- [22] Arthur Matveev, Christian G. Parthey, Katharina Predehl, Janis Alnis, Axel Beyer, Ronald Holzwarth, Thomas Udem, Tobias Wilken, Nikolai Kolachevsky, Michel Abgrall, Daniele Rovera, Christophe Salomon, Philippe Laurent, Gesine Grosche, Osama Terra, Thomas Legero, Harald Schnatz, Stefan Weyers, Brett Altschul, and Theodor W. Hänsch. Precision measurement of the hydrogen  $1s-2s$  frequency via a 920-km fiber link. *Phys. Rev. Lett.*, 110:230801, Jun 2013.
- [23] Michael I. Eides, Howard Grotch, and Valery A. Shelyuto. *Theory of light hydrogenic bound states*. Springer-Verlag Berlin Heidelberg, 2007.
- [24] Th. Udem, A. Huber, B. Gross, J. Reichert, M. Prevedelli, M. Weitz, and T. W. Hänsch. Phase-coherent measurement of the hydrogen  $1S - 2S$  transition frequency with an optical frequency interval divider chain. *Phys. Rev. Lett.*, 79:2646–2649, Oct 1997.
- [25] C. Schwob, L. Jozefowski, B. de Beauvoir, L. Hilico, F. Nez, L. Julien, F. Biraben, O. Acaf, J.-J. Zondy, and A. Clairon. Optical frequency measurement of the  $2S - 12D$  transitions in hydrogen and deuterium: Rydberg constant and lamb shift determinations. *Phys. Rev. Lett.*, 82:4960–4963, Jun 1999.
- [26] L. Hilico, N. Billy, B. Grémaud, and D. Delande. Ab initio calculation of the  $j = 0$  and  $j = 1$  states of the  $H_2^+$ ,  $D_2^+$  and  $HD^+$  molecular ions. *The European Physical Journal D - Atomic, Molecular, Optical and Plasma Physics*, 12(3):449–466, 2000.
- [27] V. I. Korobov. Coulomb three-body bound-state problem: Variational calculations of nonrelativistic energies. *Phys. Rev. A*, 61:064503, May 2000.
- [28] Vladimir I. Korobov, L. Hilico, and J.-Ph. Karr. Calculation of the relativistic bethe logarithm in the two-center problem. *Phys. Rev. A*, 87:062506, Jun 2013.
- [29] L Hilico, N Billy, B Grémaud, and D Delande. Polarizabilities, light shifts and two-photon transition probabilities between  $J = 0$  states of the  $H_2^+$  and  $D_2^+$  molecular ions. *Journal of Physics B: Atomic, Molecular and Optical Physics*, 34(3):491, 2001.
- [30] F. Bielsa. *Spectroscopie vibrationnelle à deux photons de l'ion  $H_2^+$  : développement d'une source laser à 9,166  $\mu\text{m}$* . PhD thesis, Université Paris VI, Laboratoire Kastler Brossel, 2007.
- [31] Jean-Philippe Karr, Franck Bielsa, Albane Douillet, Jofre Pedregosa Gutierrez, Vladimir I. Korobov, and Laurent Hilico. Vibrational spectroscopy of  $H_2^+$ : Hyperfine structure of two-photon transitions. *Phys. Rev. A*, 77:063410, Jun 2008.

- [32] J. C. J. Koelemeij, B. Roth, A. Wicht, I. Ernsting, and S. Schiller. Vibrational spectroscopy of  $\text{HD}^+$  with 2-ppb accuracy. *Phys. Rev. Lett.*, 98:173002, Apr 2007.
- [33] U. Bressel, A. Borodin, J. Shen, M. Hansen, I. Ernsting, and S. Schiller. Manipulation of individual hyperfine states in cold trapped molecular ions and application to  $\text{HD}^+$  frequency metrology. *Phys. Rev. Lett.*, 108:183003, May 2012.
- [34] J.C.J. Koelemeij, D.W.E. Noom, D. Jong, M.A. Haddad, and W. Ubachs. Observation of the  $v=8v=0$  vibrational overtone in cold trapped  $\text{hd}^+$ . *Applied Physics B*, 107(4):1075–1085, 2012.
- [35] B. D. Esry and H. R. Sadeghpour. Adiabatic formulation of heteronuclear hydrogen molecular ion. *Phys. Rev. A*, 60:3604–3617, Nov 1999.
- [36] D. J. Berkeland, J. D. Miller, J. C. Bergquist, W. M. Itano, and D. J. Wineland. Minimization of ion micromotion in a paul trap. *Journal of Applied Physics*, 83(10):5025–5033, 1998.
- [37] L. Hornekær, N. Kjærgaard, A. M. Thommesen, and M. Drewsen. Structural properties of two-component coulomb crystals in linear paul traps. *Phys. Rev. Lett.*, 86:1994–1997, Mar 2001.
- [38] J.-P. Karr, A. Douillet, and L. Hilico. Photodissociation of trapped  $\text{H}_2^+$  ions for REMPD spectroscopy. *Appl. Phys. B*, 107:10431052, 2012.
- [39] Yang Weijun, R. Alheit, and G. Werth. Vibrational population of  $\text{H}_2^+$  after electroionization of thermal  $\text{H}_2$ . *Zeitschrift für Physik D Atoms, Molecules and Clusters*, 28(2):87–88, 1993.
- [40] Friedrich von Busch and Gordon H. Dunn. Photodissociation of  $\text{H}_2^+$  and  $\text{D}_2^+$ : Experiment. *Phys. Rev. A*, 5:1726–1743, Apr 1972.
- [41] Jr. John H. Moore and John P. Doering. Rotational temperature of the  $\text{N}_2^+$  first negative system excited by low-energy electrons. *The Journal of Chemical Physics*, 50(3):1487–1488, 1969.
- [42] T. Schneider, B. Roth, H. Duncker, I. Ernsting, and S. Schiller. All-optical preparation of molecular ions in the rovibrational ground state. *Nat Phys*, 6(4):275–278, 2010.
- [43] M. A. O’Halloran, S. T. Pratt, P. M. Dehmer, and J. L. Dehmer. Photoionization dynamics of  $\text{H}_2 \text{ C } ^1\Pi_u$  : Vibrational and rotational branching ratios. *J. Chem. Phys.*, 87:3288, 1987.
- [44] Øjvind Burrau. Berechnung des energiewertes des wasserstoffmolekel-ions  $\text{H}_2^+$  im normalzustand. *Naturwissenschaften*, 15(1):16–17, 1927.
- [45] E. Schrödinger. Quantisierung als eigenwertproblem. *Annalen der Physik*, 385(13):437–490, 1926.

- [46] L. Wolniewicz and J.D. Poll. On the higher vibration-rotational levels of  $\text{hd}^+$  and  $\text{h}_2^+$ . *Molecular Physics*, 59(5):953–964, 1986.
- [47] E.A. Colbourn and P.R. Bunker. Accurate theoretical vibration-rotation energies and transition moments for  $\text{hd}^+$ ,  $\text{ht}^+$ , and  $\text{dt}^+$ . *Journal of Molecular Spectroscopy*, 63(2):155 – 163, 1976.
- [48] David M. Bishop. Non-adiabatic calculations for  $\text{h}_2^+$ ,  $\text{hd}^+$  and  $\text{d}_2^+$ . *Molecular Physics*, 28(6):1397–1408, 1974.
- [49] R.E. Moss. Calculations for vibration-rotation levels of  $\text{hd}^+$ , in particular for high  $n$ . *Molecular Physics*, 78(2):371–405, 1993.
- [50] R.E. Moss. Calculations for the vibration-rotation levels of  $\text{h}^+ 2$  in its ground and first excited electronic states. *Molecular Physics*, 80(6):1541–1554, 1993.
- [51] H. G. Dehmelt and K. B. Jefferts. Alignment of the  $\text{h}_2^+$  molecular ion by selective photodissociation. i. *Phys. Rev.*, 125:1318–1322, Feb 1962.
- [52] C. B. RICHARDSON, K. B. JEFFERTS, and H. G. DEHMELT. Alignment of the  $\text{h}_2^+$  molecular ion by selective photodissociation. ii. experiments on the radio-frequency spectrum. *Phys. Rev.*, 165:80–87, Jan 1968.
- [53] K. B. Jefferts. Rotational hfs spectra of  $\text{h}_2^+$  molecular ions. *Phys. Rev. Lett.*, 20:39–41, Jan 1968.
- [54] K. B. Jefferts. Hyperfine structure in the molecular ion  $\text{h}_2^+$ . *Phys. Rev. Lett.*, 23:1476–1478, Dec 1969.
- [55] William H. Wing, George A. Ruff, Willis E. Lamb, and Joseph J. Spezeski. Observation of the infrared spectrum of the hydrogen molecular ion  $\text{hd}^+$ . *Phys. Rev. Lett.*, 36:1488–1491, Jun 1976.
- [56] Alan Carrington and Juliet Buttenshaw. Vibration-rotation spectroscopy of the  $\text{HD}^+$  ion near the dissociation limit. *Molecular Physics*, 44(2):267–285, 1981.
- [57] Alan Carrington, Juliet Buttenshaw, and Richard A. Kennedy. Vibration-rotation spectroscopy of the  $\text{HD}^+$  ion near the dissociation limit. *Molecular Physics*, 48(4):775–780, 1983.
- [58] Alan Carrington and Richard A. Kennedy. Vibration-rotation spectroscopy of the  $\text{HD}^+$  ion near the dissociation limit. *Molecular Physics*, 56(4):935–975, 1985.
- [59] Alan Carrington, Iain R. McNab, and Christine A. Montgomerie. Vibration-rotation spectroscopy of the  $\text{HD}^+$  ion near the dissociation limit. *Molecular Physics*, 64(4):679–689, 1988.
- [60] Alan Carrington, Iain R. McNab, and Christine A. Montgomerie. Vibration-rotation spectroscopy of the  $\text{HD}^+$  ion near the dissociation limit. *Molecular Physics*, 64(5):983–995, 1988.

- [61] Alan Carrington, Iain R. McNab, and Christine A. Montgomerie. Spectroscopic observation of  $\text{HD}^+$  in the  $\nu = 22$  level. *Molecular Physics*, 65(3):751–755, 1988.
- [62] Alan Carrington, Iain R. McNab, Christine A. Montgomerie-Leach, and Richard A. Kennedy. Vibration-rotation spectroscopy of the  $\text{HD}^+$  ion near the dissociation limit. *Molecular Physics*, 72(4):735–762, 1991.
- [63] Masaki Hori, Anna Soter, Daniel Barna, Andreas Dax, Ryugo Hayano, Susanne Friedreich, Bertalan Juhasz, Thomas Pask, Eberhard Widmann, Dezso Horvath, Luca Venturelli, and Nicola Zurlo. Two-photon laser spectroscopy of antiprotonic helium and the antiproton-to-electron mass ratio. *Nature*, 475(7357):484–488, 2011.
- [64] Benoît Grémaud, Dominique Delande, and Nicolas Billy. Highly accurate calculation of the energy levels of the  $\text{H}_2^+$  molecular ion. *Journal of Physics B: Atomic, Molecular and Optical Physics*, 31(3):383, 1998.
- [65] J Ph Karr and L Hilico. High accuracy results for the energy levels of the molecular ions  $\text{H}_2^+$ ,  $\text{D}_2^+$  and  $\text{HD}^+$ , up to  $J = 2$ . *Journal of Physics B: Atomic, Molecular and Optical Physics*, 39(8):2095, 2006.
- [66] W.E. Caswell and G.P. Lepage. Effective lagrangians for bound state problems in qed, qcd, and other field theories. *Physics Letters B*, 167(4):437 – 442, 1986.
- [67] T. Kinoshita and M. Nio. Radiative corrections to the muonium hyperfine structure: The  $\alpha^2(Z\alpha)$  correction. *Phys. Rev. D*, 53:4909–4929, May 1996.
- [68] V. B. Berestetsky, E. M. Lifshitz, and L. P. Pitaevsky. *Relativistic Quantum Theory*. Pergamon, Oxford, 1982.
- [69] Vladimir I. Korobov. Leading-order relativistic and radiative corrections to the rovibrational spectrum of  $\text{H}_2^+$  and  $\text{Hd}^+$  molecular ions. *Phys. Rev. A*, 74:052506, Nov 2006.
- [70] Vladimir I. Korobov. Relativistic corrections of  $m\alpha^6$  order to the rovibrational spectrum of  $\text{H}_2^+$  and  $\text{hd}^+$  molecular ions. *Phys. Rev. A*, 77:022509, Feb 2008.
- [71] Vladimir I. Korobov, L. Hilico, and J.-Ph. Karr. Relativistic corrections of  $m\alpha^6(mm)$  order to the hyperfine structure of the  $\text{H}_2^+$  molecular ion. *Phys. Rev. A*, 79:012501, Jan 2009.
- [72] H. A. Bethe. The electromagnetic shift of energy levels. *Phys. Rev.*, 72:339–341, Aug 1947.
- [73] Vladimir I. Korobov, L. Hilico, and J.-Ph. Karr. Theoretical transition frequencies beyond 0.1 ppb accuracy in  $\text{H}_2^+$ ,  $\text{HD}^+$ , and antiprotonic helium. *Phys. Rev. A*, to be published.
- [74] Dimitar Bakalov, Vladimir I. Korobov, and Stephan Schiller. High-precision calculation of the hyperfine structure of the  $\text{HD}^+$  ion. *Phys. Rev. Lett.*, 97:243001, Dec 2006.

- [75] V. I. Korobov, L. Hilico, and J.-Ph. Karr. Hyperfine structure in the hydrogen molecular ion. *Phys. Rev. A*, 74:040502, Oct 2006.
- [76] J Ph Karr, S Kilic, and L Hilico. Energy levels and two-photon transition probabilities in the  $\text{HD}^+$  ion. *Journal of Physics B: Atomic, Molecular and Optical Physics*, 38(7):853, 2005.
- [77] Jean-Philippe Karr. Optique quantique dans les microcavités semi-conductrices - Spectroscopie de l'ion molculaire  $\text{H}_2^+$ , 2008. Habilitation à diriger des recherches.
- [78] Horacio Olivares Piln and Daniel Baye. Quadrupole transitions in the bound rotationalvibrational spectrum of the hydrogen molecular ion. *Journal of Physics B: Atomic, Molecular and Optical Physics*, 45(6):065101, 2012.
- [79] S.T. Pratt, P.M. Dehmer, and J.L. Dehmer. Photoionization of excited molecular states.  $\text{H}_2 \text{ C } ^1\Pi_u$ . *Chem. Phys. Lett.*, 105(1):2833, 1984.
- [80] Jinchun Xie and Richard N. Zare. Selection rules for the photoionization of diatomic molecules. *J. Chem. Phys.*, 93:3033, 1990.
- [81] S.T. Pratt. Excited-state molecular photoionization dynamics. *Rep. Prog. Phys.*, 58(8):821, 1995.
- [82] S.N. Dixit and V. McKoy. Theory of resonantly enhanced multiphoton processes in molecules. *J. Chem. Phys.*, 82:3546, 1985.
- [83] S.N. Dixit and V. McKoy. Ionic rotational selection rules for  $(n + 1)$  resonant enhanced multiphoton ionization. *Chem. Phys. Lett.*, 128(1):4954, 1986.
- [84] S.N. Dixit, D.L. Lynch, and V. McKoy. Theoretical studies of resonantly enhanced multiphoton ionization processes in molecules. In Peter Lambropoulos and Stephen J. Smith, editors, *Multiphoton Processes*, volume 2 of *Springer Series on Atoms+Plasmas*, pages 131–140. Springer Berlin Heidelberg, 1984.
- [85] S. N. Dixit, D. L. Lynch, and V. McKoy. Three-photon resonant four-photon ionization of  $\text{h}_2$  via the  $c^1 \pi_u$  state. *Phys. Rev. A*, 30:3332–3335, Dec 1984.
- [86] A.P. Hickman. Non-Franck-Condon distributions of final states in photoionization of  $\text{H}_2 \text{ C } ^1\Pi_u$ . *Phys.Rev. Lett.*, 59(14):1553, 1987.
- [87] G. Herzberg. *Molecular Spectra and Molecular Structure I. Spectra of Diatomic Molecules*. Van Nostrand Reinhold, Princeton, 1950.
- [88] F. Biraben. *Spectroscopie à deux et trois photons sans élargissement Doppler. Application à l'étude des collisions sodium - gas rare*. PhD thesis, Université Paris VI, Laboratoire de Physique de l'Ecole Normale Supérieure, 1977.
- [89] A.R. Edmonds. *Angular Momentum in Quantum Mechanics*. Princeton University Press, 1974.

- [90] Hans A. Bethe and Edwin E. Salpeter. *Quantum Mechanics of One- and Two-Electron Atoms*. Springer-Verlag, Berlin-Göttingen-Heidelberg, 1957.
- [91] Vincent McKoy and Kwanghsi Wang. private communication.
- [92] A. Aspect, C. Fabre, and G. Grynberg. *Optique Quantique A: Lasers*, volume 1. Ecole Polytechnique, 2006.
- [93] H. KOGELNIK and T. LI. Laser beams and resonators. *Appl. Opt.*, 5(10):1550–1567, Oct 1966.
- [94] Xavier Urbain. private communication.
- [95] B. Fabre. *Paquets d’onde vibrationnels créés par ionisation de  $H_2$  en champ laser intense*. PhD thesis, Université catholique de Louvain, 2005.
- [96] J. Delafosse and G. Mongodin. *Les calculs de la technique du vide*. Société Française des ingénieurs et techniciens de vide, 1961.
- [97] G. Leschhorn, S. Kahra, and T. Schaetz. Deterministic delivery of externally cold and precisely positioned single molecular ions. *Applied Physics B*, 108(2):237–247, 2012.
- [98] S. Kahra. *Trapping and cooling of single molecular ions for time resolved experiments*. PhD thesis, Ludwig-Maximilians-Universität München, 2010.
- [99] G. Leschhorn. *Time-resolved measurements on a single molecular target and Discrete Kink Solitons in Ion traps*. PhD thesis, Ludwig-Maximilians-Universität München, 2011.
- [100] Norman F. Ramsey. *Molecular Beams*. Oxford University Press, 1956.
- [101] Luc Devroye. *Non-Uniform Random Variate Generation*. Springer-Verlag, New York, 1986.
- [102] M. Goeppert-Mayer. *Über Elementarakte mit zwei Quantensprüngen*. PhD thesis, Göttingen, 1930.
- [103] L. S. Vasilenko, V. P. Chebotaev, and A. V. Shishaev. Line Shape of Two-Photon Absorption in a Standing-Wave Field in a Gas. *Pis'ma Zh. Eksp. Teor. Fiz*, 12:161, 1970.
- [104] F. Biraben, B. Cagnac, and G. Grynberg. Experimental evidence of two-photon transition without doppler broadening. *Phys. Rev. Lett.*, 32:643–645, Mar 1974.
- [105] B. Cagnac, G. Grynberg, and F. Biraben. Spectroscopie d’absorption multiphotonique sans effet doppler. *J. Phys. France*, 34:845 – 858, 1973.
- [106] J. E. Bjorkholm and P. F. Liao. Line shape and strength of two-photon absorption in an atomic vapor with a resonant or nearly resonant intermediate state. *Phys. Rev. A*, 14:751–760, Aug 1976.

- [107] C. CohenTannoudji, J. DupontRoc, and G. Grynberg. *Atom-Photon Interactions: Basic Processes and Applications*. New York, NY : Wiley, 1992.
- [108] D. S. Elliott, Rajarshi Roy, and S. J. Smith. Extracavity laser band-shape and bandwidth modification. *Phys. Rev. A*, 26:12–18, Jul 1982.
- [109] B. R. Mollow. Two-photon absorption and field correlation functions. *Phys. Rev.*, 175:1555–1563, Nov 1968.
- [110] D. S. Elliott, M. W. Hamilton, K. Arnett, and S. J. Smith. Correlation effects of a phase-diffusing field on two-photon absorption. *Phys. Rev. A*, 32:887–895, Aug 1985.
- [111] D. S. Elliott, M. W. Hamilton, K. Arnett, and S. J. Smith. Two-photon absorption from a phase-diffusing laser field. *Phys. Rev. Lett.*, 53:439–441, Jul 1984.
- [112] S. Kilic. *Le problème Coulombien à trois corps : états liés, résonances et interaction avec la lumière, vers la spectroscopie vibrationnelle dans  $H_2^+$* . PhD thesis, Université Paris VI, Laboratoire Kastler Brossel, 2005.
- [113] L. D. Landau and E. M. Lifshitz. *Quantum Mechanics*. Pergamon, Oxford, 1977.
- [114] G. Grynberg, F. Biraben, M. Bassini, and B. Cagnac. Three-photon doppler-free spectroscopy: Experimental evidence. *Phys. Rev. Lett.*, 37:283–285, Aug 1976.
- [115] A. Aspect and P. Grangier. *Optique Quantique 2: Photons*, volume 2. Ecole Polytechnique, 2006.